Etude fondamentale de la dissolution des silicates amorphes et cristallins : apport à la robustesse des modèles

Benjamin Cagnon

THÈSE

Pour obtenir le grade de

DOCTEUR DE L'UNIVERSITÉ GRENOBLE ALPES

École doctorale : STEP - Sciences de la Terre de l'Environnement et des Planètes
Spécialité : Sciences de la Terre et de l'Environnement
Unité de recherche : Institut des Sciences de la Terre

Etude fondamentale de la dissolution des silicates amorphes et cristallins : apport à la robustesse des modèles

A fundamental study of amorphous and crystalline silicate dissolution: contribution to the improvement of existing models

Présentée par :

Benjamin CAGNON

Direction de thèse :

Damien DAVAL — Directeur de thèse
CHARGE DE RECHERCHE, Université Grenoble Alpes

Stéphane GIN — Co-directeur de thèse
Université de Montpellier

Rapporteurs :

Stéphanie ROSSANO
PROFESSEURE DES UNIVERSITES, Université Gustave Eiffel

Abdessellam ABDELOUAS
PROFESSEUR, IMT Atlantique

Thèse soutenue publiquement le **8 mars 2024**, devant le jury composé de :

LAURENT TRUCHE, PROFESSEUR DES UNIVERSITES, Université Grenoble Alpes	Président
Damien DAVAL, CHARGE DE RECHERCHE HDR, CNRS délégation Alpes	Directeur de thèse
Stéphane GIN, DIRECTEUR DE RECHERCHE, CEA centre de Marcoule	Co-directeur de thèse
Stéphanie ROSSANO, PROFESSEURE DES UNIVERSITES, Université Gustave Eiffel	Rapporteure
Abdessellam ABDELOUAS, PROFESSEUR, IMT Atlantique	Rapporteur
Philippe BARBOUX, PROFESSEUR DES UNIVERSITES EMERITE, Chimie ParisTech - Université PSL	Examinateur
Odile MAJERUS, MAITRESSE DE CONFERENCES, Chimie ParisTech - Université PSL	Examinatrice
Pierre FRUGIER, CHARGE DE RECHERCHE, CEA centre de Marcoule	Examinateur

Invités :

Nicolas MICHAU
DOCTEUR EN SCIENCES, ANDRA

Anne-Line AUZENDE
MAITRESSE DE CONFERENCES, Université Grenoble Alpes

Thèse présentée pour obtenir le grade de :

DOCTEUR DE L'UNIVERSITE DE GRENOBLE ALPES

Ecole doctorale : Science de la Terre, de l'Environnement et des Planètes

Présentée par

Benjamin CAGNON

Etude fondamentale de la dissolution des silicates amorphes et cristallins : apports à la robustesse des modèles

Soutenance le 08 mars 2024 devant le jury composé de :

Stéphanie ROSSANO	Rapportrice
Abdesselam ABDELOUAS	Rapporteur
Phillipe BARBOUX	Examinateur
Odile MAJERUS	Examinatrice
Pierre FRUGIER	Examinateur
Laurent TRUCHE	Président
Damien DAVAL	Directeur de thèse
Stéphane GIN	Co-directeur de thèse
Nicolas MICHAU	Invité
Anne-Line AUZENDE	Invitée

RESUME

La sureté du stockage géologique des déchets nucléaires de haute activité est un sujet au cœur des grands challenges scientifique et technologique de notre siècle. Ces déchets, issus des combustibles nucléaires, sont vitrifiés et entreposés sur les sites de production (La Hague, Marcoule) en attendant l'ouverture d'un site de stockage définitif. Leur durabilité chimique fait l'objet de nombreux travaux pour évaluer le devenir des radionucléides dans l'environnement. Cette thèse s'inscrit dans cette thématique et repose sur deux axes d'étude.

Le premier se focalise sur l'effet du désordre structural sur la dissolution des silicates à 90°C, en milieu acide (pH 1.5 et 3). Historiquement, deux mécanismes d'altération sont proposés pour expliquer la dissolution des silicates : le mécanisme de dissolution – reprécipitation, généralement attribué aux cristaux, et le mécanisme d'hydrolyse – recondensation, généralement attribué aux verres. Cependant, des études récentes ont montré le besoin de revisiter cette dichotomie. Pour cela, nous avons étudié la dissolution d'un silicate amorphe, le verre albitique, et son équivalent cristallin, l'albite, au contact d'une solution marquée en ^{29}Si. A travers l'incorporation de cet isotope dans la couche altérée, la contribution de la solution à la formation de la couche altérée a pu être quantifiée pour discuter du poids de chacun des mécanismes dans la formation de cette couche. De plus, la présence d'aluminium dans la composition du matériau entre en synergie avec la structure du matériau. Un effet antagoniste a été mis en évidence : i) les cristaux ont une structure ordonnée où l'aluminium renforce les liaisons Si – O – Si, la matrice silicatée est plus résistante à l'hydrolyse et la vitesse de dissolution diminue ; ii) les verres ont une structure désordonnée et les liaisons Si – O – Al ont une énergie d'activation plus basse que les liaisons Si – O – Si. Par conséquent, les liaisons aluminium sont plus facilement hydrolysables, créant des canaux de diffusion au sein du matériau pour les molécules d'eau. La matrice est fragilisée et la vitesse d'altération augmente. En outre, nous avons suggéré que la limitation des propriétés de transport au sein du gel était le phénomène clé contrôlant l'altération tout au long de l'expérience.

Le deuxième axe concerne la dissolution d'un verre modèle (International Simple Glass – ISG) dans un environnement riche en Ca et Si. La sécurité du site de stockage géologique profond repose sur le concept de multi-barrière : la roche hôte du Callovo-Oxfordien, le matériau de remplissage cimentaire, un surconteneur en acier non allié, et enfin le colis en acier inoxydable qui contient le verre nucléaire. Parmi les scenarios à l'étude, il en est un où une solution plus ou moins chargée en Si et Ca entrerait en contact avec le verre. Ce dernier est un matériau complexe constitué d'une trentaine d'oxydes. A des fins de compréhension, nous avons altéré un verre simplifié simulant le verre complexe. Il s'agit du verre ISG – un verre à 6 oxydes, qui est utilisé comme référence par la

communauté verrière internationale. Ce verre a été altéré dans une solution à 90°C autour de pH 10. La littérature montre que la présence de Ca peut avoir des effets antagonistes sur la dissolution du matériau en fonction du milieu. Parmi ces effets, des silicates de calcium hydratés (CSH) peuvent précipiter et promouvoir l'altération du verre.

A travers l'évolution de la vitesse de dissolution, deux observations ont été faites : i) la vitesse d'altération est fortement corrélée à l'état de saturation de la solution par rapport à la silice amorphe. Au-delà de 9%, l'altération est contrôlée par un mécanisme diffusif ; ii) la présence de phases secondaires, en particulier de CSH, n'a qu'un effet secondaire sur la vitesse d'altération à court terme (< 20 jours). Pour les expériences d'une durée plus longue, une reprise d'altération du verre a été observée entre 19 jours et 76 jours, correspondant à une période de croissance des CSH et suggérant un basculement du mécanisme d'altération limitant de la diffusion vers l'hydrolyse. Après cette période, une compétition entre la formation des CSH et celle des carbonates de calcium limite l'altération du verre. Cette dernière est alors contrôlée à nouveau par un processus diffusif.

Enfin, l'effet du Ca et les propriétés diffusives du gel formé au cours des 20 premiers jours d'altération, a été étudié plus en détail. Nous avons constaté que l'ajout de calcium dans la solution diminue la vitesse d'altération, comme en témoigne la corrélation négative entre épaisseur des gels et teneur en Ca de la solution. Deux effets principaux sont discutés : le premier consiste en un effet catalytique du Ca sur la recondensation du gel et le second sur la formation d'une couche riche en Si et Ca qui passive le gel. De plus, nous avons étudié les propriétés diffusives du gel en calculant un coefficient de diffusion au sein de cette couche suivant trois méthodes différentes : par épaisseur totale sur la base du relargage du B en solution, par épaisseur totale sur la base des analyses du solide et par suivi de l'incorporation d'un isotope de B au sein de des couches de surface à la fin de l'expérience. Nous avons constaté que les coefficients de diffusions estimés sur l'expérience de traçage étaient systématiquement inférieurs de plusieurs ordres de grandeur à ceux basés sur l'épaisseur totale du gel. Si cette différence s'explique en partie par une différence de température, d'autres hypothèses telles que i) l'évolution des propriétés de diffusivité de la couche au cours de l'expérience, ii) une différence de diffusivité entre la pénétration et le relargage d'éléments au sein de cette couche ou encore iii) une restructuration post-mortem du gel, sont discutés.

En conclusion, ces travaux apportent plusieurs contraintes pour la compréhension du continuum mécanistique existant entre la dissolution des silicates cristallins et vitreux. L'Al joue un rôle clé dans l'altération des silicates et, combiné avec l'ordre (le désordre) structurale favorise (diminue) les propriétés de passivation de la couche. De plus, ces travaux proposent de nouvelles informations sur la dissolution des verres dans des environnements chimiques pertinents pour le

stockage géologique à long terme. Les précipités, ainsi que leurs évolutions, jouent un rôle décisif dans l'histoire de l'altération du verre.

ABSTRACT

The safety of high-level nuclear waste geological storage is a major scientific and technological challenges of our century. These wastes, inherited from nuclear fuels, are vitrified and stored on production sites (La Hague, Marcoule), waiting on the opening of a storage facility. Their chemical durability is the object of several studies to assess the impact of the release of radionuclides in the environment. Based on this background, this thesis relies on two axes.

The first axis focuses on the effect of structural disorder on the dissolution of silicates at 90°C in an acidic environment (pH 1.5 and 3). Historically, two alteration mechanisms have been identified to explain silicate dissolution: the dissolution–reprecipitation mechanism, generally attributed to crystals, and the hydrolysis–recondensation mechanism, generally attributed to glasses. However, recent studies have shown the need to revisit this dichotomy. To address this point, the dissolution of an amorphous silicate, albite glass, and its crystalline equivalent, albite feldspar, in contact with a solution marked with 29Si was studied. Through the incorporation of this isotope into the altered layer, the contribution of the solution to the formation of the altered layer was quantified to discuss the significance of each mechanism in the layer's formation. Additionally, the presence of aluminum in the material's composition acts synergistically with the material's structure. An antagonistic effect was highlighted: i) crystals have an ordered structure where aluminum strengthens the Si–O–Si bonds, making the silicate matrix more resistant to hydrolysis and reducing the dissolution rate; ii) glasses have a disordered structure, and the Si–O–Al bonds have a lower activation energy than the Si–O–Si bonds. As a result, aluminum bonds are more easily hydrolysable, creating diffusion channels for water molecules within the material. The matrix is weakened, and the alteration rate increases. Moreover, we suggested that the limitation of transport properties within the gel was the key phenomenon controlling the alteration throughout the experiment.

The second axis concerns the dissolution of a model glass (International Simple Glass – ISG) in an environment rich in Ca and Si. The safety of the deep geological storage site relies on the concept of multi-barrier protection: the Callovo-Oxfordian host rock, cementitious filling material, a non-alloyed steel overpack, and finally, the stainless-steel canister containing the nuclear glass. One of the most likely scenarios suggest that environmental fluids more or less concentrated in Si and Ca would come into contact with the glass. This glass is a complex material composed of around thirty oxides. For simplicity and comprehension purposes, we altered a glass simulating the complex glass. This is the ISG glass – a 6-oxide glass used as a reference by the international glass community. This glass was altered in a solution at 90°C with a pH around 10. Literature shows that the presence of Ca can have

antagonistic effects on the material's dissolution depending on the environment. Among these effects, calcium silicate hydrates (CSH) can precipitate and promote glass alteration.

Through the evolution of the dissolution rate, two observations were made: i) the alteration rate is strongly correlated with the solution's saturation state with respect to amorphous silica. Beyond 9%, the alteration is controlled by a diffusive mechanism ; ii) the presence of secondary phases, especially CSH, has only a secondary effect on the short-term alteration rate (<20 days). For longer duration experiments, a resumption of glass alteration was observed between 19 days and 76 days, corresponding to a period of CSH growth and suggesting a shift in the alteration mechanism from diffusion-limiting process towards hydrolysis-limited process. After this period, a competition between the formation of CSH and calcium carbonate limited the glass alteration. The latter is then controlled again by a diffusive process.

Finally, the effect of Ca and the transport properties of the gel formed during the first 20 days of alteration were studied in more detail. It was observed that the addition of calcium to the solution reduces the alteration as inferred from the decrease in the gel thickness. Two main effects are discussed: the first consists of a catalytic effect on the recondensation of the gel, and the second on the formation of a (Si, Ca)-rich layer that passivates the gel. Furthermore, the transport properties of the gel were investigated by calculating a diffusion coefficient within this layer using three different methods: based on the total gel layer thickness using the release of B into the solution, based on the total gel layer thickness from solid analyses, and based on the tracing experiment using the incorporation of a B isotope at the end of the experiment. It was found that the diffusion coefficients based on the tracing experiment were systematically several orders of magnitude lower than those based on the total thickness of the gel. If this difference is partly explained by a variation in temperature, other hypotheses such as i) the evolution of the transport properties of the gel layer during the experiment, ii) a difference in diffusivity between the penetration and release of glass elements within this layer, or iii) a post-mortem restructuration of the gel, are discussed.

In conclusion, this work brings several critical information to the understanding of the mechanistic continuum existing between the dissolution of crystalline and vitreous silicates. Aluminum plays a key role in the alteration of silicates, and, combined with structural order (respectively, disorder), it promotes (respectively, decreases) the passivation properties of the layer. Moreover, this research provides new insights into the glass dissolution in chemically relevant environments for long-term geological storage. The precipitates, along with their evolution, play a decisive role in the history of glass alteration.

Table des matières

PREFACE

A travers les âges, l'évolution de l'humanité a été inextricablement liée au développement des énergies. En commençant par la maitrise du feu, puis du vent et de l'eau, l'usage du bois, du pétrole et du gaz, chaque société a du faire preuve d'ingéniosité pour répondre à une demande énergétique toujours plus importante. Il y a à peine plus de deux siècles, notre société est entrée dans l'ère dite industrielle. L'économie, alors essentiellement agraire, s'est tournée vers une production de biens manufacturés à grande échelle. Des innovations techniques majeures comme la machine à vapeur, sociale, avec l'école et économique, avec par exemple les magasins de grande surface, voient progressivement le jour. Pour supporter cette dynamique d'industrialisation, des recherches sont menées sur une nouvelle source d'énergie : l'électricité. Un des pionniers est l'inventeur américain Thomas Edison qui conçut la première lampe électrique (un filament de bambou brûlant au sein d'une bulle de verre) en 1879. Par la suite, différents concepts sur l'électricité apparaissent vers la fin du XVIIIe siècle notamment suite aux travaux de Benjamin Franklin, Luigi Galvani ou encore Henry Cavendish. Il faudra cependant attendre la fin du XIXe siècle et le début du XXe siècle pour que cette énergie prenne son essor grâce au génie de Nikola Tesla, considéré comme le père de l'électricité moderne. L'électricité devient alors incontournable. Les méthodes de production se diversifient rapidement : à partir d'énergies fossiles comme le charbon ou le pétrole ou des énergies dites vertes, comme le soleil, le vent ou la marée. Une nouvelle source d'énergie voit le jour au milieu du XXe siècle, suite aux découvertes fondamentales sur la nature de la matière : l'énergie atomique. Cette énergie correspond à la force de cohésion entre les nucléons (protons et neutrons) avec le noyau de l'atome. Elle correspond à une énergie d'environ 940 MeV d'après la relation d'Einstein $E = mc^2$, et est un million de fois supérieur à l'énergie chimique qui représente la force de cohésion entre un électron et le noyau (par exemple, cette énergie vaut 13,6 eV pour l'hydrogène). C'est en 1963 que la première centrale nucléaire, basée sur l'énergie de l'atome et produisant de l'électricité, voit le jour en France.

Dans les années 1960 à 1970, l'énergie du nucléaire se pose comme une alternative énergétique au pétrole, jusqu'alors en plein essor, qui subit deux chocs financiers en 1973 et 1979. Dans cette même période, les consciences s'éveillent sur l'impact de l'homme et les conséquences de notre consommation énergétique sur notre planète. Le terme de « réchauffement climatique » apparait pour la première fois dans un article paru dans *Science*, écrit par le climatologue Wallace Broecker en 1975. Cela amènera à la découverte du trou dans la couche d'ozone de la haute atmosphère en 1987 qui aura un impact global et dont l'enjeu dépassera la communauté scientifique pour devenir un enjeu mondial (Rapport du Sommet de Rio, 1992).

Les limites naturelles des ressources fossiles, notamment le charbon, gaz et pétrole, ainsi que le réchauffement climatique incitent à se tourner vers de nouvelles énergies. L'attention de la société sur porte alors sur deux types d'énergies : les énergies renouvelables, notamment la géothermie, l'hydraulique et l'éolienne, ainsi que les énergies décarbonées (ou faiblement émettrice de CO_2), dont l'énergie nucléaire. Cette dernière suscite, dès son apparition, un enthousiasme global, par sa production d'électricité abondante, continue et économique compétitive. Aujourd'hui, forte de ses 56 réacteurs nucléaires, la France se positionne en tant que leader européen de l'énergie nucléaire et génère pas moins de 70% de son électricité grâce à cette énergie. Dans cette continuité, le Président Macron annonce en février 2022 un nouveau programme de construction de 6 réacteurs nucléaires nouvelle génération et 8 autres en option. EDF estime que, dans le meilleur des cas, ces 6 réacteurs nucléaires devraient être opérationnels par paire à partir de 2035, 2038 et 2042. Le gouvernement français souhaite atteindre une neutralité carbone à partir de 2050 grâce à 8 réacteurs nucléaire supplémentaires.

Cependant, certains sujets font débat. Si les conséquences dramatiques d'un accident de fusion de cœur au sein d'une centrale nucléaire figurent parmi les dangers les plus inquiétants pour le grand public, un autre inconvénient souvent mis en avant est la production de déchets radioactifs à haute activité (HA) et à vie longue (VL). Bien que ces déchets soient générés en faible quantité en comparaison avec l'énergie produite, tant qu'ils demeurent radioactifs, ils représentent un danger pour l'homme et l'environnement. Leur confinement et leur gestion est alors un sujet majeur qui amènera le gouvernement français à créer une agence dédiée à la question en 1979 (Agence Nationale pour la gestion des Déchets Radioactifs (l'Andra)). Cette dernière conduit des recherche et met en œuvre les décision prises dans le domaine. En 1991, la loi dite « Bataille » est promulguée et trois axes de recherches sont initiés sur une période de 15 ans. Le CEA est chargé du premier et second axe de recherche, à savoir la séparation et la transmutation des éléments radioactifs à vie longue, ainsi que le conditionnement et l'entreposage de longue durée des déchets HA et MA-VL en surface (CEA Marcoule et La Hague). L'Andra, quant à elle, est chargé d'étudier le stockage des déchets radioactifs en couche géologique profonde. C'est dans le cadre de ces recherches que l'Andra construit le laboratoire souterrain dans la commune de Bure (départements de la Meuse et Haute-Marne) en 2000. Cette période de 15 ans de recherche a conduit en 2006, à privilégier le stockage en couche géologique profonde pour gérer de manière définitive les déchets radioactifs à vie longue.

Ce site de stockage repose sur un concept multi barrières afin de limiter au maximum le transfert des radionucléides dans l'environnement. Le principal critère retenu est une exposition des populations qui doit rester inférieure au seuil de 0.25 mSv/an quelle que soit le temps et pour tous les scénarii d'évolution du stockage envisagés. Ce concept multi barrières comprend le verre de

conditionnement dans son conteneur en acier inoxydable, le surconteneur en acier non allié et la roche hôte. Concernant cette dernière, il s'agit d'une couche d'argilite du Callovo-Oxfordien d'environ 120 m d'épaisseur, située entre 400 et 500 m sous la surface. Elle possède une faible perméabilité aqueuse et ne comprend pas de failles géologiques qui pourraient favoriser la circulation de l'eau. Un des principaux enjeux de ce concept est de contenir les radionucléides en profondeur, en limitant les phénomènes de corrosion et les transferts via la phase aqueuse. Cependant, parmi les scenarii les plus probables, il est envisagé que l'eau finisse par entrer en contact avec le verre, entraînant son altération et une potentielle mise en solution des radionucléides. Un matériau cimentaire est envisagé pour colmater les vides situés entre les parois des alvéoles du site de stockage et les conteneurs métalliques. Ainsi il est attendu que le verre s'altère au contact d'une solution un pH basique. La compréhension des mécanismes et des cinétiques d'altération du verre sur des échelles de temps géologique dans un tel environnement devient dès lors un enjeu important pour calculer les performances des barrières de confinement et démontrer la sûreté du site de stockage.

Sur la base de nombreuses expérimentations portant sur le pH de la solution, la température et les conditions physico-chimiques, les mécanismes d'altération du verre sont identifiés, permettant l'élaboration de modèles prédictifs d'évolution cinétique. Ces derniers sont indispensables car l'expérimentation en conditions réelles ne permet pas d'accéder aux temps longs nécessaires à la démonstration de sûreté. Ces modèles permettent ainsi d'extrapoler les résultats obtenus en laboratoire et de les comparer à des études menées sur des matériaux vieux de quelques milliers, voire centaines de milliers d'années (analogues naturels ou archéologiques).

C'est dans ce cadre que s'inscrit cette thèse, issue d'une collaboration entre l'Andra, EDF, le CNRS et le CEA, et intitulée « Etude fondamentale de la dissolution des silicates amorphes et cristallins : apport à la robustesse des modèles ». Le premier chapitre reprend en détails le contexte de cette étude ainsi que le cadre général du stockage des déchets radioactifs actuellement envisagé par l'Andra. Le deuxième chapitre présente un état de l'art sur les mécanismes et les cinétiques d'altération du verre. Une attention particulière est portée sur les effets antagonistes du calcium sur la passivation du gel formé à la surface du verre lors de son altération. Sachant que le matériau de remplissage est un matériau cimentaire et que les silicates de calcium hydratés (CSH) sont le principal liant du ciment de Portland, ces derniers sont susceptibles de se retrouver dans la solution altérante du verre. De ce fait, leur structure, solubilité, mécanisme de formation et enfin, leur carbonatation en présence de CO_2 seront aussi présentés pour clôturer ce chapitre.

Les trois chapitres suivants représentent le cœur de cette thèse. Ils ont soit fait l'objet d'une publication, soit figurent en préparation d'une soumission dans une revue à comité de lecture. Afin de

répondre au mieux à la problématique proposée, l'étude a été scindée en deux axes. Le premier axe est une étude mécanistique comparative entre la dissolution d'un silicate amorphe (un verre albitique) et son équivalent cristallin (un cristal d'albite) en milieu acide. L'effet du désordre structural est étudié et les résultats sont discutés dans le troisième chapitre. Le second axe traite de l'altération d'un verre modèle, International Simple Glass (ISG), dans un milieu basique (pH 10 à 90°C) et propice à la formation de CSH, autrement dit, un environnement riche en calcium et en silice. Le chapitre quatre étudie notamment l'effet du calcium sur les propriétés de transport du gel à temps court (après 21 jours d'altération). L'effet de la silice dissoute et des phases secondaires, en commençant par les CSH puis les carbonates de calcium, sur la vitesse d'altération du verre sont présentés dans le cinquième chapitre qui clôture ce second axe.

L'ensemble de ces résultats est repris dans le sixième chapitre où l'influence des paramètres clés issus de chaque chapitre est synthétisée afin de proposer une vue globale des mécanismes d'altération du verre. Des perspectives ainsi que de futurs pistes de recherches sont proposées sur la base des résultats de cette thèse.

Chapitre I. INTRODUCTION, CONTEXTE ACTUEL DE LA GESTION DES DECHETS RADIOACTIFS

Ce premier chapitre définit le cadre dans lequel s'inscrit cette thèse, à savoir la gestion des déchets nucléaires à vie longue. Dans un premier temps, les différents secteurs produisant des déchets radioactifs seront introduits avant une présentation des différents types de déchets radioactifs existants. Nous nous focaliserons ensuite sur les déchets de haute activité (HA) et de moyenne activité à vie longue (MA-VL) qui sont au cœur de la problématique de cette thèse. Nous justifierons le développement d'une matrice vitreuse pour confiner durablement les radionucléides. Enfin, nous aborderons les différentes modalités ayant conduit au choix du stockage en couche géologique profonde. Les différentes étapes nécessaires à cette installation, les raisons de sa localisation spécifique ainsi que le devenir du site seront discutés.

I.1. Les produits issus d'une réaction nucléaire

I.1.1. Provenance des déchets radioactifs et leur appellation

La radioactivité est un phénomène par lequel certains atomes, aussi appelée radionucléides, libèrent de l'énergie sous forme de particules et/ou de rayonnement, en se désintégrant. Ce phénomène a lieu dans la nature ou peut être forcé. Il existe trois secteurs principaux qui utilisent aujourd'hui la radioactivité et produisent en conséquence des déchets radioactifs (les % représentent les volumes de déchets en équivalent conditionné déjà stockés ou destinés à être pris en charge par l'Agence nationale de gestion des déchets radioactif, l'Andra, à la fin 2021) :

- L'industrie électronucléaire (60,9 %) dont la principale utilisation est la production d'électricité. En France, près de 70% de l'électricité est produite par des centrales nucléaires. On compte aussi dans ce secteur les usines de fabrication du combustible et les usines dédiées au traitement des déchets.

- La recherche scientifique (26,6 %) dans les domaines de l'agronomie, la chimie, la biologie, la physique du nucléaire et des particules, et le nucléaire civil entre autres.

- La défense nationale (8,7 %) où la radioactivité est principalement utilisée comme force de dissuasion ou comme source de propulsion pour des bâtiments navals.

Deux autres secteurs sont aussi acteurs de la production de ces déchets mais dans un volume beaucoup plus faible. Il s'agit de :

- L'industrie non-dédiée au nucléaire (3,3 %) dont les principaux enjeux liés à la radioactivité sont l'extraction des terres rares, la stérilisation et la conservation de produits alimentaires.

- Enfin la médecine (0,5 %), à travers les activités de scanner et de radiologie telle que par exemple, la radiothérapie. Même si la médecine est un secteur qui produit peu de déchets radioactifs, elle représente 35% de l'exposition moyenne de la population à la radioactivité.

Les déchets radioactifs sont produits lors du fonctionnement des diverses installations dans chacun des secteurs susmentionnés mais aussi lors du démantèlement de ces installations. La plupart des déchets produits par les centrales nucléaires sont retraités (environ les deux tiers) et seule une faible partie d'entre eux, appelée les déchets « ultimes » est conditionnée et vitrifiée. Les déchets sont catégorisés selon leur niveau d'activité (nombre de désintégration de noyaux par seconde, exprimé en becquerel, Bq) et leur période radioactive (durée nécessaire à un radionucléide pour voir sa

radioactivité divisée par deux). On distingue 6 catégories qui sont reportées dans la Table I-1. Ce sont les déchets de haute activité (HA) et moyenne activité – vie longue (MA-VL) qui constituent le principal enjeu du traitement des déchets radioactifs à long terme et qui sont au cœur de la problématique scientifique de cette thèse.

Tableau I-1: Tableau récapitulant les différents types de déchets radioactifs en fonction de leur activité et de leur période radioactive. Les méthodes de gestion ainsi que les volumes (m^3) des colis primaires y sont reportés selon l'inventaire de l'Andra à la fin 2021 {https://inventaire.andra.fr/}.

<table>
<tr><th>Période
Activité</th><th>Vie très courte (VTC),
période < 100 jours</th><th>Vie courte (VC),
Période ≤ 31 ans</th><th>Vie longue (VL),
Période > 31 ans</th></tr>
<tr><td>Très faible activité (TFA)
< 100 Bq/g</td><td rowspan="3">Déchets VTC
Gestion par décroissance radioactive.
2 170 m³</td><td colspan="2">Déchets TFA
Stockage de surface dans un centre industriel de regroupement, d'entreposage et de stockage
633 000 m³</td></tr>
<tr><td>Faible activité (FA)
Quelques centaines Bq/g à un million Bq/g</td><td>Déchets FMA-VC
Stockage de surface dans les centres de l'Aube et de la Manche
981 000 m³</td><td>Déchets FA-VL
Stockage à faible profondeur à l'étude (entre -15m et -200m)
103 000 m³</td></tr>
<tr><td>Moyenne activité (MA)
Un million à un milliard Bq/g</td><td>Déchets MA-VL
Stockage géologique profond (à -500 m) – projet Cigéo
39 500 m³</td></tr>
<tr><td>Haute activité (HA)
Plusieurs milliards Bq/g</td><td></td><td colspan="2">Déchets HA-VL
Stockage géologique profond (à -500 m) – projet Cigéo
4 320 m³</td></tr>
</table>

I.1.2. Les déchets dans le cadre du projet Cigéo

Parmi les 6 catégories de déchets radioactifs, seuls les déchets HA et MA-VL seront stockés en formation géologique profonde étant donné le niveau élevé et la durée de leur toxicité. Ils représentent respectivement 0,2% et 2,2% du volume total de déchets produits en France, ainsi que 94,9% et 4,9%, de la radioactivité totale, toutes catégories confondues. Ensemble, ils représentent donc à peine 2,4% du volume total de déchets produits mais concentrent près de 99,8% de la radioactivité totale.

Les déchets HA sont issus du traitement des combustibles usés. Ils sont principalement constitués de produits de fission et d'actinides mineurs. Ils sont vitrifiés dans un conteneur en acier inoxydable et entreposés temporairement sur leur site de production (La Hague, Marcoule) en attente de la mise en service du site de stockage géologique profond, dans le cadre du projet Cigéo. Les déchets

MA-VL quant à eux proviennent principalement de métaux tels que les gaines et les éléments de structure des assemblages de combustibles usés, des boues issues du traitement des effluents contaminés et enfin, des outils et équipements exposés à la radioactivité lors de leur fonctionnement. Les déchets MA-VL sont conditionnés dans plusieurs types de matrices (verre, ciment ou bitume) dans des conteneurs métalliques ou en béton. Ils sont également entreposés en attendant l'ouverture du centre de stockage géologique.

I.1.3. Vitrification des déchets

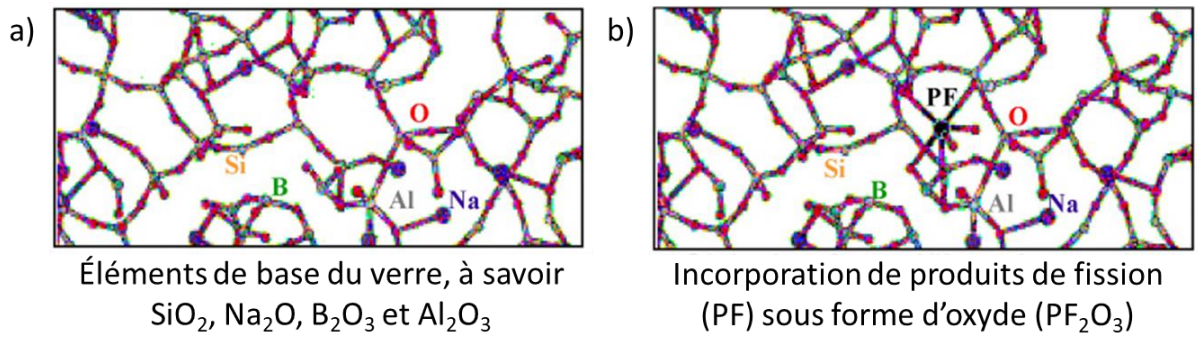

Figure I-1: Principe de confinement des radionucléides par incorporation dans un réseau borosilicaté, extrait Godon, 2004 [4]. Ces images ont été obtenues par dynamique moléculaire et représentent a) la structure amorphe du verre ainsi que ses principaux éléments ayant un rôle de formateur de réseau et b) l'incorporation d'un oxyde de produit de fission de l'U (PF_2O_3), comme La_2O_3 par exemple, confiné au sein de la matrice vitreuse en formant des liaisons avec les éléments constitutifs du verre.

Le verre borosilicaté a été choisi pour confiner les déchets HA pour sa capacité à former des liaisons chimiques avec la plupart des éléments présents (alcalins, alcalino-terreux, métaux de transition, lanthanides, actinides). Le bore est un élément essentiel, il permet de baisser la température d'élaboration du verre et d'augmenter la solubilité de certains éléments, en assurant la fabrication d'un matériau homogène. Le verre borosilicaté possède aussi une bonne stabilité thermique[1], durabilité chimique et tenue à l'auto-irradiation[2]. Cependant, chacune de ces propriétés est étroitement liée à la composition du verre, et sa durabilité chimique dépend fortement des conditions d'environnement.

Ainsi, dans les années 1970, le CEA a mis au point une formule de verre borosilicaté qui optimise le taux de charge en déchets et répond aux exigences de performance et de faisabilité technologique en caisson blindé (Fig. I-1). Ce verre, fabriqué dans les deux ateliers R7 et T7 de l'usine Orano du site de La Hague depuis 1989, porte le nom R7T7 et est composé à 80% de SiO_2, B_2O_3, Al_2O_3, Na_2O et CaO. Les 20% restant sont composés par environ 25 oxydes. Le silicium, l'aluminium et le bore jouent un rôle de formateur de réseau grâce aux liaisons iono-covalentes avec les atomes d'O. Cette structure constitue le réseau vitreux. Les autres éléments ont un rôle de modificateurs du réseau : ils forment des liaisons non-pontantes avec les oxygènes. Le verre R7T7 est en réalité un domaine de

composition au sein duquel les principaux éléments peuvent varier dans des plages prédéfinies. Un verre de référence simulant, dans lequel les radionucléides ont été remplacés par des isotopes stables a été défini pour poursuivre les recherches sur ce matériau. Il s'agit du verre SON68. D'autres verres, plus simples ont été formulés pour servir de modèles pour les études de base. On peut citer le verre ISG (*International Simple Glass*) qui se limite aux six principaux oxydes du verre SON68 et qui sert de référence pour la communauté scientifique [3]. C'est sur ce verre que porte la seconde étude de cette thèse.

I.2. Le stockage réversible en formation géologique profonde

I.2.1. Concept du stockage réversible en profondeur

Suite à l'apparition de l'énergie électronucléaire, la question sur la gestion des déchets a fait débat au niveau politique, citoyen et scientifique. Le Conseil Supérieur de la Sûreté Nucléaire (CSSN), à la demande du ministre de l'Industrie, crée en 1981 une commission chargée d'étudier le devenir de ces déchets. Dans le courant des années 1980, elle demande à la communauté scientifique d'étudier différentes formations rocheuses dans l'optique d'un stockage géologique profond. Suite aux difficultés rencontrées par l'Andra à trouver un site pour créer un laboratoire de recherche souterrain, la loi dite « Bataille », en référence au député éponyme fut promulguée en 1991. Elle offre une période de 15 ans de réflexion et de recherches sur la gestion de ces déchets, par transmutation, entreposage ou stockage géologique. Les recherches menées ont permis d'identifier un site dont la géologie est favorable à l'implantation d'un stockage profond de déchets radioactifs dans l'Est de la France et a conduit à l'implantation d'un laboratoire souterrain à la limite de la Meuse et de la Haute-Marne (voir section I.2.2.) [5]

En 2006, une nouvelle loi confirme le choix du stockage géologique profond pour les déchets à vie longue. Les études et recherches en vue de choisir un site et de concevoir un centre de stockage sont confiées à l'Andra. Une nouvelle contrainte est ajoutée au cahier des charges, rendant les installations réversibles sur une durée de cent ans. Cette disposition permet de laisser des choix aux générations suivantes et notamment la possibilité de récupérer des déchets stockés ou d'adapter les solutions techniques de stockage au regard des progrès scientifiques et technologiques.

Enfin, la dernière loi en date, c'est-à-dire celle de 2016, propose le plan directeur pour l'exploitation et la gouvernance du projet de stockage Cigéo (Centre industriel de stockage géologique). Les modalités de création de ce projet ainsi que les installations et les méthodes de réversibilité sont précisées. La figure I-2 présente le calendrier prévisionnel des grandes étapes du projet de stockage Cigéo jusqu'à la mise en service du site de stockage géologique et sa fermeture (Fig.

I-2). Ce calendrier est légèrement différent de celui annoncé dans la loi de 2006 puisqu'il prend en compte les différentes mises à jour qui ont eu lieu depuis cette loi.

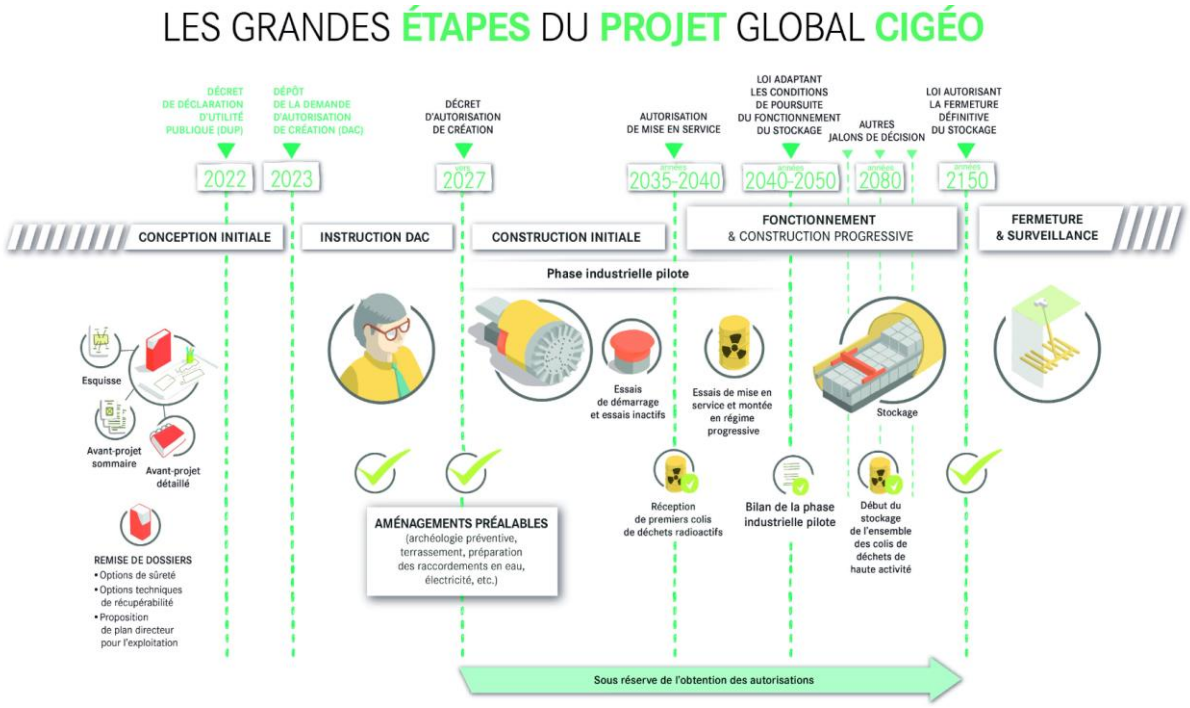

Figure I-2: Calendrier prévisionnel des différentes grandes étapes à venir du projet Cigéo allant de la conception initiale du projet jusqu'à sa mise en service et sa fermeture après la période d'exploitation, d'après l'Andra (https://www.andra.fr/).

Dans l'attente de la fin de construction de Cigéo et de sa mise en service, les colis vitrifiés sont entreposés sur les sites de production (La Hague et Marcoule). Cela permet entre autres de diminuer la température du colis ainsi que son activité en vue du stockage dans une couche géologique.

Le stockage en couche géologique profonde, par sa profondeur, sa conception et son implantation dans une roche argileuse imperméable et dans un environnement géologique stable, permet de mettre les déchets à l'abri des activités humaines et des événements naturels de surface (comme l'érosion) et d'isoler les déchets HA et MA-VL de l'homme sur de très longues échelles de temps. Il impose par principe un relâchement des radionucléides susceptibles d'atteindre la biosphère qui ne dépasserait pas une dose 0.25 mSv/an, limite réglementaire sur l'exposition des populations à la radioactivité. Le conditionnement des déchets radioactifs puis la roche argileuse permettent de confiner les éléments radioactifs contenus dans les déchets afin de limiter et ralentir le transfert de ces éléments jusqu'à la surface.

Dans un premier temps, ce sont les matériaux utilisés pour conditionner les déchets qui assureront le confinement de la radioactivité. Avec le temps, les colis de déchets se dégraderont progressivement et ce sont les propriétés de la roche qui permettront de limiter fortement le

déplacement des éléments radioactifs contenus dans les déchets : la couche géologique assure le confinement des radioéléments sur de très longues périodes.

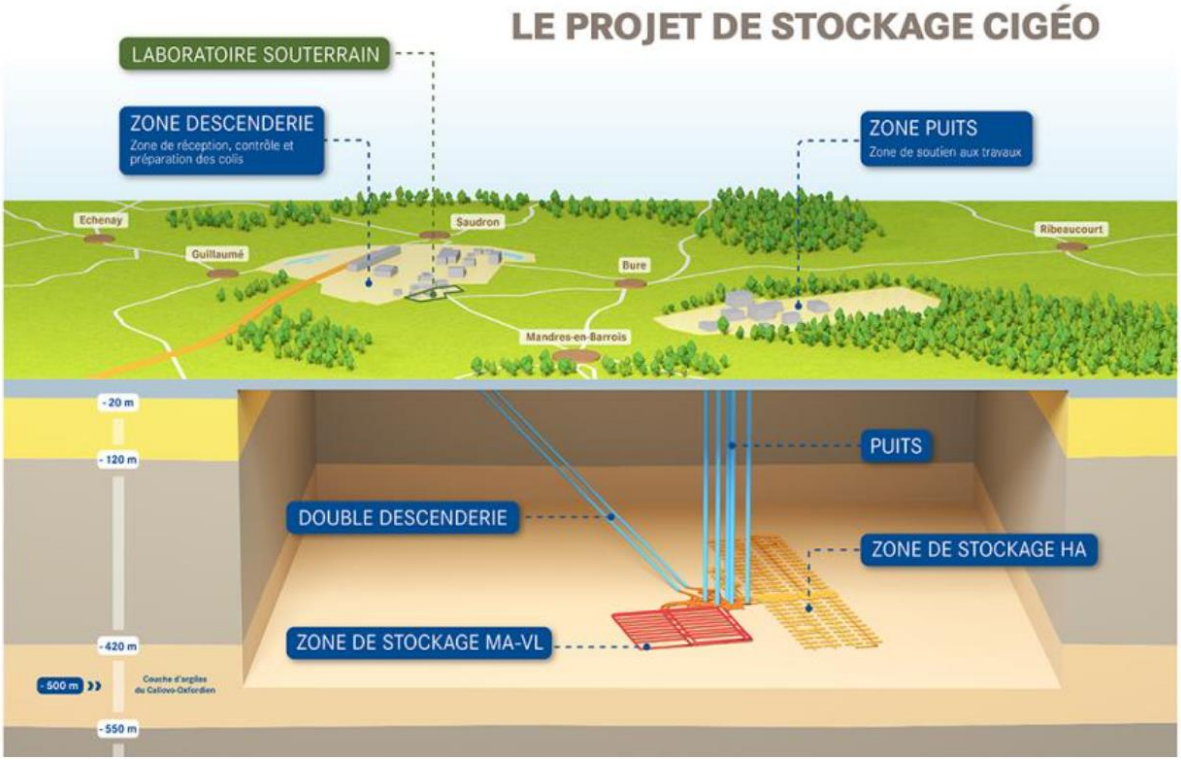

Figure I-3: Schéma de principe du projet Cigéo présentant la localisation ainsi que les différentes installations de stockage, d'après l'Andra ((https://www.andra.fr/).

I.2.2. Le site de la Meuse Haute-Marne

La zone d'implantation du centre de stockage géologique profond, choisi à l'issue de la loi Bataille, se trouve au nord-est du Bassin parisien, sur les départements de la Meuse et Haute-Marne. Depuis 2001, un laboratoire souterrain y a été construit sur la commune de Bure pour étudier les propriétés de la roche argileuse du Callovo-Oxfordien (Fig. I-3). Cette roche sédimentaire, vieille de 155 millions d'années a été sélectionnée pour plusieurs raisons : i) La stabilité géologique locale ainsi que son homogénéité sur une zone de plus de 100 km^2 et une profondeur de 400 m à 600 m, ii) l'absence de failles qui favoriseraient la circulation de l'eau, iii) les propriétés de transport et de rétention des radionucléides de la roche qui possède une faible perméabilité (10^{-12} à 10^{-14} $m.s^{-1}$)[5,6], une faible porosité (14 % à 17 %)[7], une faible diffusivité[8] ainsi qu'une capacité élevée de sorption des cations.

Les colis et zones de stockage des déchets HA et MA-VL sont différents (Fig. I-4). Les déchets HA sont introduits dans un conteneur de stockage en acier non allié, destinés à être stockés dans des alvéoles horizontales d'environ 70 cm de diamètre et d'une centaine de mètres de long, creusées dans la roche argileuse et équipées d'un tube guide (chemisage) en acier non allié. Un matériau de

remplissage cimento-bentonique est injecté entre le chemisage et la roche afin de limiter la corrosion de celui-ci. Le chemisage contribue aux principes de réversibilité puisqu'il permet aux générations futures de retirer ces colis si le besoin se présente pendant la période de fonctionnement.

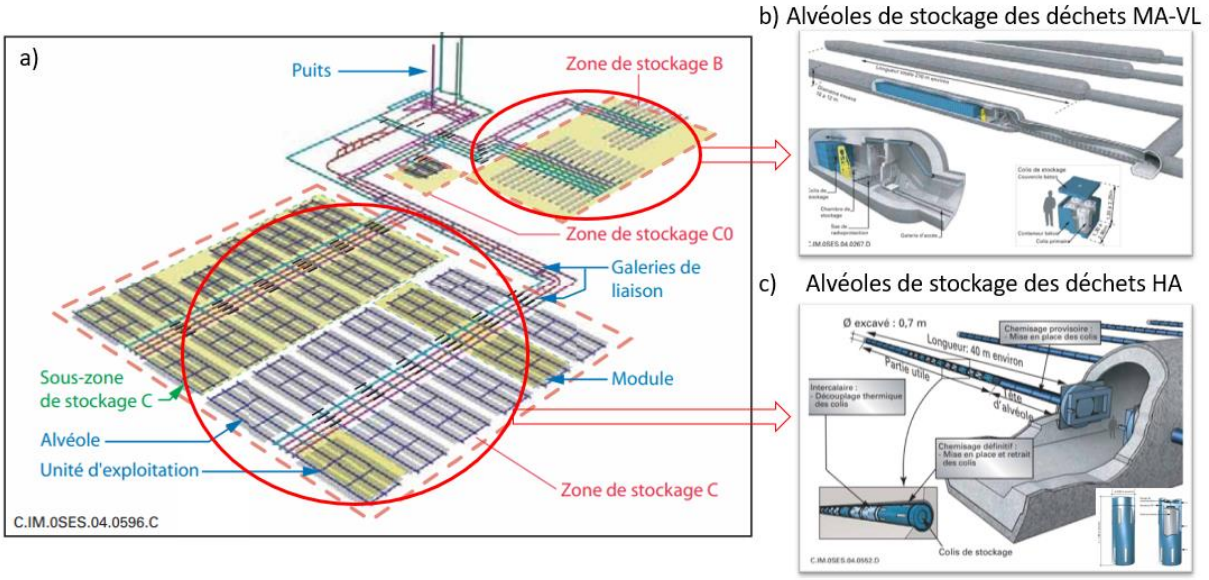

Figure I-4: Schéma du principe des installations de stockage des déchets radioactifs d'après l'Andra [9]. a) Schéma global de la disposition du stockage souterrain dans la roche du Callovo-Oxfordien. Les zones de stockage B et C correspondent respectivement à la zone de stockage des déchets MA-VL (B) et HA (C). b) Concept des alvéoles de stockage pour les déchets MA-VL ainsi que leur colis. c) Concept des alvéoles de stockage pour les déchets HA ainsi que leur colis.

I.2.3. Devenir du site

Compte tenu de du niveau de radioactivité des déchets HA, les simulations du devenir des radionucléides dans l'environnement sont conduites sur plusieurs centaines de milliers d'années. L'Andra envisage un scénario nominal (le plus probable) et des scénarios dégradés pour tester la robustesse du concept de stockage. Un des principaux scenarios est le suivant : une fois le site de stockage fermé, du fait de la présence d'oxygène apporté pendant la phase d'exploitation, une phase initiale oxydante d'une durée inférieure à une centaine d'année[10] aura lieu. Durant cette phase, l'oxygène disparaitra lentement par i) oxydation des matériaux et ii) consommation du fait de l'activité microbienne [11], pour laisser place à un environnement anoxique et réducteur.

Le concept de stockage des déchets vitrifiés HA a un double rôle : celui de retarder l'arrivée de l'eau au contact du verre et de limiter la migration des radionucléides dans l'environnement[5,12]. Le relâchement des radionucléides dépend directement de l'altération de la matrice vitreuse en conditions de stockage. Ainsi, un des principaux enjeux scientifiques est de comprendre les mécanismes d'altération du verre afin d'estimer, à l'aide de modèles prédictifs, sa cinétique d'altération en fonction des conditions d'environnement du milieu [13]. De plus, la chimie de l'eau susceptible d'altérer le verre résultera des interactions entre l'eau porale de l'argilite du Callovo-

Oxfordien et le matériau de remplissage, l'acier du chemisage et du conteneur de stockage et les produits de corrosion associés. Il est nécessaire d'étudier l'influence de ces matériaux sur la chimie de l'eau arrivant au contact du verre et d'évaluer les conséquences potentielles sur la cinétique d'altération de la matrice vitreuse. L'introduction d'un matériau de remplissage à base cimentaire peut ainsi conduire à une eau avec un pH élevé (> 10) et des concentrations élevées en Si et Ca. Ces deux éléments ainsi que les phases impliquées dans ces réactions avec le verre sont des paramètres clés afin de mieux appréhender les évolutions de la cinétique d'altération. Un état de l'art sur ces deux points, à savoir les mécanismes d'altération et les effets du calcium sur la dissolution du verre, est présenté dans le chapitre II.

REFERENCES

1 Orlhac, X. Thermal stability of the French nuclear waste glass - long term behavior modeling; Etude de la stabilite thermique du verre nucleaire. Modelisation de son evolution a long terme. (France, 2000).

2 Bonniaud, R., Cohen, P. & Sombret, C. Experiments on the incorporation of concentrated solutions of fission products in glasses and micas; Essais d'incorporation de solutions concentrees de produits de fission dans des verres et des micas. (France, 1958).

3 Gin, S. *et al.* An international initiative on long-term behavior of high-level nuclear waste glass. *Materials Today* **16**, 243-248, doi:https://doi.org/10.1016/j.mattod.2013.06.008 (2013).

4 Godon, N. Reference document on the long life behavior of nuclear glasses; Dossier de reference sur le comportement a long terme des verres nucleaires. (France, 2004).

5 Andra. Dossier, 2005 - Les recherches de l'Andra sur le stockage géologique des déchets radioactifs à haute activité et à vie longue. (2005).

6 Delay, J., Trouiller, A. & Lavanchy, J.-M. Propriétés hydrodynamiques du Callovo-Oxfordien dans l'Est du bassin de Paris : comparaison des résultats obtenus selon différentes approches. *Cr Geosci* **338**, 892-907, doi:https://doi.org/10.1016/j.crte.2006.07.009 (2006).

7 Sammartino, S., Bouchet, A., Prêt, D., Parneix, J. C. & Tevissen, E. Spatial distribution of porosity and minerals in clay rocks from the Callovo-Oxfordian formation (Meuse/Haute-Marne, Eastern France)—implications on ionic species diffusion and rock sorption capability. *Applied Clay Science* **23**, 157-166, doi:https://doi.org/10.1016/S0169-1317(03)00098-X (2003).

8 Marty, B., Dewonck, S. & France-Lanord, C. Geochemical evidence for efficient aquifer isolation over geological timeframes. *Nature* **425**, 55-58, doi:10.1038/nature01966 (2003).

9 Andra. Dossier, 2005 Argile - Tome architecture and management of a geological repository. (2005).

10 De Windt, L., Marsal, F., Corvisier, J. & Pellegrini, D. Modeling of oxygen gas diffusion and consumption during the oxic transient in a disposal cell of radioactive waste. *Appl Geochem* **41**, 115-127, doi:https://doi.org/10.1016/j.apgeochem.2013.12.005 (2014).

11 Chautard, C. *Iron-clay reactivity in radioactive waste disposal - Impacts of bacterial activities and heterogeneities; Interactions fer/argile en conditions de stockage geologique profond - Impacts d'activites bacteriennes et d'heterogeneites*, (2013).

12 Andra. Dossier 2022 - Dossier d'autorisation de création de l'installation nucléaire de base (INB) Cigéo. (2022).

13 Poinssot, C. & Gin, S. Long-term Behavior Science: The cornerstone approach for reliably assessing the long-term performance of nuclear waste. *Journal of Nuclear Materials* **420**, 182-192, doi:https://doi.org/10.1016/j.jnucmat.2011.09.012 (2012).

Chapitre II. ETAT DE L'ART SUR L'ALTERATION DES SILICATES, PRESENTATION DES MECANISMES ET PHASES SECONDAIRES (CSH)

Ce second chapitre définit les deux grands axes de cette étude. Dans un premier temps, le mécanisme d'hydrolyse – recondensation sera introduit étape par étape avec les cinétiques macroscopiques associées. Un second mécanisme sera ensuite présenté, il s'agit de la dissolution – reprécipitation. Nous discuterons alors l'application de ce dernier mécanisme, initialement proposé pour les silicates cristallins, pour les silicates vitreux. Enfin, une attention particulière sera portée sur les effets antagonistes du calcium sur les vitesses d'altération d'un verre de référence. Nous privilégierons l'étude des silicates de calciums hydratées (CSH) à travers un état de l'art sur leur structure, leur solubilité, les mécanismes de nucléation/croissance et leur carbonatation.

II.1. Cinétiques et mécanismes d'altération des verres

Les verres nucléaires, tout comme la plupart des verres silicatés, se corrodent en présence d'eau [1-7]. Historiquement, c'est le processus d'hydrolyse – recondensation, aussi appelé « leaching », qui a été proposé pour principal mécanisme d'altération. Il se découpe en plusieurs étapes mécanistiques et cinétiques comme présenté dans la Fig. II-1. Chacun des différents couples mécanismes – vitesses de dissolution sera détaillée par la suite.

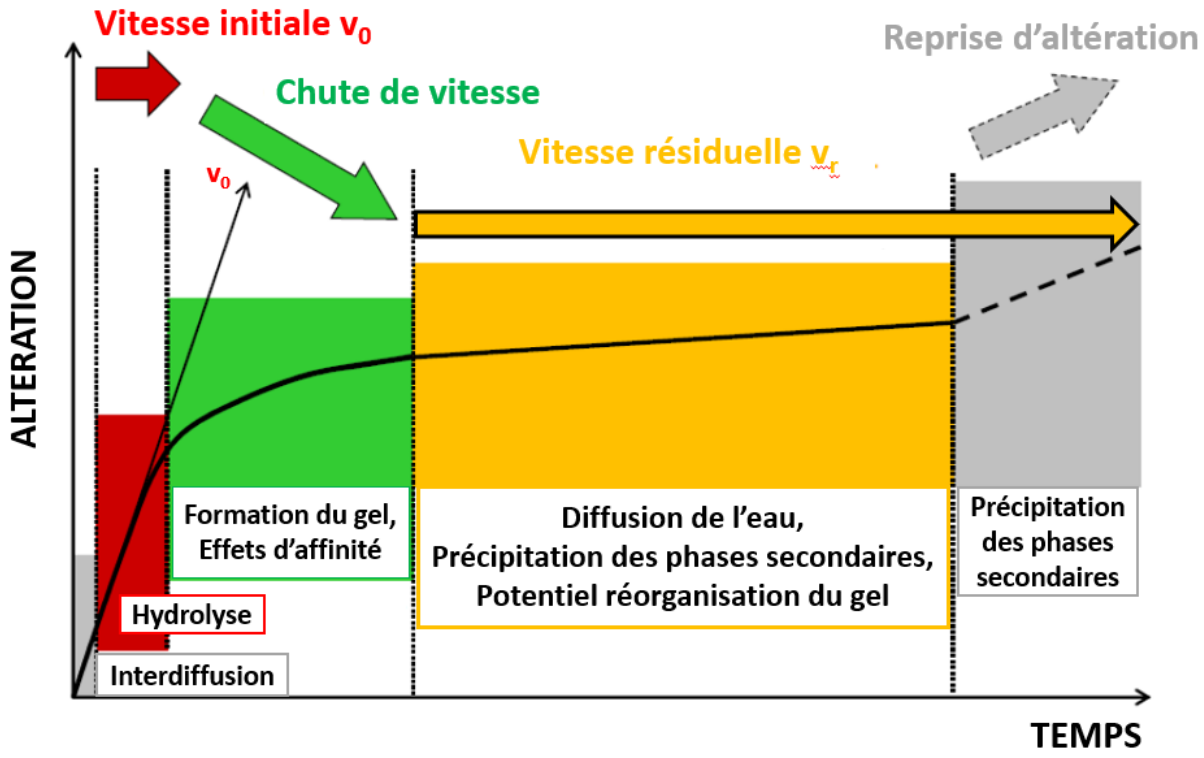

Figure II-1: Représentation schématique des différentes étapes mécanistiques qui constituent le mécanisme d'altération par hydrolyse – recondensation, ainsi que la vitesse macroscopique d'altération des verres associée. La durée des différents mécanismes peut varier en fonction de la composition de la solution ou du verre. Adapté de Gin et al., 2012[8].

II.1.1. Interdiffusion et hydrolyse

Lors du premier contact entre le verre silicaté et la solution, les molécules d'eau pénètrent dans le réseau silicaté du verre : c'est l'étape d'*hydratation*. Il en résulte un échange avec les éléments alcalins, comme le sodium, associés aux oxygènes non pontants (aussi appelés modificateurs du réseau silicaté), mais aussi certaines espèces formatrices du réseau, comme le bore, qui sont plus facilement hydrolysables que le silicium. Cet échange, qui progresse via un mécanisme d'*interdiffusion*, se traduit physiquement par des profils élémentaires sigmoïdaux et anti-corrélés au sein de la couche altérée (Fig. II-2), et chimiquement par l'équation suivante :

$$\equiv Si - O - alcalin + H^+ \rightarrow \equiv Si - OH + alcalin^+ \qquad \text{(Eq. II-1)}$$

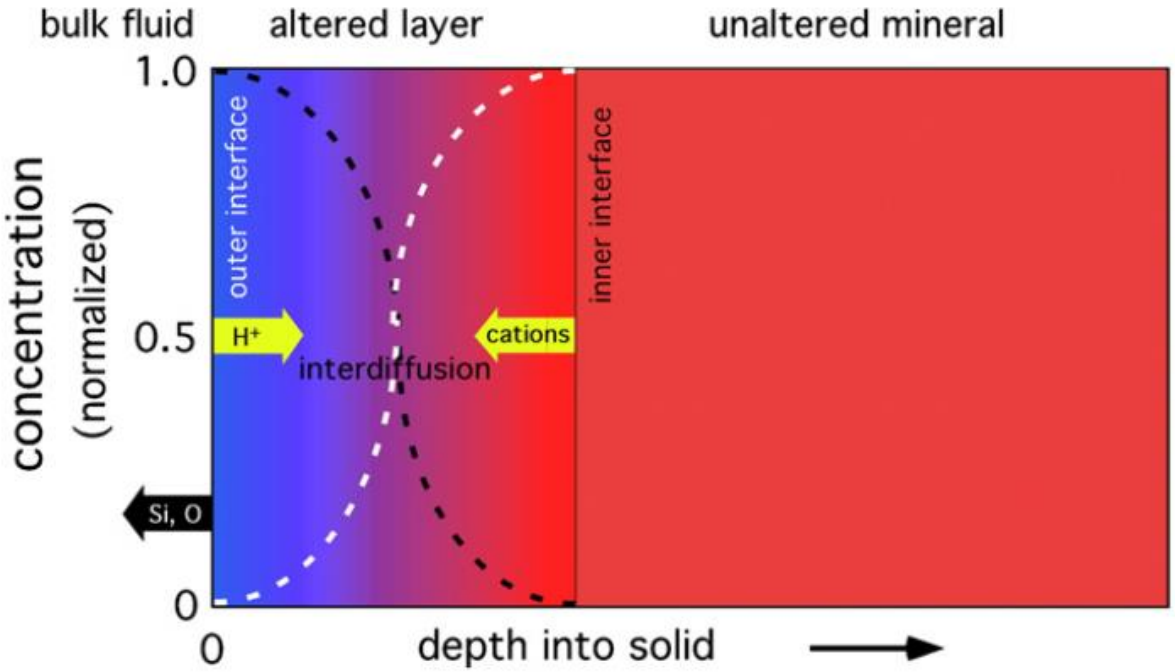

Figure II-2 : Représentation schématique des profils élémentaires des protons et des cations lors de l'étape d'interdiffusion par Hellmann et al, 2012 [9]. Les profils sont anti-corrélés et sigmoïdaux en termes de concentration. Ils sont créés par un relargage préférentiel de certains cations (profil blanc) au profit d'une incorporation d'ions H^+ issus de la solution (profil noir). La couche altérée ainsi créée est une relique du matériau sain. Son épaisseur est contrôlée par la diffusion interne et la vitesse des réactions d'hydrolyse à la surface.

Cette première étape d'interdiffusion est irréversible car elle entraine un relargage sélectif et non-congruent des éléments du verre ainsi qu'une réorganisation locale du réseau, impliquant notamment une modification de la coordinance de certains atomes formateurs du réseau [3,10]. Elle est, par ailleurs, favorisée en pH acide [2] et entraine la formation d'une couche désalcalinisée et hydratée, distincte du verre-parent [8,11,12].

En parallèle, le réseau silicaté subit des réactions *d'hydrolyse* correspondant à une attaque des liaisons pontantes (Si – O – Si, Si – O – Al, Si – O – Zr, etc.) pour former des groupement silanols [13]. Ce processus d'hydrolyse conduit à une dissolution congruente du verre et une dépolymérisation de la matrice silicatée selon la réaction suivante :

$$\equiv Si - O - Si \equiv + H_2O \rightarrow 2 \equiv Si - OH \qquad \text{(Eq. II-2)}$$

Sur le court terme, cette réaction se traduit par une vitesse d'altération qui est dominée par la vitesse du processus d'hydrolyse, elle-même proportionnelle au temps. Pour les compositions de verres nucléaires ; elle domine le processus global. La vitesse correspondante, nommée vitesse initiale et notée v_0, est la plus rapide observée expérimentalement [14,15]. Cette vitesse est dépendante de la composition de la solution [16], du verre [17,18], du pH et de la température [19,20].

D'après l'Eq. II-2, il est nécessaire de rompre les quatre liaisons d'un silicium pour libérer l'acide orthosilicique H_4SiO_4 en solution. Criscenti et al., [17] ont notamment démontré que l'étape limitante pour cette libération était la rupture de la dernière ou avant-dernière liaison pontante. Les ruptures des liaisons pontantes des autres éléments formateurs de réseau diffèrent en fonction de la barrière énergétique (énergie nécessaire à la rupture de cette liaison) associée à cet élément [21-23]. Par exemple, les liaisons Si – O – Al ont une barrière énergétique moins élevée que les liaisons Si – O – Si, elles sont donc préférentiellement hydrolysées et suivant leur nombre peuvent plus ou moins affecter le processus global de dissolution du verre. Toutefois, il a été observé que la présence d'Al en 2nd voisin du Si renforce les liaisons Si – O. Ainsi, lorsque l'Al est en dessous d'une teneur critique, il augmente la durabilité chimique du verre [23]. Cette teneur critique n'a cependant pas encore été estimée.

Les modèles basés sur l'affinité chimique issus de la théorie de l'état de transition ont conduit Aagaard et Helgeson [24] à proposer la loi cinétique suivante :

$$v_0 = k \times \prod a_i^{n_{ij}} \left(1 - \frac{Q}{K}\right) \qquad \text{(Eq. II-3)}$$

Où a_i est l'activité du réactif i de l'étape limitante j et n_{ij} est le coefficient stoechiométrique de cet élément à cette étape. Enfin Q représente le monôme des activités de la réaction et K, sa constante d'équilibre. Le ratio $\frac{Q}{K}$ représente donc l'écart à l'équilibre de la réaction Eq. II-2.

II.1.2. Formation du gel et vitesse résiduelle

Si le milieu est statique, comme ce sera le cas pour les expériences menées durant cette thèse, une *chute de la vitesse de dissolution* est observée après le régime initial contrôlé par l'hydrolyse. Cela est dû au fait que i) la solution se sature en silice, diminuant l'enthalpie libre de la réaction de dissolution du verre (on dit aussi que l'affinité entre le verre et la solution diminue) par approche d'un équilibre thermodynamique [25,26] et ii), une réaction inverse à l'hydrolyse a lieu, à la surface du verre, formant une couche poreuse et hydratée, aussi appelée « gel » ou « couche d'altération » [15,27,28] : c'est la *condensation*. Le gel ainsi formé est constitué principalement par de la silice et des espèces faiblement solubles (Zr, Al, Ca et terres rares). La couche néoformée se distingue structurellement du verre parent et du verre hydraté car elle résulte d'un équilibre local dans le solide entre hydrolyse des liaisons formatrices du réseau et leur recondensation [29,30]. Une seconde réaction, issue d'un équilibre avec la solution à la surface du gel, participe à sa formation : c'est la *précipitation.* Il s'agit de H_4SiO_4 qui, en créant des liaisons siloxanes contribue à la structure tridimensionnelle du gel. D'autres phases, amorphes ou cristallisées peuvent aussi précipiter à la surface du gel. Les vitesses de réactions de ces mécanismes ainsi que leur prédominance varient en fonction de la composition du verre altéré, de la solution et des conditions d'altération.

Cependant, une fois formé, le gel n'est pas une couche statique. C'est une couche dynamique qui évolue avec le temps et qui peut passiver la surface du verre suivant des mécanismes de densification et de fermeture des pores [31,32] (Fig. II-3). Elle limite ainsi la vitesse d'altération à une valeur faible et quasiment constante en diminuant la capacité d'hydrolyse de la solution [33] et en limitant le transport des espèces entre le verre et la solution [20,34-36]. Le transport des espèces au sein du gel se fait par diffusion [8], il est donc possible de suivre l'évolution du gel au cours du temps en calculant périodiquement son coefficient diffusif avec l'équation suivante :

$$D = D_0 \times [HO^-]^n \times exp\left(-\frac{E_a}{R \times T}\right) \qquad \text{(Eq. II-4)}$$

Où D est le coefficient d'interdiffusion ($m^2.s^{-1}$), D_0 est la constante de diffusion ($m^2.s^{-1}$) aussi appelé facteur de fréquence (sa valeur est celle du coefficient de diffusion pour $\frac{1}{T} = 0$, autrement dit pour une température infinie), n est le coefficient de dépendance en pH, E_a est l'énergie d'activation ($J.mol^{-1}$), R est la constante des gaz parfait et vaut 8.314 $J.mol^{-1}.K^{-1}$ et T est la température (K).

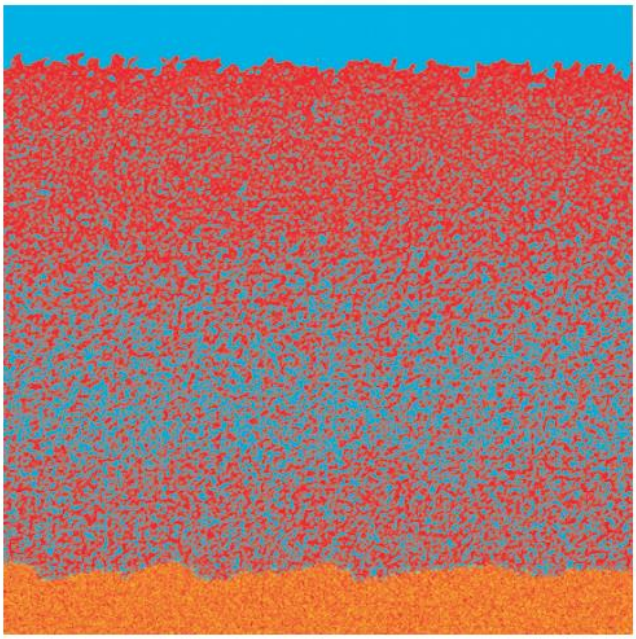

Figure II-3: Simulation Monte Carlo de la couche de gel par Cailleteau et al., 2008 [31]. Section longitudinale d'une couche de gel où une recondensation des atomes de silices (en rouge) est simulée à la surface. L'eau est en bleu, et les autres éléments sont en jaunes.

Suite à la formation de ce gel et à la diminution de l'affinité entre le verre sain et la solution, la vitesse d'altération diminue, parfois de plusieurs ordres de grandeur en comparaison avec la vitesse initiale v_0 [37]. Cette vitesse d'altération, appelée *vitesse résiduelle*, peut être maintenue à une valeur plus ou moins constante par la précipitation de phases secondaires, thermodynamiquement plus stables que le gel [8], comme les phyllosilicates (voir Fig. II-4) ou les zéolites (voir section II.1.3.). Ces précipités proviennent du relargage des éléments constitutifs du verre en solution, de la composition

initiale de la solution ou de l'altération d'autres matériaux environnants. La vitesse résiduelle est étroitement liée à la stabilité cinétique et thermodynamique de l'environnement (condition de saturation des éléments en solution, température, pH, précipités en solution etc.) [38].

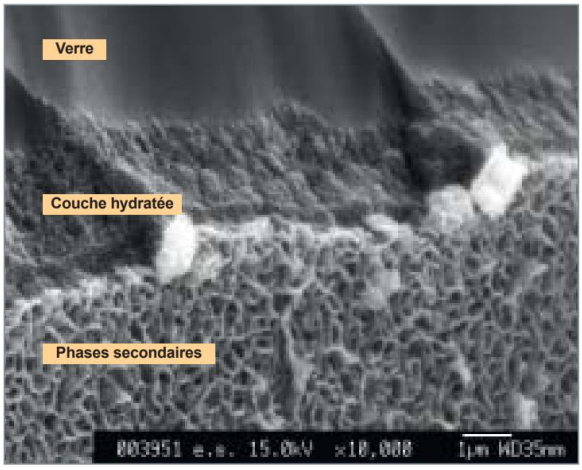

Figure II-4 : Image de Microscope Electronique à Balayage (MEB) d'un échantillon de verre R7T7, altéré dans une solution d'eau pure à 150°C pendant 4 mois, par Feron et al., 2010 [39]. Ce semi-profil montre les différentes couches d'altérations successives à la surface du verre en commençant par une couche de phyllosilicate, phases secondaires issus de la précipitation des éléments en solution, puis vient le gel, ici notée « couche hydratée », et enfin le verre-parent.

II.1.3. Reprise d'altération et phases secondaires

Dans certaines conditions, il est possible d'observer une nouvelle augmentation de la vitesse d'altération. Cette *reprise d'altération* a été étudiée pour le verre SON68 à pH > 10.5, T ≤ 90°C ou à des températures très supérieures à 90°C [38,40-43] mais aussi pour le verre ISG, *International Simple Glass*, [44-46] qui est un verre simple à 6 oxydes [47] et qui fera l'objet d'étude des chapitres IV et V. Ce phénomène est favorisé à pH basique [48]. Il entraine une déstabilisation du gel et, par suite, une précipitation massive de phases secondaires au détriment du gel [49] (Fig. II-5). On retrouve parmi ces phases secondaires les phyllosilicates, les zéolites mais aussi des silicates de calcium hydratés (CSH) [50].

Les phyllosilicates sont des cristaux de tailles submicrométriques avec une structure en feuillets. Dans un contexte d'altération des verres, ils se forment généralement par dissolution – reprécipitation en incorporant des éléments du verre – notamment la silice et l'aluminium, qui après diffusion précipitent à la surface du verre après avoir atteint la limite de solubilité de la phase cristalline. On peut aussi retrouver dans ces phases des métaux de transition tels que Zn, Fe et Ni, mais aussi des éléments tels que le Na, Ca, Mg dans de faibles proportions.

Les zéolites se forment, elles aussi, préférentiellement en milieu basique ou à haute température [42,52] et ont une structure cristalline résultante d'un agencement tridimensionnel de SiO_4 et AlO_4. Le rapport Si/(Al+Si) est une caractéristique de ces zéolites et peut varier de 0,5 à 1. Pour compenser la présence d'aluminium trivalent, ces phases incorporent des alcalins (K^+, Na^+…) ou des alcalino-terreux (Ca^{2+}, Ba^{2+}…) comme compensateurs de charges.

Les CSH sont des phases secondaires initialement amorphes qui peuvent subir un processus de cristallisation [53,54]. La nature et le comportement de ces phases seront détaillés dans la section II.3. Enfin, d'autres phases de types phosphates de terres rares, oxydes métalliques ou hydroxydes métalliques peuvent aussi précipiter mais elles impactent beaucoup moins l'altération du verre [1].

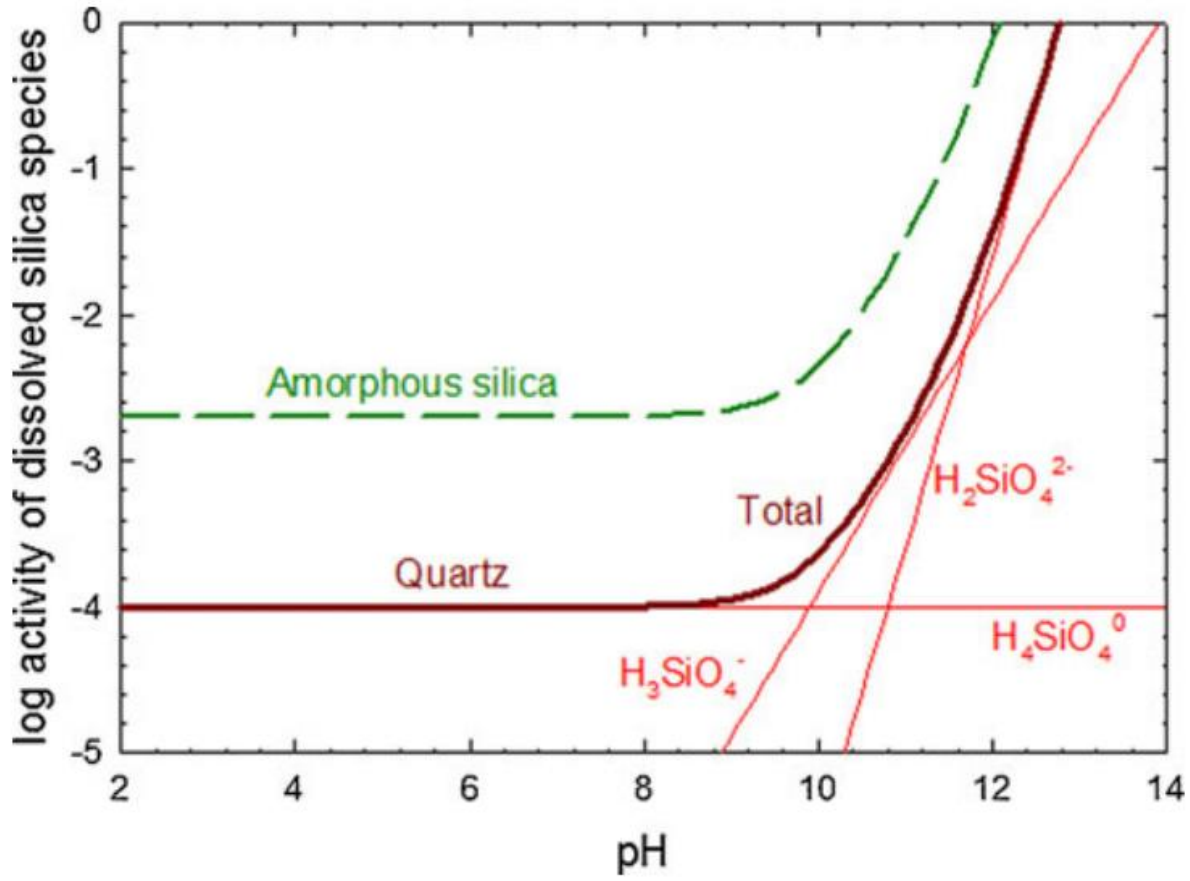

Figure II-5 : Graphique représentant la solubilité de la silice amorphe et du quartz en fonction du pH, par Makhlouf et al., 2014 [51]. La forte solubilité de la silice amorphe, qui est le polymorphe le plus soluble de SiO_2, en milieu basique explique la déstabilisation du gel, matériau principalement composé d'agencement de SiO_2.

II.2. Cinétique et mécanismes d'altération des minéraux silicatés

II.2.1. Le mécanisme d'hydrolyse – recondensation

Historiquement, le mécanisme de leaching présenté dans la section précédente est communément accepté comme s'appliquant aux minéraux silicatés : les différentes caractérisations menées sur ces matériaux pointent vers l'idée qu'une étape d'interdiffusion prend place durant leur altération [55,56]. Des études plus récentes, comme celle de Schott et al., 2012 sur la wollastonite [57] continuent de soutenir un mécanisme d'hydrolyse – recondensation comme principal mécanisme d'altération des minéraux.

Ces différentes caractérisations ont notamment été modélisées sur la base d'expériences par Hellmann et al., 1997 à travers une étude conséquente en 4 parties sur l'altération de l'albite en milieu aqueux [58-61]. Les auteurs ont notamment démontré la formation d'une couche enrichie en proton et appauvrie en sodium à la surface d'un cristal d'albite $NaAlSi_3O_8$, en utilisant des techniques de spectroscopie (c'est-à-dire *Resonant Nuclear Reaction Analysis*, RNRA, *Rutherford Backscattering Spectroscopy*, RBS and *Elastic Recoil Detection Analysis*, ERDA). Les profils élémentaires des constituants du verre étant sigmoïdaux et anti-corrélés, les auteurs ont conclu qu'un phénomène d'interdiffusion avait eu lieu et que le mécanisme d'altération était similaire à celui des verres.

Ce modèle mécanistique a été généralisé aux minéraux silicatés multi-oxydes dans le cadre de la théorie de complexation surfacique [62]. En outre, une des principales conclusions de cette étude est que la vitesse de dissolution des silicates amorphes ou cristallins (feldspaths et quartz), V (g.m^{-2}.j^{-1}), ne devait pas s'exprimer en fonction de l'affinité entre la solution et le matériau sain, mais plutôt en fonction de l'affinité entre la solution et la couche altérée, A^* (en J.mol^{-1}) :

$$V = v_0 \left\{1 - exp\left(\frac{-A^*}{RT}\right)\right\} \qquad \text{(Eq. II-5)}$$

où v_0 est la vitesse de dissolution initiale (g.m^{-2}.j^{-1}). A^* est l'affinité chimique pour la dissolution irréversible du gel à la l'interface avec la solution. Elle se traduit par $A^* = -RT\ln(\frac{Q}{K})$ où $\frac{Q}{K}$ représente l'écart à l'équilibre de cette réaction de dissolution irréversible.

Cette équation signifie que la dissolution du silicate s'arrête une fois que la couche altérée atteint un état d'équilibre avec la solution. Ce comportement a été observé par Daux et al., 1997 [63] lors de l'altération d'un verre basaltique quand sa vitesse de dissolution s'est approchée de zéro en même temps que l'affinité de la couche altérée riche en Si, Al et Fe s'approchait de zéro. Des observations similaires ont été établies pour l'olivine [64] et le diopside [65].

II.2.2. Le phénomène de dissolution – reprécipitation couplée à l'interface, le CIDR

Dans les années 2000, les analyses spectroscopies précédemment menées sur les minéraux ont été revisitées. En utilisant la microscopie électronique à transmission (MET) de haute résolution et avec des filtres en énergies, Hellmann et al., [66] ont étudié les interfaces internes (entre la couche altérée et le matériau sain) de cristaux de wollastonite et de labradorite (feldspaths). Ces interfaces abruptes de quelques nm d'épaisseurs présentaient des profils élémentaires proches d'une fonction de type marche qui ne peuvent être prédits par un mécanisme diffusif (Fig. II-6). Par la suite, d'autres études ont présenté des observations similaires sur l'altération des minéraux [9,64,67].

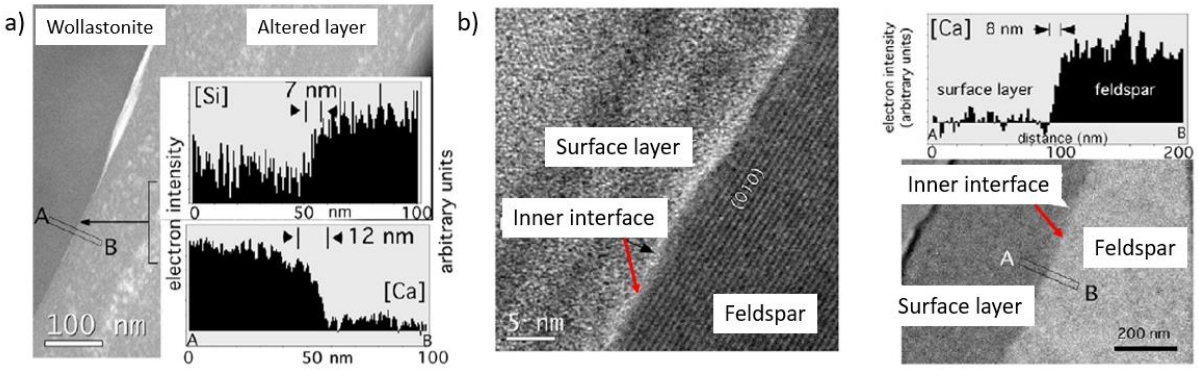

Figure II-6 : Image MET à haute résolution de cristaux a) de wollastonite et b) de labradorite (feldspar) altérée en laboratoire ainsi que les profils élémentaires de silice et de calcium à l'interface interne observés en utilisant un filtre à énergie, par Hellmann et al., 2012[9].

A la suite de ces observations un nouveau mécanisme a été proposé : le mécanisme de dissolution – reprécipitation couplée interfaciale, noté CIDR. Il est à noter que cette théorie remonte aux travaux d' O'Neil et Taylor [68]. Ces derniers l'ont proposé pour expliquer l'échange du couple $Na^{+}_{Feldspar} \leftrightarrow K^{+}_{solution}$ lors de l'altération d'un feldspath, l'hypothèse du phénomène *d'interdiffusion* n'ayant pas encore été émise. Les auteurs expliquent que le mécanisme d'échange cationique implique une mise en solution puis une reprécipitation dans une fine pellicule de fluide à l'interface entre le matériau sain et le gel. Un an plus tard, une seconde étude [69] promeut ce mécanisme en expliquant que l'interface formée lors de l'altération d'un verre basaltique était issue d'un mécanisme de reprécipitation dans une micro-solution. Ce mécanisme de dissolution – reprécipitation n'est plus évoqué dans la littérature jusqu'en 2002 [70] et 2003 [66] où la théorie sera développée et complétée par la suite [71-74].

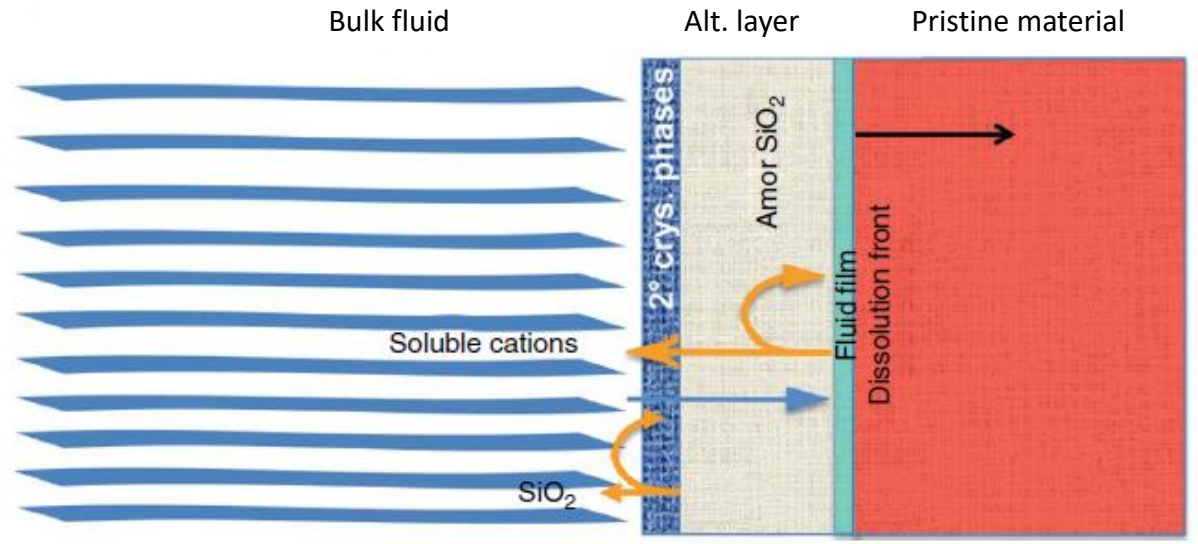

Figure II-7 : Représentation schématique du mécanisme de CIDR proposé pour les minéraux silicatés. Les flèches jaunes correspondent aux flux des cations et éléments formateurs du réseau (micro)cristallins, diffusant au sein des couches ou reprécipitant dans la pellicule de fluide ou parmi les phases secondaires. La flèche bleue représente le flux des molécules issues de la solution. Les trois couches formant la couche altérée sont présentées, à savoir une couche formée par la précipitation de

phases secondaires, le gel et une pellicule de fluide qui vient remplacer la couche d'interdiffusion présent dans le mécanisme d'hydrolyse – recondensation. Par Hellmann et al., 2021 [74].

Le mécanisme de dissolution – reprécipitation interfaciale commence par un déséquilibre chimique local entre la surface du matériau sain et une pellicule de fluide à l'interface. Ce déséquilibre entraine l'hydrolyse totale des liaisons formatrices du réseau qui crée ainsi une interface abrupte. Cette dissolution à la surface chimiquement réactive du minéral sain entraine un relargage stœchiométrique des éléments constitutifs du minéral dans une pellicule de fluide ultra fine (Fig. II-7). Cette dernière, composée d'à peine deux ou trois couches de molécules d'eau pour une épaisseur totale inférieur à 1,3 nm, diffère chimiquement et thermodynamiquement de la solution d'altération [75,76]. Cette différence permet ainsi à cette pellicule de fluide d'être sursaturée vis-à-vis de la silice amorphe lors de la dissolution, même si la solution demeure macroscopiquement insaturée, et de reprécipiter les phases insolubles pour former le gel [77]. Cette reprécipitation est quasi instantanée et couplée avec la dissolution du minéral. Le gel ainsi formé est une entité différente du matériau sain, constitué de silice amorphe hydraté mais aussi d'autres phases insolubles tels que des oxyhydroxydes de métal (Fe, Al, Zr, Zn, etc…). Les cations, quant à eux, sont libérés du matériau sain lors de la dissolution et diffusent à travers la nano-porosité du gel pour atteindre l'interface externe (interface entre le gel et la solution) [78].

Tout comme le premier mécanisme, l'épaisseur du gel évolue en fonction des réactions de dissolution – reprécipitation, et du rapport de leur vitesse, à l'interface externe mais aussi, dans le cas du CIDR, à l'interface interne. Si les réactions à l'interface externe sont contrôlées par la chimie de la solution, les réactions à l'interface interne le sont par la thermodynamique particulière de la pellicule de fluide. De ce fait, un déficit est observé entre la quantité élémentaire dissoute du minéral et la quantité d'éléments qui reprécipitent, conduisant à la formation de pores au sein du gel [70]. Cette porosité permet alors les échanges diffusifs entre les éléments dissouts et les éléments initialement présents dans la solution. Par la suite, il est possible de retrouver les étapes précédemment discutées, à savoir une chute de vitesse due à une recondensation à la surface du gel et une fermeture des pores localement [79], une vitesse résiduelle et enfin, une potentielle reprise d'altération par précipitation de phases secondaires [80,81].

En résumé, une des principales différences entre le mécanisme d'hydrolyse – recondensation et le mécanisme de dissolution – reprécipitation se situe au niveau de l'étape de l'interdiffusion. Là où le leaching défend une hydrolyse partielle des liaisons formatrices du réseau au profit d'un relargage préférentiel de certains cations, le CIDR promeut une hydrolyse totale de ces liaisons, ce qui se traduit par une interface ultra fine et abrupte.

II.3. La transposition du mécanisme de CIDR des cristaux vers les verres

De manière similaire à l'histoire des minéraux, une remise en question des précédentes caractérisations et du mécanisme de la dissolution des verres a eu lieu. Geisler et al., [77] ont notamment présenté des résultats d'altération d'un verre borosilicaté en milieu acide, qui apportaient des éléments de contradiction avec le mécanisme d'hydrolyse – recondensation, obtenus à l'aide de caractérisations chimiques, texturales et isotopiques (traçage avec ^{18}O et ^{26}Mg). Les auteurs ont alors expliqué ces résultats en utilisant le mécanisme de dissolution – reprécipitation.

Tableau II-1 : Tableau récapitulatif des épaisseurs de gradient (nm) issus des profiles élémentaires de B réalisés à la l'interface entre le gel et le matériau sain d'un verre SON68 à partir de différentes méthodes analytiques. ToF-SIMS signifie « spectroscopie de masse à ions secondaires à temps de vol ». EFTEM signifie « microscopie électronique de transmission à filtre énergétique ». APT signifie « sonde atomique tomographique ». Par Gin et al., [14]

	Epaisseur du profil de B (nm)	**Références**
ToF-SIMS	> 1000	
NanoSIMS (O^- beam)	350 ± 150	Gin et al., 2011 [82]
NanoSIMS (Cs^+ beam)	170 ± 30	Gin et al., 2011 [82]
EFTEM	≤ 30	Gin et al., 2013 [14]
APT	3 – 4	Gin et al., 2013 [14]

Cependant, un point clé de ce débat mécanistique réside dans les profils élémentaires de cations et de protons qui sont anti-corrélés, sigmoïdaux et avec un large gradient de concentration élémentaire, lors d'analyses de spectroscopies de masse à ions secondaires à temps de vol (ToF-SIMS). La provenance de ces profils, censés prouver la présence d'une étape d'interdiffusion, a alors été suggérée comme résultant d'un défaut analytique lié à la faible résolution latérale des faisceaux utilisés, qui élargissent artificiellement les profils [9,66] (voir Tableau II-1). Il en a résulté une étude importante [73] qui, à travers deux méthodes analytiques différentes, le ToF-SIMS et l'APT (Sonde Atomique Tomographique), a démontré cet élargissement artificiel sur les profils élémentaires d'un verre borosilicaté après 1 mois d'altération (Fig. II-8). Même si les deux profils révèlent des tendances similaires en termes de composition de la couche altérée, la principale différence se situe au niveau du gradient de concentration à l'interface entre le gel et le verre sain. L'APT, qui possède une très grande résolution spatiale en profondeur, est supposée montrer les profils élémentaires « vrais », à savoir un profil abrupt et un gradient de concentration s'étendant seulement sur quelques nm. Il en résulte que l'élargissement de ce gradient observé lors de l'analyse ToF-SIMS et attribué à la présence d'une réaction d'interdiffusion, serait un biais résultant de la formation de zones de mélanges lors de l'analyse.

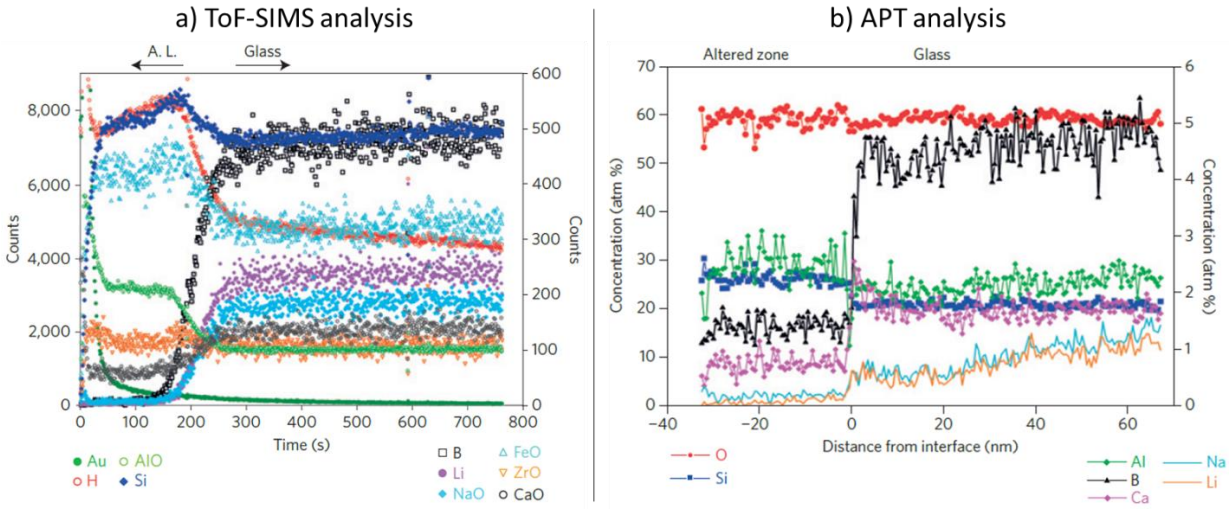

Figure II-8 : Profils élémentaires d'un verre borosilicaté altéré pendant 1 mois en fonction de la profondeur d'analyse (temps de découpe, en s, pour le ToF-SIMS et en nm pour l'APT) mesurés par a) ToF-SIMS et b) APT, par Hellmann et al., 2015 [73].

En réponse à cette dernière étude, Gin et al., [83] ont aussi utilisé l'ATP afin de retrouver ces interfaces mais ils ont démontré, quelques années plus tard [84], que le mécanisme d'altération pouvait varier entre le leaching et le CIDR, en fonction de la présence d'Al dans le verre. En effet, ils ont étudié la formation de la couche altérée sur deux verres simples, CJ1 – un verre à 3 oxides, et CJ2 – CJ1 dopé avec 4.1 mol % de Al_2O_3, en pH basique à 90°C en utilisant les marqueurs isotopiques ^{18}O et ^{29}Si. Ils ont découvert que la dissoution du verre CJ1 était dans un premier temps contrôlé par le mécanisme de dissolution – reprécipitation (incorporation de ^{29}Si dans le gel), suivi par un mécanisme de recondensation menant à une réorganisation *in situ* du réseau silicaté. Cette observation où la signature isotopique du gel est intermédiaire entre la solution et le matériau sain avait précédemment été utilisée pour défendre le mécanisme d'hydrolyse – recondensation [29]. Par suite, à l'aide de simulation Monte Carlo, les auteurs ont présenté l'Al, en condition diluée dans CJ2, comme un élément qui renforce le second mécanisme, expliquant ainsi que la formation de la couche passivante est plus lente sur CJ2. En contrepartie, l'hydrolyse partielle des éléments Si et Al suivie de la réorganisation *in situ* rendent le gel plus poreux et le relargage des éléments constitutifs du verre plus rapide. De manière similaire, d'autres études tentant de réconcilier ces deux mécanismes à travers un mécanisme hybride verront le jour [74,85].

En outre, la composition du verre joue un rôle clé pour expliquer le mécanisme d'altération ainsi que les vitesses de dissolution observées. A travers 9 verres simples, CJ1 à CJ9 – borosilicate de sodium contenant différents éléments dopant présents dans les verre nucléaires, et un verre complexe, SON68, Gin et al., 2012 [8] ont établi des corrélations entre la composition d'un verre et sa vitesse d'altération initiale et résiduelle. Ces 10 verres ont été altérés dans une eau pure à 90°C pendant près de 14 ans. Les auteurs ont démontré que l'utilisation de verres simplifiés permettaient

de rendre compte de l'évolution de système plus complexe : les verres CJ4 à CJ6 sont de bons analogues du verre nucléaire R7T7 et SON68. De plus certains éléments comme l'Al, le Ca et le Zr présentent des synergies qui limitent significativement l'évolution de la vitesse d'altération résiduelle. Dans le cas de CJ8, le caractère passivant du calcium est temporaire puisqu'après 90 jours d'altération, la solution altérante est proche de la saturation de l'okenite et kenyaite – deux silicates de calcium hydratées, susceptibles d'être responsable de la reprise d'altération du verre. Ainsi, ce verre en particulier n'atteint jamais une vitesse résiduelle mais subit un cycle de reprise d'altération jusqu'à observer une dissolution totale du matériau.

II.4. Altération du verre en milieu calcique

L'eau porale des argilites du Callovo-Oxfordien devra traverser les différentes barrières avant d'atteindre le verre. Le matériau de remplissage cimentaire des alvéoles impose un pH basique à l'interface entre les argilites et le chemisage en acier. Cela permet de neutraliser ces argilites oxydées lors du creusement de la roche pour la construction du site de stockage et de créer un milieu favorable aux faibles cinétiques de corrosion des aciers. Cependant, l'eau porale se chargera en éléments issus du ciment, dont du calcium. En contact avec le verre, toutes les conditions (pH, calcium, silice) seront réunies pour favoriser la précipitation de phases secondaires tels que des phyllosilicates, des CSH ou encore des zéolites.

II.4.1. Effets antagonistes du calcium sur l'altération du verre

La présence de calcium dans le milieu altérant peut avoir des effets antagonistes sur la vitesse d'altération en fonction du pH, du rapport surface de verre sur volume de solution (SA/V) mais aussi et surtout, en fonction de sa concentration [46,86-88]. Mercado et al., [89] distinguent ainsi plusieurs réactions en fonction du pH et de ce rapport qui traduit également la quantité de silice relâchée lors de l'altération du verre et disponible pour réagir avec le calcium, impactant ainsi la vitesse de dissolution de celui-ci (Fig. II-9).

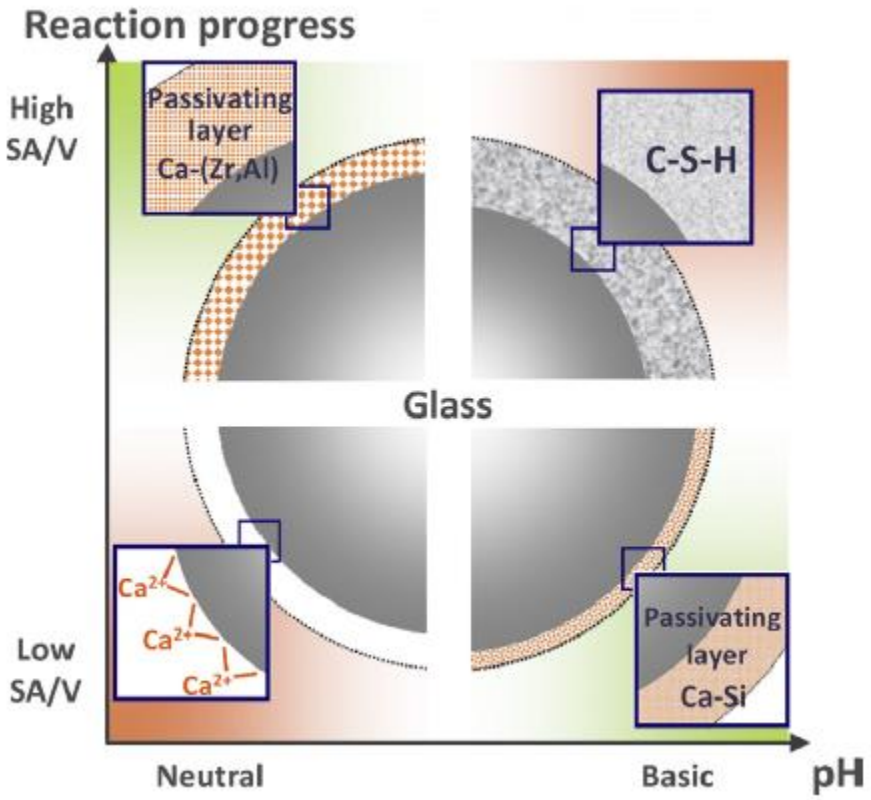

Figure II-9 : Représentation schématique des quatre principaux effets du calcium sur les conditions d'altération d'un verre en fonction du pH et du rapport SA/V, par Mercado-Depierre et al., 2013 [89]. Les zones vertes correspondent à une augmentation des propriétés de passivation de la couche alors que les zones rouges correspondent à une accélération de l'altération.

II.4.1.1. Formation d'une couche passivante par incorporation du calcium

Parmi les quatre catégories distinguées dans la Fig. II-9, les zones vertes correspondent aux effets du calcium inhibant la vitesse d'altération :

- A faible rapport SA/V et à pH basique, le calcium présent en solution pénètre dans la couche externe du gel et interagit avec la silice qui le forme. Cette interaction va augmenter la rétention des éléments constitutifs du gel qui diffusaient à travers celui-ci après relargage par le verre sain. Ainsi, le transport des ions dans le gel diminue et la vitesse de dissolution aussi [46].
- A fort rapport SA/V et à pH proche de la neutralité, le calcium réagit avec le silicium à la surface de la couche altérée en formant une couche protectrice riche en Si-Ca. La présence d'éléments faiblement soluble tels que Zr ou Al peut augmenter les propriétés de passivation de cette couche [23].

Chave et al., [90] ont notamment constaté qu'après l'ajout de Ca dans une solution saturée en silice, à $pH_{90°C}$ = 9, la vitesse de dissolution diminue. Les auteurs ont alors émis l'hypothèse que le

calcium participe à la densification du gel et jouant un rôle de catalyseur de la recondensation d'après les réactions suivantes :

$$\equiv Si - OH + Ca^{2+} + HO - Si \equiv \rightarrow [\equiv Si - O - Ca - O - Si \equiv] + 2H^{+} \quad \text{(Eq. II-6)}$$

$$[\equiv Si - O - Ca - O - Si \equiv] + H_2O \rightarrow \equiv Si - O - Si \equiv + Ca^{2+} + 2HO^{-} \quad \text{(Eq. II-7)}$$

Le réactif $[\equiv Si - O - Ca - O - Si \equiv]$ est un complexe de transition instable qui facilite la formation de siloxane, refermant la porosité et diminuant ainsi la vitesse d'altération du verre.

II.4.1.2. Entretien de l'altération par effet du calcium

De manière similaire aux deux catégories précédentes qui correspondaient aux couples 'faible SA/V – pH basique' et 'fort SA/V – pH neutre', on peut distinguer deux autres catégories dans lesquelles le calcium a plutôt pour effet d'entretenir l'altération du verre :

- A faible rapport SA/V et à pH neutre, le Ca ne pénètre pas dans la couche altérée mais demeure à l'interface entre le gel et la solution. Il forme alors un complexe avec les atomes de silicium présents en occupant les sites des autres alcalino-terreux. Cela a pour effet d'affaiblir les liaisons Si – O, ce qui les rend plus facilement hydrolysables [91,92]. Ce complexe induit ainsi une augmentation de la vitesse d'altération.
- A fort SA/V et à pH basique, la solution se retrouve rapidement saturée par rapport aux silicates de calcium hydratés (calcium silicate hydrates – CSH, cf. section II.4.2), qui précipitent au détriment de la couche passivante et du gel. Ces CSH entretiennent l'altération du verre en consommant la silice en solution. La vitesse d'altération est alors supposée proche de la vitesse d'altération initiale [86,93,94]. Cependant, un second effet de ces CSH, antagoniste au premier a aussi été suggéré. En effet, il est possible que des CSH fortement liés puissent créer une couche protectrice dense et non-poreuse, limitant la vitesse d'altération du verre [88,89].

Ce deuxième point, où la présence d'une phase secondaire entretient la vitesse d'altération est un sujet particulièrement étudié. Gin et al., [44] ont notamment questionné le lien entre pH, précipitation de phases secondaires et reprise d'altération. Un coupon de verre ISG a été altéré à 90°C, pH 9 pendant 209 jours dans une solution saturée en Si afin de créer un gel passivant. Le pH a ensuite été augmenté à 11.5 et une reprise d'altération a été observée. Après 15 jours d'altération, les premières phases secondaires à précipiter furent les CSH, suivi par des zéolites 15 jours plus tard. Les auteurs ont alors conclu que la précipitation de ces phases amorphes ou cristallines promeut l'hydrolyse des liaisons Si – O – X (X = Al, Si, Zr) qui est la force motrice de cette reprise d'altération.

II.4.1.3. Rétention de l'altération par complexation du calcium

Un dernier point à souligner sur les effets possibles du calcium sur l'altération des verres borosilicatés concerne l'effet conjoint du B et du Ca. Utton et al., [95] ont en effet avancé un autre effet du calcium sur la vitesse initiale de dissolution à différentes températures (de 30°C à 90°C), en présence de bore et à pH élevé (pH ≈ 12.5). Initialement, ils ont observé un retard de l'altération du verre (Fig. II-10a) et un comportement anti-corrélé du relargage du B avec la concentration de calcium initialement en solution (Fig. II-10b). Ils ont alors suggéré que le Ca en solution précipite avec le bore relargué pour former le solide $Ca[B(OH)_4]_2(s)$ suivant l'équation suivante :

$$Ca^{2+} + 2\,B(OH)_4^- \rightarrow Ca[B(OH)_4]_2(s) \qquad \text{(Eq. II-8)}$$

Ce solide crée une couche passivante qui inhibe, jusqu'à un certain point, la dissolution du verre en limitant l'hydrolyse de la matrice silicatée. Quand la solubilité des CSH est atteinte, $Ca[B(OH)_4]_2(s)$ devient instable et se dissout suivant la réaction inverse de Eq. II-8. Le calcium ainsi relargué peut alors être consommé par les CSH, dont la croissance réactive la dissolution du verre. En résumé, la présence de bore dans le système Ca-Si résulte en une période d'incubation au début de l'altération. Cependant, ce temps d'incubation et le pouvoir partiellement inhibiteur de ce solide décroissent avec la température, jusqu'à presque disparaitre à 90°C.

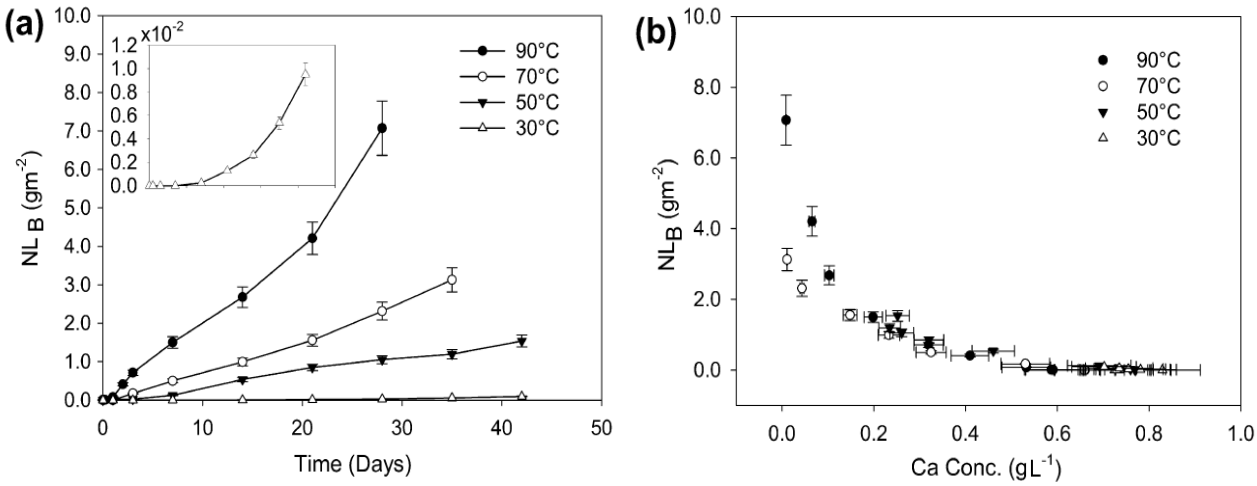

Figure II-10 : Graphique représentant la perte en masse normalisée du B, mesurée en ICP-MS/OES, à 90°C, 70°C, 50°C et 30°C, à pH 12.5 en fonction a) du temps et b) de la concentration de calcium en solution, par Utton et al., 2013 [95]

II.4.2. Silicates de calcium hydratés, CSH

II.4.2.1. Formation des CSH

Dans les ciments, la portlandite, est un hydroxyde de calcium issu de l'hydratation de deux silicates de calcium : le silicate tricalcique de formule chimique $3CaO.SiO_2$, aussi appelé alite et noté

C_3S, et le silicate bicalcique de formule chimique $2CaO.SiO_2$, aussi appelé bélite et noté C_2S. Elle se forme généralement en milieu basique suivant les équations suivantes [96-98] :

Une première étape d'hydratation des deux types de silicates calciques C_3S et C_2S a lieu :

$$C_3S + 3\,H_2O \rightarrow 3Ca^{2+} + H_2SiO_4^{2-} + 4OH^- \quad \text{(Eq. II-9)}$$

$$C_2S + 3\,H_2O \rightarrow 2Ca^{2+} + H_2SiO_4^{2-} + 4OH^- \quad \text{(Eq. II-10)}$$

Une fois ces silicates dissouts, une seconde réaction de précipitation a lieu afin de former le ciment de Portland :

$$xCa^{2+} + H_2SiO_4^{2-} + 2(x-1)OH^- + y\,H_2O \rightarrow C_xSH_y \quad \text{(Eq. II-11)}$$

$$Ca^{2+} + 2\,OH^- \rightarrow Ca(OH)_2\ (Portlandite) \quad \text{(Eq. II-12)}$$

Ainsi, la portlandite est accompagnée d'un précipité de silicates de calcium hydratés, de formule $CaO_x \cdot SiO_2 \cdot H_2O_y$ et appelé CSH (Calcium Silicate Hydrate) qui est la principale phase liante de ce ciment. De ce fait, ils sont aussi responsables de la résistance mécanique du ciment. La nature des CSH et leurs propriétés se définissent par rapport à leur rapport Ca/Si : dans le cas des ciments de Portland, ce rapport oscille entre 1,2 et 2,1 avec une moyenne générale autour de 1,75 [99-101] alors qu'en laboratoire, il est possible de synthétiser un CSH avec un rapport aussi bas que 0,6 [102]. Cette synthèse ne résulte pas de l'hydratation des phases cimentaires mais de la réactivité entre le calcium et le silicium à pH basique en solution.

II.4.2.2.Structure des CSH

A une échelle nanométrique, le CSH forme un gel avec une structure partiellement ordonnée. L'arrangement local dépend fortement du rapport Ca/Si lors de sa formation [103-105]. De ce fait, la structure lamellaire des CSH fait encore débat au sein de la communauté scientifique [99,102,104,106]. En 1950, deux types de structures ont été initialement distingués : les CSH(I), dont la structure ressemble à une tobermorite défective, et les CSH(II), qui contiennent des nano cristaux de portlandite [107]. Par la suite, différents modèles structuraux ont émergé [108-111] et, de manière générale, on décrit les CSH(I) avec un faible rapport Ca/Si en utilisant le modèle de la tobermorite (rapport Ca/Si proche de 0.8) [112] et les CSH(II) avec un fort rapport Ca/Si en utilisant le modèle de la jennite (rapport Ca/Si proche de 1.5) [113].

Les études structurales des CSH ont démontré des similitudes avec celles de la tobermorite (Fig. II-11) [115,116]. Cette structure est dite en feuillets car elle s'organise en couches successives d'oxyde de calcium octaédrique, enfermée de part et d'autre par deux chaines silicatés formées par des

groupes de trois tétraèdres (*dreierketten*) [117]. Un espace existe cependant entre ces feuillets qui peut être rempli par des molécules d'eau ou des ions calcium [106]. C'est cet espace qui caractérise le matériau : tobermorite 14 Å, 11 Å et 9 Å. Si les deux premiers existent naturellement, la tobermorite 9 Å résulte de leur déshydratation.

Enfin, le rapport Ca/Si des CSH impacte fortement la structure de ces minéraux. En effet, plusieurs études [118-120] ont constaté que plus le rapport Ca/Si est élevé, plus la longueur de la chaine silicatée est courte, et inversement. De plus, une augmentation de la quantité de calcium dans l'interfeuillet de la structure du CSH modifie l'environnement proche des atomes de silicium. Cela se traduit par des angles Si – O – Si plus faibles [121,122] et les dimensions des tétraèdres de silicium sont plus petites [123].

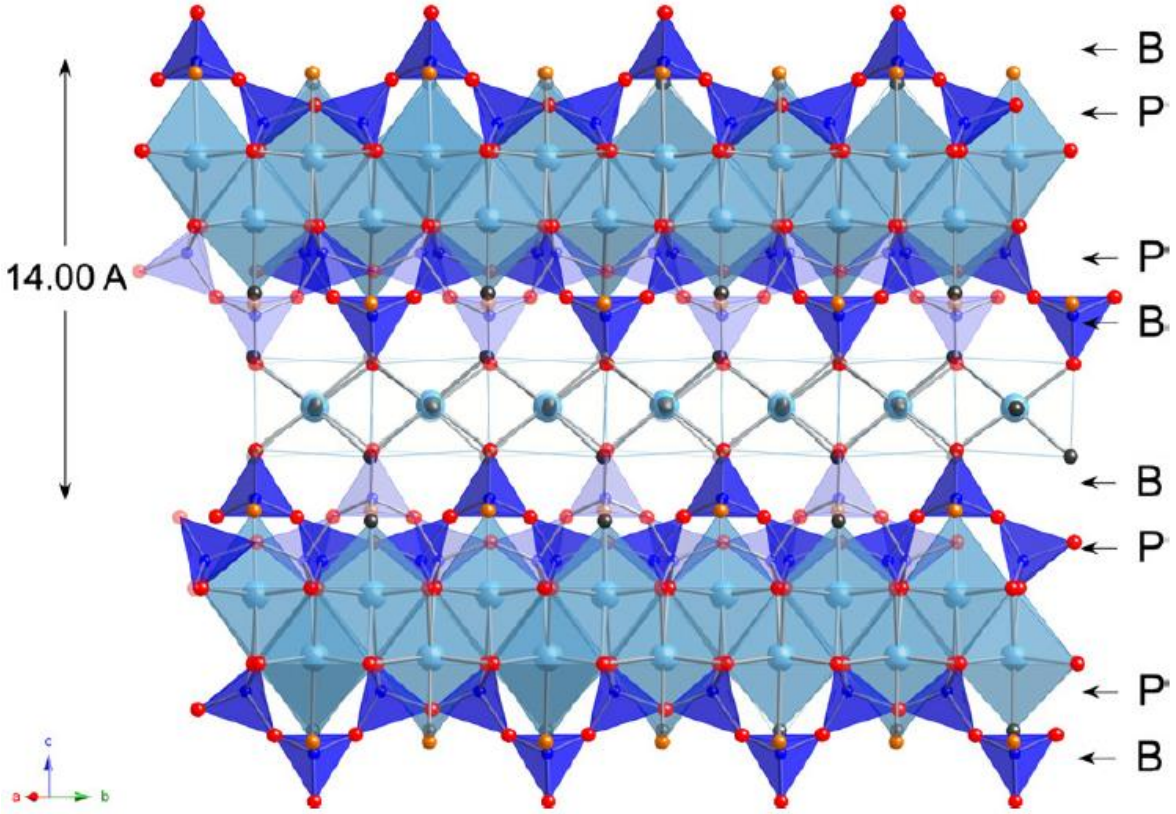

Figure II-11 : Schéma de la structure d'une tobermorite 14Å, par Richardson, 2008[99], adapté des travaux de Bonaccorsi et al.,[114]. Les atomes bleu foncé correspondent au silicium, les atomes rouges aux oxygènes pontants, les atomes orange aux oxygènes non-pontants et les atomes bleu clair au calcium. Les chaines silicatées présentent des tétraèdres en quinconce qui se partagent soit avec la couche Ca – O (« paired » tétraèdre, noté P) soit avec d'autres couches (« bridging » tétraèdre, noté B). Notons que les deux chaines silicatées ne sont pas reliées aux milieux par les oxygènes.

II.4.2.3.Solubilité des CSH

Malgré une distinction duale de la structure des CSH, lorsque l'on considère leur solubilité, un modèle à trois phases prend place en fonction de leur rapport Ca/Si [124-126]. La réaction d'équilibre de la solubilité des CSH peut s'écrire de la façon suivante :

$$(CaO)_x \cdot (SiO_2) \cdot (H_2O)_y + 2xH^+ \rightarrow xCa^{2+} + H_4SiO_4 + zH_2O \qquad \text{(Eq. II-13)}$$

Avec une constante de solubilité qui peut s'écrire :

$$K_s = \frac{a_{Ca}^x \times a_{H_4SiO_4}}{\left(a_{H^+}^x\right)^2} \qquad \text{(Eq. II-14)}$$

où x est la rapport Ca/Si du CSH et $z = x + y - 2$.

Ce modèle a été réutilisé dans cette étude afin de calculer les états de saturation de la solution, en fonction de ces trois types de CSH, sur la base des travaux de Blanc et al., 2010 [127,128]. On considère ainsi :

- Les CSH-α, qui possèdent un rapport Ca/Si compris entre 0.6 et 1. La solution interstitielle possède généralement une concentration en ions calcium inférieure à 2 mmol.L^{-1} et la constante de solubilité vaut $logK_s = 53{,}5129$. Dans notre étude, ils correspondent aux CSH0.8.
- Les CSH-β qui possèdent un rapport Ca/Si compris entre 1 et 1,5. La solution interstitielle possède généralement une concentration en ions calcium entre 2 et 22 mmol.L^{-1} et la constante de solubilité vaut $logK_s = 29.6129$. Dans notre étude, ils correspondent aux CSH1.2.
- Les CSH-γ qui possèdent un rapport Ca/Si compris entre 1.5 et 2. La solution interstitielle possède généralement une concentration en ions calcium supérieure à 22 mmol.L^{-1} et la constante de solubilité vaut $logK_s = 104.9129$. Dans notre étude, ils correspondent aux CSH1.6.

Les deux premiers CSH-α et -β peuvent se retrouver dans des matrices carbonatées (voir section II.4.2.5.). Le troisième CSH-γ correspond à une concentration en équilibre avec la portlandite à 25°C. De fait, c'est la principale phase des CSH qui se retrouvent dans les ciments de Portland. La teneur en eau des CSH, autrement dit le rapport H/Si, peut varier de 1 en condition sèche et basse en température (-80°C) à 4 lorsqu'il est en état de saturation en eau [130-132]. Ainsi, les trois types de CSH (voir Fig. II-12) pourront précipiter dans cette étude au regard de l'état de saturation de la solution vis-à-vis de ces phases. Cependant, la distinction entre ces trois phases n'est pas notre principal objectif et seule leur présence ainsi que l'état d'avancement de leur processus de formation nous intéresseront afin de borner le domaine d'étude.

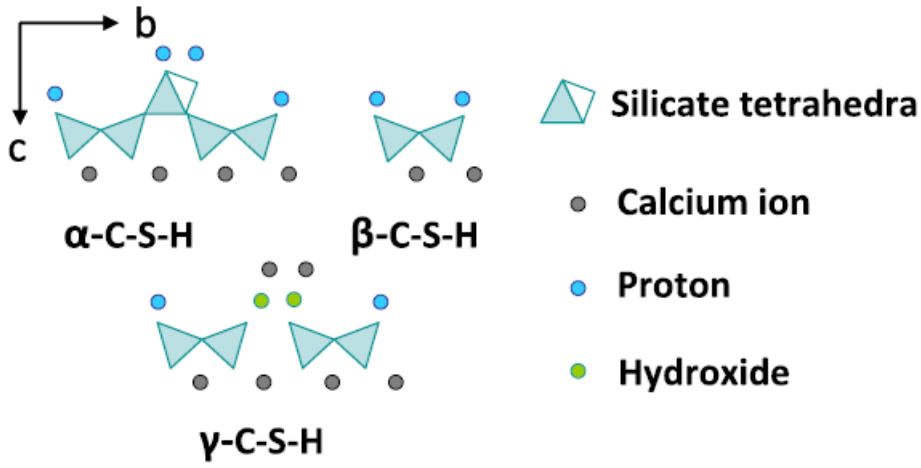

Figure II-12 : Schéma représentant les blocs élémentaires des différents types de CSH (CSH-α, CSH-β et CSH-γ), utilisés dans les calculs thermodynamiques de la solubilité de ces matériaux, par Haas et al.[126].

II.4.2.4. Mécanismes de précipitation des CSH

Initialement, la formation des CSH peut être décrite par une nucléation hétérogène ou homogène suivie d'une étape de croissance [133,134]. La sursaturation en solution par rapport aux CSH est alors un des principaux facteurs qui contrôlent la vitesse de nucléation. Cependant, en se focalisant sur les premiers stades de la nucléation et à l'aide de mesures de la turbidité du milieu (Fig. II-13), Krautwurst et al., [135] ont différencié deux étapes élémentaires : premièrement, des sphères amorphes dispersées se forment en solution par nucléation homogène. Ces sphères ont une composition similaire aux CSH-β mais sont néanmoins appauvries en calcium en comparaison avec le CSH final. En contrepartie, ils incorporent des ions Na^+ en tant que compensateurs de charge. Et deuxièmement, les CSH cristallisent pour former une structure similaire à la tobermorite. Cette cristallisation des CSH s'accompagne i) d'un échange cationique entre les sodiums des CSH et les ions calcium en solution, et ii) d'un phénomène d'agrégation des CSH [136].

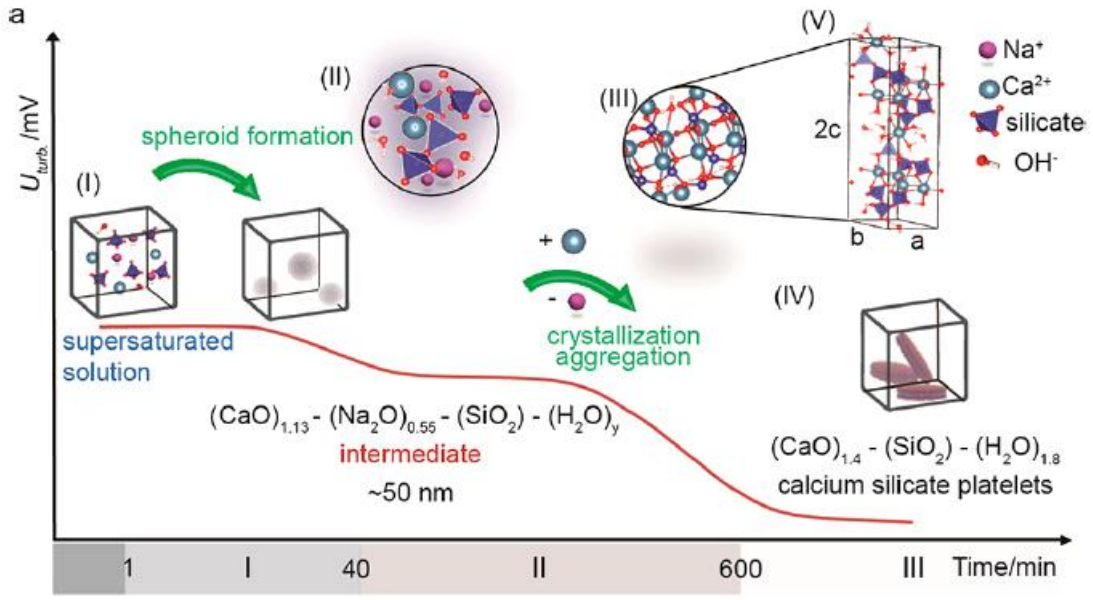

Figure II-13 : Représentation des deux étapes élémentaires dans la nucléation des CSH par Krautwurst et al.,[135]. La courbe rouge représente l'évolution de la turbidité de la solution avec les différentes espèces et états des CSH en fonction du temps de synthèse. (I) Initialement, la solution est sursaturée, (II) des sphères amorphes de CSH se forment, (III) ces sphères s'agrègent, les cations Ca^{2+} et Na^{+} s'échangent, et les précipités cristallisent pour (IV) former le produit final, le CSH-β. Le modèle (V) représente la structure du CSH proche de celui de la tobermorite 14Å.

Cette approche est fondamentalement différente de la théorie classique de la nucléation, qui décrit ce processus comme l'addition successive de monomères jusqu'à l'atteinte d'un nucléus critique stable et dont la cristallinité et la composition chimique sont identiques à celles de la phase finale, un tel nucléus critique évoluant alors spontanément vers des phases microscopiques. D'autres études [137,138] ont apporté des preuves supplémentaires soutenant une formation non classique des CSH. En utilisant des méthodes de simulation atomique (Théorie de la Fonctionnelle de la Densité – DFT), des algorithmes évolutionnaires et des modélisations de dynamique moléculaire, Aretxabaleta et al., [139] ont recherché la brique élémentaire des CSH. Ils ont ainsi proposé le chemin de formation des CSH suivant : dans un premier temps, des petits agrégats de dimère de silice fusionnent entre eux pour en former des plus grands, cette étape constitue le cœur du modèle alternatif. Suite à une réaction de déshydratation, la brique élémentaire des CSH $(CaO)_4 \cdot (SiO_2)_4 \cdot (H_2O)_2$ peut se former parmi ces agrégats, indépendamment les uns des autres. Les CSH amorphes ainsi formés peuvent par la suite cristalliser et entamer leur croissance.

II.4.2.5.Carbonatation des CSH

Les CSH sont des matériaux qui ont une forte tendance à se carbonater en présence de dioxyde de carbone [112,140-145]. La carbonatation est due à une réaction entre les ions calciums présents dans les interfeuillets et les ions carbonates présents en solution qui se traduit par l'équation suivante [146,147] :

$$(CaO)_x \cdot (SiO_2) \cdot (H_2O)_y + xCO_3^{2-} \rightarrow xCaCO_3 + H_4SiO_4 + (x + y - 2)H_2O \quad \text{(Eq. II-15)}$$

Du fait de la forte implication du calcium dans cette réaction, le rapport Ca/Si modifie grandement la résistance à la carbonatation du CSH. Cependant, un consensus n'a toujours pas été atteint : si certaines études [148] expliquent que plus le rapport Ca/Si est faible et plus la résistance à la carbonatation est élevée, d'autres [143,149] soutiennent le contraire – le CSH se décompose plus rapidement lorsque le rapport est faible.

Le mécanisme de carbonatation des CSH dans le ciment de Portland se décompose en deux étapes. La première consiste en une *décalcification* du CSH [150]. Les CSH restant peuvent se recondenser pour former des CSH de rapport Ca/Si plus faible [151,152]. Cette décalcification a lieu jusqu'à obtenir un rapport Ca/Si proche de 0,66 [149] qui correspond à la structure de la tobermorite 14Å avec le rapport Ca/Si le plus bas [100]. La seconde étape consiste en la formation d'un *gel de silice* suite à la décomposition du CSH [153]. Notons qu'une polymérisation de la chaine silicatée des CSH est observée lorsque le rapport Ca/Si diminue dans la première étape [149,154]

Cependant, une étude plus récente a conduit à diviser ce processus en milieu aqueux en trois phases [142] :

i) Une première période de dissolution et de décalcification où le rapport Ca/Si et le pH en solution diminuent. En parallèle, des carbonates de calcium commencent à se former en solution.
ii) Puis vient une période de diffusion où les CSH se lient entre eux pour former une phase amorphe, appelée « gel de silice modifiée avec calcium ».
iii) Enfin, les CSH se dissolvent complètement pour former des carbonates de calcium, en laissant derrière un gel de silice modifié avec calcium.

Les carbonates de calcium précipitent initialement en tant que phase amorphe mais peuvent aussi évoluer vers des phases cristallines qui sont l'aragonite, la vatérite et la calcite [145,155].

II.5. Synthèse

Au cours de ce chapitre, nous avons vu que la question sur les mécanismes d'altération des silicates (hydrolyse – recondensation et dissolution – reprécipitation) fait encore débat au sein de la communauté scientifique. Cette question est au cœur du premier axe de cette thèse. A travers une comparaison entre l'altération d'un silicate amorphe (verre albitique) et de son équivalent cristallin (albite), le chapitre III abordera les mécanismes d'altération des silicates et l'effet de leur désordre structurel sur leur comportement. Dans un contexte plus global, si cette question mécanistique est fondamentale, elle ne représente qu'une partie des enjeux associés à l'altération des verres, matrice de confinement des déchets radioactifs, dans leur environnement de stockage.

En effet, lors de l'altération des différentes barrières protectrices du stockage géologique profond, on s'attend à observer une solution alcaline chargée en silice et en calcium, à pH basique, en contact avec le verre. Ces conditions sont par ailleurs favorables à différents mécanismes d'altération du verre, tous mettant en œuvre les effets antagonistes du calcium sur la vitesse de dissolution des verres. Le chapitre IV portera sur l'effet du calcium sur les propriétés diffusives du gel formé sur le verre ISG en pH basique, à 90°C, durant les 21 premiers jours d'altération. Différentes méthodes analytiques seront employées afin de calculer les coefficients de diffusion d'espèces aqueuses au travers de gels formés dans des solutions avec différentes teneurs en calcium et précipités. Par la suite, notre analyse privilégie la formation des CSH sur un temps plus long (environ 3 mois). L'examen des effets du Ca et Si dissous et des néoformations de phases secondaires sur la vitesse d'altération du verre constitue un des principaux enjeux du second axe de cette thèse. Le chapitre V abordera notamment l'évolution de cette vitesse à pH basique, 90°C avec la formation des CSH : depuis leur nucléation, leur agrégation, leur croissance et *in fine*, leur carbonatation.

REFERENCES

1 Advocat, T., Vernaz, E. & Crovisier, J. L. Aqueous corrosion of french R7T7 nuclear waste glass: selective then congruent dissolution by pH increase. *Comptes Rendus de l'Academie des Sciences Serie 2* **313**, 407-412 (1991).

2 Bunker, B. C. MOLECULAR MECHANISMS FOR CORROSION OF SILICA AND SILICATE-GLASSES. *Journal of Non-Crystalline Solids* **179**, 300-308 (1994).

3 Chave, T., Frugier, P., Ayral, A. & Gin, S. Solid state diffusion during nuclear glass residual alteration in solution. *Journal of Nuclear Materials* **362**, 466-473, doi:https://doi.org/10.1016/j.jnucmat.2007.01.095 (2007).

4 Grambow, B. A general rate equation for nuclear waste glass corrosion. *Mater. Res. Soc. Symp. Proc.* **44**, 15-27 (1985).

5 Gin, S., Delaye, J.-M., Angeli, F. & Schuller, S. Aqueous alteration of silicate glass: state of knowledge and perspectives. *npj Materials Degradation* **5**, 42, doi:10.1038/s41529-021-00190-5 (2021).

6 Frankel, G. S. *et al.* Recent Advances in Corrosion Science Applicable To Disposal of High-Level Nuclear Waste. *Chemical Reviews* **121**, 12327-12383, doi:10.1021/acs.chemrev.0c00990 (2021).

7 Grambow, B. Nuclear Waste Glasses - How Durable? *Elements* **2**, 357-364, doi:10.2113/gselements.2.6.357 (2006).

8 Gin, S., Beaudoux, X., Angéli, F., Jégou, C. & Godon, N. Effect of composition on the short-term and long-term dissolution rates of ten borosilicate glasses of increasing complexity from 3 to 30 oxides. *Journal of Non-Crystalline Solids* **358**, 2559-2570, doi:https://doi.org/10.1016/j.jnoncrysol.2012.05.024 (2012).

9 Hellmann, R. *et al.* Unifying natural and laboratory chemical weathering with interfacial dissolution–reprecipitation: A study based on the nanometer-scale chemistry of fluid–silicate interfaces. *Chem Geol* **294–295**, 203-216 (2012).

10 Geneste, G., Bouyer, F. & Gin, S. Hydrogen–sodium interdiffusion in borosilicate glasses investigated from first principles. *Journal of Non-Crystalline Solids* **352**, 3147-3152, doi:https://doi.org/10.1016/j.jnoncrysol.2006.04.023 (2006).

11 Hou, X., Kirkpatrick, R. J., Struble, L. J. & Monteiro, P. J. M. Structural Investigations of Alkali Silicate Gels. *Journal of the American Ceramic Society* **88**, 943-949, doi:https://doi.org/10.1111/j.1551-2916.2005.00145.x (2005).

12 C.E. Tambelli, J. F. S., N.P. Hasparyk, P.J.M. Monteiro,. Study of the structure of alkali–silica reaction gel by high-resolution NMR spectroscopy,. *Journal of Non-Crystalline Solids* **352**, 3429-3436, doi:https://doi.org/10.1016/j.jnoncrysol.2006.03.112. (2006).

13 Zapol, P., He, H., Kwon, K. D. & Criscenti, L. J. First-Principles Study of Hydrolysis Reaction Barriers in a Sodium Borosilicate Glass. *International Journal of Applied Glass Science* **4**, 395-407, doi:https://doi.org/10.1111/ijag.12052 (2013).

14 Gin, S., Ryan, J. V., Schreiber, D. K., Neeway, J. & Cabié, M. Contribution of atom-probe tomography to a better understanding of glass alteration mechanisms: Application to a nuclear glass specimen altered 25 years in a granitic environment. *Chem Geol* **349–350**, 99-109, doi:http://dx.doi.org/10.1016/j.chemgeo.2013.04.001 (2013).

15 Ribet, I. & Godon, N. Altération par l'eau des verres borosilicatés--Exemple des verres nucléaires. *Techniques de l'ingénieur Matériaux: résistance à la corrosion et au vieillissement* **25** (2014).

16 Jollivet, P. *et al.* Effect of clayey groundwater on the dissolution rate of the simulated nuclear waste glass SON68. *Journal of Nuclear Materials* **420**, 508-518, doi:https://doi.org/10.1016/j.jnucmat.2011.10.026 (2012).

17 Criscenti, L. J., Kubicki, J. D. & Brantley, S. L. Silicate glass and mineral dissolution: Calculated reaction paths and activation energies for hydrolysis of a Q(3) si by H3O+ using ab initio methods. *Journal of Physical Chemistry A* **110**, 198-206, doi:10.1021/jp044360a (2006).
18 Wolff-Boenisch, D., Gislason, S. R., Oelkers, E. H. & Putnis, C. V. The dissolution rates of natural glasses as a function of their composition at pH 4 and 10.6, and temperatures from 25 to 74 degrees C. *Geochim Cosmochim Ac* **68**, 4843-4858, doi:DOI 10.1016/j.gca.2004.05.027 (2004).
19 Inagaki, Y., Kikunaga, T., Idemitsu, K. & Arima, T. Initial Dissolution Rate of the International Simple Glass as a Function of pH and Temperature Measured Using Microchannel Flow-Through Test Method. *International Journal of Applied Glass Science* **4**, 317-327 (2013).
20 Nathalie Valle, A. V.-C., Jérôme Sterpenich, Guy Libourel, Etienne Deloule, Patrick Jollivet,. Elemental and isotopic (29Si and 18O) tracing of glass alteration mechanisms. *Geochim Cosmochim Ac* **74**, 3412-3431, doi:https://doi.org/10.1016/j.gca.2010.03.028 (2010).
21 Godon, N., Gin, S., Rebiscoul, D. & Frugier, P. SON68 Glass Alteration Enhanced by Magnetite. *Procedia Earth and Planetary Science* **7**, 300-303, doi:https://doi.org/10.1016/j.proeps.2013.03.039 (2013).
22 Yang, Y., Min, Y. & Jun, Y.-S. A mechanistic understanding of plagioclase dissolution based on Al occupancy and T–O bond length: from geologic carbon sequestration to ambient conditions. *Physical Chemistry Chemical Physics* **15**, 18491-18501 (2013).
23 Damodaran, K., Delaye, J.-M., Kalinichev, A. G. & Gin, S. Deciphering the non-linear impact of Al on chemical durability of silicate glass. *Acta Materialia*, 117478, doi:https://doi.org/10.1016/j.actamat.2021.117478 (2021).
24 Aagaard, P. & Helgeson, H. C. THERMODYNAMIC AND KINETIC CONSTRAINTS ON REACTION-RATES AMONG MINERALS AND AQUEOUS-SOLUTIONS .1. THEORETICAL CONSIDERATIONS. *Am J Sci* **282**, 237-285 (1982).
25 Bourcier, W. L., Peiffer, D. W., Knauss, K. G., McKeegan, K. D. & Smith, D. K. A Kinetic Model for Borosilicate Glass Dissolution Based on the Dissolution Affinity of a Surface Alteration Layer. *MRS Online Proceedings Library Archive* **176**, null-null, doi:doi:10.1557/PROC-176-209 (1989).
26 Grambow, B. & Muller, R. First-order dissolution rate law and the role of surface layers in glass performance assessment. *Journal of Nuclear Materials* **298**, 112-124 (2001).
27 K. Ferrand, A. A., B. Grambow,. Water diffusion in the simulated French nuclear waste glass SON 68 contacting silica rich solutions: Experimental and modeling,. *Journal of Nuclear Materials* **355**, 54-67, doi:https://doi.org/10.1016/j.jnucmat.2006.04.005 (2006).
28 Collin, M., Fournier, M., Charpentier, T., Moskura, M. & Gin, S. Impact of alkali on the passivation of silicate glass. *npj Materials Degradation* **2**, 16 (2018).
29 Valle, N. Isotope tracing (29Si and 18O) of the alteration mechanisms of the French glass 'SON68' used for the storage of nuclear waste. 250 (France, 2001).
30 Jégou, C., Gin, S. & Larché, F. Alteration kinetics of a simplified nuclear glass in an aqueous medium: effects of solution chemistry and of protective gel properties on diminishing the alteration rate. *Journal of Nuclear Materials* **280**, 216-229, doi:https://doi.org/10.1016/S0022-3115(00)00039-8 (2000).
31 Cailleteau, C. *et al.* Insight into silicate-glass corrosion mechanisms. *Nature Materials* **7**, 978-983, doi:10.1038/nmat2301 (2008).
32 Casey, W. H. GLASS AND MINERAL CORROSION Dynamics and durability. *Nature Materials* **7**, 930-932, doi:10.1038/nmat2326 (2008).
33 Gin, S. *et al.* Dynamics of self-reorganization explains passivation of silicate glasses. *Nature communications* **9**, 2169 (2018).
34 Rebiscoul, D. *et al.* Morphological evolution of alteration layers formed during nuclear glass alteration: new evidence of a gel as a diffusive barrier. *Journal of Nuclear Materials* **326**, 9-18, doi:http://dx.doi.org/10.1016/j.jnucmat.2003.10.015 (2004).

35 Diane Rebiscoul, P. F., Stéphane Gin, André Ayral,. Protective properties and dissolution ability of the gel formed during nuclear glass alteration. *Journal of Nuclear Materials* **342**, 26-34, doi:https://doi.org/10.1016/j.jnucmat.2005.03.018 (2005).

36 Jollivet, P. *et al.* Investigation of gel porosity clogging during glass leaching. *Journal of Non-Crystalline Solids* **354**, 4952-4958, doi:10.1016/j.jnoncrysol.2008.07.023 (2008).

37 Vienna, J. D., Ryan, J. V., Gin, S. & Inagaki, Y. Current Understanding and Remaining Challenges in Modeling Long-Term Degradation of Borosilicate Nuclear Waste Glasses. *International Journal of Applied Glass Science* **4**, 283-294, doi:https://doi.org/10.1111/ijag.12050 (2013).

38 Frugier, P. *et al.* SON68 nuclear glass dissolution kinetics: Current state of knowledge and basis of the new GRAAL model. *Journal of Nuclear Materials* **380**, 8-21, doi:10.1016/j.jnucmat.2008.06.044 (2008).

39 Feron, D., Richet, C. & Bonin, B. *Corrosion et altération des matériaux du nucléaire*. (CEA Saclay; Groupe Moniteur, 2010).

40 Fournier, M., Frugier, P. & Gin, S. Effect of Zeolite Formation on Borosilicate Glass Dissolution Kinetics. *Procedia Earth and Planetary Science* **7**, 264-267, doi:https://doi.org/10.1016/j.proeps.2013.03.085 (2013).

41 Gin, S. & Mestre, J. P. SON 68 nuclear glass alteration kinetics between pH 7 and pH 11.5. *Journal of Nuclear Materials* **295**, 83-96, doi:https://doi.org/10.1016/S0022-3115(01)00434-2 (2001).

42 Ribet, S. & Gin, S. Role of neoformed phases on the mechanisms controlling the resumption of SON68 glass alteration in alkaline media. *Journal of Nuclear Materials* **324**, 152-164, doi:https://doi.org/10.1016/j.jnucmat.2003.09.010 (2004).

43 Van Iseghem, P. & Grambow, B. The Long-Term Corrosion and Modelling of Two Simulated Belgian Reference High-Level Waste Glasses. *MRS Proceedings* **112**, 631, doi:10.1557/proc-112-631 (1987).

44 Gin, S. *et al.* The fate of silicon during glass corrosion under alkaline conditions: A mechanistic and kinetic study with the International Simple Glass. *Geochim Cosmochim Ac* **151**, 68-85, doi:https://doi.org/10.1016/j.gca.2014.12.009 (2015).

45 Fournier, M. *et al.* Effect of pH on the stability of passivating gel layers formed on International Simple Glass. *Journal of Nuclear Materials* **524**, 21-38, doi:https://doi.org/10.1016/j.jnucmat.2019.06.029 (2019).

46 Aréna, H. *et al.* Impact of Fe, Mg and Ca elements on glass alteration: Interconnected processes. *Geochim Cosmochim Ac* **239**, 420-445, doi:https://doi.org/10.1016/j.gca.2018.08.007 (2018).

47 Gin, S. *et al.* An international initiative on long-term behavior of high-level nuclear waste glass. *Materials Today* **16**, 243-248, doi:https://doi.org/10.1016/j.mattod.2013.06.008 (2013).

48 Fournier, M., Gin, S. & Frugier, P. Resumption of nuclear glass alteration: state of the art. *Journal of Nuclear Materials* **448**, 348-363 (2014).

49 Fournier, M., Frugier, P. & Gin, S. Application of GRAAL model to the resumption of International Simple Glass alteration. *npj Materials Degradation* **2**, 21, doi:10.1038/s41529-018-0043-4 (2018).

50 Mercado-Depierre, S., Fournier, M., Gin, S. & Angeli, F. Influence of zeolite precipitation on borosilicate glass alteration under hyperalkaline conditions. *Journal of Nuclear Materials* **491**, 67-82, doi:https://doi.org/10.1016/j.jnucmat.2017.04.043 (2017).

51 Makhlouf, I. M., Tarawneh, K., Moumani, K. & Ibrahim, K. M. Recognition of quartz geodes in the Upper Cretaceous Wadi Umm Ghudran Formation, Ras En Naqab, South Jordan. *Arabian Journal of Geosciences* **8**, 1535-1547, doi:10.1007/s12517-014-1281-6 (2015).

52 Caurel, J., Vemaz, E. & Beaufort, D. Hydrothermal Leaching of R7-T7 Borosilicate Glass. *MRS Online Proceedings Library* **176**, 309, doi:10.1557/proc-176-309 (1989).

53 Grangeon, S. *et al.* On the nature of structural disorder in calcium silicate hydrates with a calcium/silicon ratio similar to tobermorite. *Cement and Concrete Research* **52**, 31-37, doi:https://doi.org/10.1016/j.cemconres.2013.05.007 (2013).

54 Gaboreau, S. *et al.* Hydration Properties and Interlayer Organization in Synthetic C-S-H. *Langmuir* **36**, 9449-9464, doi:10.1021/acs.langmuir.0c01335 (2020).
55 Petit, J. C., Dellamea, G., Dran, J. C., Schott, J. & Berner, R. A. MECHANISM OF DIOPSIDE DISSOLUTION FROM HYDROGEN DEPTH PROFILING. *Nature* **325**, 705-707 (1987).
56 Schott, J. & Berner, R. A. X-Ray Photoelectron Studies of the Mechanism of Iron Silicate Dissolution during Weathering. *Geochim Cosmochim Ac* **47**, 2233-2240, doi:Doi 10.1016/0016-7037(83)90046-7 (1983).
57 Schott, J. *et al.* Formation, growth and transformation of leached layers during silicate minerals dissolution: The example of wollastonite. *Geochim Cosmochim Ac* **98**, 259-281, doi:DOI 10.1016/j.gca.2012.09.030 (2012).
58 Hellmann, R. The albite-water system: Part I. The kinetics of dissolution as a function of pH at 100, 200 and 300°C. *Geochim Cosmochim Ac* **58**, 595-611 (1994).
59 Hellmann, R. The albite-water system: Part II. The time-evolution of the stoichiometry of dissolution as a function of pH at 100, 200, and 300 C. *Geochim Cosmochim Ac* **59**, 1669-1697 (1995).
60 Hellmann, R., Dran, J. C. & DellaMea, G. The albite-water system .3. Characterization of leached and hydrogen-enriched layers formed at 300 degrees C using MeV ion beam techniques. *Geochim Cosmochim Ac* **61**, 1575-1594 (1997).
61 Hellmann, R. The albite-water system .4. Diffusion modeling of leached and hydrogen-enriched layers. *Geochim Cosmochim Ac* **61**, 1595-1611 (1997).
62 Oelkers, E. H. General kinetic description of multioxide silicate mineral and glass dissolution. *Geochim Cosmochim Ac* **65**, 3703-3719, doi:Doi 10.1016/S0016-7037(01)00710-4 (2001).
63 Daux, V., Guy, C., Advocat, T., Crovisier, J. L. & Stille, P. Kinetic aspects of basaltic glass dissolution at 90 degrees C: role of aqueous silicon and aluminium. *Chem Geol* **142**, 109-126 (1997).
64 Daval, D. *et al.* Influence of amorphous silica layer formation on the dissolution rate of olivine at 90 degrees C and elevated pCO(2). *Chem Geol* **284**, 193-209, doi:10.1016/j.chemgeo.2011.02.021 (2011).
65 Daval, D., Hellmann, R., Saldi, G. D., Wirth, R. & Knauss, K. G. Linking nm-scale measurements of the anisotropy of silicate surface reactivity to macroscopic dissolution rate laws: New insights based on diopside. *Geochim Cosmochim Ac* **107**, 121-134, doi:http://dx.doi.org/10.1016/j.gca.2012.12.045 (2013).
66 Hellmann, R., Penisson, J.-M., Hervig, R. L., Thomassin, J.-H. & Abrioux, M.-F. An EFTEM/HRTEM high-resolution study of the near surface of labradorite feldspar altered at acid pH: evidence for interfacial dissolution-reprecipitation. *Phys Chem Miner* **30**, 192-197 (2003).
67 Daval, D. *et al.* Mechanism of wollastonite carbonation deduced from micro- to nanometer length scale observations. *Am Mineral* **94**, 1707-1726, doi:10.2138/am.2009.3294 (2009).
68 O'Neil, J. R. & Taylor, H. P., Jr. The oxygen isotope and cation exchange chemistry of feldspars1. *Am Mineral* **52**, 1414-1437 (1967).
69 Hay, R. L. & Iijima, A. in *Studies in Volcanology* Vol. 116 (eds Robert R. Coats, Richard L. Hay, & Charles A. Anderson) 0 (Geological Society of America, 1968).
70 Putnis, A. in *18th General Meeting of the International-Mineralogical-Association.* 689-708 (Mineralogical Society).
71 Putnis, A. Mineral Replacement Reactions. *Rev Mineral Geochem* **70**, 87-124, doi:10.2138/rmg.2009.70.3 (2009).
72 Putnis, A. Why Mineral Interfaces Matter. *Science* **343**, 1441-1442, doi:10.1126/science.1250884 (2014).
73 Hellmann, R. *et al.* Nanometre-scale evidence for interfacial dissolution–reprecipitation control of silicate glass corrosion. *Nat Mater* **14**, 307-311, doi:10.1038/nmat4172

http://www.nature.com/nmat/journal/v14/n3/abs/nmat4172.html#supplementary-information (2015).

74 Hellmann, R. in *Encyclopedia of Glass Science, Technology, History, and Culture* 647-662 (2021).
75 Fenter, P. & Sturchio, N. C. Mineral–water interfacial structures revealed by synchrotron X-ray scattering. *Progress in Surface Science* **77**, 171-258, doi:https://doi.org/10.1016/j.progsurf.2004.12.001 (2004).
76 Marry, V., Rotenberg, B. & Turq, P. Structure and dynamics of water at a clay surface from molecular dynamics simulation. *Physical Chemistry Chemical Physics* **10**, 4802-4813, doi:10.1039/b807288d (2008).
77 Geisler, T. *et al.* Aqueous corrosion of borosilicate glass under acidic conditions: A new corrosion mechanism. *Journal of Non-Crystalline Solids* **356**, 1458-1465, doi:10.1016/j.jnoncrysol.2010.04.033 (2010).
78 Ruiz-Agudo, E. *et al.* Control of silicate weathering by interface-coupled dissolution-precipitation processes at the mineral-solution interface. *Geology* **44**, 567-570, doi:10.1130/g37856.1 (2016).
79 Daval, D. *et al.* Dynamics of altered surface layer formation on dissolving silicates. *Geochim Cosmochim Ac* **209**, 51-69, doi:https://doi.org/10.1016/j.gca.2017.04.010 (2017).
80 Saldi, G. D., Daval, D., Morvan, G. & Knauss, K. G. The role of Fe and redox conditions in olivine carbonation rates: An experimental study of the rate limiting reactions at 90 and 150 °C in open and closed systems. *Geochim Cosmochim Ac* **118**, 157-183, doi:http://dx.doi.org/10.1016/j.gca.2013.04.029 (2013).
81 Sissmann, O. *et al.* The deleterious effect of secondary phases on olivine carbonation yield: Insight from time-resolved aqueous-fluid sampling and FIB-TEM characterization. *Chem Geol* **357**, 186-202, doi:http://dx.doi.org/10.1016/j.chemgeo.2013.08.031 (2013).
82 Gin, S. p. *et al.* Nuclear Glass Durability: New Insight into Alteration Layer Properties. *The Journal of Physical Chemistry C* **115**, 18696-18706, doi:10.1021/jp205477q (2011).
83 Gin, S. *et al.* Atom-probe tomography, TEM and ToF-SIMS study of borosilicate glass alteration rim: a multiscale approach to investigating rate-limiting mechanisms. *Geochim Cosmochim Ac* **202**, 57-76 (2017).
84 Gin, S. *et al.* A general mechanism for gel layer formation on borosilicate glass under aqueous corrosion. *The Journal of Physical Chemistry C* **124**, 5132-5144 (2020).
85 Perez, A. *et al.* Comparing the reactivity of glasses with their crystalline equivalents: The case study of plagioclase feldspar. *Geochim Cosmochim Ac* **254**, 122-141, doi:https://doi.org/10.1016/j.gca.2019.03.030 (2019).
86 Liu, S., Ferrand, K. & Lemmens, K. Transport- and surface reaction-controlled SON68 glass dissolution at 30°C and 70°C and pH=13.7. *Appl Geochem* **61**, 302-311, doi:https://doi.org/10.1016/j.apgeochem.2015.06.014 (2015).
87 Jollivet, P., Gin, S. & Schumacher, S. Forward dissolution rate of silicate glasses of nuclear interest in clay-equilibrated groundwater. *Chem Geol* **330–331**, 207-217, doi:http://dx.doi.org/10.1016/j.chemgeo.2012.09.012 (2012).
88 Maraghechi, H., Rajabipour, F., Pantano, C. G. & Burgos, W. D. Effect of calcium on dissolution and precipitation reactions of amorphous silica at high alkalinity. *Cement and Concrete Research* **87**, 1-13, doi:https://doi.org/10.1016/j.cemconres.2016.05.004 (2016).
89 Mercado-Depierre, S., Angeli, F., Frizon, F. & Gin, S. Antagonist effects of calcium on borosilicate glass alteration. *Journal of Nuclear Materials* **441**, 402-410, doi:https://doi.org/10.1016/j.jnucmat.2013.06.023 (2013).
90 CHAVE, T., Frugier, P., Gin, S. & Ayral, A. Glass–water interphase reactivity with calcium rich solutions. *Geochim Cosmochim Ac* **75**, 4125 - 4139, doi:10.1016/j.gca.2011.05.005 (2011).
91 Dove, P. M. & Nix, C. J. The influence of the alkaline earth cations, magnesium, calcium, and barium on the dissolution kinetics of quartz. *Geochim Cosmochim Ac* **61**, 3329-3340, doi:Doi 10.1016/S0016-7037(97)00217-2 (1997).

92 Wallace, A. F., Gibbs, G. V. & Dove, P. M. Influence of Ion-Associated Water on the Hydrolysis of Si−O Bonded Interactions. *The Journal of Physical Chemistry A* **114**, 2534-2542, doi:10.1021/jp907851u (2010).
93 Ferrand, K. *et al.* Dissolution Kinetics of International Simple Glass and Formation of Secondary Phases at Very High Surface Area to Solution Ratio in Young Cement Water. *Materials* **14** (2021).
94 Neeway, J. J. *et al.* Acceleration of glass alteration rates induced by zeolite seeds at controlled pH. *Appl Geochem* **113**, 104515, doi:https://doi.org/10.1016/j.apgeochem.2019.104515 (2020).
95 Utton, C. *et al.* Dissolution of Vitrified Wastes in a High-pH Calcium-Rich Solution. *Journal of Nuclear Materials* **435**, 112–122, doi:10.1016/j.jnucmat.2012.12.032 (2013).
96 Uchikawa, H., Ogawa, K. & Uchida, S. Influence of character of clinker on the early hydration process and rheological property of cement paste. *Cement and Concrete Research* **15**, 561-572, doi:https://doi.org/10.1016/0008-8846(85)90053-5 (1985).
97 Granju, J. L. & Grandet, J. Characterization of the hydration state of Portland cement pastes. *Cement and Concrete Research* **18**, 886-894, doi:https://doi.org/10.1016/0008-8846(88)90024-5 (1988).
98 Bullard, J. W. *et al.* Mechanisms of cement hydration. *Cement and Concrete Research* **41**, 1208-1223, doi:http://doi.org/10.1016/j.cemconres.2010.09.011 (2011).
99 Richardson, I. G. The calcium silicate hydrates. *Cement and Concrete Research* **38**, 137-158, doi:10.1016/j.cemconres.2007.11.005 (2008).
100 Nonat, A. The structure and stoichiometry of C-S-H. *Cement and Concrete Research* **34**, 1521-1528, doi:https://doi.org/10.1016/j.cemconres.2004.04.035 (2004).
101 Girão, A. V., Richardson, I. G., Taylor, R. & Brydson, R. M. D. Composition, morphology and nanostructure of C–S–H in 70% white Portland cement–30% fly ash blends hydrated at 55°C. *Cement and Concrete Research* **40**, 1350-1359, doi:https://doi.org/10.1016/j.cemconres.2010.03.012 (2010).
102 Zhakiyeva, Z. *Structure et dynamique de l'eau dans le ciment Portland et dans des ciments bas carbone*, (2021).
103 Chen, J. J., Thomas, J. J., Taylor, H. F. W. & Jennings, H. M. Solubility and structure of calcium silicate hydrate. *Cement and Concrete Research* **34**, 1499-1519, doi:https://doi.org/10.1016/j.cemconres.2004.04.034 (2004).
104 Grangeon, S. *et al.* Quantitative X-ray pair distribution function analysis of nanocrystalline calcium silicate hydrates: a contribution to the understanding of cement chemistry. *Journal of Applied Crystallography* **50**, 14-21 (2017).
105 Lothenbach, B. & Nonat, A. Calcium silicate hydrates: Solid and liquid phase composition. *Cement and Concrete Research* **78**, 57-70, doi:https://doi.org/10.1016/j.cemconres.2015.03.019 (2015).
106 Richardson, I. G. Model structures for c-(a)-sh (i). *Acta Crystallographica Section B: Structural Science, Crystal Engineering and Materials* **70**, 903-923 (2014).
107 Taylor, H. W. 726. Hydrated calcium silicates. Part I. Compound formation at ordinary temperatures. *Journal of the Chemical Society (Resumed)*, 3682-3690 (1950).
108 Pellenq, R. J. M. *et al.* A realistic molecular model of cement hydrates. *Proceedings of the National Academy of Sciences* **106**, 16102-16107, doi:10.1073/pnas.0902180106 (2009).
109 Kunhi Mohamed, A., Parker, S. C., Bowen, P. & Galmarini, S. An atomistic building block description of C-S-H - Towards a realistic C-S-H model. *Cement and Concrete Research* **107**, 221-235, doi:https://doi.org/10.1016/j.cemconres.2018.01.007 (2018).
110 Androniuk, I. *Effects of cement organic additives on the adsorption of uranyl ions on calcium silicate hydrate phases: experimental determination and computational molecular modelling*, Ecole nationale supérieure Mines-Télécom Atlantique Bretagne Pays de la Loire, (2017).

111 Androniuk, I. & Kalinichev, A. G. Molecular dynamics simulation of the interaction of uranium (VI) with the C–S–H phase of cement in the presence of gluconate. *Appl Geochem* **113**, 104496, doi:https://doi.org/10.1016/j.apgeochem.2019.104496 (2020).
112 Garbev, K. *et al.* Structural Features of C–S–H(I) and Its Carbonation in Air—A Raman Spectroscopic Study. Part I: Fresh Phases. *Journal of the American Ceramic Society* **90**, 900-907, doi:https://doi.org/10.1111/j.1551-2916.2006.01428.x (2007).
113 Gard, J. A. & Taylor, H. F. W. Calcium silicate hydrate (II) ("C-S-H(II)"). *Cement and Concrete Research* **6**, 667-677, doi:https://doi.org/10.1016/0008-8846(76)90031-4 (1976).
114 Bonaccorsi, E., Merlino, S. & Kampf, A. R. The crystal structure of tobermorite 14 A (Plombierite), a C-S-H phase. *Journal of the American Ceramic Society* **88**, 505-512 (2005).
115 Renaudin, G., Russias, J., Leroux, F., Frizon, F. & Cau-dit-Coumes, C. Structural characterization of C–S–H and C–A–S–H samples—Part I: Long-range order investigated by Rietveld analyses. *Journal of Solid State Chemistry* **182**, 3312-3319, doi:https://doi.org/10.1016/j.jssc.2009.09.026 (2009).
116 Renaudin, G., Russias, J., Leroux, F., Cau-dit-Coumes, C. & Frizon, F. Structural characterization of C–S–H and C–A–S–H samples—Part II: Local environment investigated by spectroscopic analyses. *Journal of Solid State Chemistry* **182**, 3320-3329, doi:https://doi.org/10.1016/j.jssc.2009.09.024 (2009).
117 Gmira, A. *Etude texturale et thermodynamique d'hydrates modèles du ciment*, Orléans, (2003).
118 Viallis-Terrisse, H. *Interaction des silicates de calcium hydratés (CSH), principaux constituants du ciment, avec les chlorures d'alcalins. Analogie avec les argiles*, Dijon, (2000).
119 Grutzeck, M., Benesi, A. & Fanning, B. Silicon-29 Magic Angle Spinning Nuclear Magnetic Resonance Study of Calcium Silicate Hydrates. *Journal of the American Ceramic Society* **72**, 665-668, doi:https://doi.org/10.1111/j.1151-2916.1989.tb06192.x (1989).
120 Brunet, F., Bertani, P., Charpentier, T., Nonat, A. & Virlet, J. Application of 29Si Homonuclear and 1H−29Si Heteronuclear NMR Correlation to Structural Studies of Calcium Silicate Hydrates. *The Journal of Physical Chemistry B* **108**, 15494-15502, doi:10.1021/jp031174g (2004).
121 Klur, I., Pollet, B., Virlet, J. & Nonat, A. in *Nuclear Magnetic Resonance Spectroscopy of Cement-Based Materials.* (eds Pierre Colombet, Hélène Zanni, Arnd-Rüdiger Grimmer, & Piero Sozzani) 119-141 (Springer Berlin Heidelberg).
122 Cong, X. & Kirkpatrick, R. J. 17O MAS NMR Investigation of the Structure of Calcium Silicate Hydrate Gel. *Journal of the American Ceramic Society* **79**, 1585-1592, doi:https://doi.org/10.1111/j.1151-2916.1996.tb08768.x (1996).
123 Cong, X. & Kirkpatrick, R. J. 29Si and 17O NMR investigation of the structure of some crystalline calcium silicate hydrates. *Advanced Cement Based Materials* **3**, 133-143, doi:https://doi.org/10.1016/S1065-7355(96)90045-0 (1996).
124 Lecoq, X. *Etude de l'hydratation à concentration contrôlée du silicate tricalcique ca# 3sio# 5 et des caractéristiques de ses produits de réaction*, Dijon, (1993).
125 Nonat, A. & Lecoq, X. in *Nuclear Magnetic Resonance Spectroscopy of Cement-Based Materials.* (eds Pierre Colombet, Hélène Zanni, Arnd-Rüdiger Grimmer, & Piero Sozzani) 197-207 (Springer Berlin Heidelberg).
126 Haas, J. & Nonat, A. From C–S–H to C–A–S–H: Experimental study and thermodynamic modelling. *Cement and Concrete Research* **68**, 124-138, doi:http://doi.org/10.1016/j.cemconres.2014.10.020 (2015).
127 Blanc, P., Bourbon, X., Lassin, A. & Gaucher, E. C. Chemical model for cement-based materials: Temperature dependence of thermodynamic functions for nanocrystalline and crystalline C–S–H phases. *Cement and Concrete Research* **40**, 851-866, doi:https://doi.org/10.1016/j.cemconres.2009.12.004 (2010).
128 Blanc, P., Bourbon, X., Lassin, A. & Gaucher, E. C. Chemical model for cement-based materials: Thermodynamic data assessment for phases other than C–S–H. *Cement and Concrete Research* **40**, 1360-1374, doi:https://doi.org/10.1016/j.cemconres.2010.04.003 (2010).
129 (!!! INVALID CITATION !!!).

130 Taylor, H. F. W. Proposed Structure for Calcium Silicate Hydrate Gel. *Journal of the American Ceramic Society* **69**, 464-467, doi:https://doi.org/10.1111/j.1151-2916.1986.tb07446.x (1986).
131 Jennings, H. M. A model for the microstructure of calcium silicate hydrate in cement paste. *Cement and Concrete Research* **30**, 101-116, doi:https://doi.org/10.1016/S0008-8846(99)00209-4 (2000).
132 Jennings, H. M. & Tennis, P. D. Model for the Developing Microstructure in Portland Cement Pastes. *Journal of the American Ceramic Society* **77**, 3161-3172, doi:https://doi.org/10.1111/j.1151-2916.1994.tb04565.x (1994).
133 Garrault-Gauffinet, S. & Nonat, A. Experimental investigation of calcium silicate hydrate (C-S-H) nucleation. *Journal of Crystal Growth* **200**, 565-574, doi:https://doi.org/10.1016/S0022-0248(99)00051-2 (1999).
134 Garrault-Gauffinet, S. *Etude expérimentale et par simulation numérique de la cinétique de croissance et de la structure des hydrosilicates de calcium, produits d'hydratation des silicates tricalcique et dicalcique*, Dijon, (1998).
135 Krautwurst, N. *et al.* Two-Step Nucleation Process of Calcium Silicate Hydrate, the Nanobrick of Cement. *Chem Mater* **30**, 2895-2904, doi:10.1021/acs.chemmater.7b04245 (2018).
136 Krautwurst, N. *Nucleation of calcium silicate hydrate in aqueous solution and the influence of biomolecules on cement hydration*, Dissertation, Mainz, Johannes Gutenberg-Universität, 2017, (2017).
137 Aretxabaleta, X. M., López-Zorrilla, J., Labbez, C., Etxebarria, I. & Manzano, H. A potential C-S-H nucleation mechanism: atomistic simulations of the portlandite to C-S-H transformation. *Cement and Concrete Research* **162**, 106965, doi:https://doi.org/10.1016/j.cemconres.2022.106965 (2022).
138 Schönlein, M. & Plank, J. A TEM study on the very early crystallization of C-S-H in the presence of polycarboxylate superplasticizers: Transformation from initial C-S-H globules to nanofoils. *Cement and Concrete Research* **106**, 33-39, doi:https://doi.org/10.1016/j.cemconres.2018.01.017 (2018).
139 Aretxabaleta, X., López-Zorrilla, J., Etxebarria, I. & Manzano, H. CSH nucleation pathway from atomistic simulations. (2023).
140 Young, J. F., Berger, R. L. & Breese, J. Accelerated Curing of Compacted Calcium Silicate Mortars on Exposure to CO2. *Journal of the American Ceramic Society* **57**, 394-397, doi:https://doi.org/10.1111/j.1151-2916.1974.tb11420.x (1974).
141 Fernández Bertos, M., Simons, S. J. R., Hills, C. D. & Carey, P. J. A review of accelerated carbonation technology in the treatment of cement-based materials and sequestration of CO2. *Journal of Hazardous Materials* **112**, 193-205, doi:https://doi.org/10.1016/j.jhazmat.2004.04.019 (2004).
142 Liu, X. *et al.* Carbonation behavior of calcium silicate hydrate (C-S-H): Its potential for CO2 capture. *Chemical Engineering Journal* **431**, 134243, doi:https://doi.org/10.1016/j.cej.2021.134243 (2022).
143 Wu, B. & Ye, G. Study of carbonation rate of synthetic CSH by XRD, NMR and FTIR. *Heron* **64**, 21-38 (2019).
144 Morandeau, A. E. & White, C. E. In situ X-ray pair distribution function analysis of accelerated carbonation of a synthetic calcium–silicate–hydrate gel. *Journal of Materials Chemistry A* **3**, 8597-8605, doi:10.1039/c5ta00348b (2015).
145 Chang, J. & Fang, Y. Quantitative analysis of accelerated carbonation products of the synthetic calcium silicate hydrate(C–S–H) by QXRD and TG/MS. *J Therm Anal Calorim* **119**, 57-62, doi:10.1007/s10973-014-4093-8 (2015).
146 Bonen, D. & Diamond, S. Occurrence of large silica fume-derived paticles in hydrated cement paste. *Cement and Concrete Research* **22**, 1059-1066, doi:https://doi.org/10.1016/0008-8846(92)90036-U (1992).
147 Lachowski, E. E. & Diamond, S. Investigation of the composition and morphology of individual particles of portland cement paste: 1. C・S・H gel and calcium hydroxide particles. *Cement*

and Concrete Research **13**, 177-185, doi:https://doi.org/10.1016/0008-8846(83)90100-X (1983).
148 Li, J., Yu, Q., Huang, H. & Yin, S. Effects of Ca/Si Ratio, Aluminum and Magnesium on the Carbonation Behavior of Calcium Silicate Hydrate. *Materials* **12** (2019).
149 Sevelsted, T. F. & Skibsted, J. Carbonation of C–S–H and C–A–S–H samples studied by 13C, 27Al and 29Si MAS NMR spectroscopy. *Cement and Concrete Research* **71**, 56-65, doi:https://doi.org/10.1016/j.cemconres.2015.01.019 (2015).
150 Black, L., Garbev, K. & Gee, I. Surface carbonation of synthetic C-S-H samples: A comparison between fresh and aged C-S-H using X-ray photoelectron spectroscopy. *Cement and Concrete Research* **38**, 745-750, doi:https://doi.org/10.1016/j.cemconres.2008.02.003 (2008).
151 Dunster, A. M. An investigation of the carbonation of cement paste using trimethylsilylation. *Advances in Cement Research* **2**, 99-106, doi:10.1680/adcr.1989.2.7.99 (1989).
152 Kobayashi, K., Suzuki, K. & Uno, Y. Carbonation of concrete structures and decomposition of C-S-H. *Cement and Concrete Research* **24**, 55-61 (1994).
153 Suzuki, K., Nishikawa, T. & Ito, S. Formation and carbonation of C-S-H in water. *Cement and Concrete Research* **15**, 213-224, doi:https://doi.org/10.1016/0008-8846(85)90032-8 (1985).
154 Saillio, M. *Interactions physico-chimiques ions-matrice dans les bétons sains ou carbonatés: influence sur le transport ionique*, Université Paris-Est, (2012).
155 Goto, S., Suenaga, K., Kado, T. & Fukuhara, M. Calcium Silicate Carbonation Products. *Journal of the American Ceramic Society* **78**, 2867-2872, doi:https://doi.org/10.1111/j.1151-2916.1995.tb09057.x (1995).

Chapitre III. ETUDE COMPARATIVE DES MECANISMES DE DISSOLUTION D'UN FELDSPATH AMORPHE ET CRISTALLIN EN CONDITION DE pH ACIDE

La dissolution d'un oligoclase amorphe et cristallin, un feldspath sodique avec des traces de Ca et K, a été étudiée à 90 °C, pH 1,5 et 3, afin d'étudier l'impact du désordre structural à long et courte distance sur les mécanismes de dissolution des silicates. Les solutions d'altération ont été enrichies en $^{29}SiO_2$(aq) et saturées vis-à-vis de SiO_2(am). À travers des caractérisations morphologiques, structurales et chimiques, nous avons montré que sur les échantillons de verre, la couche altérée était principalement formée par lessivage préférentiel (mécanisme d'hydrolyse – recondensation), tandis qu'une combinaison de précipitation interfaciale et de lessivage préférentiel explique les couches formées sur l'échantillon cristallin. L'épaisseur du gel était moins importante dans des conditions moins acides (pH 3) jusqu'à devenir passivante sur l'échantillon cristallin. L'altération était plus rapide sur l'oligoclase amorphe que sur son équivalent cristallin en raison de la structure plus ouverte du verre. La libération préférentielle d'aluminium semble jouer un rôle clé en affaiblissant le réseau silicaté des deux substrats. Enfin, dans cette étude, une importante surestimation de l'altération globale des matériaux a été constatée sur la base des analyses de la solution : les divergences avec les analyses solides ont été attribuées à une sous-estimation (facteur ≥ 2) de la surface réactive totale.

Le chapitre III fait l'objet d'une publication dans la revue npj Materials Degradation :
"Cagnon, B., Daval, D., Cabié, M., Lemarchand, D., & Gin, S. (2022). A comparative study of the dissolution mechanisms of amorphous and crystalline feldspars at acidic pH conditions. npj Materials Degradation, 6(1), 34."

A comparative study of the dissolution mechanisms of amorphous and crystalline feldspars at acidic pH conditions

Benjamin Cagnon[1,2], Damien Daval[1,2], Martiane Cabié[3], Damien Lemarchand[1], Stéphane Gin[4]

[1] Université de Strasbourg / CNRS / ENGEES, ITES, Strasbourg, France

[2] Univ. Grenoble Alpes, Univ. Savoie Mont Blanc, CNRS, IRD, IFSTTAR, ISTerre, Grenoble, France

[3] Aix Marseille Univ, CNRS, Centrale Marseille, FSCM, CP2M, Marseille, France

[4] CEA, DEN, DE2D, University of Montpellier, Marcoule, France

Correspondence: B. Cagnon (benjamin.cagnon@univ-grenoble-alpes.fr)

ABSTRACT

The dissolution of amorphous and crystalline oligoclase, a Na-feldspar with traces of Ca and K, was investigated at 90 °C and acidic pH of 1.5 and 3 to unravel the impact of long- and short-range orders on silicate dissolution mechanisms. Experiments were conducted in solutions spiked with $^{29}SiO_2$(aq) and saturated with respect to SiO_2(am). Through morphology, structural and composition characterizations, we showed that on the amorphous samples (glass samples), the altered layer was mostly formed by leaching, while a combination of both interfacial precipitation and leaching explains the layers formed on the crystalline sample. As expected, the altered layer was thicker at the most acidic pH and it became passivating on crystalline sample at pH 3. The alteration was faster on amorphous oligoclase than on its crystalline equivalent due to the more open structure of the glass. The preferential release of Al was suggested to play a key role, by weakening the silicate network of both substrates. Finally, in this study, a large overestimation of the global alteration of the materials was noticed based on the solution analyses. Discrepancies with solid analyses were attributed to an underestimation (≥ 2 fold factor) of the total reactive surface area.

III.1. INTRODUCTION

Silicates represent the most abundant group of minerals on Earth. They can also be amorphous, such as those found on the seafloor, under the form of silicate glass. Silicate minerals and glasses are structurally different, leading to a different reactivity with water. Both are made of the same structural units (for instance SiO_4^{4-} or AlO_2^- tetrahedrons) but with varying bond lengths and angles between them, yielding some disorder at short range. At longer distance (> 1-5 nm), silicate glasses are generally homogeneous. The structural disorder in glass results in a broad distribution of the dissolution rate parameters and associated bond dissociation activation energies. Conversely, minerals are ordered at both short and long distances, meaning that a limited number of atomic bond lengths and angles is found periodically in the structure. In turn, the long-range order shapes crystal habit and the reactivity of individual crystal faces[1].

Understanding the aqueous reactivity of silicates is important as they are involved in fundamental processes such as the biogeochemical cycle of elements [2], as well as industrial processes such as carbon dioxide (CO_2) sequestration [3] and vitrified nuclear waste disposal [4-6] among others.

Historically, several mechanisms have been suggested to take place in parallel and control aluminosilicate glass dissolution:

1) Diffusion of water into the glass through the largest silicate rings[7], resulting in an exchange between dissociated water and alkali atoms near non bridging oxygen (NBO) atoms, and the formation of silanol groups[8]. These simultaneous processes, also called interdiffusion, result in the formation of a distinct layer from the parent glass. This layer can be revealed from its porous texture, amorphous structure (compared to the pristine crystal material) [9,10] and its chemical composition depleted in glass modifiers (such as Na) and potentially enriched in exogenous elements (H^+, Li^+ or other elements from the solution)[11]. Such reactions are favored at acid pH.

2) Matrix dissolution, leading to a progressive depolymerization of the structure through hydrolysis of Si–O–M (M = Si, Al or other glass formers) linkages [12]:

$$\equiv Si - O - Si \equiv \ + H_2O \ \rightarrow 2 \equiv Si - OH \qquad \text{(Eq. III-1)}$$

As long as the solution remains far from the equilibrium, Si is released into the solution at a constant rate called initial or forward rate. This rate is pH- and temperature-dependent [13]. When the concentration of H_4SiO_4(aq) increases, backward reactions of condensation of silanol groups take place at the glass surface, leading to the formation of a porous and hydrated material, called gel layer [14,15].

In this regime, the glass dissolution rate can drop by several orders of magnitude as compared to the initial dissolution rate [16]. This decrease in glass reactivity results both from the reduced affinity of the dissolution reaction of silicate network[17], and the transport-limiting properties of the growing gel layer [18-21]. In the first case, the concentration of glass elements increases in the solution and when

it reaches a steady state with the material, the thickness of the gel layer would remain constant. However, the gel layer is not in equilibrium with the solution and evolves over time[21,22]: reorganization and densification of the gel occur gradually, resulting from the condensation of silanol groups into siloxane bonds [23,24]. With the second process, because of the closure of the pores, the transport properties of the surface layer between the glass and the bulk solution are hindered, explaining the observed drop in the dissolution rate [25]. The resulting dissolution is then controlled by the concentration of H_4SiO_4(aq) in the solution, which affects the distance from equilibrium at the interface between the gel layer and the solution [26].

3) Once steady-state is achieved, glass dissolution continues at a slow and near-constant rate called “residual rate” or “final rate”. The origin of this residual rate has been discussed in a recent article [27,28]. Globally, it is to be attributed to the absence of thermodynamic equilibrium between the glass, the gel and the solution, although the latter can be highly concentrated in glass constituents. These conditions favor the precipitation of secondary phases, which, in turn, can impact the solution chemistry. The secondary phases first precipitate following heterogeneous nucleation at the interface between the solution and the gel layer. In circum-neutral to mildly basic conditions (pH 6 – 9), mainly phyllosilicates precipitate while in basic condition (pH > 10), zeolite (among others silicate minerals) may form. The precipitation of secondary phases can trigger the resumption of glass alteration [29-33].

Historically, the leaching process described in 1) was supposed to apply to silicate minerals as well [34,35]. Using spectroscopic techniques, Hellmann et al. [36] demonstrated the formation of layers enriched in H and depleted in Na at the surface of dissolved albite ($NaAlSi_3O_8$). The depth profiles of these elements were found to be sigmoidal and anti-correlated, leading the authors to suggest that the layers form through an interdiffusion mechanism, similarly to glass alteration. However, these diffusion profiles have been challenged in subsequent studies, which suggested that they represent an analytical artefact resulting from the poor lateral resolution of the ion or X-ray beam measurements. Instead, more recent results concluded to profiles with step-like functions [37]. Diffusion models fail to predict such observations [37-39], pointing out that the reaction is not diffusion-controlled. In addition, the sharp structural transition between the crystalline (mineral) and the amorphous (altered layer) zones is at odds with a diffusion-controlled leaching process.

Following the early conclusion of Hellmann et al. [37], a growing number of studies [40-44] has subsequently supported another mechanism. Whereas the leached layer mechanism suggests that the altered layer represents a relict structure of the primary silicate (formed via hydrolysis – condensation reactions with no detachment of Si from the glass network), this alternative mechanism, called coupled interfacial dissolution – reprecipitation (CIDR), suggests that all Si–O bonds are broken simultaneously to release Si atoms to the interfacial solution. Hellmann et al. [39] suggested that the mineral dissolves congruently in a thin water film in contact with its surface. In this thin water film, the concentration of

H_4SiO_4(aq) becomes supersaturated with respect to amorphous silica, leading to the precipitation of porous amorphous silica – the so-called altered layer, distinct from the mineral. The remaining elements then diffuse through the nanoporosity of the reprecipitated layer [42]. The formation and densification (due to local chemical composition, local concentration gradient and local diffusivity and porosity) of the altered layer may control the temporal decrease of silicate dissolution rate, as suggested by Daval et al. [45] for wollastonite.

Recently, a study conducted by Hellmann et al. [46] suggested that the CIDR mechanism could also apply to glass alteration. Confirming the results of Geisler et al. [40], Hellmann et al. [46] evidenced (i) a sharp interface between the pristine glass and the altered layer, (ii) nm-wide concentration gradient in the solid materials and (iii) a thickness of altered layer which is, as diffusion profiles, independent of the charge of cation (usually, the cationic charge is negatively correlated with the diffusion length). Conversely, Gin et al. [47] used atom probe tomography to prove the existence of such gradients and demonstrated that depending on the presence of Al in the glass, alteration can proceed following the leaching mechanism or the CIDR mechanism [48].

In order to predict and model the behavior of glass and mineral dissolution, it is therefore important to develop a unified approach that overcomes the opposition between the two mechanisms. In a recent study, Pérez et al. [1] investigated the dissolution mechanisms of oligoclase glass and its crystalline equivalent over a wide range of pH. Whereas for the crystalline materials, altered layers likely formed following the CIDR mechanism, conversely, the altered layer developed on oligoclase glass was suggested to form –at least partly– by leaching. The dissolution mechanisms may therefore depend on the long-range order of the materials, leading to an absence of mechanistic continuum between minerals and glasses. Moreover, the mechanism may change according to the pH domain.

Building upon the work of Pérez et al. [1], the alteration mechanisms of amorphous and crystalline oligoclase with composition close to the albite end-member were here investigated at 90°C in acidic solutions (pH 1.5 and 3) saturated with respect to amorphous silica enriched in $H_4{}^{29}SiO_4$(aq) (see section III.4. Material and Methods). The main difference with previous work[1] is that the present study does not focus on the measurement of dissolution rates through ICP-AES analyses and surface topography measurements, but rather on the dissolution mechanisms occurring at the molecular scale, unraveled using isotopic analyses and nm-scale analyses of the reacted solids (ToF-SIMS and FIB TEM). Furthermore, additional specific experiments were conducted to compare the reactivity of amorphous and crystalline oligoclase at pH 3, which is close to the supposed threshold for the passivation of crystalline feldspars (around pH 2.5 [49]). As Gin et al. [50] confirmed the passivating role of the altered layer using ^{18}O labelled water and rejected the CIDR mechanism for a reference 6 oxide borosilicate glass called ISG [51] by showing that ^{29}Si is not incorporated in passivating gels formed under silica

saturated conditions, the diffusivity and the exchange rate of Si with the growing altered layer were investigated through ^{29}Si labelling, providing direct information on the corrosion mechanism at acidic conditions. In addition, Valle et al.[21] and Bouakkaz et al.[52] demonstrated that secondary phases such as phyllosilicates formed at equilibrium with the bulk solution and that ^{29}Si from solution could also incorporate in porous and low passivating gel layer formed far from silica saturation. In those cases, the isotopic signature of the gel layer was intermediate between the glass and the solution, leading Gin et al. to conclude that a hydrolysis – condensation reaction mechanism controls the formation of passivating gel layers on silicate glass[48]

In the following, we test the hypothesis of the mechanistic continuum proposed in the conclusion of Pérez et al. between the reactivity of amorphous and crystalline glasses and the effect of long-range atomic order on the dissolution mechanisms of silicates. We show below that our results are compatible with the existence of a mechanistic continuum between glass and mineral dissolution, i.e., depending on the reaction conditions, both the CIDR and the leaching mechanisms may (sequentially) apply.

III.2. RESULTS

III.2.1. Initial parameters

Tableau III-1: Experimental parameters used for oligoclase dissolution. The first column refers to the sample. The surface area exposed to the solution is then reported, with the Top Surface area corresponding to the upper surface, the Total Surface area corresponding to the surface area of the Top Surface plus the lateral surfaces and last, the uncertainty of the surface area measurement. The initial pH measured at 25°C and the total duration of the experiment are listed in the subsequent columns.

Sample	Surface (mm^2)			pH initial	Exp. time (d)
	Top Surface Area	Total Surface Area	Uncertainty		
pH 1.5					
C1-1	16.8	33	± 36%	1.4	12
C1-2	14.1	33	± 21%	1.5	33
G1-1	9.0	54	± 24%	1.4	12
G1-2	13.7	54	± 20%	1.5	33
pH 3					
C3-1	19.1	34	± 24%	2.9	12
C3-2	22.4	33	± 18%	2.9	33
G3-1*	8.6	30	± 33%	2.9	12
G3-2	5.4	38	± 26%	2.9	33

**Note that the experiment conducted with the glass sample at pH 3, which lasted around 12 days, was found to be contaminated with trace concentrations of Mg and Fe resulting from imperfect cleaning of the reactor (0.62 ppm of Mg and*

0.082 ppm of Fe). Thermodynamic calculations demonstrated that this contamination did not affect the dissolution of oligoclase sample.

Two sets of experiments were conducted in order to study the dissolution of oligoclase samples, one amorphous, one crystalline, for two different durations (12 and 33 days) at two different pH (1.5 and 3; see Methods). For a better understanding, the glass sample is labelled with a capital 'G' and the crystalline sample with a capital 'C'. The number that follows the letters refers to the pH of the solution at which the experiment was conducted. So G1 refers to the glass sample dissolved at pH 1.5 and G3 at pH 3. The same holds for crystalline samples C1 and C3. The last number refers to the series (e.g., C1-1 refers to the C1 sample altered 12 days and C1-2, the C1 sample altered 33 days). The starting parameters are listed in Table III-1. All experiments conducted with crystalline samples were performed at far-from-equilibrium conditions with respect to albite (ΔG < -70 and -35 $kJ.mol^{-1}$ for experiments conducted at pH 1.5 and 3, respectively, see Supplementary Tables III-1 and III-2).

III.2.2. Characterization of altered sample surfaces

A common trait of all characterized samples consists in (i) the lack of surface retreat that could have resulted from dissolution, as evidenced by vertical scanning interferometry (VSI) measurements and (ii) the formation of amorphous silica-rich surface layers (ASSLs). However, their morphology, thickness, texture, and chemical composition revealed by transmission electron microscopy (TEM) analyses realized on cross-sections prepared by focused ion beam (FIB) milling significantly differ from one sample to another (Fig. III-1 and Fig. III-2).

III.2.2.1. Crystalline oligoclase samples reacted at pH 1.5 and pH 3

The dissolution of crystalline samples is characterized by the formation of striations in the plane of the surface exposed to the solution (Fig. III-1a and Supplementary Fig. 2). As can be seen in Fig. III-1a and Fig. III-1b, such striations result from the alternation of 30 to 44 nm-wide lamellae either enriched (Ca/Si =0.024) or depleted (Ca/Si=0.013) in Ca, which dissolved at specific rates, revealing a preferential alteration of the Ca-rich lamellae (this observation is consistent with the greater reactivity of Ca-rich vs. Na-rich feldspars, see e.g. [53]). This heterogeneous dissolution is more pronounced at pH 1.5 (depth of one groove after 33 days ranging between 98 nm and 137 nm) than at pH 3 (depth < 4 nm), so that the striations of the surface of C3-2 is hardly visible on scanning electron microscopy (SEM) images of the surface (Fig. III-1b). Interestingly, most of the ASSL is located in-between the Na-rich lamellae revealed by dissolution at pH 1.5, ranging between 43 nm and 128 nm in thickness after 33 days (Fig. III-1a). Conversely, the ASSL is much thinner (7 nm) and more homogenously distributed at the surface of the sample reacted at pH 3 (Fig. III-1b).

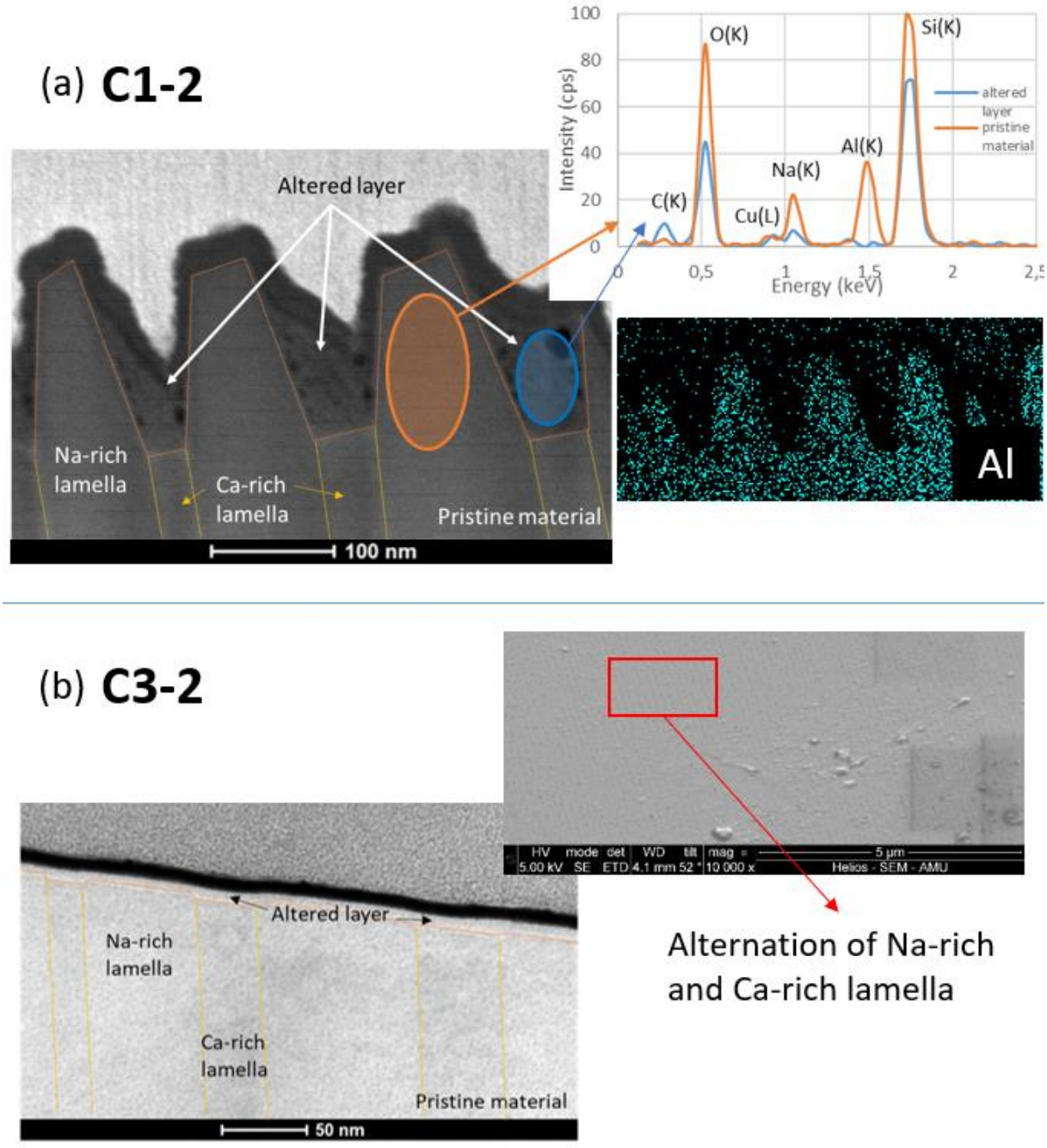

Figure III-1 : Characterization by FIB-TEM of the surface of the crystal samples after 33 days of alteration. The composition of the altered layer and the pristine material was obtained by STEM-EDX. a) TEM dark field image of the interface between the crystalline oligoclase and the altered layer at pH 1.5 after 33 days of alteration (sample C1-2). A STEM-EDX map at the Al K edge is also shown, as well as EDX spectra collected on the crystalline sample and the altered layer. b) TEM image of the crystalline sample altered at pH 3 after 33 of alteration (sample C3-2) shown in cross section. The striation of the surface resulting from the difference of reactivity between Ca-rich and Na-rich lamellae can be seen on the top view of the sample imaged by SEM (sample tilted at 52°).

Nanometer-sized pores are observed in the ASSL developed on the surface of C1-2 sample, appearing as dark spots in dark field STEM images (Fig. III-1a). The porosity is estimated to be ~ 12% by thresholding of dark field STEM images [54]. In addition, high resolution TEM images show that the interface between the altered layer and the pristine material is well delimited, with a sharp boundary

between the crystalline and amorphous regions (Supplementary Fig. 3). The ASSL developed on C1-2 sample is depleted in Al and Na (Fig. III-1a), as revealed by energy dispersive X-ray (EDX) analyses – note however that the results of Na concentrations are poorly reliable due to the typical migration of alkali ions under the electron beam. The Al profile at the interface between the ASSL and oligoclase is quite sharp (Fig. III-1a and Supplementary Fig. 4). Of note, ASSLs developed on samples reacted at pH 3 are too thin to be analyzed by EDX.

III.2.2.2. Oligoclase glass samples reacted at pH 1.5 and pH 3

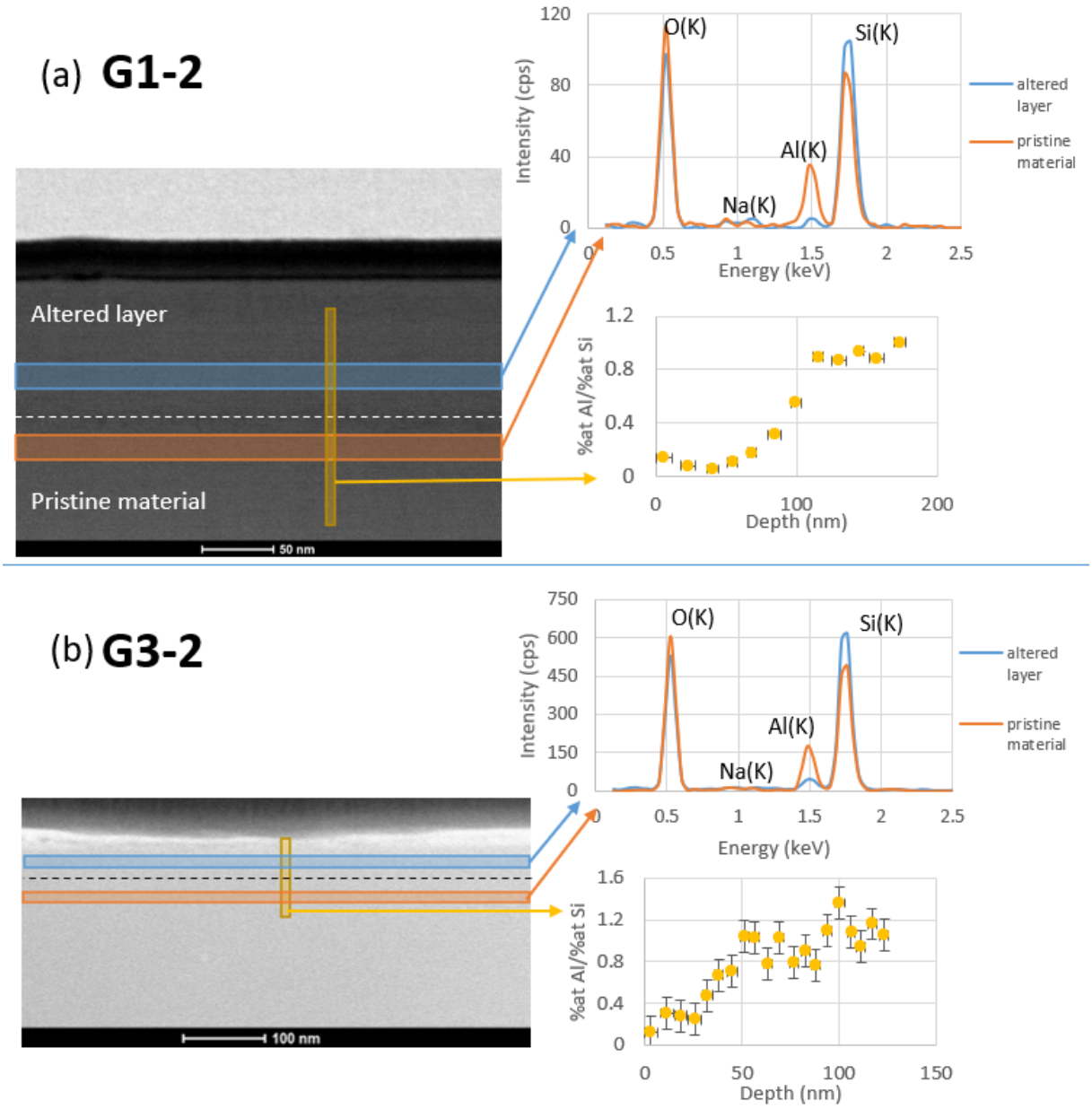

Figure III-2: Characterization by FIB-TEM of the surface of the glass samples after 33 days of alteration. The composition of the altered layer and the pristine material was obtained by STEM-EDX. a) TEM dark field image of the interface between the amorphous oligoclase and the altered layer at pH 1.5 after 33 days of alteration (sample G1-2). EDX spectra collected on the glass sample and on the altered layer are shown. The dashed line corresponds to the interface between altered layer and pristine material. b) TEM image of the amorphous sample altered at pH 3 after 33 days of alteration (sample G3-2) shown in

cross section. The interface between altered layer and pristine material represented by the dashed line was revealed using EDX analyses.

As opposed to the ASSLs developed on the crystalline samples, the altered layers developed on the glass samples are continuous and cover the uncorroded glass homogenously (Fig. III-2a). The ASSLs are thicker on G1-2 (~ 120 nm) than on G3-2 (30-50 nm). In addition, altered layers are systematically thicker for glass samples compared to their crystalline equivalent at similar pH. Finally, EDX analyses performed on G1-2 (respectively G3-2) reveal that the depletion of Al is more gradual than for C1-2 (respectively C3-2), extending from a depth located between 50 nm to 110 nm from the sample surface (respectively between 25 nm and 50 nm).

III.2.3. ToF-SIMS analyses

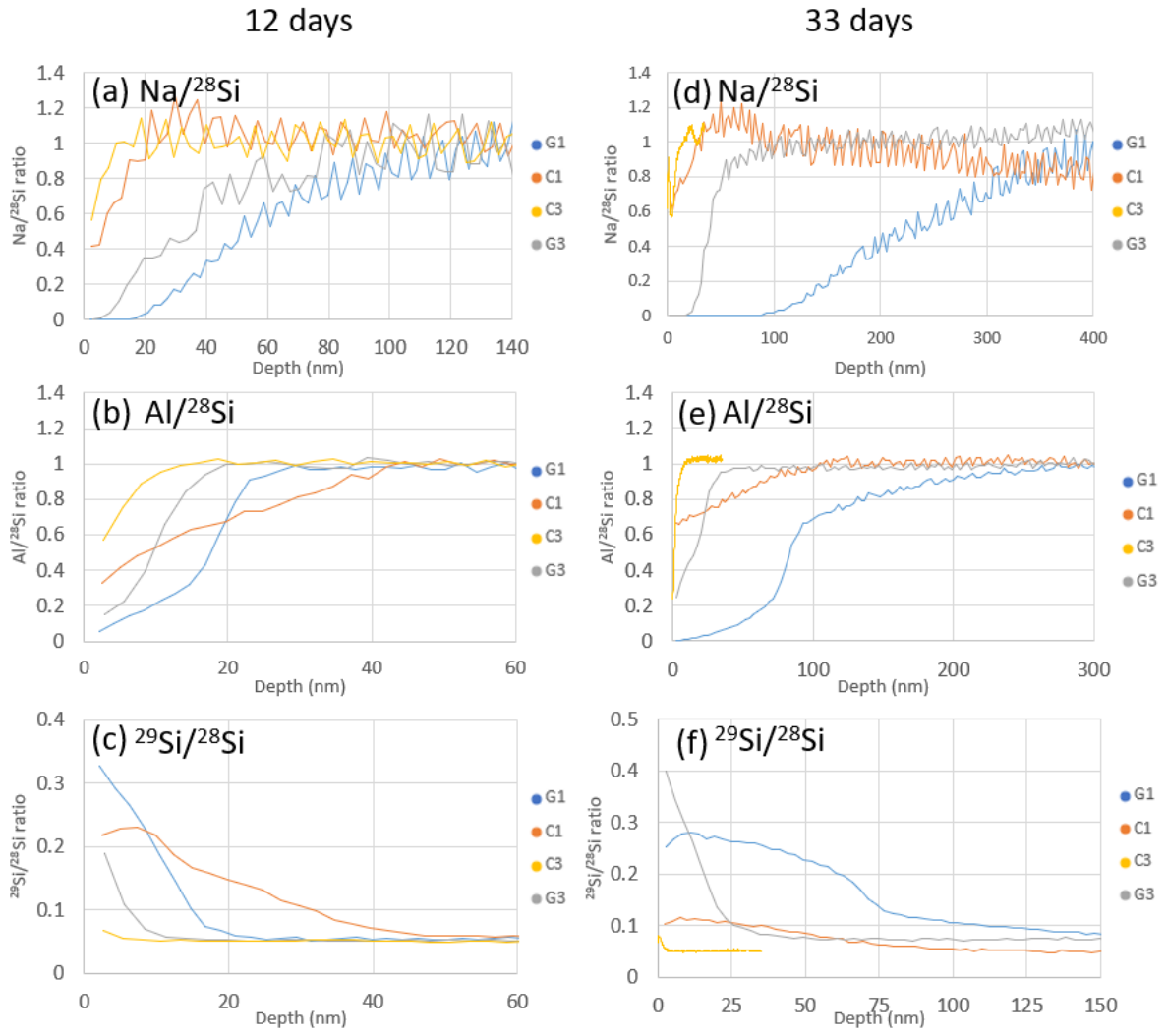

Figure III-3: Depth profiles of Al, Na and 29Si collected with ToF-SIMS after 12 days and 33 days of alteration. Curves were normalized to the amount of 28Si. The blue curves, G1, refer to the profiles collected on the glass samples altered at pH 1.5. The orange curves, C1, refer to the mineral samples altered at pH 1.5. The grey curves, G3, refer to the glass samples altered at pH 3. The yellow curves, C3, refer to the mineral samples altered at pH 3.

ToF-SIMS analyses provide information regarding the alteration of the core material using the depth profiles of Na, Al, ^{28}Si and ^{29}Si. Such profiles are shown under the form of $(X/^{28}Si)/(X/^{28}Si)_{substrate}$ ratios (hereafter referred to as X/Si ratios) in Fig. III-3, where X=Na, Al. Because the $^{29}Si/^{28}Si$ ratio is quantitative (the ionization efficiency being the same for both isotopes), the corresponding ratio is not re-normalized to its value in the parent materials. As emphasized in the previous section, the ASSLs are depleted in Na and Al, so that the Na/Si and Al/Si ratios are usually used as a proxy for the thickness of the altered layer.

A common feature of all profiles, regardless of the considered element, is that no sharp transition between the ASSL and the pristine sample is observed. In addition, the Al/Si profiles at the very surface (depth = 0 nm) never reach 0 for the crystalline samples, which is at odds with the TEM results, at least for those reacted at pH 1.5 (Fig. III-1a). Those results stem from the fact that the profiles are artificially broadened due to the poor lateral resolution of the ion beam imprint and the roughness of the altered surface, so that part of the parent substrate is analyzed right from the first cycles of Tof-SIMS measurements, together with the ASSL. To carefully address this problem, below we first describe the raw depth profiles, prior to reporting the results of the profile deconvolution. Overall, the depth profiles vary as a function of the pH conditions, the long-range order of the samples, and the nature of the considered element.

III.2.3.1. Crystalline oligoclase samples reacted at pH 1.5 and pH 3

Consistent with the TEM results, the ASSLs developed on C1 samples are thicker than those developed on C3 samples, regardless of the element considered to estimate their thickness. In addition, the profiles extend over larger distances for samples reacted over longer durations (quantitative estimates based on the deconvolution of the profiles are discussed in section III.2.3.3).

Regarding samples reacted at pH 1.5, the depth over which the $X/^{28}Si$ ratios ($d_{X/28Si}$) vary until reaching a plateau observes the following trend, regardless of the duration of the experiment: $d_{29Si/28Si} \sim d_{Al/28Si} > d_{Na/28Si}$. Conversely, the samples reacted at pH 3 exhibit the following trend: $d_{29Si/28Si} \sim d_{Al/28Si} \sim d_{Na/28Si}$, for both durations (Fig. III-3). The $^{29}Si/^{28}Si$ ratio is higher in the altered layer than in the pristine material and decreases until reaching the natural abundance around 0.05 (Fig. III-3c and III-3f). Similarly to the other ratios, the $^{29}Si/^{28}Si$ ratio decreases over shorter distances at pH 3.

III.2.3.2. Oligoclase glass samples reacted at pH 1.5 and pH 3

Similarly to the crystalline samples, the ASSLs developed on G1 samples are thicker than those developed on G3 samples, regardless of the element considered to estimate their thickness. For a same pH, the ASSLs developed on glass samples are also thicker than those developed on crystalline samples.

The depth over which the X/^{28}Si ratios vary until reaching a plateau displays the following trend, regardless of the duration of the experiment or pH: $d_{29Si/28Si}$ ~ $d_{Al/28Si}$ < $d_{Na/28Si}$. Conversely, the samples reacted at pH 3 exhibit the following trend: $d_{29Si/28Si}$ ~ $d_{Al/28Si}$ ~ $d_{Na/28Si}$, for both durations (Fig. III-3).

III.2.3.3. Deconvolution of the Tof-SIMS depth profiles

As mentioned above, the X/^{28}Si profiles appear to be broadened due to the lateral ion beam imprint (and the patterning of the surface for altered crystalline samples). For each sample, the artificial broadening of the signal measured by ToF-SIMS is corrected by using a convolution function which is supposed to reflect the combined effects of the instrument resolution and surface roughness (see Supplementary Note 3). The outputs of the procedures are referred to as the "numerical profiles" and are supposed to be close to the actual depth profile of ^{29}Si/^{28}Si. The fitting procedure consists in optimizing the parameters of the Gaussian function accounting for the broadening of the profiles, so that the difference between the measured profiles provided by ToF-SIMS and the convolution of the known actual Al/Si profiles (obtained from FIB-TEM measurements) with the Gaussian function (i.e. the "convoluted" profiles), is minimized (see Supplementary Note 3). The same Gaussian function is then applied to the ^{29}Si/^{28}Si profile measured by ToF-SIMS to estimate the corresponding ^{29}Si/^{28}Si "numerical profiles".

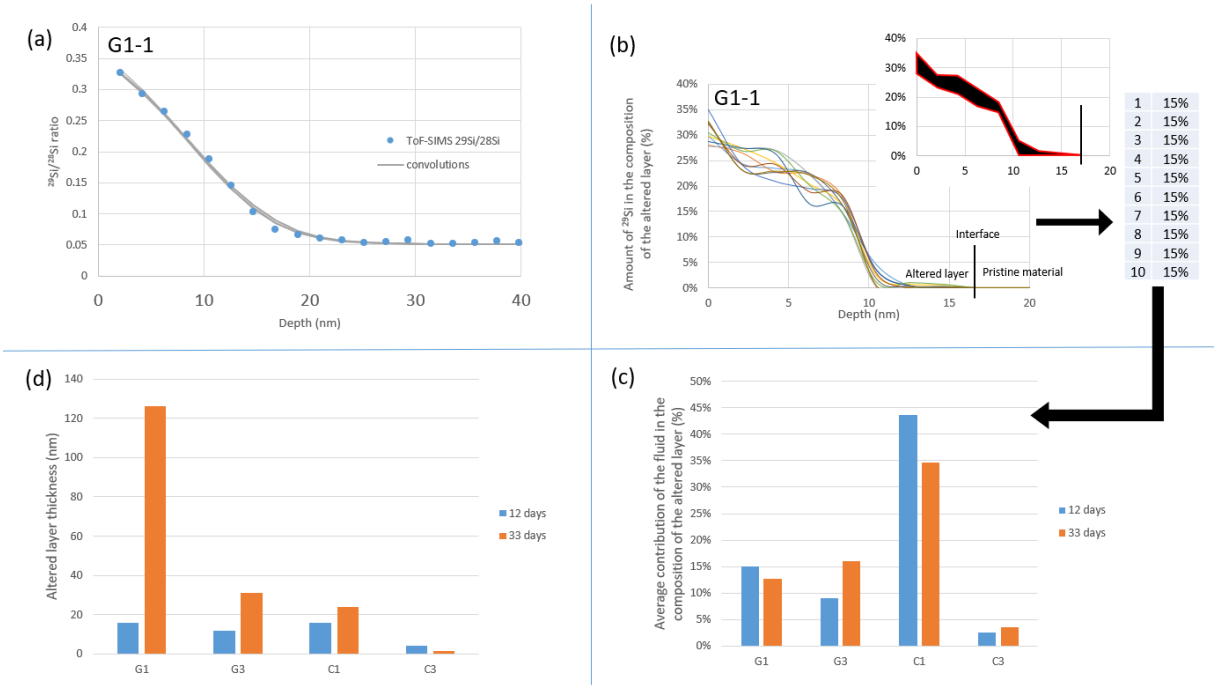

Figure III-4: Results from the deconvolution of the ToF-SIMS depth profiles. a) Comparison between the ToF-SIMS depth profile and the numerical profiles of the amorphous oligoclase altered at pH 1.5 after 12 days (sample G1-1) b) Plots depicting the best 10 numerical profiles of G1-1, the envelop created by those profiles and the average contribution of the solution to the composition of the altered layer for each profile c) Representation of the average contribution of the fluid in the composition of the altered layer for each sample. d) Representation of the altered layer thickness for each sample based on Al/28Si ToF-SIMS profiles.

The sample G1-1 is chosen below as an example for the whole process. As can be seen in Fig. III-4a, the fit between the $^{29}Si/^{28}Si$ convoluted profiles and the measured ToF-SIMS profile is satisfactory. The difference between each convolution and the measured profile is calculated using the root mean square (RMS) over a depth twice the size of the altered layer. The highest relative RMS is 11% for G3-1 while the lowest is 4% for G3-2. An average relative RMS, representative of the experiment, is around 5% to 7% for C1-1, C1-2, C3-1, C3-2, and G1-1. An exception is observed for G1-2, which has a relative RMS between 19% and 41%.

The best 10 numerical profiles corresponding to those with the lowest RMS are illustrated in Fig. III-4b for G1-1. All profiles are located inside a narrow envelop that is suggested to reflect the actual $^{29}Si/^{28}Si$ profile. Knowing the $^{29}Si/^{28}Si$ ratio in the solution and in the pristine glass (which is the natural abundance), the contribution of the solution to the ASSL can be retrieved all along the depth profile.

Furthermore, we note that the average contribution of those profiles to the composition of the altered layer is almost identical for all profiles (15% ±1%). In other words, the solution contributed to 15% of the Si content of the altered layer.

The average contribution for all samples is shown in Fig. III-4c. Except for sample G3-2, the contribution of the fluid is systematically greater in strongly acidic condition, which is consistent with the observation of the raw $^{29}Si/^{28}Si$ profiles depicted in Fig. III-3. The contribution of the fluid is larger for the crystal at pH 1.5 than for the glass at a similar pH and vice versa at pH 3. No systematic temporal trend is observed.

Regarding the thickness of the ASSL estimated from $Al/^{28}Si$ profiles, the following observations can be drawn (Fig. III-4d): (i) the layers grow with time, except for C3, where the layer seems to have a steady-state thickness, (ii) as suggested by the raw Tof-SIMS profiles, for a given pH, the layers are thicker on glass than on crystalline oligoclase and (iii) the layers are thicker at pH 1.5 than at pH 3.

III.2.4. ASSL thickness estimated from solution analyses

In addition to the characterization of the reacted solids, the solutions were analyzed regularly by inductively coupled plasma - atomic emission spectroscopy (ICP-AES) in order to monitor the oligoclase dissolution. As expected, the Si and Na concentrations remain constant, within uncertainties (± 3%), because of the elevated background level of those elements (see Methods). Based on the release of Al in solution, the thickness of the altered layer is calculated (see Methods) and compared with the thickness provided by ToF-SIMS / FIB-TEM characterizations. The thickness calculated using ICP-AES is 10 times greater than that estimated using ToF-SIMS measurements for oligoclase glass, and

30 to 70 times greater for the crystalline oligoclase (see Supplementary Table III-1 and III-2 for ICP-AES data and Supplementary Table III-4 and III-5 for ICP-MS data). A careful investigation of the reacted samples reveals several features that might contribute to such discrepancies (see Fig. III-5 and section III.3.1):

(i) First, a ~40 to 100 µm-wide gap is observed between the epoxy resin and the oligoclase samples for all experiments (Fig. III-5a-c). Observations performed on unreacted spare samples show that this detachment is present for all samples prepared on the same day. It can therefore be reasonably assumed that the lateral faces of each sample, which were not polished before the reaction, contributed to the flux of Al released to the solution.

(ii) Bubbles of ~10 to 150 µm in diameter resulting from the manufacturing of the glass samples are found to outcrop at the surface of all oligoclase glass samples (Fig. III-5a-c).

(iii) Finally, regarding the crystalline oligoclase samples, deep trenches are observed on reacted surfaces, as well as K-feldspar veins, revealing the perthitic nature of the crystals (Fig. III-5d-e). The accurate depth of those trenches is out of reach of VSI measurements.

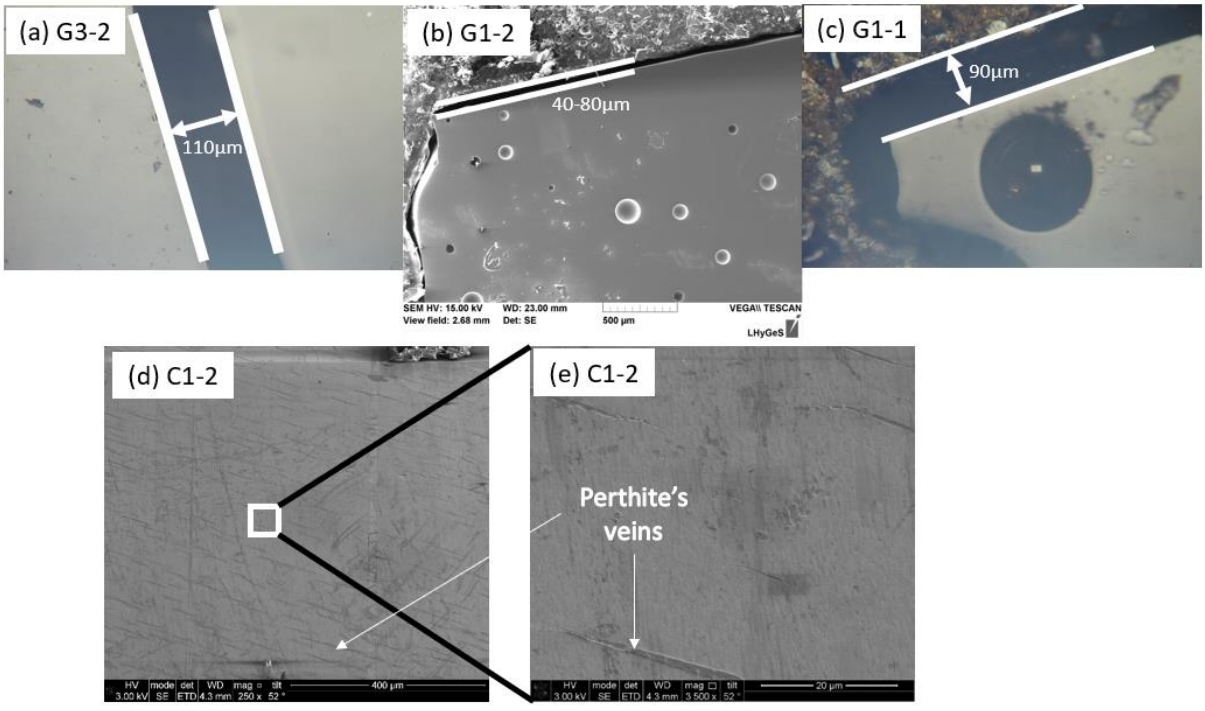

Figure III-5 : Optical microscope and SEM images of the surface of the altered samples. (a-c) Pictures showing the retraction of the resin and the gap of several tens of micrometer created between the sample and the resin. Those microscopy images are from amorphous oligoclase altered at pH 3 for 33 days ((a) sample G3-2) and at pH 1.5 for 12 days ((c) sample G1-1) and 33 days ((b) sample G1-2). A similar retraction is observed on crystalline oligoclase. (d-e) Pictures showing the presence of K-feldspar veins on the surface of crystalline oligoclase at pH 1.5 after 33 days of alteration (sample C1-2) with a magnitude of (d) 250x and (e) 3500x. The K-feldspar veins are labelled as perthite's veins as they are a consequence of the perthitic nature of the material.

Overall, the surface area in contact with the solution was recalculated after measuring the surface of the lateral faces to consider their contribution in the alteration process. The corresponding altered layer thicknesses estimated based on ICP-AES data are significantly lowered (Fig. III-6), reducing the gap between the thickness estimated from solution analyses ($h_{solution}$) and those estimated from ToF-SIMS measurements ($h_{ToF\text{-}SIMS}$). Whereas the $h_{solution}$/ $h_{ToF\text{-}SIMS}$ ratios of three of the four reacted glass samples are within a 2-fold factor, the $h_{solution}$/ $h_{ToF\text{-}SIMS}$ ratios still exceed one order of magnitude for most of the reacted crystalline samples.

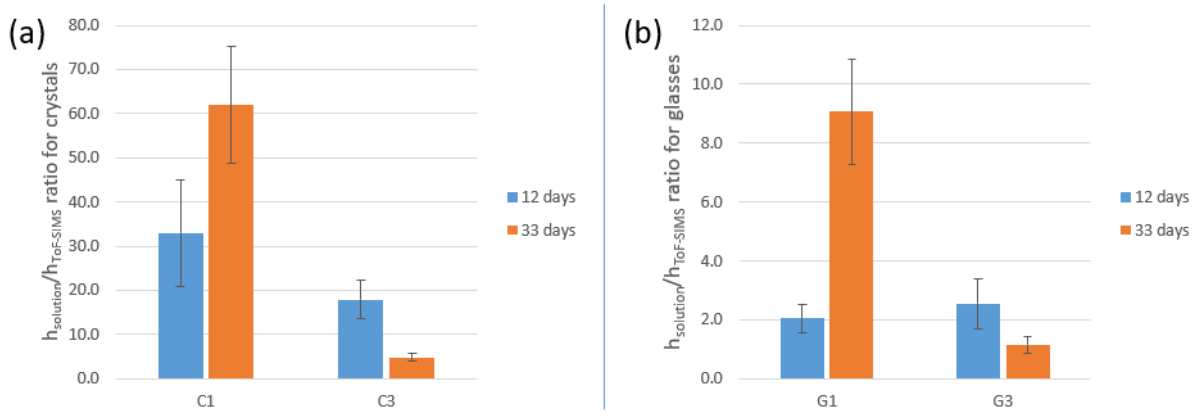

Figure III-6: representation of $h_{solution}/h_{ToF\text{-}SIMS}$ ratio for (a) crystalline oligoclase altered at pH 1.5 (labelled as C1) and at pH 3 (labelled as C3) and (b) amorphous oligoclase altered at pH 1.5 (labelled as G1) and at pH 3 (labelled as G3). Uncertainties are detailed in Supplementary Note 3.

III.3. DISCUSSION

III.3.1. Discrepancies between solid and fluid characterizations: a possible evidence for the development of extra reactive surface area for crystalline samples

When the thickness of altered oligoclase glass estimated from solution analyses is compared with that estimated from solid characterizations (ToF-SIMS and FIB-TEM analyses), a ≥two-fold factor between each estimation is found (Fig. III-6). This factor is calculated after accounting for all the adjacent surfaces. Because of the amorphous structure of the glass, the dissolution of such samples is isotropic, so that the lateral faces should dissolve at the same rate as the top face and should not increase the total dissolution rate. Considering however the extra surface area resulting from (i) the numerous bubbles outcropping at the surface (Fig. III-6a) and (ii) the fact that the lateral faces were not polished, this two-fold factor between the Tof-SIMS and the ICP-AES estimates could be reasonably considered as negligible. Interestingly, such discrepancies are similar to those reported by Fournier et al. [55] when comparing the reactivity of polished glass monoliths to that of glass powders, which is typical of the additional contribution of surface roughness.

Regarding the crystalline samples, the ratios between altered thickness estimates from fluid data to solid characterizations range from 16 for C3-1 to 60 for C1-2. The top face was determined to be a (001) face, which represents the fastest dissolving faces among the (001), (010) and $(10\bar{1})$ faces studied by Pérez et al. [1]. Due to the crystalline structure of the sample, dissolution is expected to be anisotropic, and the rate of the unpolished lateral faces may be either greater or lower than that of the top (001) face, which may partly explain the large discrepancies between estimates derived from fluid vs. solid characterizations. However, even the thorough work of Pollet-Villard et al. [56] dedicated to the dissolution anisotropy of K-feldspar did not evidence discrepancies as large as ~ two orders of magnitude between two dissolving faces. This observation leads us to suggest that intra-crystalline reaction might have occurred as well, partly due to the perthitic nature of the sample we used, as testified from the deep trenches observed at the surface of the sample (Fig. III-5d-e). Lee et al. [57] demonstrated that the microtexture of feldspars and especially, the boundaries between the feldspar matrix and exsolution lamellae represent hotspots of reactivity. The dissolution rate at the interface between those two phases is greater, and since this interface gets deeper into the core material, the dissolution proceeds unhindered along their interface. In other words, those interfaces may represent additional surface area where dissolution occurred. Moreover, an alternation of Ca-rich and Na-rich lamellae was observed, leading to the preferential dissolution of Ca-rich lamellae. The edges and corners of this structure may contribute to increase the dissolution rate. Finally, Worden et al. [58] demonstrated that the turbidity of feldspars is correlated with the presence of micro-pores. The coarsening of the perthites on the surface involves the development of those micro-pores. The border between boundaries gets thinner and diffusive intra-crystalline channels may develop, increasing the exchange surface with the solution. Once the dissolution front crosses those micro-pores and channels, intra-crystalline reaction takes place and increases the dissolution rate.

In summary, while the results obtained to quantify the dissolution rate of oligoclase glass can be reasonably well explained by the contribution of unpolished lateral faces, it is more difficult to draw a similar conclusion for the crystalline samples. The discrepancies between the estimations based either on fluid data or solid characterizations may be ascribed to an additional intra-crystalline reactivity fostered by the perthitic nature of the crystalline samples.

III.3.2. Dissolution mechanisms inferred from solid characterizations

III.3.2.1. FIB-TEM characterizations and elemental depth profile suggest that the dissolution mechanisms depend on the long-range order of the materials

Figure 1 and Figure 2 summarize FIB-TEM characterizations for the samples altered over 33 days. When these results are coupled with Na and Al depth profiles collected using ToF-SIMS (Fig. III-3), a first approach to the alteration mechanism can be proposed.

Regarding oligoclase glass, FIB-TEM characterizations reveal that the Al/Si ratio exhibits a gradual transition from the pristine sample to the ASSL, spreading over 50 nm at pH 1.5 and 25 nm at pH 3 (Fig. III-2a and III-2b). Such a gradual transition can also be observed from ToF-SIMS characterizations (Fig. III-3), although one must keep in mind that such profiles are more sensitive than FIB-TEM measurements to broadening. A more robust observation stems from the comparison of the profiles as a function of the considered element: the depletion depth is element-dependent. While Na is depleted to a depth of 500 nm in the glass sample at pH 1.5 after 33 days, the Al depletion front reaches barely 300 nm. A similar observation can be made for all amorphous samples at pH 1.5 and 3, after 12 days or 33 days. Based on those observations, a leaching mechanism is likely to occur during the dissolution of oligoclase glass. In addition, while under strongly acidic conditions, the dissolution rate does not decrease with time, a significant decrease in the dissolution is observed at pH 3 between 12 and 33 days (Fig. III-4d), which is consistent with the pH-dependent passivating properties of ASSLs formed on silicate glass [28,59].

Regarding crystalline oligoclase, STEM-EDX characterizations of the C1-2 sample show that the Al/Si profile is very sharp at the interface between the altered layer and the pristine crystal (note that this step-like profile supports the model used in the Supplementary Note 3 to deconvolute the ToF-SIMS profiles). Furthermore, the structural interface is sharp and well delimited, extending over a few nanometers only. Finally, the alternation of Ca-rich and Na-rich lamellae translates into a difference of reactivity of each domain. A similar observation prompted Wild et al [49] to reject a leaching mechanism for the dissolution of labradorite at pH 1.5 and 3. Instead, all these observations suggest that crystalline oligoclase dissolve following the CIDR mechanism at pH 1.5 [37-39]. This hypothesis is further supported by the porosity of the altered layer: The difference between the molar volumes of amorphous SiO_2 and oligoclase is consistent with the porosity estimated from TEM images. At pH 3, we can observe a slight preferential dissolution of Ca-rich lamellae, resulting in a similar (though greatly attenuated) grooved interface, consistent with the CIDR mechanism. However, the altered layer is only a few nanometers in thickness, and does not evolve between 12 days and 33 days (Fig. III-4d). Consistent with the

observation of Wild et al [49] for labradorite, we conclude that the crystalline oligoclase is passivated at pH > 3. The limited thickness of the ASSL prevented us from getting detailed information on its chemical composition, so that detailed dissolution mechanisms remain out of reach. However, we suggest that the difference in the evolution of altered layer thickness between the crystals at pH 1.5 and pH 3 can be explained by a competition between the dissolution rate of the oligoclase and the densification of the ASSL, as proposed by Daval et al. [45] for wollastonite. Under strongly acidic conditions, the densification kinetics may be slower than the dissolution rate, resulting in non-passivating surface layers, as opposed to those developed under less acidic pH conditions.

In summary, the combination of FIB-TEM characterizations with depth profiles measured by ToF-SIMS suggests that oligoclase glass dissolution may follow a leaching mechanism, whereas oligoclase crystal dissolution observes a CIDR mechanism.

III.3.2.2. Dissolution mechanisms inferred from $^{29}Si/^{28}Si$: a new perspective on the dissolution process for crystalline samples?

As mentioned previously, we used ^{29}Si as a proxy for the alteration mechanism. If the altered layer is a relic structure of the pristine material resulting from preferential leaching, the isotopic composition of the leached layer should be the same as that of the pristine material. Conversely, if the layer is formed following a CIDR mechanism, it should record the isotopic composition of the fluid [22,50]. This protocol was previously successfully applied on borosilicate alteration [50] vs. Si-K-Ca glass alteration [60], with contrasted results regarding the isotopic signature of the ASSLs, and therefore, their mechanisms of formation. Fig. III-4c summarizes the contribution of the solution in the composition of the altered layer.

As a confirmation of the previous conclusions (see section III.3.2.1), we note a negligible incorporation of ^{29}Si in the layer of glass samples reacted at pH 1.5 and pH 3 (contribution of the fluid ≤ 16%). Thus, most of the Si is inherited from the glass samples. The altered layers are essentially relics of the pristine glass, which therefore mainly dissolves by releasing first Na and to a lesser extent Al without getting the silica matrix dissolved (depletion front of Al at 30 nm for G1-1 or 20 nm for G3-1 versus a depletion front of Na at 140 nm for G1-1 or 80 nm for G3-1). The slight incorporation of ^{29}Si from the fluid may indicate a minor contribution of precipitated silica in the layers.

The results obtained on crystalline samples are more intriguing: the $^{29}Si/^{28}Si$ ratios measured with ToF-SIMS indicate that the contribution of the fluid only amounts to 35%-45% for the ASSLs developed on crystalline samples altered at pH 1.5. According to the FIB-TEM observations, a much higher value (close to 100%) reflecting the CIDR mechanism was expected. Therefore, those results suggest that the CIDR mechanism cannot fully explain the alteration process of the crystalline samples.

Two scenarios may be envisioned to solve this paradox. Both are based on a putative gradual modification of the transport properties of the altered layer with time (this assertion is supported by the non-linear growth of the altered layer with time, cf. Fig. III-4d):

(i) If the ASSLs transport properties decreased, the pristine material became increasingly isolated from the ^{29}Si-enriched bulk fluid. Still, at such low pH, the oligoclase crystal remained undersaturated, and kept dissolving, so that the $^{29}Si/^{28}Si$ ratio in the pore fluid of the ASSL gradually decreased, and the isotopic signature of the precipitated silica gradually approached that of the pristine crystal.

(ii) Alternatively, part of the silicon from the oligoclase crystals might have not been released in the aqueous phase prior to its incorporation into the ASSL. Daval et al. [61] proposed a similar mechanism for the dissolution of crystalline olivine, where the ASSL forms following the CIDR mechanism first, while subsequent structural rearrangement of the altered layer results in solid state diffusion of dissolved species throughout the ASSL. Of note, this scenario would contradict the premise that all Si-O-Si bonds must be broken simultaneously in order to release a Si atom in the solution (as suggested by the CIDR model). It could then be possible that Si-O-Si bonds are sequentially broken to release separately O and Si atoms into the solution. As long as one bond is not broken, Si is attached to the silica matrix and does not dissolve forming, thus, a leached layer. The *in situ* reorganization of the altered layer after the release of Na and Al then becomes the source of the formation of the altered layer. This reorganization implies that Si can form new bonds with other Si to reform a silicate network. This mechanism is supported by Gin et al., [48] who conducted a study on the mechanism of formation of altered layer on borosilicate glass. Despite the difference in the structure of the materials, the common point of both studied materials is their composition with and without Al-bearing materials. The effect of the presence of Al will be discussed in the following section.

Overall, both scenarios account for (i) the temporal decrease in the contribution of the fluid to the composition of the ASSL developed on C1 samples (Fig. III-4c) and (ii) the (modest) decrease in the dissolution rate of crystalline oligoclase with time (Fig. III-4d). Similar scenarios could be envisioned for C3 samples, where the alteration might have taken place early before the formation of a passivation layer on the surface (Fig. III-4d), and the contribution of the fluid to the ASSL became negligible (Fig. III-4c).

III.3.3. Structure and texture effects on the dissolution rate

III.3.3.1. Penetration of water in the material and the impact of Al on dissolution rates and mechanisms

The presence of Al in the network of silicate glasses and minerals increases locally the bond-breaking activation energy of Si-O-Si bonds [62-64]. The corresponding Si atoms are then harder to dissolve. As a matter of fact, Al-bearing glasses dissolve slower than Al-free glasses [48]. Pierce et al. [65] promoted the cleavage of Al-O as the rate limiting step in Al-bearing glass dissolution. Conversely, the activation energy for dissolving Al-O bonds is much lower than that of Si-O bonds [64], leading to a preferential release of Al in the solution. Once Al is depleted, the silicate network is weakened and the hydrolysis of the siloxane is much faster. By studying the dissolution of albite, jadeite and nepheline glasses, Hamilton et al. [66] demonstrated that the higher the Al/Si ratio is in the glass, the faster the dissolution is in acidic condition. Stone-Weiss et al. [67] explained this observation by the hydrolysis of the Si surrounding Al (and B) which decreases the network connectivity. Taken together, those observations suggest that small amounts of Al in the glass strengthen the silicate network, while a more important amount is in favour of the network dissolution. The boundary between the two regimes remains to be determined.

From this point, a striking difference between crystalline and amorphous oligoclase is the more open structure of the latter (cf. Fig. 15 in Pérez et al. [1]). Molecular dynamics simulations conducted in this previous study show that the structure of the glass is more open, with interstitial sites having a radius that exceeds 1.3 Å. Such dimensions are compatible with molecular water diffusion into the material [7]. As a consequence, the inward flux of water may contribute to Si-O-Al and Si-O-Na hydrolysis. Those channels not only explain the depletion depth of Al and Na elements observed in our experiments for glass samples, but also the difference between the evolution of the altered layer thickness between 12 days and 33 days for glass and crystal samples. Indeed, because diffusion channels do not exist in the crystalline oligoclase, its dissolution should be limited at the very surface. In order for this surface to be altered, Al depletion is needed and only after this step, the breakdown of the silicate network can occur. But since the altered Si-rich layer condenses on the surface, the transport properties of this layer decrease, resulting in a decrease of the alteration rate. Conversely, the more open structure of the glass results in an alteration at the surface, but also within the glass. The deeper depletion of Al in the material implies a faster alteration of the silicate network. Because the reaction rate between the pristine material and the bulk solution remains high, the altered layer cannot densify or reorganize itself quickly enough to affect the dissolution rate, explaining its high value and thus, the dramatic increase in the thickness of the altered layer of G1 samples after 33 days.

Such a reasoning would be consistent with the observation of Hamilton et al. [68] regarding the rate-limiting step of glass vs. crystalline albite dissolution.

Finally, Yang et al. [69] modelled the effect of Al/Si ordering on the development of interfacial layers on dissolved feldspars. They demonstrated that, in a disordered structure, the diffusivity of aqueous species in the material is limited by the hydrolysis rate of Si-O-Al bonds. The disordering of Al atoms that are gradually released to the solution may result in the development of channels within the material. On contrary, in an ordered structure, the diffusivity of aqueous species is limited by both the hydrolysis rate of Si-O-Si and Si-O-Al bonds. Those observations support the fast dissolution of oligoclase glass at pH 1.5 and the slower dissolution of (ordered or disordered) oligoclase crystal in Fig. III-4d.

III.3.3.2. A pH threshold for the passivating properties of ASSLs developed on crystalline samples

In a recent study, Daval et al [45] reported that the passivating properties of ASSLs developed on various faces of a Ca-rich pyroxene (wollastonite) are negatively correlated with their absolute dissolution rates (i.e., the dissolution rates of ASSL-free faces). They proposed that the passivating properties of ASSLs result from a competition between the hydrolysis rate of the mineral and the densification rate of the ASSL. As a consequence, they speculated that any parameter favoring the densification of the layer at the expense of the hydrolysis of the mineral would result in a decrease of the transport properties of the ASSLs. Our results are consistent with this assumption: the hydrolysis rate of silicates is known to increase when pH decreases [70], whereas the condensation rate of silica is slower in acidic solutions [71]. As a consequence, one could expect that the reaction becomes transport-limited for layers developed at mildly acidic pH. Our results are also consistent with Wild et al. [49], who determined experimentally a pH threshold of 2.5, above which ASSLs become passivating for labradorite feldspar.

III.3.4. Discussion summary

Whether or not the mechanisms of silicate dissolution depend on their long-range order has long remained an open question. By comparing the reactivity of crystalline and amorphous oligoclase at pH 1.5 and 3, the following conclusions can be drawn:

(i) Regarding crystals, the estimated evolution of the thickness of surface layers with time suggests that the transport properties of surface layers decrease with pH. Whereas oligoclase dissolution rate is moderately impacted by the surface layers developed at pH 1.5, the oligoclase surface is passivated at pH 3.

(ii) Regarding crystals, FIB-TEM characterizations first suggested that the surface layers are formed following a coupled interfacial dissolution-reprecipitation (CIDR) mechanism (particularly evident at pH 1.5). However, Tof-SIMS measurements revealed that incorporation of ^{29}Si from the solution is only modest at pH 1.5 (between 35% and 45%) and insignificant at pH 3 (< 5%), challenging the CIDR mechanism (which should correspond to a fluid contribution close to 100%, as noticed by Gin et al [48]). We suggest that the evolution of the transport properties of the surface layers with time gradually isolate the oligoclase surface from the bulk fluid, so that the growth of the surface layers continues either without a full depolymerization of the silicate framework (solid state diffusion), or through the uptake of SiO_2(aq) from the nanopores that is increasingly enriched in Si provided by the substrate.

(iii) Conversely, both FIB-TEM characterizations and Tof-SIMS measurements converge towards the same conclusion that proton diffusion inside the oligoclase glass structure could have contributed to the preferential leaching of Na and (to some extent) Al cations. The contribution of the CIDR mechanism is minor, but measurable (< 20%). The existence of diffusion channels in the structure (as suggested by Pérez et al. [1]) favors the release of Al cations, resulting in the weakening of the silicate framework and an enhanced dissolution of the structure.

(iv) Finally, even if the understanding of the alteration mechanism is important in order to model the corrosion of such material over geological timescale, the key point is therefore the transport properties of altered layers. The ingress of protons is the driving force of hydrolysis and Si-O-Si or Si-O-Al bonds cleavages. From this inward flow, a second outward flow starts with the depletion of material elements such as Na or Al. Those elements diffuse into the solution, leaving a weakened silicate network prone to dissolve. More experiments must be conducted in order to characterize the transport properties of those layers.

III.4. MATERIAL AND METHODS

III.4.1. Sample preparation

Oligoclase glass and mineral samples were prepared during the previous work of Pérez et al. [1]. According to this study, the chemical composition of the sample is $Na_{0.83}K_{0.02}Ca_{0.07}Al_{1.06}Si_{2.96}O_8$. The orientation of the oligoclase crystals was (001), as determined by electron backscatter diffraction (EBSD). Glass sample was prepared from melting the crystalline oligoclase at 1500 °C for 2 h and then 1650 °C for 2 h in a high temperature furnace Carbolite HTF 1700 (see details in Pérez et al. [1]). As shown above, the cooling step resulted in the formation of bubbles within the oligoclase glass.

Oriented crystal and glass samples were embedded in epoxy resin so that only the surface of interest was exposed at the surface of the resin (as emphasized above, this treatment was however unsuccessful, due to a strong retraction of the resin during its solidification). The samples were then polished through different steps of abrasion sequence, and subsequently divided into smaller pieces. The lateral sides of the samples that were not embedded in the resin were covered with room-temperature-vulcanizing (RTV) glue to prevent dissolution of unpolished parts of the samples. A small part (< 1 mm², on average < 9% of the top surface of the sample) of the polished surface of interest was protected as well with RTV glue spots to create a non-reacted reference surface.

III.4.2. Solution preparation

The experiments were conducted in solutions saturated with respect to amorphous silica (SiO_2(am)) to stabilize the Si-rich layer developed at the surface of the oligoclase during dissolution. The concentrations of Si were 175ppm and 140ppm (on average) for the 12 days and 33 days alteration experiments, respectively. The solution for the sample dissolution was enriched in ^{29}Si using amorphous silica $^{29}SiO_2$(am) powder (Cortecnet, 99.69% purity of ^{29}Si). To circumvent the sluggishness of SiO_2(am) dissolution, an alkali-fusion protocol was followed, where the $^{29}SiO_2$(am) powder was mixed with potassium hydroxide in an agate mortar ($mKOH/mSiO_2$ = 10). Mixed powder was placed in a zirconia crucible and introduced in a high-temperature oven (NABERTHERM). The temperature was increased to 300°C in 2 hours and kept constant for 15 minutes while Ar gas was introduced. Then, it was increased again to 600°C within an hour and kept constant during 45 min before cooling down the oven. At 300°C, Ar gas delivery was shut down and around 100°C, the crucible was recovered from the furnace. The crucible was then immersed in a solution of HNO_3 0.1N at 90°C to dissolve the resulting Si-rich solid and stirred overnight at 90°C. The analyses of dissolved Si concentration indicated that the yield of the fusion was approximately 60% to 70% of $^{29}SiO_2$ initially introduced. In a second stage, K^+ ions were removed from the solution, because of their potential effect on the transport properties of the altered layers [15]. We used a K^+/H^+ exchange resin column (AG50W – X12) to remove selectively potassium. Finally, in order to reach saturation with respect to amorphous silica at 90°C, sodium metasilicate (Na_2SiO_3) was added to the solution, because of its large solubility and fast dissolution rate (see Supplementary Tables III-4 and III-5). The solution pH was then adjusted to either 1.5 or 3.0 (the given pH corresponds to the pH of the solution at 90 °C. It was measured at ambient temperature and then back calculated at 90 °C using the thermodynamic code JChess, which accounts for the evolution of logK of the various species in solution with the temperature), using LiOH (Prolabo) and HNO_3 (distilled). Four 60 mL PFA Savillex® reactors were filled with ~35 ml of solution and placed in an oven at 90 °C. Each reactor contained either a glass or a crystalline sample placed on PTFE tripods inserted in the reactors. The solution was continuously stirred with magnetic bars.

After introducing the glass and crystalline samples in the reactors containing the prepared solution, the dissolution of the samples started in the oven at 90 °C. The dissolution was controlled by collecting a small amount of solution regularly. At the end of the experiment, both solution and sample provided information on oligoclase alteration.

III.4.3. Analyses

The dissolution process was controlled by collecting 1 ml of the solution every 5-7 days. The aqueous samples were then diluted 5x and analyzed with ICP-AES (Thermo ICAP 6000) for Na, Al and Si, or 10x and analyzed with Inductively Coupled Plasma Mass Spectroscopy (ICP-MS) to determine the aqueous $^{29}Si/^{28}Si$ ratio of the solution. The measured concentrations were used to estimate the dissolution rate of the interface between the altered layer and the pristine substrate, which is referred to as the "internal interface" (see Wild et al. [49] for details), and provides indirect information on the growth rate of the altered layer. The depth profile of elements of interest was measured using Time-of-Flight Secondary Ion Mass Spectrometry (ToF-SIMS). This isotope sensitive technique provides information about the mechanism of formation of the altered layer.

III.4.3.1. ICP-AES and ICP-MS analyses of aqueous solutions

Because of the small volume of solution, only a few intermediate samplings were performed to monitor the dissolution of oligoclase samples. At each sampling step, the amount of element *i* (mol) released into the fluid was calculated based on ICP-AES measurements following:

$$n_{\mathrm{t}}^{i} = \frac{F_t \times [i]_t \times V_t}{M_i} + \sum_{l=1}^{t-1} \frac{[i]_l \times V_{ct} \times F_l}{M_i} \qquad \text{(Eq. III-2)}$$

where n_t^i is the amount (mol) of element *i* at time *t*, F_t is the dilution factor of the aqueous sample collected at time *t*, $[i]_t$ and $[i]_l$ are the concentrations of element *i* at time *t* and $t - \Delta t$, respectively, V_t and V_{ct} are the volumes of the solution in the reactor just before collection and the volume of the solution collected at time *t* respectively, and M_i is the molar mass of element *i*.

ICP-MS analyses were also performed to determine the aqueous $^{29}Si/^{28}Si$ ratio and estimate the incorporation of the ^{29}Si from the solution into the altered layer. However, being the uncertainties of the ICP-MS measurements around 3%, the difference between the initial and final ratios were not statistically significant. Consequently, the ICP-MS measurements were not accurate enough to estimate the thickness of the altered layers containing ^{29}Si.

Because sodium metasilicate was used to bring the solution at saturation with respect to SiO_2(am), the background concentrations of Na and Si were too high to provide any reliable information on the dissolution rate of oligoclase. Therefore, the dissolution rate at the internal

interface (between the pristine material and the altered layer) was estimated based on Al concentration. Based on thermodynamic simulation and ICP-AES analyses, the solution remained undersaturated with respect to Al precipitates (diaspore, boehmite and gibbsite) all over the duration of the experiment. After plotting the amount of Al as a function of time, we proceeded to a linear regression. The slope of the regression was then divided by the surface area of the corresponding sample to estimate the dissolution rate (r_{disso}, see Supplementary Fig. 1 and Supplementary Table III-3):

$$r_{\mathrm{disso}} = \frac{a_{\mathrm{lr}}}{S_{\mathrm{total}}} \qquad \text{(Eq. III-3)}$$

where a_{lr} is the slope of the linear regression (mol.s^{-1}) and S_{total} is the total surface area – taking the lateral surfaces into account – (m²) of the sample in contact with the solution.

Since the solution was saturated with amorphous SiO_2, no external surface retreat is expected at the interface between the solid and the solution. Topography data collected by vertical scanning interferometry (Zygo NewView 7300) confirmed this statement, as no difference of elevation between the masked reference surface and the reacted surface could be evidenced, consistent with Perez et al. [1]. The thickness of the altered layer estimated using fluid data (h_{ICP}) was therefore calculated as follows:

$$h_{\mathrm{ICP}} = \frac{r_{\mathrm{disso}} \times t_{\mathrm{exp}} \times M_{\mathrm{olg}}}{\rho_{\mathrm{olg}}} \qquad \text{(Eq. III-4)}$$

where t_{exp} is the duration of the experiment, M_{olg} is the molar mass of oligoclase (262.2 g.mol^{-1}) and ρ_{olg} is the density of oligoclase (2.62 g.cm^{-3}).

III.4.3.2. ToF-SIMS analyses of the reacted surface

The altered solid samples were analyzed by an IONTOF GmbH® TOF 5 spectrometer from TESCAN Analytics (France). The external surface was abraded on an area of 200x200 µm² for an analyzed area of 50x50 µm². The ToF-SIMS operated as cycles of abrasion and analysis. After each cycle, the surface charge was neutralized by a low energy electron beam (<20 eV) in order to prepare the area for the next cycle. The depth of the crater (h_{crater}) created by ion milling after a given number of abrasion cycles (N_{cycles}) was measured using 3D profilometer. The depth associated to one cycle of abrasion (z_{cycle}) is then assumed to be simply given by:

$$z_{\mathrm{cycle}} = h_{\mathrm{crater}} / N_{\mathrm{cycles}} \qquad \text{(Eq. III-5)}$$

Uncertainties are approximately 15% of the result value. Depth profiles of positive ions, O^+, Na^+, Al^+, $^{28}Si^+$ and $^{29}Si^+$ were recorded thanks to Bi_1^+ 25 keV, 1.2 pA beam for the analyses and O_2^+ 2 keV, 600 nA beams for the ablation.

The ion depth profiles are known to be artifactually broadened as a result of the instrumental resolution and because of the roughness of the reacted surface of the sample [37,45]. Therefore, the $Al/^{28}Si$ and $^{29}Si/^{28}Si$ profiles from ToF-SIMS were deconvoluted following the method described in Daval et al. [45] in order to estimate the actual profile for the ratios of interest. See Supplementary Note 3.A for more details. The $Al/^{28}Si$ profile was then used to define the altered layer thickness and the $^{29}Si/^{28}Si$ profile was used to determine the average contribution of the solution in the composition of the altered layer following equation (A6) (see Supplementary Note 3.A).

III.4.3.3. Electron microscopy characterizations of the reacted surface

Scanning electron microscopy observations were conducted either with a Tescan VEGA II SEM operated at ITES (Strasbourg, France) or with a FEI Helios 600 Nanolab dual beam operated at CP2M (Marseille, France). The reacted samples after 33 days were then carbon-coated, and ultrathin electron transparent cross sections were subsequently prepared by focused ion beam (FIB) milling using the FEI Helios 600 Nanolab dual-beam operated at CP2M (Marseille, France) following methods previously described by Daval et al. [37]. In brief, FIB Ga^+ ion milling was carried out at an ion beam voltage of 30 kV and beam currents ranging from 9 nA to 90 pA for the final steps. Micrometer-thick sections were lifted out *in situ* using an Omniprobe 200 micromanipulator and transferred to a half copper grid for final ion milling to electron transparency (final thickness of ~100 nm). This milling was performed at a reduced acceleration voltage of 5 kV to reduce beam damage. For the same reasons, the final cleaning steps were then operated at 2 and 1 kV. The thin sections were oriented perpendicular to the striations at the surface of the crystals.

TEM and scanning transmission electron microscopy (STEM) observations were performed on FIB foils using a FEI Tecnaï G2 microscope operated at CP2M (Marseille, France) with a LaB_6 electron source operating at 200 kV. EDX spectra were acquired in STEM mode to probe the chemical composition of the interface between the altered layer and the substrate, with an Energy Dispersive X-ray Detector (Oxford XMax 80). The analyses were conducted on a total of four FIB thin sections (G1-2, C1-2, G3-2 and C3-2). The EDX maps were then processed as described in the Supplementary Note 3.B.

DATA AVAILABILITY STATEMENT

The authors declare that the data supporting the findings of this study are available on demand (benjamin.cagnon@univ-grenoble-alpes.fr)

ACKNOWLEDGEMENTS

The authors thank Gilles Morvan (ITES), Thierry Perrone (ITES) and René Boutin (ITES) for performing EBSD, providing advice and help for the experiments and helping with ICP-AES and ICP-MS measurements, respectively. The authors are also grateful to Loan Lai, Elodie Chauvet, Amandine David and Yves Depuydt from Tescan Analytics for performing ToF-SIMS analyses and operating one FIB thin section. Nicolas Michau and Christelle Martin are thanked for their inputs on an earlier version of this manuscript. This work was funded by Andra and EDF.

COMPETING INTERESTS

The authors declare no competing interests.

AUTHOR CONTRIBUTIONS

B.C. performed the experiments and analyzed data. M.C. prepared FIB thin sections, performed and analyzed the TEM measurements. D.L. contributed to design the alkali fusion and cation exchange column protocols. D.D. and S.G. analyzed data and supervised the research. B.C., D.D., and S.G. wrote the manuscript, with contributions from all authors.

REFERENCES

1 Perez, A. *et al.* Comparing the reactivity of glasses with their crystalline equivalents: The case study of plagioclase feldspar. *Geochim Cosmochim Ac* **254**, 122-141, doi:https://doi.org/10.1016/j.gca.2019.03.030 (2019).

2 Huntington, T. *et al.* Calcium depletion in a southeastern United States forest ecosystem. *Soil Science Society of America Journal* **64**, 1845-1858 (2000).

3 Daval, D. Carbon dioxide sequestration through silicate degradation and carbon mineralisation: promises and uncertainties. *npj Materials Degradation* **2**, 11, doi:10.1038/s41529-018-0035-4 (2018).

4 Grambow, B. Nuclear Waste Glasses - How Durable? *Elements* **2**, 357-364, doi:10.2113/gselements.2.6.357 (2006).

5 Frankel, G. S. *et al.* Recent Advances in Corrosion Science Applicable To Disposal of High-Level Nuclear Waste. *Chemical Reviews* **121**, 12327-12383, doi:10.1021/acs.chemrev.0c00990 (2021).

6 Gin, S., Delaye, J.-M., Angeli, F. & Schuller, S. Aqueous alteration of silicate glass: state of knowledge and perspectives. *npj Materials Degradation* **5**, 42, doi:10.1038/s41529-021-00190-5 (2021).

7 Bunker, B. C. MOLECULAR MECHANISMS FOR CORROSION OF SILICA AND SILICATE-GLASSES. *Journal of Non-Crystalline Solids* **179**, 300-308 (1994).

8 Jabraoui, H., Gin, S., Charpentier, T., Pollet, R. & Delaye, J.-M. Leaching and Reactivity at the Sodium Aluminosilicate Glass–Water Interface: Insights from a ReaxFF Molecular Dynamics Study. *The Journal of Physical Chemistry C*, doi:10.1021/acs.jpcc.1c07266 (2021).

9 Hou, X., Kirkpatrick, R. J., Struble, L. J. & Monteiro, P. J. M. Structural Investigations of Alkali Silicate Gels. *Journal of the American Ceramic Society* **88**, 943-949, doi:https://doi.org/10.1111/j.1551-2916.2005.00145.x (2005).

10 C.E. Tambelli, J. F. S., N.P. Hasparyk, P.J.M. Monteiro,. Study of the structure of alkali–silica reaction gel by high-resolution NMR spectroscopy,. *Journal of Non-Crystalline Solids* **352**, 3429-3436, doi:https://doi.org/10.1016/j.jnoncrysol.2006.03.112. (2006).

11 Zhuravlev, L. T. The surface chemistry of amorphous silica. Zhuravlev model. *Colloids and Surfaces A: Physicochemical and Engineering Aspects* **173**, 1-38, doi:https://doi.org/10.1016/S0927-7757(00)00556-2 (2000).

12 Zapol, P., He, H., Kwon, K. D. & Criscenti, L. J. First-Principles Study of Hydrolysis Reaction Barriers in a Sodium Borosilicate Glass. *International Journal of Applied Glass Science* **4**, 395-407, doi:https://doi.org/10.1111/ijag.12052 (2013).

13 Inagaki, Y., Kikunaga, T., Idemitsu, K. & Arima, T. Initial Dissolution Rate of the International Simple Glass as a Function of pH and Temperature Measured Using Microchannel Flow-Through Test Method. *International Journal of Applied Glass Science* **4**, 317-327 (2013).

14 K. Ferrand, A. A., B. Grambow,. Water diffusion in the simulated French nuclear waste glass SON 68 contacting silica rich solutions: Experimental and modeling,. *Journal of Nuclear Materials* **355**, 54-67, doi:https://doi.org/10.1016/j.jnucmat.2006.04.005 (2006).

15 Collin, M., Fournier, M., Charpentier, T., Moskura, M. & Gin, S. Impact of alkali on the passivation of silicate glass. *npj Materials Degradation* **2**, 16 (2018).

16 Vienna, J. D., Ryan, J. V., Gin, S. & Inagaki, Y. Current Understanding and Remaining Challenges in Modeling Long-Term Degradation of Borosilicate Nuclear Waste Glasses. *International Journal of Applied Glass Science* **4**, 283-294, doi:https://doi.org/10.1111/ijag.12050 (2013).

17 Grambow, B. & Muller, R. First-order dissolution rate law and the role of surface layers in glass performance assessment. *Journal of Nuclear Materials* **298**, 112-124 (2001).

18 Rebiscoul, D. *et al.* Morphological evolution of alteration layers formed during nuclear glass alteration: new evidence of a gel as a diffusive barrier. *Journal of Nuclear Materials* **326**, 9-18, doi:http://dx.doi.org/10.1016/j.jnucmat.2003.10.015 (2004).

19 Diane Rebiscoul, P. F., Stéphane Gin, André Ayral,. Protective properties and dissolution ability of the gel formed during nuclear glass alteration. *Journal of Nuclear Materials* **342**, 26-34, doi:https://doi.org/10.1016/j.jnucmat.2005.03.018 (2005).
20 Gin, S., Ribet, I. & Couillard, M. in *International Topical Workshop on Glass in its Disposal Environment.* 1-10 (Elsevier Science Bv).
21 Nathalie Valle, A. V.-C., Jérôme Sterpenich, Guy Libourel, Etienne Deloule, Patrick Jollivet,. Elemental and isotopic (29Si and 18O) tracing of glass alteration mechanisms. *Geochim Cosmochim Ac* **74**, 3412-3431, doi:https://doi.org/10.1016/j.gca.2010.03.028 (2010).
22 Gin, S. *et al.* Dynamics of self-reorganization explains passivation of silicate glasses. *Nature communications* **9**, 2169 (2018).
23 Cailleteau, C. *et al.* Insight into silicate-glass corrosion mechanisms. *Nature Materials* **7**, 978-983, doi:10.1038/nmat2301 (2008).
24 Casey, W. H. GLASS AND MINERAL CORROSION Dynamics and durability. *Nature Materials* **7**, 930-932, doi:10.1038/nmat2326 (2008).
25 Jollivet, P. *et al.* Investigation of gel porosity clogging during glass leaching. *Journal of Non-Crystalline Solids* **354**, 4952-4958, doi:10.1016/j.jnoncrysol.2008.07.023 (2008).
26 Bourcier, W. L., Peiffer, D. W., Knauss, K. G., McKeegan, K. D. & Smith, D. K. A Kinetic Model for Borosilicate Glass Dissolution Based on the Dissolution Affinity of a Surface Alteration Layer. *MRS Online Proceedings Library Archive* **176**, null-null, doi:doi:10.1557/PROC-176-209 (1989).
27 Gin, S. *et al.* Insights into the mechanisms controlling the residual corrosion rate of borosilicate glasses. *npj Materials Degradation* **4**, 1-9 (2020).
28 Ojovan, M. I., Pankov, A. & Lee, W. E. The ion exchange phase in corrosion of nuclear waste glasses. *Journal of Nuclear Materials* **358**, 57-68, doi:https://doi.org/10.1016/j.jnucmat.2006.06.016 (2006).
29 Frugier, P. *et al.* SON68 nuclear glass dissolution kinetics: Current state of knowledge and basis of the new GRAAL model. *Journal of Nuclear Materials* **380**, 8-21, doi:10.1016/j.jnucmat.2008.06.044 (2008).
30 Fournier, M., Gin, S. & Frugier, P. Resumption of nuclear glass alteration: state of the art. *Journal of Nuclear Materials* **448**, 348-363 (2014).
31 Ribet, S. & Gin, S. Role of neoformed phases on the mechanisms controlling the resumption of SON68 glass alteration in alkaline media. *Journal of Nuclear Materials* **324**, 152-164, doi:https://doi.org/10.1016/j.jnucmat.2003.09.010 (2004).
32 Ebert, W. L. & Bates, J. K. A Comparison of Glass Reaction at High and Low Glass Surface/Solution Volume. *Nuclear Technology* **104**, 372-384, doi:10.13182/nt93-a34898 (1993).
33 Van Iseghem, P. & Grambow, B. The Long-Term Corrosion and Modelling of Two Simulated Belgian Reference High-Level Waste Glasses. *MRS Proceedings* **112**, 631, doi:10.1557/proc-112-631 (1987).
34 Petit, J. C., Dellamea, G., Dran, J. C., Schott, J. & Berner, R. A. MECHANISM OF DIOPSIDE DISSOLUTION FROM HYDROGEN DEPTH PROFILING. *Nature* **325**, 705-707 (1987).
35 Hellmann, R. The albite-water system .4. Diffusion modeling of leached and hydrogen-enriched layers. *Geochim Cosmochim Ac* **61**, 1595-1611 (1997).
36 Hellmann, R., Dran, J. C. & DellaMea, G. The albite-water system .3. Characterization of leached and hydrogen-enriched layers formed at 300 degrees C using MeV ion beam techniques. *Geochim Cosmochim Ac* **61**, 1575-1594 (1997).
37 Hellmann, R., Penisson, J.-M., Hervig, R. L., Thomassin, J.-H. & Abrioux, M.-F. An EFTEM/HRTEM high-resolution study of the near surface of labradorite feldspar altered at acid pH: evidence for interfacial dissolution-reprecipitation. *Phys Chem Miner* **30**, 192-197 (2003).
38 Daval, D. *et al.* Mechanism of wollastonite carbonation deduced from micro- to nanometer length scale observations. *Am Mineral* **94**, 1707-1726, doi:10.2138/am.2009.3294 (2009).

39 Hellmann, R. *et al.* Unifying natural and laboratory chemical weathering with interfacial dissolution–reprecipitation: A study based on the nanometer-scale chemistry of fluid–silicate interfaces. *Chem Geol* **294–295**, 203-216 (2012).
40 Geisler, T. *et al.* Aqueous corrosion of borosilicate glass under acidic conditions: A new corrosion mechanism. *Journal of Non-Crystalline Solids* **356**, 1458-1465, doi:10.1016/j.jnoncrysol.2010.04.033 (2010).
41 Ruiz-Agudo, E., Putnis, C. V., Rodriguez-Navarro, C. & Putnis, A. Mechanism of leached layer formation during chemical weathering of silicate minerals. *Geology* **40**, 947-950, doi:Doi 10.1130/G33339.1 (2012).
42 Ruiz-Agudo, E. *et al.* Control of silicate weathering by interface-coupled dissolution-precipitation processes at the mineral-solution interface. *Geology* **44**, 567-570, doi:10.1130/g37856.1 (2016).
43 Putnis, A. Mineral Replacement Reactions. *Rev Mineral Geochem* **70**, 87-124, doi:10.2138/rmg.2009.70.3 (2009).
44 Putnis, A. Why Mineral Interfaces Matter. *Science* **343**, 1441-1442, doi:10.1126/science.1250884 (2014).
45 Daval, D. *et al.* Dynamics of altered surface layer formation on dissolving silicates. *Geochim Cosmochim Ac* **209**, 51-69, doi:https://doi.org/10.1016/j.gca.2017.04.010 (2017).
46 Hellmann, R. *et al.* Nanometre-scale evidence for interfacial dissolution–reprecipitation control of silicate glass corrosion. *Nat Mater* **14**, 307-311, doi:10.1038/nmat4172

http://www.nature.com/nmat/journal/v14/n3/abs/nmat4172.html#supplementary-information (2015).
47 Gin, S. *et al.* Atom-probe tomography, TEM and ToF-SIMS study of borosilicate glass alteration rim: a multiscale approach to investigating rate-limiting mechanisms. *Geochim Cosmochim Ac* **202**, 57-76 (2017).
48 Gin, S. *et al.* A general mechanism for gel layer formation on borosilicate glass under aqueous corrosion. *The Journal of Physical Chemistry C* **124**, 5132-5144 (2020).
49 Wild, B. *et al.* pH-dependent control of feldspar dissolution rate by altered surface layers. *Chem Geol* **442**, 148-159, doi:http://dx.doi.org/10.1016/j.chemgeo.2016.08.035 (2016).
50 Gin, S. *et al.* Origin and consequences of silicate glass passivation by surface layers. *Nat Commun* **6**, doi:10.1038/ncomms7360 (2015).
51 Gin, S., Ryan, J. V., Schreiber, D. K., Neeway, J. & Cabié, M. Contribution of atom-probe tomography to a better understanding of glass alteration mechanisms: Application to a nuclear glass specimen altered 25 years in a granitic environment. *Chem Geol* **349–350**, 99-109, doi:http://dx.doi.org/10.1016/j.chemgeo.2013.04.001 (2013).
52 Bouakkaz, R., Abdelouas, A., El Mendili, Y., Grambow, B. & Gin, S. SON68 glass alteration under Si-rich solutions at low temperature (35–90 °C): kinetics, secondary phases and isotopic exchange studies. *RSC Advances* **6**, 72616-72633, doi:10.1039/c6ra12404f (2016).
53 Stillings, L. L. & Brantley, S. L. Feldspar dissolution at 25°C and pH 3: Reaction stoichiometry and the effect of cations. *Geochim Cosmochim Ac* **59**, 1483-1496, doi:http://dx.doi.org/10.1016/0016-7037(95)00057-7 (1995).
54 Hopf, J. *et al.* Toward an understanding of surface layer formation, growth, and transformation at the glass–fluid interface. *Geochim Cosmochim Ac* **229**, 65-84, doi:https://doi.org/10.1016/j.gca.2018.01.035 (2018).
55 Fournier, M. *et al.* Glass dissolution rate measurement and calculation revisited. *Journal of Nuclear Materials* **476**, 140-154 (2016).
56 Pollet-Villard, M. *et al.* Does crystallographic anisotropy prevent the conventional treatment of aqueous mineral reactivity? A case study based on K-feldspar dissolution kinetics. *Geochim Cosmochim Ac* **190**, 294-308, doi:http://dx.doi.org/10.1016/j.gca.2016.07.007 (2016).

57 Lee, M. R., Hodson, M. E. & Parsons, I. The role of intragranular microtextures and microstructures in chemical and mechanical weathering: direct comparisons of experimentally and naturally weathered alkali feldspars. *Geochim Cosmochim Ac* **62**, 2771-2788 (1998).
58 Worden, R. H., Walker, F. D. L., Parsons, I. & Brown, W. L. Development of microporosity, diffusion channels and deuteric coarsening in perthitic alkali feldspars. *Contrib Mineral Petr* **104**, 507-515 (1990).
59 Fournier, M. *et al.* Effect of pH on the stability of passivating gel layers formed on International Simple Glass. *Journal of Nuclear Materials* **524**, 21-38, doi:https://doi.org/10.1016/j.jnucmat.2019.06.029 (2019).
60 Verney-Carron, A. *et al.* Understanding the mechanisms of Si–K–Ca glass alteration using silicon isotopes. *Geochim Cosmochim Ac* **203**, 404-421 (2017).
61 Daval, D. *et al.* Influence of amorphous silica layer formation on the dissolution rate of olivine at 90 degrees C and elevated pCO(2). *Chem Geol* **284**, 193-209, doi:10.1016/j.chemgeo.2011.02.021 (2011).
62 Kurganskaya, I. & Luttge, A. A comprehensive stochastic model of phyllosilicate dissolution: Structure and kinematics of etch pits formed on muscovite basal face. *Geochim Cosmochim Ac* **120**, 545-560, doi:http://dx.doi.org/10.1016/j.gca.2013.06.038 (2013).
63 Xiao, Y. & Lasaga, A. C. Ab initio quantum mechanical studies of the kinetics and mechanisms of silicate dissolution: H+(H3O+) catalysis. *Geochim Cosmochim Ac* **58**, 5379-5400, doi:https://doi.org/10.1016/0016-7037(94)90237-2 (1994).
64 Damodaran, K., Delaye, J.-M., Kalinichev, A. G. & Gin, S. Deciphering the non-linear impact of Al on chemical durability of silicate glass. *Acta Materialia*, 117478, doi:https://doi.org/10.1016/j.actamat.2021.117478 (2021).
65 Pierce, E. *et al.* Experimental determination of the effect of the ratio of B/Al on glass dissolution along the nepheline (NaAlSiO 4)–malinkoite (NaBSiO 4) join. *Geochimica Et Cosmochimica Acta - GEOCHIM COSMOCHIM ACTA* **74**, 2634-2654, doi:10.1016/j.gca.2009.09.006 (2010).
66 Hamilton, J. P., Brantley, S. L., Pantano, C. G., Criscenti, L. J. & Kubicki, J. D. Dissolution of nepheline, jadeite and albite glasses: toward better models for aluminosilicate dissolution. *Geochim Cosmochim Ac* **65**, 3683-3702 (2001).
67 Stone-Weiss, N. *et al.* An insight into the corrosion of alkali aluminoborosilicate glasses in acidic environments. *Physical Chemistry Chemical Physics* **22**, 1881-1896, doi:10.1039/c9cp06064b (2020).
68 Hamilton, J. P., Pantano, C. G. & Brantley, S. L. Dissolution of albite glass and crystal. *Geochim Cosmochim Ac* **64**, 2603-2615 (2000).
69 Yang, Y., Min, Y. & Jun, Y.-S. A mechanistic understanding of plagioclase dissolution based on Al occupancy and T–O bond length: from geologic carbon sequestration to ambient conditions. *Physical Chemistry Chemical Physics* **15**, 18491-18501 (2013).
70 Brantley, S. L. & Olsen, A. A. in *Treatise on Geochemistry (Second Edition)* (ed Karl K. Turekian) 69-113 (Elsevier, 2014).
71 Iler, R. K. *The chemistry of silica : solubility, polymerization, colloid and surface properties, and biochemistry / Ralph K. Iler*. (Wiley, 1979).

Supplementary Information

A comparative study of the dissolution mechanisms of amorphous and crystalline feldspars at acidic pH conditions

Benjamin Cagnon[1,2], Damien Daval[1,2], Martiane Cabié[3], Damien Lemarchand[1], Stéphane Gin[4]

[1] Université de Strasbourg / CNRS / ENGEES, ITES, Strasbourg, France

[2] Univ. Grenoble Alpes, Univ. Savoie Mont Blanc, CNRS, IRD, IFSTTAR, ISTerre, Grenoble, France

[3] Aix Marseille Univ, CNRS, Centrale Marseille, FSCM, CP2M, Marseille, France

[4] CEA, DEN, DE2D, University of Montpellier, Marcoule, France

Supplementary Note 1: Fluid data

Supplementary Table III-1: Table of the results from ICP-AES for all samples of the first series, altered for 12 days. The first column to the fourth column refer to the sampling parameters with its name, the time after the beginning of the dissolution experiment, the dilution factor to use ICP-AES and the volume of solution before the sampling. The fifth, seventh and nineth columns refer to the result of ICP-AES (ppm). The sixth, eighth and tenth columns refer to the amount of Al, Na and Si in solution calculated on ICP-AES results.

Samples Name	Time (hour)	Factor of dilution	Volume of solution (ml)	Al, ICP-AES (ppm)	Al (mol)	Na, ICP-AES (ppm)	Na (mol)	Si, ICP-AES (ppm)	Si (mol)	ΔG (kJ/mol)
G1_01	0	5.08	30.7	0.007	4.04×10^{-8}	18.4	1.24×10^{-4}	32.6	1.81×10^{-4}	-75
G1_02	64	5.14	29.6	0.008	4.50×10^{-8}	19.3	1.28×10^{-4}	33.6	1.82×10^{-4}	-75
G1_03	208	5.37	27.9	0.010	5.54×10^{-8}	18.9	1.23×10^{-4}	33.0	1.76×10^{-4}	-74
G1_04	303	5.29	26.7	0.010	5.22×10^{-8}	19.0	1.17×10^{-4}	33.1	1.67×10^{-4}	-75
C1_01	0	5.49	30.6	0.005	3.11×10^{-8}	17.3	1.27×10^{-4}	30.5	1.83×10^{-4}	-76
C1_02	64	5.16	29.6	0.010	5.65×10^{-8}	18.8	1.25×10^{-4}	33.1	1.80×10^{-4}	-74
C1_03	209	5.26	28.4	0.027	1.49×10^{-7}	18.6	1.21×10^{-4}	32.7	1.74×10^{-4}	-72
C1_04	303	5.34	27.1	0.035	1.88×10^{-7}	18.0	1.13×10^{-4}	31.9	1.65×10^{-4}	-71
G3_01	0	4.94	27.8	0.008	4.06×10^{-8}	18.8	1.12×10^{-4}	34.3	1.68×10^{-4}	-36
G3_02	48	5.36	26.6	0.010	5.28×10^{-8}	18.6	1.15×10^{-4}	33.3	1.70×10^{-4}	-34
G3_03	192	5.22	25.1	0.009	4.36×10^{-8}	19.4	1.10×10^{-4}	35.0	1.64×10^{-4}	-35
G3_04	286	5.12	23.7	0.010	4.48×10^{-8}	20.1	1.06×10^{-4}	36.4	1.57×10^{-4}	-36
C3_01	0	5.04	27.6	0.009	4.65×10^{-8}	18.6	1.13×10^{-4}	33.7	1.68×10^{-4}	-36
C3_02	48	5.15	26.5	0.012	6.06×10^{-8}	18.7	1.11×10^{-4}	33.9	1.65×10^{-4}	-35
C3_03	192	5.17	24.9	0.014	6.68×10^{-8}	19.2	1.08×10^{-4}	34.4	1.58×10^{-4}	-36
C3_04	286	5.15	23.7	0.015	6.79×10^{-8}	20.1	1.07×10^{-4}	36.3	1.58×10^{-4}	-36

Supplementary Table III-2: Table of the results from ICP-AES for all samples of the second series, altered for 33 days. The first column to the fourth column refers to the sampling parameters with its name, the time after the beginning of the dissolution experiment, the dilution factor to use ICP-AES and the volume of solution before the sampling. The fifth, seventh and nineth columns refer to the result of ICP-AES (ppm). The sixth, eighth and tenth columns refer to the amount of Al, Na and Si in solution calculated on ICP-AES results.

Samples Name	Time (hour)	Factor of dilution	Volume of solution (ml)	Al, ICP-AES (ppm)	Al (mol)	Na, ICP-AES (ppm)	Na (mol)	Si, ICP-AES (ppm)	Si (mol)	ΔG (kJ/mol)
G1_01	0	4.99	35.8	0.004	2.64×10^{-8}	16.7	1.29×10^{-4}	26.7	1.70×10^{-4}	-80
G1_02	69	5.19	34.7	0.020	1.34×10^{-7}	17.0	1.37×10^{-4}	26.1	1.72×10^{-4}	-75
G1_03	238	5.21	33.4	0.038	2.50×10^{-7}	15.7	1.26×10^{-4}	25.4	1.67×10^{-4}	-73
G1_04	402	5.25	31.5	0.055	3.48×10^{-7}	15.7	1.23×10^{-4}	26.6	1.71×10^{-4}	-72
G1_05	575	5.28	30.2	0.061	3.82×10^{-7}	15.2	1.19×10^{-4}	26.3	1.68×10^{-4}	-72
G1_06	810	5.23	28.9	0.068	4.14×10^{-7}	15.8	1.21×10^{-4}	27.0	1.69×10^{-4}	-71
C1_01	0	5.12	36.0	0.005	3.42×10^{-8}	19.9	1.60×10^{-4}	27.4	1.81×10^{-4}	-78
C1_02	69	5.33	34.9	0.010	6.99×10^{-8}	19.8	1.65×10^{-4}	26.0	1.78×10^{-4}	-76
C1_03	238	5.27	33.7	0.024	1.61×10^{-7}	20.1	1.64×10^{-4}	26.5	1.78×10^{-4}	-73
C1_04	402	5.39	32.5	0.036	2.41×10^{-7}	18.7	1.56×10^{-4}	25.9	1.76×10^{-4}	-72
C1_05	575	3.95	31.1	0.074	3.51×10^{-7}	24.7	1.49×10^{-4}	35.6	1.75×10^{-4}	-71
C1_06	810	5.24	29.3	0.089	5.34×10^{-7}	17.4	1.39×10^{-4}	27.3	1.75×10^{-4}	-70
G3_01	0	5.14	33.9	0.005	3.22×10^{-8}	16.0	1.21×10^{-4}	26.3	1.64×10^{-4}	-40
G3_02	69	5.29	32.8	0.021	1.36×10^{-7}	16.1	1.25×10^{-4}	26.1	1.66×10^{-4}	-34
G3_03	238	5.31	31.6	0.024	1.54×10^{-7}	15.9	1.23×10^{-4}	26.1	1.66×10^{-4}	-34
G3_04	403	5.21	30.4	0.025	1.56×10^{-7}	15.0	1.14×10^{-4}	26.5	1.64×10^{-4}	-36
G3_05	575	5.30	28.1	0.025	1.52×10^{-7}	15.2	1.12×10^{-4}	27.5	1.65×10^{-4}	-36
G3_06	810	5.22	26.6	0.026	1.52×10^{-7}	14.0	1.02×10^{-4}	27.2	1.59×10^{-4}	-38
C3_01	0	5.08	34.1	0.005	3.20×10^{-8}	15.9	1.20E-04	26.6	1.64E-04	-40
C3_02	69	5.31	32.8	0.006	3.97×10^{-8}	16.1	1.25E-04	25.9	1.66E-04	-38
C3_03	238	5.19	31.5	0.004	2.63×10^{-8}	16.7	1.26E-04	26.8	1.66E-04	-39
C3_04	403	5.40	30.3	0.006	3.90×10^{-8}	16.3	1.26E-04	26.1	1.66E-04	-37
C3_05	575	5.27	29.1	0.007	4.36×10^{-8}	16.2	1.22E-04	26.6	1.64E-04	-38
C3_06	810	5.21	27.8	0.006	3.74×10^{-8}	16.6	1.22E-04	27.1	1.64E-04	-38

Element concentrations measured by ICP AES (See Supplementary Table III-1 and Supplementary Table III-2) were plotted as a function of time (see Supplementary Fig. 1 for Al plots). Si and Na are nearly constant in the solution, because of their elevated concentration before the onset of the experiment. Experimentally, a variation of less than 3% of the average concentration is observed, which corresponds to the experimental uncertainty.

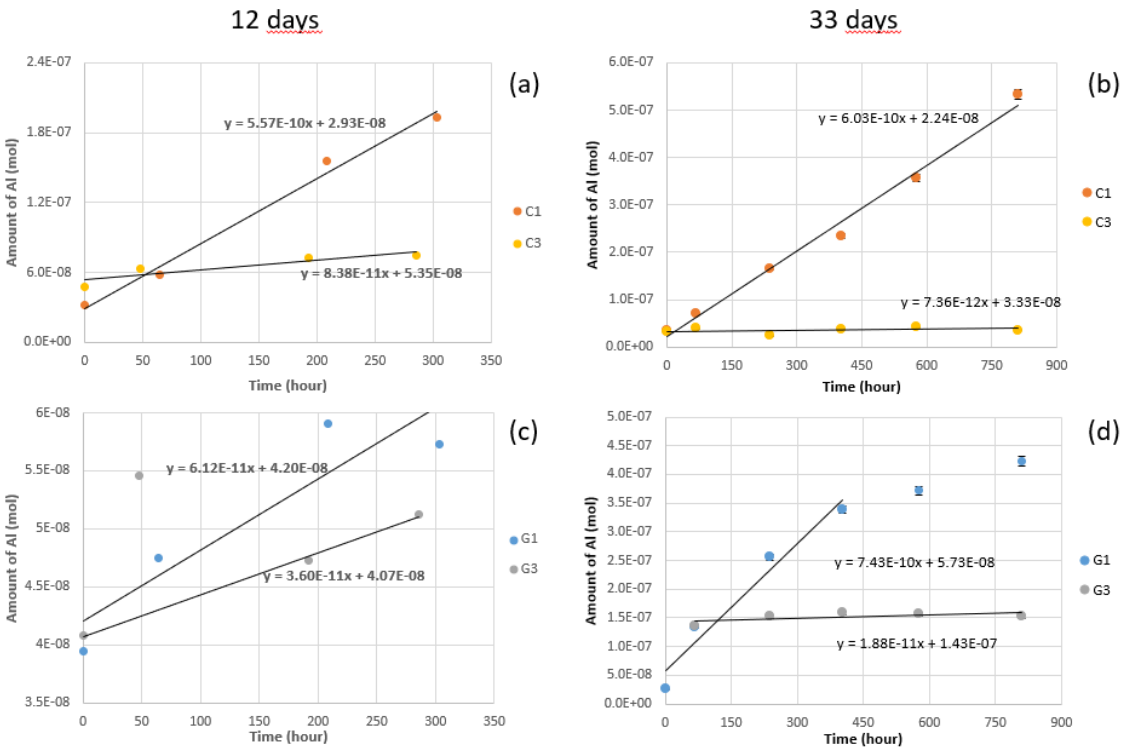

Supplementary Figure 1: *Plots depicting the evolution of the amount of Al (mol) released in the solution as a function of time (hour). G refers to the glass sample and C to the crystalline sample. 1 and 3 refer respectively to the pH 1.5 and 3. Uncertainties on the measurements are 3%. a) and c) Plots corresponding to the first experiment that lasted 12 days. The second point of G3 has been removed from the linear regression as it appears to be completely out of the regression. b) and d) Plots corresponding to the second experiment that lasted 33 days. The first point of G3 was removed from the linear regression as it is close to 0. The two last points of G1 was removed from the linear regression as they represent a drop of the dissolution rate.*

The slope of each Al curve is divided by the surface of the corresponding sample to calculate its dissolution rates (r_{disso}, mol/s/m²). The total surface (corresponding to the top surface and the adjacent surfaces in contact with the solution) of each sample was measured with an uncertainty on each measured length of 0.5 mm. The uncertainty on $h_{solution}$ is estimated to be equal to the uncertainty of the total surface (see Supplementary Table III-3).

***Supplementary Table III-3**: Top surface and total surface (top surface and adjacent surfaces in contact with the solution) are reported below. The uncertainty of the total surface was calculated assuming a measurement uncertainty of 0.5 mm. The uncertainty calculated is assumed to be the same for h_{ICP}.*

	r_{disso} (mol.m^{-2}.s^{-1})			$h_{solution}$ (nm)
	Considering Top Surface	Considering Total Surface	Uncertainties	
G1-1	1.8 x 10^{-9}	3.0 x 10^{-10}	24%	33
C1-1	9.3 x 10^{-9}	6.7 x 10^{-9}	36%	528
G3-1	1.0 x 10^{-9}	2.9 x 10^{-10}	33%	31
C3-1	1.2 x 10^{-9}	6.7 x 10^{-10}	24%	72
G1-2	1.5 x 10^{-8}			
C1-2	1.2 x 10^{-8}	1.0 x 10^{-8}	21%	1487
G3-2	8.6 x 10^{-10}	1.2 x 10^{-10}	26%	36
C3-2	1.0 x 10^{-10}			

ICP-MS analysis was also performed in order to follow the evolution of $^{29}Si/^{28}Si$ in the solution (see Supplementary Table III-4 and Supplementary Table III-5). But despite the incorporation of $^{29}Si/^{28}Si$ in the material, the evolution shown by ICP-MS remains under the uncertainties (3%).

***Supplementary Table III-4:** Table of the results from ICP-MS for all samples of the first series, altered for 12 days. The first column refers to the name of the sample and the second to the time after the beginning of the dissolution experiment. The third and fourth columns refer to the result of ICP-MS. The fifth is the ratio of $^{29}Si/^{28}Si$ in the solution, also calculated in percentage in column six.*

Samples Name	Time (hour)	Signal cps ^{28}Si	Signal cps ^{29}Si	$^{29}Si/^{28}Si$	$\%^{29}Si$
G1_01	0	3795733	5370053	1.41	0.59
G1_02	64	3860154	5470596	1.42	0.59
G1_03	208	4010823	5716953	1.43	0.59
G1_04	303	3900870	5507803	1.41	0.59
C1_01	0	3686282	5067359	1.37	0.58
C1_02	64	4059850	5616842	1.38	0.58
C1_03	209	4101721	5618737	1.37	0.58
C1_04	303	3932224	5368476	1.37	0.58
G3_01	0	4021747	5583554	1.39	0.58
G3_02	48	4100185	5520166	1.35	0.57
G3_03	192	4204516	5652827	1.34	0.57
G3_04	286	3803132	4871558	1.28	0.56
C3_01	0	4180243	5563381	1.33	0.57
C3_02	48	4147522	5235962	1.26	0.56
C3_03	192	4328747	5399074	1.25	0.56
C3_04	286	4601077	5730315	1.25	0.55

Supplementary Table III-5: *Table of the results from ICP-MS for all samples of the second series, altered for 33 days. The first column refers to the name of the sample and the second to the time after the beginning of the dissolution experiment. The third and fourth columns refer to the result of ICP-MS. The fifth is the ratio of $^{29}Si/^{28}Si$ in the solution, also calculated in percentage in column six.*

Samples Name	Time (hour)	^{28}Si (ppm)	^{29}Si (ppm)	$^{29}Si/^{28}Si$	$\%^{29}Si$
G1_01	0	1.2207	1.3980	1.11	0.53
G1_02	69	1.2235	1.3964	1.10	0.53
G1_03	238	1.2158	1.3821	1.10	0.53
G1_04	402	1.2398	1.4094	1.10	0.53
G1_05	575	1.2802	1.4493	1.09	0.53
G1_06	810	1.3898	1.5665	1.09	0.53
C1_01	0	1.1017	1.2612	1.11	0.53
C1_02	69	1.1716	1.3409	1.11	0.53
C1_03	238	1.2222	1.3896	1.10	0.53
C1_04	402	1.2167	1.3738	1.09	0.53
C1_05	575	1.6656	1.8835	1.09	0.53
C1_06	810	1.3029	1.4609	1.08	0.53
G3_01	0	1.2543	1.4290	1.10	0.53
G3_02	69	1.2306	1.3982	1.10	0.53
G3_03	238	1.2500	1.4195	1.10	0.53
G3_04	403	1.2726	1.4439	1.10	0.53
G3_05	575	1.3212	1.5013	1.10	0.53
G3_06	810	1.3765	1.5596	1.09	0.53
C3_01	0	1.2740	1.4537	1.10	0.53
C3_02	69	1.2892	1.4666	1.10	0.53
C3_03	238	1.3264	1.5075	1.10	0.53
C3_04	403	1.2810	1.4544	1.10	0.53
C3_05	575	1.3137	1.4900	1.10	0.53
C3_06	810	1.3517	1.5299	1.09	0.53

Supplementary Note 2: Surface characterization of crystal sample

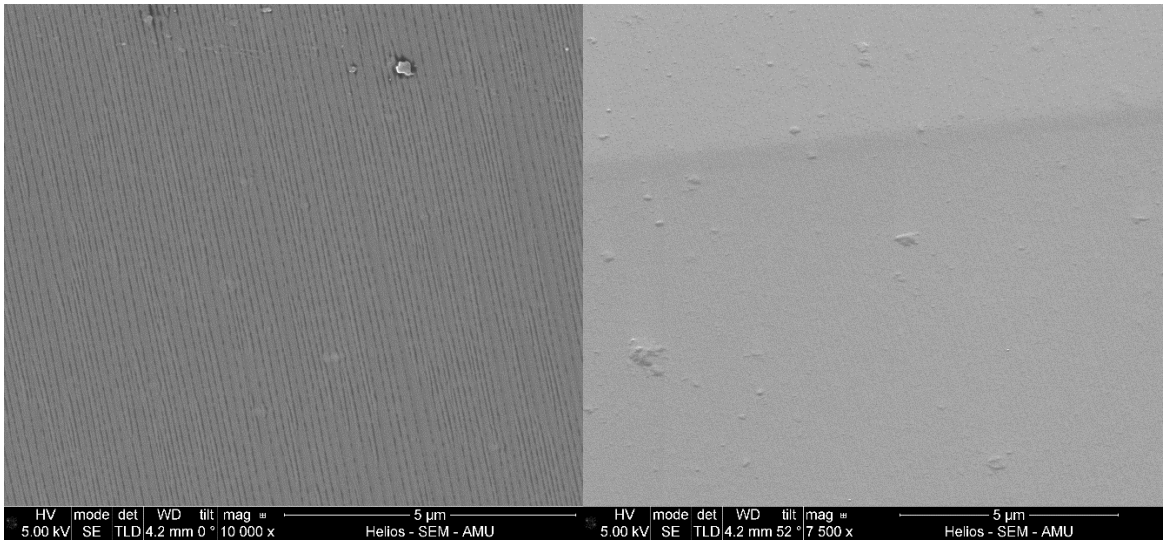

Supplementary Figure 2: *Pictures of striations by SEM on the top surface of crystalline sample altered at pH 1.5 after 33 days (sample C1-2) resulting from the alternation of Ca-rich and Na-rich lamellae dissolution.*

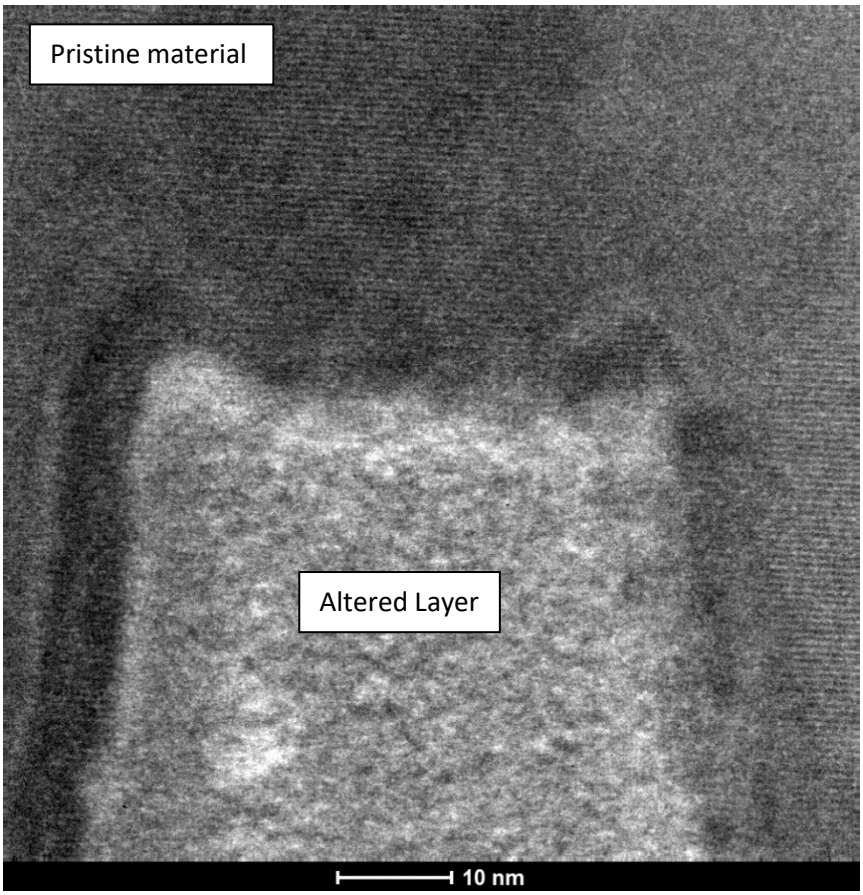

Supplementary Figure 3: *High resolution TEM images showing the interface between altered layer (light grey) and the pristine material (dark grey) of a crystalline sample (C1-2). The distance inter-reticular is around 6.6 Å indicating a (010) face.*

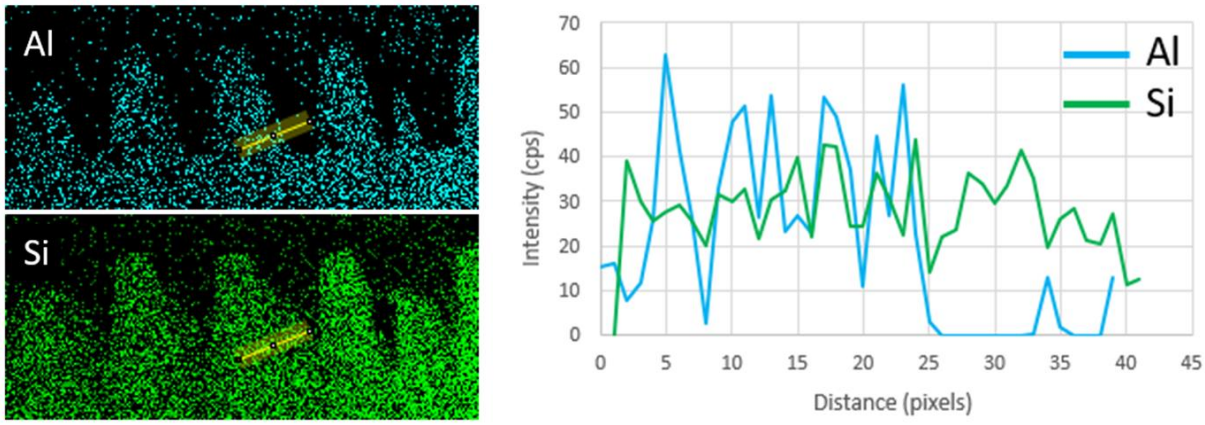

Supplementary Figure 4: *STEM-EDX spectra at the Al K edge and Si K edge of the crystalline sample altered at pH 1.5 during 12 33days are displayed. Al and Si profiles are collected following the yellow line, 10 pixels wide and tilted at 23°, resulting in the graph presented.*

Supplementary Note 3: Deconvolution of the ToF-SIMS signal

The ToF-SIMS operates as cycles of surface abrasion and analysis. The resulting signal thus depends on the surface topography and on the instrumental resolution. Because of the poor lateral resolution of Tof-SIMS analyses, the depth profiles are artificially broadened. To estimate the actual shape of the $^{29}Si/^{28}Si$ depth profile on each sample, the actual Al/Si profiles were collected in cross-section by TEM measurements performed on FIB thin sections. Such profiles were convoluted with a Gaussian function (see below) that accounts for the broadening due to roughness of the sample and/or the instrumental resolution. Once the parameters describing the Gaussian function were determined, they were used to deconvolute the $^{29}Si/^{28}Si$ depth profiles obtained by Tof-SIMS and estimate the actual $^{29}Si/^{28}Si$ depth profiles within the altered layer. In turn, this treatment allowed us to calculate the average contribution of the fluid to the Si composition of the surface altered layer.

A. Deconvolution of the profiles collected on the altered glass samples

At first, we assumed that the Al/Si profile measured in cross-section by TEM on FIB thin sections correspond to the actual Al/Si profile within the altered layer [1]:

$$Al/Si\ (k)_{real} = Al/Si\ (k)_{TEM} \quad \text{(A1)}$$

where $Al/Si\ (k)_{real}$ is the actual Al/Si ratio at depth *k* from the surface of the sample. For the sake of simplicity, *k* is an integer that corresponds to the number of abrasion cycles. Therefore, the depth profile is defined with a vertical resolution corresponding to the abrasion depth of one cycle. In addition, note that all ratios were normalized to the Al/Si ratio in the bulk glass, so that $Al/Si\ (k)_{real}$ varies between 0 and 1. The same treatment was applied to the ratio measured by Tof-SIMS, to circumvent the fact that ionization yields can differ between the altered and pristine glass.

It was then assumed that this function was convoluted with another function responsible for the broadening of the signal, resulting in an apparent Al/Si profile ($Al/Si\ (k)_{app}$) calculated as follow:

$$Al/Si\ (k)_{app} = \frac{\sum_{i=\mu-k}^{2\mu-k} Al/Si\ (i-(\mu-k))_{real} \times G(i)}{\sum_{i=\mu-k}^{2\mu-k} G(i)} \quad \text{(A2)}$$

where μ is the expected value of the Gaussian function $G(i)$:

$$G(i) = \frac{1}{\sigma\sqrt{2\pi}} exp\left(\frac{-(i-\mu)^2}{2\sigma}\right) \quad \text{(A3)}$$

where σ^2 is the variance. The value of σ and μ were determined by fitting the modelled curve to the measured profile. The best values of σ and μ were determined through the minimization of the following parameter:

$$RMS = \sqrt{\frac{1}{N}\sum_{k=1}^{N}\left(\left(Al/Si\ (k)_{app}\right) - \ (Al/Si\ (k)_{meas})\right)^2} \qquad \text{(A4)}$$

where *RMS* is the root-mean-square and *N* is the number of measured Al/^{28}Si ratios. The $Al/Si\ (k)_{meas}$ ratio corresponds to the signal of Al/^{28}Si measured by the ToF-SIMS normalized to 1 in the bulk glass (see above). The value of μ is high enough so that equation (A2) can be applied to the whole depth profile. After fitting the values of μ and σ^2 to minimize the discrepancies between the $Al/Si\ (k)_{app}$ and $Al/Si\ (k)_{meas}$ ratios, the parameters of the Gaussian function, μ and σ^2, were kept constant to process the ^{29}Si/^{28}Si profile.

In order to back-calculate $\frac{^{29}Si}{^{28}Si}(k)_{real}$, a numerical code was developed. It consisted in generating *N* $\frac{^{29}Si}{^{28}Si}(k)$ random values that must observe the following relation: $\frac{^{29}Si}{^{28}Si}(k) > \frac{^{29}Si}{^{28}Si}(k+1)$, with $\frac{^{29}Si}{^{28}Si}_{fluid} \geq \frac{^{29}Si}{^{28}Si}(k=1) \geq \frac{^{29}Si}{^{28}Si}_{glass}$ (as opposed to elementary ratios, isotopic ratios measured with Tof-SIMS are quantitative (the ionization yield of ^{28}Si being the same as that of ^{29}Si), so that it was not necessary to normalize the isotopic ratios to their values in the bulk glass). The series of $\frac{^{29}Si}{^{28}Si}(k)$ values were then convoluted to the Gaussian function determined from the treatment of the Al/Si data described above. The difference between the $\frac{^{29}Si}{^{28}Si}(k)$ values generated numerically ($\frac{^{29}Si}{^{28}Si}(k)_{num}$) and those measured with Tof-SIMS ($\frac{^{29}Si}{^{28}Si}(k)_{meas}$) was calculated following:

$$RMS = \sqrt{\frac{1}{N}\sum_{k=1}^{N}\left(\left(^{29}Si/^{28}Si\ (k)_{num}\right) - \ \left(^{29}Si/^{28}Si\ (k)_{meas}\right)\right)^2} \qquad \text{(A5)}$$

Several hundreds of thousands of $\frac{^{29}Si}{^{28}Si}(k)_{num}$ series were generated, and the ten profiles corresponding to the 10 lowest RMS were stored. Those ten profiles were assumed to be close to the real depth profile of $\frac{^{29}Si}{^{28}Si}$.

Finally, knowing the actual $\frac{^{29}Si}{^{28}Si}$ ratios in the glass sample and in the solution, the respective contribution of the glass and the fluid to the Si content in the altered layer was then calculated as followed:

$$x(k) \times \frac{^{29}Si}{^{28}Si}(k)_{solution} + (1 - x(k)) \times \frac{^{29}Si}{^{28}Si}(k)_{material} = \frac{^{29}Si}{^{28}Si}(k)_{real}, \forall k \qquad \text{(A6)}$$

where x is the contribution of Si from the solution and, consequently, $(1-x)$ the contribution from the glass.

Finally, the average contribution of the fluid to the composition of the altered layer was then estimated as follows:

$$\bar{x} = \frac{\sum_{i=0}^{k_{step}} x(i)}{k_{step}} \quad \text{(A7)}$$

where k_{step} corresponds to the cycle at which the pristine glass is reached, which is estimated based on the thickness of the altered layer measured by TEM.

B. Deconvolution of the profiles collected on the altered crystalline samples

Consistent with our TEM observations on altered crystalline samples, the real Al/Si profile across the altered layer/crystal interface is close to a step-like function, so that $Al/Si\ (k)_{real}$ can be approximated following:

$$Al/Si\ (k)_{real} = \begin{cases} 0, \forall k \in [0, k_{step}] \\ 1, \ \forall k > k_{step} \end{cases} \quad \text{(A8)}$$

As opposed to the glass sample, the roughness of the altered crystal is not homogenous and observes a specific periodic pattern, resulting from the presence of Na-rich and Ca-rich domains elongated following the [001] axis. As a consequence, we developed a geometric model to account for the impact of the roughness observed at the surface of the altered crystals on the profiles measured with Tof-SIMS.

The surface roughness of the crystal sample at pH 1.5 after 33 days of alteration is presented in Supplementary Fig. 5. For each crenel, the interface between the altered layer and the solution varies from horizontal ($\vartheta 3$ = 90°, right hand side of Supplementary Fig. 5) to almost vertical ($\vartheta 1$ = 132°). Thus, a zone defined by three adjacent crenels was chosen because the angle between the [001] axis and the surface altered layer (132°, 117°, 90°) are representative of the whole surface. This specific geometry was then implemented in the procedure described above (see A.) to account for the surface roughness during each cycle of the ToF-SIMS.

The ratio between the crystalline surface and the altered layer surface is the key point of the broadening effect of the roughness. Indeed, during the first abrasion, not only the elements from the altered layer are measured by the ToF-SIMS, but elements from the pristine crystal are measured as well. This ratio is calculated using the following equation:

$$\frac{Lc(k)}{Lc(k)+Lx(k)} \times \%Al/Si_{alt.layer} + \frac{Lx(k)}{Lc(k)+Lx(k)} \times \%Al/Si_{pristine\ material} = Al/Si_{mod} \quad \text{(A9a)}$$

where Lc(k) and $Lx(k)$ are respectively the total contribution of the altered layer and pristine material abraded at the *k*-th cycle by ToF-SIMS. The parameter $\%Al/Si_{alt.layer}$ represents the normalized Al/Si

ratio present in the altered layer and $\%Al/Si_{pristine\ material}$ the normalized Al/Si ratio in the pristine material. Since the Al/Si_{real} profile is assumed to be a step-like function (see Results), one can write:

$$\begin{cases} \%Al/Si_{alt.layer} = 0 \\ \%Al/Si_{pristine\ material} = 1 \end{cases}$$

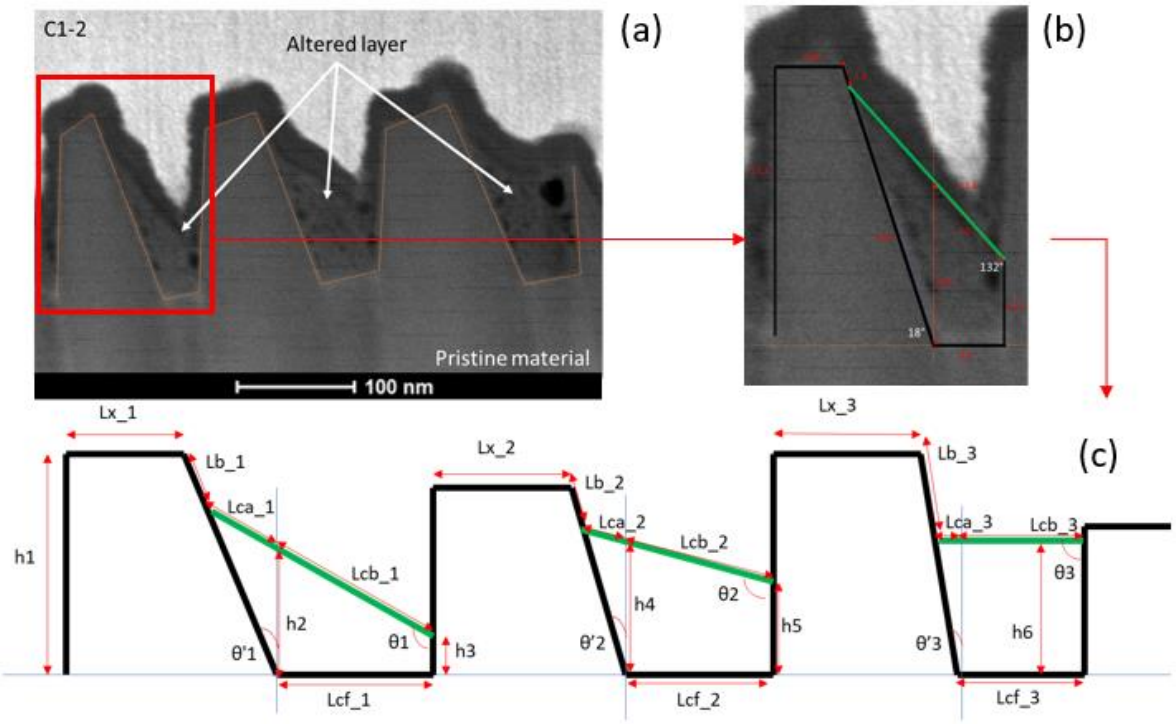

Supplementary Figure 5*: TEM images of the interface (seen in cross section) showing its roughness and the schematic model used to account for this topography. (a) Those three crenels were considering as representative of the whole surface roughness (b) the first one is taken as an example of the geometry model. Each length has been measured prior to develop the geometrical model. (c) This model was used to estimate the ratio of crystal and altered layer analyzed after each ToF-SIMS abrasion cycle.*

As a consequence, the equation (A9a) can be simplified following:

$$\frac{Lx(k)}{Lc(k)+Lx(k)} = Al/Si_{mod} \qquad \text{(A9b)}$$

At the first cycle (z = 0 nm), the configuration of the interface corresponds to the pattern shown in Supplementary Fig. 5b. After each cycle of abrasion, the new surface configuration is generated iteratively. Each new surface configuration is labelled at a depth of $z_{k+1} = z_k + z_{cycle}$ nm, where z_k refers to the depth in the pristine glass and z_{cycle} refers to the thickness of materials abraded by ToF-SIMS at each cycle. In addition, it was assumed that the abrasion was deeper in the altered layer due to its porosity. From Supplementary Fig. 5a, the porosity (Φ) was estimated to be around 12%, and the thickness of the altered layer abraded at each cycle is then calculated as $z'_{cycle} = \frac{z_{cycle}}{1-\Phi}$ nm.

Below, we detail the main equations that control the surface configuration at each cycle for the crenel shown in Fig. 1b. Similar equations are applied to describe the abrasion of the second and third crenels. The set of equation to determine the *k*+1-th surface configuration of the crenel schematized in Supplementary Fig. 5b is as follows:

$$\begin{cases} h2_{k+1} = h2_k - z'_{cycle} \\ h3_{k+1} = h3_k - z'_{cycle} \end{cases}$$

$$\begin{cases} Lca\_1_{k+1} = Lca\_1_k \times \dfrac{h2_{k+1}}{h2_k} \\ Lcb\_1_{k+1} = Lcb\_1_k \\ Lc\_1_{k+1} = Lca\_1_{k+1} + Lcb\_1_{k+1} \end{cases}$$

$$Lcf\_1_{k+1} = Lcf\_1_k$$

$$Lx\_1_{k+1} = Lx\_1_k + z_{cycle} \times \tan(\theta' 1)$$

$$Lb\_1_{k+1} = Lb\_1_k + \sqrt{z'^2_{cycle} + (Lca\_1_k - Lca\_1_{k+1})^2 - 2\, z'_{cycle}(Lca_{1_k} - Lca_{1_{k+1}})\cos(\theta 1)} - \frac{z_{cycle}}{\cos(\theta' 1)}$$

Note that all parameters in the above equations are reported in Supplementary Fig. 5. This set of equation is valid as long as $h3 > 0$. When this condition is no longer observed, a few changes occur, and the set of equation then becomes:

$$h2_{k+1} = h2_k - z'_{cycle}$$

$$Lc\_1_{k+1} = Lc\_1_k \times \frac{h2_{k+1}}{h2_k}$$

$$Lcf\_1_{k+1} = Lcf\_1_k \times \frac{Lc\_1_{k+1}}{Lc\_1_k}$$

$$Lx\_1_{k+1} = Lx\_1_k + z_{cycle} \times \tan(\theta' 1) + (Lcf\_1_k - Lcf\_1_{k+1})$$

$$Lb\_1_{k+1} = Lb\_1_k + \sqrt{z'^2_{cycle} + (Lca\_1_k - Lca\_1_{k+1})^2 - 2\, z'_{cycle}(Lca_{1_k} - Lca_{1_{k+1}})\cos(\theta 1)} - \frac{z_{cycle}}{\cos(\theta' 1)}$$

This set of equation is valid as long as $h2 > 0$. When this condition is no longer observed, the altered layer is completely abraded.

As illustrated in equation (A9b), the total surface of the altered layer ($Lc(k)$) and of the pristine crystal ($Lx(k)$) at each *k*-th cycle are required to model the abrasion. It comes that, at each cycle, such quantities can be expressed following:

$$\begin{cases} Lc(k) = Lc\_1_k + Lc\_2_k + Lc\_3_k \\ Lx(k) = (Lx\_1_k + Lb\_1_k) + (Lx\_2_k + Lb\_2_k) + (Lx\_3_k + Lb\_3_k) \end{cases}$$

The profile generated following this treatment is then convoluted to a Gaussian function, and the next step of the treatment are identical to those described for the altered glass samples (See Equations (A2) to (A7)).

Supplementary references

1 Hellmann, R., Penisson, J.-M., Hervig, R. L., Thomassin, J.-H. & Abrioux, M.-F. An EFTEM/HRTEM high-resolution study of the near surface of labradorite feldspar altered at acid pH: evidence for interfacial dissolution-reprecipitation. *Phys Chem Miner* **30**, 192-197 (2003).

Chapitre IV. IMPACT OF CALCIUM ON ISG ALTERATION IN ALKALINE CONDITIONS AT 90°C: MECHANISM OF FORMATION AND TRANSPORT PROPERTIES OF THE GEL LAYER

Le précédent chapitre a mis en lumière l'impact de l'ordre à longue de la structure des silicates sur les mécanismes de formation du gel, soit donc une propriété intrinsèque du matériau. Comme rappelé en introduction, des paramètres extrinsèques, tels que la composition chimique de la solution, peuvent également impacter de tels mécanismes. Dans le présent chapitre, la dissolution de l'International Simple Glass (ISG) a été étudiée à 90 °C en conditions basiques pendant 21 jours, dans une solution à 51% de saturation par rapport à la silice amorphe et avec des concentrations de Ca variant de 0 à 240 ppm. La solution a été marquée avec ^{29}Si et ^{18}O. Les signatures isotopiques du gel analysées par ToF-SIMS ont permis de conclure que les atomes d'oxygène présents dans le gel proviennent principalement de la solution, tandis que le Si provient presque exclusivement de l'ISG. Une forte corrélation a été trouvée entre la concentration initiale de calcium et l'épaisseur du gel, suggérant soit la formation d'une couche passivante riche en Si et Ca, soit un effet catalytique du Ca sur la densification du gel, ou une combinaison de ces deux possibilités. Une expérience de traçage utilisant du ^{10}B et le bleu de méthylène, à température ambiante, a été réalisée sur les échantillons d'ISG après leur altération afin d'étudier la diffusivité des espèces au sein du gel. Les coefficients de diffusion calculés en fonction de l'expérience de traçage et de l'épaisseur de la couche de gel ont été comparés. Plusieurs divergences ont été mises en évidence et discutées dont la plus importante peut être expliquée par la différence de température entre les expériences d'altération (90 °C) et de traçage (25 °C). Enfin, l'incorporation similaire de ^{10}B et de S^- (bleu de méthylène) suggère que les propriétés de transport du gel ne sont pas limitées par la taille des pores et des canaux de diffusion.

Le chapitre IV fait l'objet d'un manuscrit en préparation pour la revue Journal of Nuclear Materials : "Cagnon, B., Gin, S., Cabié, M. & Daval, D. (in prep.). Impact of calcium on ISG alteration in alkaline conditions at 90°C: Mechanism of formation and transport properties of the gel layer."

Impact of calcium on ISG alteration in alkaline conditions at 90°C: Mechanism of formation and transport properties of the gel layer

Benjamin Cagnon[1], Stéphane Gin[2], Martiane Cabié[3], and Damien Daval[1]

[1] Univ. Grenoble Alpes, Univ. Savoie Mont Blanc, CNRS, IRD, IFSTTAR, ISTerre, Grenoble, France

[2] CEA, DES, DPME, SEME, University of Montpellier, Marcoule, France

[3] Aix Marseille Univ, CNRS, Centrale Marseille, FSCM, CP2M, Marseille, France

Correspondence : B. Cagnon (benjamin.cagnon@univ-grenoble-alpes.fr)

ABSTRACT

The dissolution of International Simple Glass (ISG) was investigated at 90°C and alkaline condition, for 21 days, with a concentration of dissolved silica corresponding to 51% of the saturation with respect to amorphous silica and concentrations of Ca ranging from 0 to 240 ppm. The solution was labelled with ^{29}Si and ^{18}O. Based on the isotopic signatures of the gel layer analyzed using ToF-SIMS, it was concluded that oxygen atoms mostly originate from the solution for all investigated conditions, while Si almost exclusively originate from ISG. A strong correlation was found between the initial concentration of calcium and the gel layer thickness, suggesting either the formation of a passivating (Si, Ca)-rich layer, a catalytic effect of Ca on the gel densification or a combination of both. A tracer experiment using ^{10}B and methylene blue as tracers were performed after alteration on samples at room temperature to study the diffusivity of the alteration gel layer. Diffusion coefficients calculated based on the tracer experiment and the gel layer thickness were compared. Several discrepancies were highlighted and critically discussed with the major one being explained by the difference of temperature between alteration and tracer experiments. Finally, the similar incorporation of ^{10}B and S^- (methylene blue) suggested that the transport properties of the gel was not limited by the size of pores and diffusion channels.

IV.1. INTRODUCTION

The aqueous reactivity of silicates is a subject of interest in various fields such as the biogeochemical cycle of elements [1], carbon dioxide sequestration [2] as well as vitrified nuclear waste disposal [3-5]. In the latter case, the resistance of glass with respect to aqueous corrosion is the ultimate step of the multi-barrier concept that controls the performance of the geological repository over timescales extending up to several thousands of years. In contact with water, the silicate matrix of the borosilicate glass is depolymerized via the hydrolysis of its network former's elements [6]. Simultaneously, backward reactions, called recondensation, occur. This process results in the formation of a porous and hydrated layer, often referred to as gel layer [7,8].

The gel layer formed at the surface of the glass is a key process in the understanding of glass dissolution kinetics [7,9-12]. Once the gel starts to form, the glass dissolution rate can drop by several orders of magnitude [13]. This decrease results from the transport-limiting properties of the growing gel layer [10,14,15] and the reduced affinity of the dissolution reaction with respect to the pristine material [16,17]. The gel layer's porosity, thickness and the transport properties of various species through this layer greatly impact the dissolution rate of the glass [18]. Two reactions control the thickness of the gel layer: the alteration at the interface with the pristine material that maintains the growth of the gel layer on the one hand, and a dissolution reaction that may occur at the interface with the solution on the other hand. Due to both reactions, the concentration of glass elements increases in solution. When/if a steady state is achieved, the thickness of the gel layer remains constant.

However, the gel layer formation should be considered as a dynamic process that may evolve over time [15,19]. Its stability can be ensured by an *in situ* reorganization of its structure and the condensation of silanol groups into siloxane bonds [20,21]. This densification of the gel leads to the closure of the pores and a decrease in the transport properties of the surface layer [18]. Overall, the passivation properties of the gel layer may therefore spontaneously evolve. Additionally, the precipitation of secondary phases such as (alumino)phyllosilicate or zeolites on the surface of the gel layer can form an additional protective coating. Under certain conditions, the low porosity and high density of this coating may prevent the exchange of species between the solution and the glass [22]. Conversely, other precipitates such as calcium silicate hydrates (CSH) destabilize the gel layer by consuming the silica in solution and increasing the affinity at the interface between the gel layer and the solution [23-26]. The precipitation of such secondary phases can in turn trigger the resumption of the glass alteration [27-29].

The composition of the pristine glass is another parameter that can greatly influence its dissolution mechanisms and rate [30]. Through 14-year long alteration experiments of 10 simple sodium borosilicate glasses containing various elements, and that of the 30-oxide nuclear glass SON68, in pure

water at 90°C, Gin et al., 2012 [30] highlighted strong correlations between the glass composition and the dissolution rates. As an example, glasses containing Al, Ca and Zr (referred to as CJ2 and CJ7 in their study) exhibited a lower dissolution rate due to the incorporation of those element in the gel layer [12]. Conversely, the passivation properties of Ca for CJ8 only lasted 90 days before secondary phases precipitated and destabilized the gel layer, leading to a resumption of the alteration and the complete dissolution of CJ8.

Finally, the passivating properties of the gel layer are strongly correlated with the various elements composing the chemical environment. Regarding the solution, Collin et al., 2018 [8] investigated the influence of exogenous alkaline ions such as Li^+, Na^+, K^+ and Cs^+ on the formation and passivation properties of the gel layer of the International Simple Glass (ISG) [31]. The authors observed little to no effect of Li^+ and Na^+ on the alteration kinetics. However, the presence of K^+ and Cs^+ decreases the alteration rate by incorporating those elements in the gel layer. These alkalis replaced the Ca in the gel layer structure as the new charge compensation for aluminum and this exchange greatly affected the total quantity of water within the gel layer, providing another explanation for the decrease in glass dissolution. The impact of alkaline earth cations has also been studied. For example, Mercado-Depierre et al., 2013 [23] focused on the antagonist effect of calcium on the passivating properties of the gel layer according to the pH and the SA/V ratio. On one hand, calcium can form complex bonds with Si atoms at the interface between the gel layer and the solution, resulting in weakened and more hydrolysable Si – O bonds [32,33]. On the other hand, Ca can be absorbed in the gel layer resulting in an increase in the retention of the glass constitutive elements. The ionic species transportation through the gel layer decreases and the dissolution rate drops [34]. Furthermore, calcium can act synergistically with silica and form a (Si, Ca)-rich passivating layer. As such, Ca actively participates in the densification of the gel layer as a catalyst [35]. The presence of other elements with low solubility such as Zr and Al can also increase the passivating properties of this (Si, Ca)-rich layer [36]. However, the impact of calcium on the diffusivity of the gel has yet to be quantify, especially in basic condition and in presence of various secondary phases, such as amorphous silica, CSH and calcium carbonate.

In this study, five ISG coupons were altered at 90°C, pH 10.3 for 21 days. The initial concentration of aqueous silica in solution was around 51% on average of the equilibrium value with respect to amorphous silica, and the initial concentration of calcium increased from 0 ppm to 240 ppm over 5 distinct experiments. The altering solution was labelled with ^{18}O ($^{18}O/^{16}O$ = 0.035) and ^{29}Si ($^{29}Si/^{28}Si$ = 0.74) to investigate the gel layer formation mechanism based on the potential incorporation of those elements in the gel structure. Additionally, the role of calcium on the passivation properties of the gel layer was tackled. After alteration at 90 °C, the coupons were recovered and immersed in a

solution to probe the incorporation of ^{10}B and S^- in order to provide insight on the gel layer diffusivity. The results were then compared with the diffusion coefficient calculated based on the total gel layer thickness. Taken together, these characterizations were used to discuss the mechanisms and transport properties of the gel layer in the first 21 days of alteration. Finally, knowledge gained from the various methods used in this study was critically discussed.

IV.2. MATERIAL AND METHODS

IV.2.1. Sample preparation

The ISG glass coupons (wt% 56.2 SiO_2, 17.3 B_2O_3, 12.2 Na_2O, 6.1 Al_2O_3, 5.0 CaO, 3.3 ZrO_2) measuring 2 x 2 x 0.1cm^3 were obtained from CEA Marcoule, France. These coupons were polished by PrimeVerre, Montpellier, France, on all 6 faces using a 1/4 µm diamond grain paste in the final step. The specific ISG starting material used in this work, denoted as ISG-1, was elaborated according to the conditions outlined in Ryan et al., 2022 [37]. On each corner, top and bottom surfaces of ISG samples, a small part (<1 mm², on average <5% of the polished surface) was protected with room-temperature-vulcanizing (RTV) glue spots to create a non-reacted reference surface used for subsequent topography analyses run with vertical scanning interferometry (VSI; Zygo NewView 7300). Those topography data were investigated alongside other series in Chapter 5.

The experiments were conducted in alkaline solutions with increasing concentrations of Ca from experiments hereafter referred to as H0 to H4, and a constant concentration of Si (see Table IV-1). On average, the total Si concentration in solution was brought to 51% of the equilibrium value with respect to amorphous silica (SiO_2(am)) using nanopowder silica (specific surface area 175 – 225 $m^2.g^{-1}$, 99.8% trace metals basis) and $^{29}SiO_2$(am) powder (Eurisotop, 99.35% purity of ^{29}Si), so that the $^{29}Si/^{28}Si$ ratio in solution of 0.74 ± 0.01. The solution was also labelled with ^{18}O (Eurisotop, 99.7% purity of ^{18}O) in a $^{18}O/^{16}O$ ratio of 0.035. The pH was measured at high temperature (90°C) and adjusted to 10.3 by addition of LiOH (Prolabo) on a daily basis. Once the solution reached stability (within approximately 10 days), the CO_2 in the solution was removed through degassing with N_2 (0.15 $L.min^{-1}$) at high temperature (near water ebullition, T > 90°C) during 30 min for 500 mL of solution. PFA Savillex® vessels, containing a Teflon basket, were filled with approximately 35 mL of solution and placed in a N_2 atmosphere-controlled glove box. The appropriate amount of Ca was added to H0, H1 and H2 reactor by sampling 1 mL or 2 mL aliquots from a stock solution prepared with dissolved $CaCl_2$. H3 and H4 reactors were 100% spiked with calcium carbonate powder in the form of $^{44}CaCO_3$ (Eurisotop, 99.2% purity of ^{44}Ca) to test the source of Ca in the gel layer and/or secondary precipitates. After the addition of calcium, each reactor was placed in an oven at 90°C for a duration of 24 h as the chemical composition has been shown in our previous study to evolve spontaneously over the first day of

solution preparation. The initial sample of solution was collected right before the addition of the ISG coupon. Each reactor was then placed in the oven at 90°C and the solutions were continuously stirred with magnetic bars. The collected aqueous sample was filtered using a 0.45 µm pore size filter before dilution.

Table IV-1 : Summary of the initial conditions for the series H. The first column refers to the name of the experiment. The second, third and fourth columns refer to the $SiO_2(aq)/SiO_2(aq)_{eq}$ ratio (which is the saturation state of the solution with respect to amorphous silica) measured by ICP-OES, the $^{29}Si/^{28}Si$ ratio, measured by ICP-MS, and the concentration of Ca (ppm) in the solution, respectively. Note that the concentration of Ca reported with (*) is the theoretical value based on weighing, as the ICP-OES analyses failed for the corresponding sample.

Name	Si/Si_{eq}	$^{29}Si/^{28}Si$	Ca(ppm)
H0	35%	73%	2.50
H1	54%	73%	1.72
H2	55%	75%	73.91
H3	57%	76%	117.26
H4	56%	75%	240*

After introducing the glass sample into the reactors filled with the prepared solution, the reactors were placed back in the oven at 90°C, which corresponded to the onset of the experiments. Following a 13-day period, each reactor was moved to the glove box to collect a second aqueous sample. At the experiment's conclusion, all reactors were transferred to the glove box to collect both the solutions and the ISG coupons.

ISG coupons were then dipped three seconds in ultrapure water (18.2 MOhm.cm) before being dipped in ethanol for three seconds. They were dried and stored in the glove box at room temperature until being cut into smaller pieces using a diamond saw in order to perform various surface analyses. A third and last sampling of the solution was performed at the conclusion of the experiments.

IV.2.2. ICP-OES analyses of aqueous solution

The progress of the dissolution process was monitored by extracting 2 mL of the solution at the experiment's onset, after 13 days of reaction, and at its conclusion. Subsequently, the samples underwent filtration, followed by 5x, 150x, and 1500x dilutions. Analysis was performed using an Inductively Coupled Plasma Optical Emission Spectrometer (ICP-OES) (Varian 720-ES) to measure the concentrations of B, Si, and Ca. The concentration of B was then used to determine the position of the 'internal interface,' which represents the boundary between the gel layer and the pristine glass, as detailed in Wild et al., 2016 [38]. Of note, the pH was adjusted to 10.3 initially and did not evolve during the experiment.

The equivalent thickness of altered glass, $Eth(B)$ (mm), was calculated as follows:

$$Eth(B) = \frac{[B]_t \times F_t \times V_t}{SA \times \rho \times x(B)} \quad \text{(Eq. IV-1)}$$

where $[B]_t$ is the B concentrations (ppm) at time t measured by ICP-OES, F_t is the dilution factor of the aqueous sample collected at time t, V_t is the volume (L) of the solution in the reactor just before collection, SA is the glass sample surface area (mm²), ρ is the specific volume of ISG glass ($\rho = 2.498\ \mathrm{mg.mm^{-3}}$) and $x(B)$ is the mass proportion of B in ISG ($x(B) = 0.0537$). *Eth*(i) is equal to the gel layer thickness assuming the alteration is isovolumetric.

Based on $Eth(B)$ calculated between two different samplings, the corresponding dissolution rates, $r\_disso(B)$ ($g.m^{-2}.d^{-1}$), were calculated following:

$$r\_disso(B) = \frac{\Delta Eth(B) \times \rho}{\Delta t} \quad \text{(Eq. IV-2)}$$

IV.2.3. Solid characterizations

IV.2.3.1. FIB-TEM analyses

Scanning electron microscopy examinations were carried out using a FEI Helios 600 Nanolab dual beam at CP2M (Marseille, France). The reacted glass samples underwent carbon coating, and ultrathin electron-transparent cross-sections were then prepared with focused ion beam (FIB) milling, using the FEI Helios 600 Nanolab dual-beam at CP2M (Marseille, France), following methods previously outlined by Daval et al. [39]. In summary, FIB Ga+ ion milling was conducted at an ion beam voltage of 30 kV, with beam currents varying from 9 nA to 90 pA in the final stages. Micrometer-thick sections were gently lifted out in situ using an Omniprobe 200 micromanipulator and subsequently transferred to a half copper grid for the final ion milling process to achieve electron transparency, resulting in a final thickness of approximately 100 nm. This milling procedure was executed at a reduced acceleration voltage of 5 kV to mitigate beam damage. Similarly, the final cleaning steps were carried out at 2 and 1 kV for the same reason.

Transmission electron microscopy (TEM) and scanning transmission electron microscopy (STEM) observations were performed on FIB foils using a FEI Tecnaï G2 microscope operated at CP2M (Marseille, France) with a LaB6 electron source operating at 200 kV. Energy dispersive X-ray (EDX) spectra were acquired in STEM mode to probe the chemical composition of the interface between the altered layer and the substrate, with an EDX Detector (Oxford XMax 80). The analyses were conducted on two FIB thin sections (H0 and H4).

IV.2.3.2. ToF-SIMS analyses

ISG coupons were analyzed by an IONTOF GmbH® TOF 5 spectrometer from TESCAN Analytics (France). The external surface was abraded on an area of 200x200 µm² for an analyzed area of 50x50 µm². The ToF-SIMS operated as cycles of abrasion and analysis. After each cycle, the surface charge was neutralized by a low energy electron beam (<20 eV) in order to prepare the area for the next cycle. The depth of the crater (h_{crater}) created by ion milling after a given number of abrasion cycles (N_{cycles}) was measured using 3D profilometer. The depth associated to one cycle of abrasion (z_{cycle}) is then assumed to be simply given by:

$$z_{cycle} = h_{crater} / N_{cycles} \quad \text{(Eq. IV-3)}$$

Uncertainties are approximately 15% of the result value. Depth profiles of positive ions were recorded thanks to Bi_1^+ 25 keV, 1.5 pA beam for the analyses and O_2^+ 1 keV, 210 nA beams for the ablation. Depth profiles of negative ions were recorded thanks to Bi_3^{++} 25 keV, 0.5 pA beams for the analysis and Cs^+ 2 keV, 185 nA beams for the ablation. The gel layer thickness was measured for a Na/Si ratio of 0.5 with a 2 nm uncertainty (considering Na/Si = 0.50 ± 0.15) based on the depth profile.

Furthermore, the diffusivity of the gel layer was investigated through a tracer experiment at room temperature. After the alteration experiment, several ISG coupons were dipped into a solution containing ^{10}B with a $^{10}B/^{11}B$ ratio of 100.9 and around 1.05 x10^{-4} mol.L^{-1} of methylene blue during 1 day for all ISG coupons. The diffusion of the later molecule of around 1 nm in size was tracked thanks to the record of S, an element solely present in this dye. Additional characterizations were performed on H0 and H4 with two additional tracer experiments lasting 1 hour and 10 days. At the conclusion of the tracer experiment, those coupons were frozen in liquid nitrogen and analyzed in negative polarity using a cryogenic mode. This mode prevents pore water evaporation during the analysis.

IV.2.4. Diffusion coefficient calculation

IV.2.4.1. Total gel layer thickness

The diffusion coefficient of the gel layer was calculated through different methods. The first one considers the total gel layer thickness, $TGLT$, from the depth profiles of Na, Ca and Al elements determined by Tof-SIMS. The hypothesis is that the alteration rate was diffusion-controlled, which is in good agreement with Chapter 5. The diffusion coefficient, D_{TGLT}^{ToF}, can then be calculated as follows:

$$D_{TGLT}^{ToF} = \frac{TGLT^2 \times \pi}{4 \times t} \quad \text{(Eq. IV-4)}$$

Another method is based on the equivalent thickness of the gel layer calculated from the results of ICP-OES, using Eq. IV-1. An analytical failure prevented measurement of B concentration of

the last collected samples. As a consequence, the $r\_disso(B)$ calculated in this study at t = 13 days from Eq. IV-2 was used, and the corresponding diffusion coefficient, D_{TGLT}^{ICP}, was calculated as follows:

$$D_{TGLT}^{ICP} = \frac{Eth(B)^2 \times \pi}{4 \times t} \qquad \text{(Eq. IV-5)}$$

where $Eth(B)$ is the equivalent gel layer thickness calculated at $t = 13$ days of alteration.

This method is justified by the results obtained by [11], and in particular, their experiment S2-sat-10.3, conducted in conditions similar to those used in the present study. Both their and our dissolution rates were found to be in reasonable agreement. Furthermore, S2-sat-10.3 experiment highlighted a boron release that was linear with the root square of time (see Supplementary Fig. IV-1), suggesting that the dissolution rate of ISG was diffusion-limited.

The total gel layer thickness at the end of the experiments conducted in the present study was then extrapolated based on those calculated diffusion coefficients.

IV.2.4.2. Experiment with the tracer solution

The last method is through the B-tracing experiment and the ToF-SIMS analysis. In this method, the depth profiles of the $^{10}B/^{11}B$ ratio are considered using both the negative ions analyses before the tracer experiment and the cryogenic mode of negative ions analyses after the tracer experiment. The average measured $^{10}B/^{11}B$ ratio in the pristine glass might slightly be different compared with the natural isotopic ratio, which is around 0.2446. A first correction is then applied to the raw $^{10}B/^{11}B$ ratio in order to match the natural isotopic ratio in the pristine glass in both analyses. This normalized corrected $^{10}B/^{11}B$ ratio is called CNB (see Damodaran et al. [40])

In addition, some other differences between the two analyses may exist such as the intrinsic gel layer thickness between two different locations (may vary around 6% between all depth profiles), referred as $h_{gel\ layer}^{Neg}$ based on the negative ions analyses and $h_{gel\ layer}^{cryo}$ based on the cryogenic mode analyses, and the depth estimation associated to each cycle (the depth-step of the analyses), referred as z_{cycle}^{NEG} and z_{cycle}^{cryo}. First, the gel layer thickness, $h_{gel\ layer}$, can be corrected by adjusting z_{cycle}^{cryo} as follows:

$$z_{cycle}^{New\ Cryo} = z_{cycle}^{Old\ cryo} \times \frac{h_{gel\ layer}^{Neg}}{h_{gel\ layer}^{cryo}} \qquad \text{(Eq. IV-6)}$$

where $z_{cycle}^{Old\ cryo}$ is the original depth-step of the cryogenic mode analyses and $z_{cycle}^{New\ Cryo}$ is the new one that leads to a similar gel layer thickness between both negative and cryogenic analyses.

Once the gel layer thickness is rescaled, the contribution of ^{10}B from the solution needs to be isolated. The B signal is divided into two contributions: B_g for the B coming from the glass and B_s for the B coming from the solution. From this point, it is reasonable to assume that the depth profile of the negative ion before the tracer experiment provides information on $^{10}B_g$ and $^{11}B_g$. Knowing those two values, the $\frac{^{10}B_s}{^{11}B_s}$ ratio in the tracer solution, named BTS with a value of 100.9, and the CNB previously calculated, the ^{10}B and ^{11}B from the solution can be calculated as follows:

$$^{10}B_s = BTS \times {}^{10}B_g - \frac{CNB \times BTS \times {}^{11}B_g}{CNB - BTS} \qquad \text{(Eq. IV-7)}$$

$$^{11}B_s = \frac{^{10}B_s}{BTS} \qquad \text{(Eq. IV-8)}$$

After establishing the amount of $^{10}B_s$ in the gel, the diffusion coefficient of B in the gel layer based on the tracer solution, D_{TS}, can be calculated by solving the Fick's 2nd law satisfying the following conditions: $^{10}B_{MODEL} = C_0$ for z = 0 and t > 0, and the initial condition C = b for z > 0 and t = 0:

$$^{10}B_{MODEL} = C_0 \left[1 - ERF\left(\frac{z_{cycle}^{NEG}}{2\sqrt{D_{TS} \times t}}\right)\right] + b \qquad \text{(Eq. IV-9)}$$

Of note, b corresponds to a plateau observed experimentally within the gel with a value higher than in the pristine glass, and likely accounts for the 'instantaneous' transport of boron through main diffusion channels.

The value of C_0, b and D_{TS} were determined by fitting $^{10}B_{MODEL}$ curve to the $^{10}B_s$ profile. The best values were found by minimizing the following criterion:

$$RMS = \sqrt{\frac{1}{N}\sum_{k=1}^{N}\left(^{10}B_{MODEL} - {}^{10}B_s\right)^2} \qquad \text{(Eq. IV-10)}$$

where *RMS* is the root-mean-square and *N* is the number of discrete measurements of ^{10}B in the gel.

IV.2.4.3. Temperature related diffusion coefficient

The diffusion coefficient is temperature-dependent. The relation between the temperature and the diffusion coefficient is given by:

$$D = D_0 \exp\left(\frac{-Ea}{RT}\right) \qquad \text{(Eq. IV-11)}$$

where D_0 is a constant, Ea is the activation energy (J.mol^{-1}), R is the gas constant 8.314 J.mol^{-1}.K^{-1}, and T is the temperature (K). The tracer solution experiment was performed at room temperature while the dissolution experiment was performed at 90°C. The activation energy of ISG gel layer diffusivity is given in the literature by Gin et al., [41] where $Ea = 60\ kJ.mol^{-1}$. It is thus possible to compare the

various methods using this activation energy to re-estimate the diffusion coefficient from 25°C to 90°C (Fig. IV-4) as follows:

$$D_{90} = D_{25} \times exp\left(\frac{T_{25} - T_{90}}{T_{25} \times T_{90}} \times \frac{-Ea}{R}\right) \quad \text{(Eq. IV-12)}$$

IV.3. RESULTS

IV.3.1. ToF-SIMS characterizations

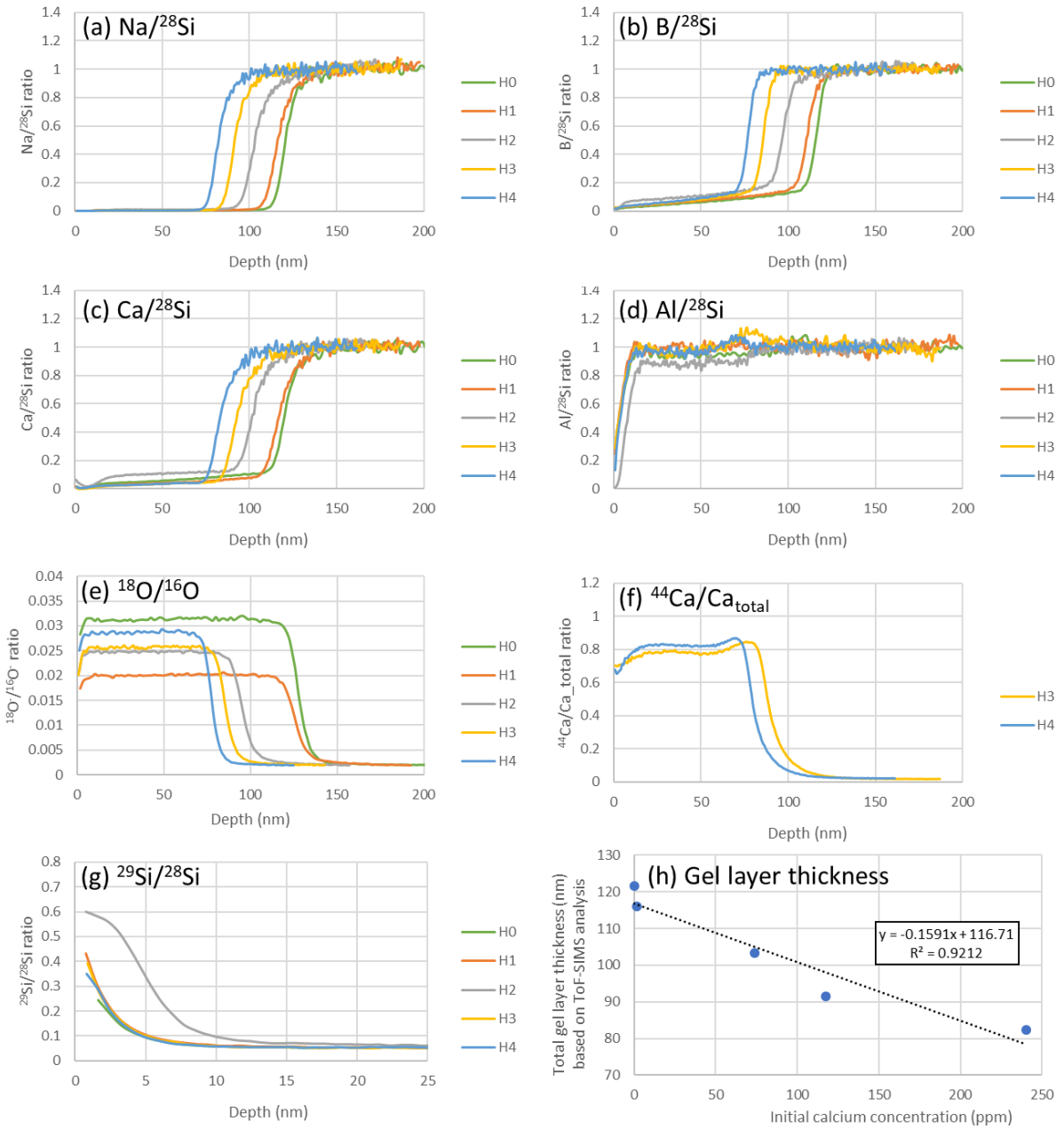

Figure IV-1 : Normalized element depth profiles of a) Na, b) B, c) Ca, d) Al, e) $^{18}O/^{16}O$, f) ^{44}Ca and g) ^{29}Si collected by ToF-SIMS. Each element profile was collected using positive ion detection mode except e) which was collected using negative ion detection mode. Each element was normalized to ^{28}Si prior to be normalized with respect to X/^{28}Si ratio (X = Na, B, Ca and Al) of the pristine material. The $^{29}Si/^{28}Si$ and $^{18}O/^{16}O$ profiles were normalized to the natural abundance in the pristine glass while ^{44}Ca was normalized to the total calcium, i.e. $^{44}Ca + ^{40}Ca$. Of note, z = 0 corresponds to the outer surface of the alteration layer.

The position of the interface between the alteration layer and the pristine glass, also called alteration front, is defined as the z value for which Na/^{28}Si = 0.5. h) Plot representing the total gel layer thickness (nm) as a function of the initial concentration of calcium (ppm) in the solution.

The starting fluid composition of the series H is listed in Table IV-1. The initial concentration of calcium in solution increased from H0 to H4, ranging from 0 ppm to 240 ppm. The solution was labeled with the isotope ^{29}Si, with a ratio of ^{29}Si/^{28}Si close to 0.74 +/- 0.2, and with ≈100% of the isotope ^{44}Ca for H3 and H4. Each ISG coupon was analyzed using Time-of-Flight Secondary Ion Mass Spectrometry (ToF-SIMS). Results for the major elements making up the glass are shown in Fig. IV-1. Each element has been normalized to the X/^{28}Si ratio (X = Al, Ca, B, and Na) of the pristine glass.

As a first observation, the alteration fronts of the different elemental profiles are consistent. The thickness of the gel (H0 > H1 > H2 > H3 > H4) is strongly negatively correlated (R^2 = 0.92) with the initial amount of calcium in solution (see Fig. IV-1h).

A slight retention is observed within the gel for B and Ca. It is worth noting that the first 5 to 10 nm of the gel are depleted in Al. Additionally, these initial 5 nm correspond to the location where the incorporation of ^{29}Si is at a maximum for H0 to H3. Regarding H2, ^{29}Si penetrates into the first 10 nm of analysis. Finally, the calcium cations that remained trapped within the gel mainly have the isotopic signature of the solution. The ^{44}Ca from the solution penetrated up to the alteration front, and the ^{44}Ca/(^{44}Ca + ^{40}Ca) ratio stabilized around 0.8 for H3 and H4.

IV.3.2. FIB-TEM characterizations

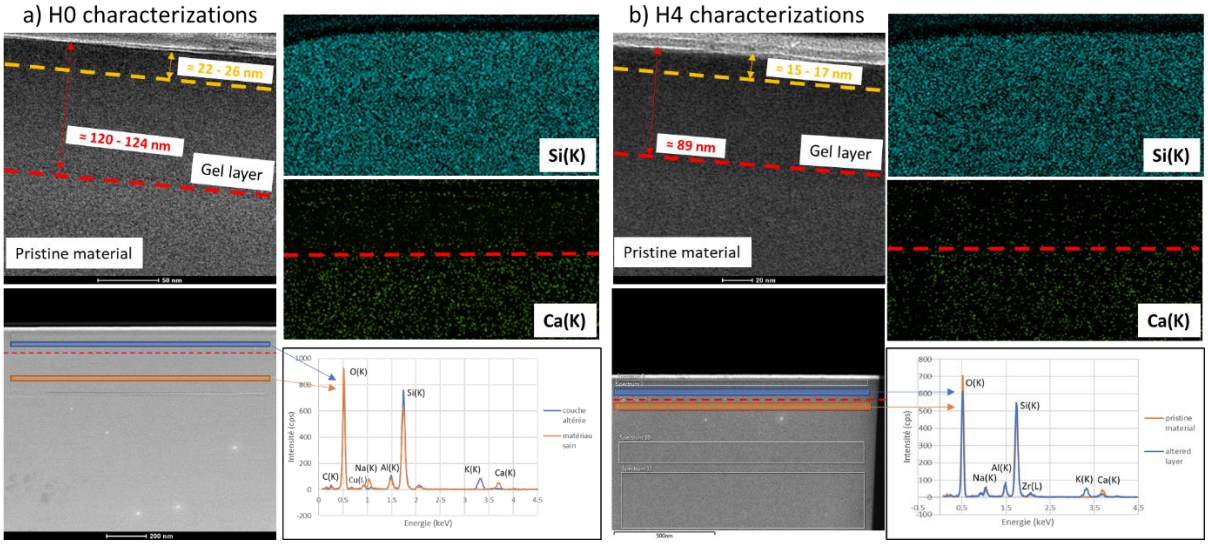

Figure IV-2: FIB-TEM characterizations of a) H0 and b) H4 ISG coupons. The composition of the gel layer and the pristine material was obtained by STEM-EDX. The top left image is a TEM bright field image where the gel layer thickness is measured. The red dashed line corresponds to the interface between the gel layer and the pristine material, and the yellow dashed line corresponds to the limit between the gel layer with an intermediate electron density and the outer surface, which has a higher electron density. The bottom left panel represents a TEM dark field image where EDX spectra were collected. EDX map for the Si(K) and Ca(K) are also displayed in the bottom part.

The characterizations of the two FIB foils prepared on H0 and H4 ISG coupons show similar results as those obtained by ToF-SIMS (see Fig. IV-2). The gel thickness is approximately 122 nm for H0 and 89 nm for H4 which is consistent with the ToF-SIMS results (Fig. IV-1a and IV-1b) where H0's gel layer thickness is 122 nm and H4's is 82 nm (see Table IV-2). The interface between the gel and the pristine material is continuous, and the alteration front is straight. Finally, a zone of approximately 22 to 26 nm for H0 and 15 to 17 nm for H4, with a higher electron density is present near the surface of the glasses. STEM-EDX maps confirm the position of the interface with a depletion in calcium in the gel, more pronounced for H0 than for H4. However, it is impossible to conclude regarding a difference in silicon atom density.

The STEM-EDX spectra collected on H0 and H4 FIB foils are similar: an incorporation of potassium (K comes from the pH electrode, not measured in solution) within the gel can be evidenced, while the gel is depleted in Ca and Na cations. However, a retention of calcium of 5% ± 1% for H0 and 21% ± 2% for H4 is also observed within the gel.

IV.3.3. Diffusion coefficients based on the total gel layer thickness

Table IV-2: Diffusion coefficients calculated based on the total gel layer thickness measured by ToF-SIMS and calculated from the release of B during the alteration, by ICP-OES, at 90°C. The first column refers to the name of the experiment. The second and third refer to the gel layer thickness (nm) measured by ToF-SIMS and the diffusion coefficient, D_{TGLT}^{ToF} ($m^2.s^{-1}$), calculated based on Eq. IV-4, respectively. The fourth column refers to the dissolution rate ($g.m^{-2}.d^{-1}$) calculated based on the release of B after 13 days of alteration. The fifth and sixth columns refer to the gel layer equivalent thickness (nm) after 13 days of alteration based on B release and the diffusion coefficient, D_{TGLT}^{ICP} ($m^2.s^{-1}$), respectively. The seventh columns refer to the gel layer equivalent thickness (nm) extrapolated at 21 days considering a diffusion-controlled mechanism.

Name	ToF-SIMS analysis		ICP-OES analysis			
	$Eth(B)$	D_{TGLT}^{ToF}	$r\_disso(B)$	$Eth(B)$ 13 days	D_{TGLT}^{ICP}	$Eth(B)$ 21 days
H0	122	6.4E-21	0.0148	77	4.2E-21	125
H1	116	5.8E-21	0.0066	35	8.4E-22	56
H2	103	4.6E-21	0.0067	35	8.5E-22	56
H3	91	3.6E-21	0.0109	57	2.2E-21	91
H4	82	2.9E-21	0.0188	98	6.7E-21	158

An apparent diffusion coefficient of the gel layer was calculated based on the total gel layer thickness (TGLT). The gel thicknesses considered here are those measured by ToF-SIMS and those calculated based on the release of B in solution by ICP-OES, during the 90°C alteration experiment. Similar to the results obtained for the gel layer thickness by ToF-SIMS, the diffusion coefficients are identically correlated with the initial calcium concentration in solution (R^2 = 0.9).

Regarding the D_{TGLT}^{ICP} calculated based on Eq. IV-5, they are in the same order of magnitude as D_{TGLT}^{ToF}, but do not exhibit the same decreasing trend. Except for H4 where D_{TGLT}^{ICP} is higher by a 2.3 factor, D_{TGLT}^{ICP} is globally lower than D_{TGLT}^{ToF} by only a factor 1.5 and 1.6 for H0 and H3 respectively, and a factor 6.9 and 5.4 for H1 and H2, respectively. Both D_{TGLT}^{ICP} and D_{TGLT}^{ToF} are listed in Table IV-2.

IV.3.4. Diffusion coefficients based on tracer experiment at 25°C

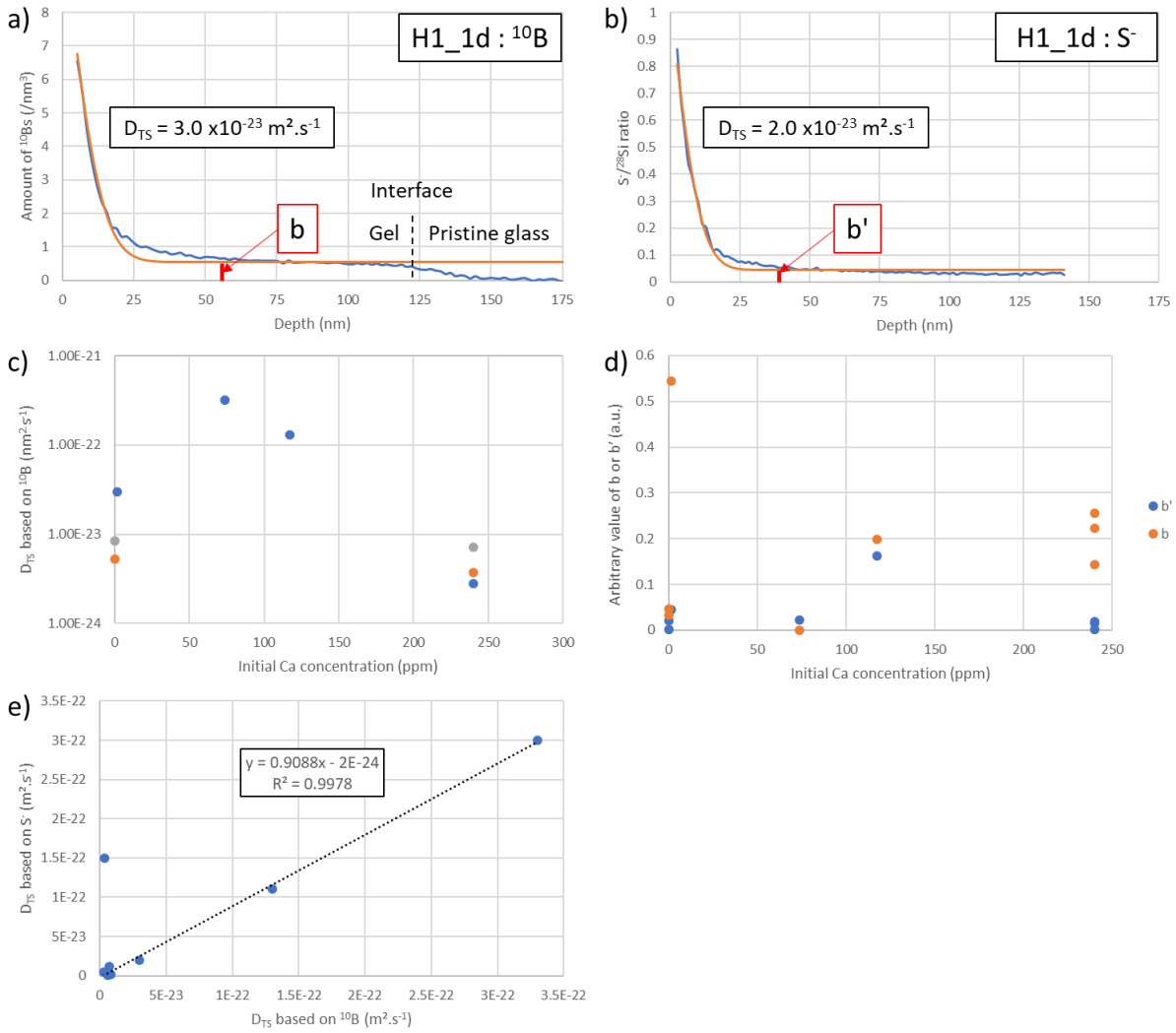

Figure IV-3: Results of the fitting exercise of the incorporation of a) ^{10}B and b) sulfur from the tracer solution into the gel layer of H1 ISG coupon. H1 was chosen as a representative example among the others experiments. a) the blue curve represents the depth profile of ^{10}B while the orange curve represents the fit based on Fick's law. The black dash line corresponds to the interface between the gel layer and the pristine glass. The b value represents the average plateau value of ^{10}B within the gel. b) the blue curve represents the depth profile of S^- while the orange curve represents the fit. The b' value represents the average plateau value of S^- within the gel. c) Plot representing the value of the diffusion coefficient calculated based on the incorporation of ^{10}B from the tracer experiment as a function of the initial calcium concentration (ppm). The orange, blue and grey circles correspond to an experiment that lasted 1 hour, 1 day and 10 days, respectively. d) the plot represents the value of b (orange) and b' (blue) based on the incorporation of ^{10}B from the solution e) Plot representing D_{TS}^{S} as a function of D_{TS}^{B}. The dashed lined corresponds to a linear regression.

After the alteration experiment, ISG coupons were placed at room temperature in a tracer solution containing ^{10}B and methylene blue, which contains S^-. This experiment lasted 24 hours for all

samples, after which ToF-SIMS characterizations were conducted in cryogenic mode to preserve pore water during the analysis. Two additional experiments of 1 hour and 10 days were conducted on ISG samples from H0 and H4. For clarity purpose, the different experiments will be named by the alteration experiment followed by the tracing time: for example, H0_10d corresponds to the H0 sample that remained in the tracer solution for 10 days. This tracer experiment aims to investigate the transport properties of species within the gel by tracking their incorporations into the gel (Fig. IV-3a and IV-3b). From the ToF-SIMS profiles, a diffusion coefficient for B (D_{TS}^{B}) and S (D_{TS}^{S}) was calculated (see Fig. IV-3c). The various calculated diffusion coefficients are presented in Table IV-3. Note that the H0_1d experiment was not successful.

The decreasing trend in the diffusion coefficient starting from H2 is consistent with previous observations on gel thickness (H2 > H3 > H4). However, D_{TS}^{B} values for H1 and H0 experiments do not follow this trend. The D_{TS}^{B} values for H0 after 1 hour and 10 days of tracing are in the same order of magnitude. They remain however lower than those for H1, H2, and H3, while being higher than those for H4. Regarding the D_{TS}^{B} values for H4 after 1 hour, 1 day, and 10 days of tracing, they are in the same order of magnitude, and qualitatively in line with the estimates based on the gel thicknesses, the lowest value being 2.8 x 10^{-24} $m^2.s^{-1}$ for H4_1d.

Table IV-3: Diffusion coefficients calculated based on the incorporation of ^{10}B and S^- during the tracer experiments at 25°C and re-calculated at 90°C for D_{TS}^{B}. The first and second columns refer to the name of the experiment and the initial calcium concentration (ppm). The third, fourth and fifth columns refer to the estimated diffusion coefficient ($m^2.s^{-1}$) based on ^{10}B at 25°C, the gel layer thickness (nm) calculated based on the diffusion coefficient in the third column and the b value, respectively. The sixth and seventh columns refer to the diffusion coefficient ($m^2.s^{-1}$) based on S^- at 25°C and the b' value, respectively. The eighth and ninth columns refer the diffusion coefficient ($m^2.s^{-1}$) based on ^{10}B recalculated at 90°C and the gel layer thickness (nm) calculated based this diffusive coefficient.

Name	Ca (ppm)	D_{TS} calculated at 25°C					D_{TS} calculated at 90°C	
		D_{TS}^{B}	$Eth(B)$ (nm)	b	D_{TS}^{S}	b'	D_{TS}^{B}	$Eth(B)$ (nm)
H0_1h	0	5.7E-24	3.6	0.033	9.0E-25	0.002	6.6E-22	38.9
H0_1d								
H0_10d	0	8.4E-24	4.4	0.046	2.0E-24	0.021	9.7E-22	47.2
H1_1d	1.7	3.0E-23	8.3	0.545	2.0E-23	0.045	3.5E-21	89.3
H2_1d	73.9	3.3E-22	27.6	0.000	3.0E-22	0.023	3.8E-20	296.1
H3_1d	117.3	1.3E-22	17.3	0.199	1.1E-22	0.162	1.5E-20	185.9
H4_1h	240	3.7E-24	2.9	0.144	1.5E-22	0.016	4.3E-22	31.4
H4_1d	240	2.8E-24	2.5	0.256	5.0E-24	0.019	3.2E-22	27.3
H4_10d	240	7.2E-24	4.1	0.223	1.2E-23	0.002	8.3E-22	43.7

The value of b (respectively, b') represents the average normalized concentration ($atom/nm^3$) of ^{10}B (respectively, S^-) that has penetrated into the gel layer (Table IV-2). The b values measured at different tracing times are consistent, remaining in the same order of magnitude. For H0_1h and H0_10d, it evolves from 0.033 to 0.046, while for the H4 sample, it evolves between 0.144 and 0.256.

Overall, a negative trend emerges with the incorporation of calcium in solution (Fig. IV-3d). Except for samples H0 and H2, a decreasing trend is observed. However, with the exception of H3, b' value highlight a trend that is mostly constant.

Finally, both Fig. IV-3a and IV-3b provide an example of the comparison of the incorporation of ^{10}B and S^- within the gel layer during the tracer experiment for the H1_1d sample. The D_{TS}^{S} values are reported in Table IV-3 and compared to D_{TS}^{B} in Fig. IV-3e. Except for a significant difference between the incorporation of the two elements for H4_1h, a correlation can be established with R^2 = 0.998 between D_{TS}^{B} and D_{TS}^{S}. The linear regression shows a slight deviation of -2 x10^{-24} from the origin and a slope of 0.9, indicating that overall, $D_{TS}^{B} > D_{TS}^{S}$.

IV.3.5. Extrapolation to 90°C of the coefficient diffusions estimated at 25°C from tracer experiments

Gin et al., 2020 [41] investigated the dissolution rate of ISG at 90°C, pH 3, 5, 7 and 9 in solutions saturated with respect to amorphous silica and no initial addition of calcium. They evidenced a strong correlation between the diffusion coefficient, calculated from the B release in the solution by ICP-OES, and pH at 90°C. Those results were extrapolated at pH 10.3, resulting in a diffusion coefficient of 1.25 x10^{-19} $m^2.s^{-1}$. The diffusion coefficients estimated in the previous section (at 25°C) are found to be several orders of magnitude lower, with a factor ranging from 10^3 to 10^4.

Of note these diffusion coefficients reported in section III.c. were estimated from the tracer experiments conducted at 25°C. For a better comparison with literature data, they were recalculated at 90°C using Eq. IV-12 (see Table IV-3) and Ea = 60 kJ.mol^{-1} calculated in Gin et al., 2020. The overall trend is identical to that depicted at 25°C, but the D_{TS}^{B} at 90°C is closer to that of Gin et al., 2020, with a factor ranging from 10^1 to 10^2.

IV.3.6. Comparison of the various diffusion coefficients

In order to compare the diffusion coefficients calculated based on various approaches, the one calculated from the total gel layer thickness based on ToF-SIMS, D_{TGLT}^{ToF}, were chosen as a reference (Fig. IV-4a). The diffusion coefficients calculated from the total gel thickness are generally closer to the literature even if they remain lower by a factor 20 for H0, and 43 for H4. They also range within the same order of magnitude, whereas those derived from the tracer experiment span over two orders of magnitude. The recalculated D_{TS}^{B} at 90°C falls within a similar order of magnitude as D_{TGLT}^{ToF} and D_{TGLT}^{ICP}. Based on the work of Gin et al., 2020 [41], uncertainties for the different diffusion coefficients were estimated with a factor of 2 for positive uncertainties and a factor of 0.5 for negative uncertainties.

Fig. IV-4b represents the equivalent thickness of the gel layer as a function of time. The blue curve depicts the gel layer thickness if the alteration is diffusion-controlled with a diffusion coefficient D_Fick = 1.25 x10^{-19} m².s^{-1} extrapolated from Gin et al., 2020 [41]. Other curves represent the gel layer thickness for D values ranging from 1.25 x10^{-19} m².s^{-1} to 1.25 x10^{-24} m².s^{-1}. The observations are similar to those mentioned earlier: i) a greater dispersion of gel thicknesses for those calculated based on the tracer experiment, ii) a clustering within the same order of magnitude around the thicknesses derived from ToF-SIMS at 90°C, and iii) thicknesses consistently lower than those from the literature.

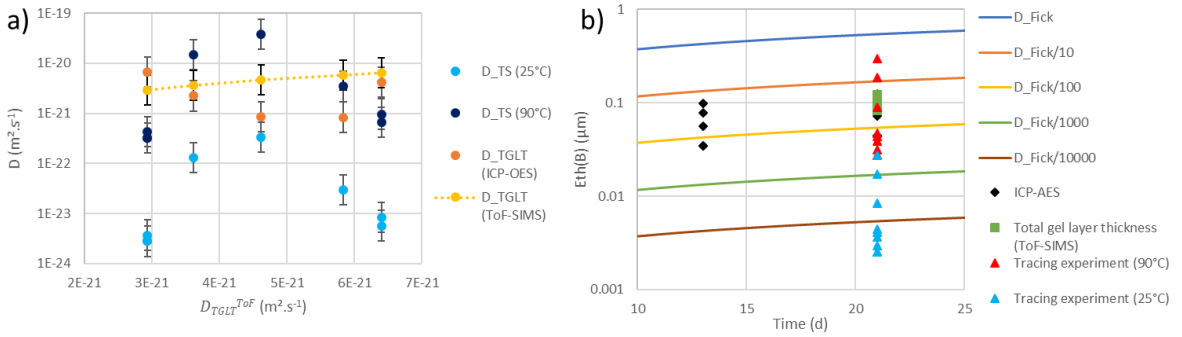

Figure IV-4: Comparison of the methods to obtain a diffusion coefficient. a) comparison of the diffusion coefficients with D_{TGLT}^{ToF} as the reference (yellow dash line). b) comparison of the equivalent gel layer thickness from the various methods. The Fick's law in blue line corresponds to the Eth(B) with the diffusion coefficient from Gin et al., 2020 [41] worth 1.25 x10^{-19} m².s^{-1}. The other lines correspond diffusion coefficient one order of magnitude lower, each.

IV.4. DISCUSSION

IV.4.1. Mechanisms of gel layer formation

The alteration solution was labeled with ^{29}Si and ^{18}O isotopes to study their incorporation into the gel. The measured ^{29}Si/^{28}Si ratio of the starting solution is around 0.74 ± 0.02 (in good agreement with the expected value (0.75)). An enrichment in ^{29}Si is noticed only in the outermost layer (5 to 10 nm depending on the samples) (Fig. IV-1e), evidencing that the gel layer was mostly formed without incorporating ^{29}Si from the solution. This enriched layer also corresponds to a depletion in Al and Ca, suggesting the presence of precipitates on the surface of the sample instead of a gel. In a companion study focused on the characterization of these precipitates (cf. chapter 5), we showed that they mainly consist of amorphous silica (H0 and H1), calcium silicate hydrates (CSH) (H2), and calcium carbonates (H3 and H4). Such secondary phases could form a discontinuous 5-10 nm thick layer on the altered surface of ISG. Note that the actual thickness of precipitates could differ from those estimates, as we assume that the abrasion rate remained constant during ToF-SIMS analysis, while it actually depends on the density of the different layers.

In comparison, the isotopic signature of oxygen within the gel suggests an exchange between the oxygen from water molecules and those from the glass (Fig. IV-1g). This observation suggests that after the hydrolysis of Si–O–Si bonds to form silanols, a recondensation reaction takes place that incorporates $H_2{}^{18}O$ molecules from the solution. For all experiments, those results present a plateau that is lower than the solution's $^{18}O/^{16}O$ ratio, which is around 0.035 ± 0.005 (the solution of all experiment comes from the same mother one). However, a second ToF-SIMS analysis for H0 and H4 presents a plateau for both experiment that is similar to the $^{18}O/^{16}O$ ratio in solution (Supplementary Fig. IV-2): the isotopic signature of the gel layer is in equilibrium with that of the solution. This result suggests that water molecules diffuse freely within the gel layer, and each Si-O-Si bond has been hydrolyzed. The fact that ^{29}Si from the solution has not been incorporated into the gel structure highlights either that the hydrolysis of all bonds that link the network-forming elements to the glass occurred sequentially or that hydrolysis and condensation reactions competed, preventing the release of Si [19]. Furthermore, the Si concentration in the solution remains mostly constant (see Supplementary Information), and no retreat has been observed on the sample's surface based on VSI analysis (see chapter 5 for more details): there is no gel layer dissolution.

In conclusion, similarly to previous studies [15,41-44], the characterizations suggest that ISG gel layer was formed through an *in situ* hydrolysis–recondensation mechanism, excluding the diffusion of orthosilicic acid in the gel. Overall, siloxane bond breaking and reformation allowed the exchange between ^{18}O and ^{16}O, but not that between ^{29}Si and ^{28}Si [19]. Following the formation of this gel layer, an area on the outer part of the gel, with thickness ranging from around 16 ± 1 nm (for H4) to 24 ± 2 nm (for H0), and with a higher electron density was evidenced on the FIB-TEM images (Fig. IV-2). This higher electron density suggests an *in-situ* reorganization of the gel, which might have favored its densification and gradually limited the transport of species. This densification mechanism through the recondensation of silanols and *in situ* reorganization of network-forming elements has been demonstrated by Cailleteau et al., 2008 [20,21]. The present study suggests that this mechanism is favored in alkaline solutions, whatever the Ca concentration in the solution.

Furthermore, the ToF-SIMS results show that the gel layer incorporated K and ^{44}Ca from the solution (Fig. IV-1f). Despite its densification, it remains permeable to some elements from the solution. Therefore, the gel is not completely passivating and exchange with the solution allows the dissolution to continue. However, its transport properties for species seem closely related to the initial calcium concentration in solution.

IV.4.2. Calcium effect on the formation of the gel

A strong negative correlation between the initial concentration of calcium in solution and the gel layer thickness (R^2 = 0.92) was noticed from the ToF-SIMS results. Subsequently, a diffusion coefficient was calculated at pH 10.3, 90°C. Based on such results, a relationship (R^2 = 0.90) can be established between the initial concentration of calcium in solution and the diffusion coefficient of the gel layer, D_{TGLT}^{ToF} ($m^2.s^{-1}$):

$$D_{TGLT}^{ToF} = -1.40 \times 10^{-23}[Ca^{2+}] + 5.87 \times 10^{-21} \quad \text{(Eq. IV-13)}$$

A few precipitates were observed in solution, namely silica (H0 and H1), CSH (H2), and calcium carbonates (H3 and H4). Given the correlation between the gel layer thickness and the initial amount of calcium in solution, it can be proposed that the nature of the precipitates does not have an effect on glass alteration rate, at least during the first 21 days of the experiment.

However, calcium is known to potentially impact the gel layer formation. Damodaran et al., 2022 [40] demonstrated that the alteration depth of ISG in a (Si, B, Ca, Na)-saturated solution could be 50 times thinner compared to that in Si-saturated solution, free of the other elements. However, if either the B or Ca is removed from the solution, the ISG alteration depth is only about 3 times thinner. Since the alteration depth increases, the B or Ca element limit the dissolution rate of the glass. The pH of all those solutions was maintained near neutrality, pH 6 to 7. Two hypotheses can be suggested regarding the role of calcium in gel passivation.

The first hypothesis is related to the work of Mercado-Depierre et al., 2013 [23]: calcium from the solution can be absorbed into the growing gel layer, creating a layer enriched in calcium that increases the retention of glass constituents. The FIB-TEM data (Fig. IV-2) highlight a higher retention of Ca for H4 (21%) than for H0 (5%), which is consistent with the solution of H4 being more concentrated in calcium than H0. This (Si, Ca)-rich layer decreases the transport properties of the layer and, consequently, its rate of formation [34,40]. Additionally, ISG also contains Al and Zr, which are poorly soluble elements in basic solutions: studies have also shown that the presence of these elements can enhance the passivating character of such a layer [23,36].

A second hypothesis relying on the work of Chave et al., 2011 [35] can be proposed. The authors hypothesized that calcium could play a catalytic role in the recondensation reaction of the gel, according to the following reactions:

$$\equiv Si - OH + Ca^{2+} + HO - Si \equiv \rightarrow \equiv Si - O - Ca - O - Si \equiv + 2H^+ \quad \text{(Eq. IV-14)}$$

$$\equiv Si - O - Ca - O - Si \equiv + 2H^+ \rightarrow \equiv Si - O - Si \equiv + Ca^{2+} + H_2O \quad \text{(Eq. IV-15)}$$

Based on FIB-TEM images (Fig. IV-2), a densification reaction of the gel layer occurs at the surface. Considering the gel thickness vs calcium correlation, the condensation reaction seems to become more dominant with the increase in calcium in the solution. However, the densification of the gel is also observed in H0 (Fig. IV-2a) where no calcium was initially added, challenging this hypothesis. Ultimately, in the context of a catalytic role, it is possible that the low quantity of calcium in ISG, along with a 5% retention, is sufficient for the calcium to efficiently contribute to the gel layer densification.

In conclusion, during the first 21 days of alteration, the secondary phases that precipitate in solution have little to no effect on the glass alteration rate and gel formation. However, the concentration of calcium initially introduced into the solution moderately impacts the gel layer formation, either by i) being incorporated into the growing gel to form a passivating (Si, Ca)-rich layer, ii) playing a catalytic role in the gel layer recondensation and densification, or by iii) both being incorporated into the gel to form a passivating layer and participating in its densification.

IV.4.3. Comparison of the various diffusion coefficient

IV.4.3.1. Reliability of each method

Initially, the two methods for calculating the diffusion coefficients, D_{TS}^{B} and D_{TGLT}^{ToF}, showed significant differences. On average, there was a factor of 543 between both coefficients with a standard deviation of 443. This difference is largely explained by the difference in temperature at which each experiment was conducted. The D_{TS}^{B} coefficient is based on the incorporation of boron into the gel layer during a tracer experiment at 25°C after a first alteration step at 90°C, while D_{TGLT}^{ToF} is based on glass alteration in a solution only at 90°C. By using Eq. IV-12 and considering Ea = 60 kJ.mol^{-1} [41], the D_{TS}^{B} coefficient was recalculated at 90°C, reducing the mean difference factor to 4.7 with a standard deviation of 3.8. The results are generally consistent between both methods. Note that, the mean difference factor between D_{TGLT}^{ToF} and D_{TGLT}^{ICP} is only 1.6 with a standard deviation of 0.8, highlighting the reasonable agreement between both methods.

The uncertainty applied to these values is a factor of 2 for positive uncertainty and a factor of 0.5 for negative uncertainty. In the end, despite the reduction in the difference between the two methods, not all diffusion coefficients overlap (Fig. IV-4). This is mainly due to data dispersion: D_{TS}^{B} has a standard deviation of 1.3 x10^{-20}, while D_{TGLT}^{ToF} has a standard deviation of 1.4 ×10^{-21}, similar to D_{TGLT}^{ICP} with a standard deviation of 2.5 x10^{-21}. This difference in standard deviation highlights a dispersion of an order of magnitude larger for the results arising from tracer experiments compared to those relying on the total gel layer thickness. Both methods show similar results, but those from the tracer experiments are less precise.

Several hypotheses can be proposed to explain these differences. Firstly, the diffusion coefficients calculated based on the tracer experiment account for the diffusion properties of the post-alteration gel layer, while those derived from the gel layer thickness include a potential temporal evolution of the transport properties of the gel. In particular, the densification reaction limits the transport of species and consequently reduces the diffusion coefficient. As a consequence, it can be expected that the diffusion coefficient at the end of the experiment, D_{TS}^{B}, is lower than the diffusion coefficient averaged over the 21 days of alteration, D_{TGLT}^{ToF} and D_{TGLT}^{ICP}. While such a hypothesis is confirmed for H0 ($\frac{D_{TGLT}^{ToF}}{D_{TS}^{B}} = 8.1$ on average), H1 ($\frac{D_{TGLT}^{ToF}}{D_{TS}^{B}} = 1.7$) and H4 ($\frac{D_{TGLT}^{ToF}}{D_{TS}^{B}} = 6.4$ on average over the three tracing times), it is not verified for H2 ($\frac{D_{TGLT}^{ToF}}{D_{TS}^{B}} = 0.12$) and H3 ($\frac{D_{TGLT}^{ToF}}{D_{TS}^{B}} = 0.24$). As a consequence, it cannot be concluded that the differences between the two methods can be ascribed to a possible systematic decrease of the gel diffusivity over time.

A second hypothesis could be that the diffusivity within the gel layer is not identical depending on whether the element is released by the glass during its alteration or penetrates into the gel layer during the tracer experiment. Through the alteration of ISG at pH 3 and pH 9 followed by a tracer experiment with ^{10}B, Damodaran et al., 2022 [40] have demonstrated that B diffuses slower in a gel layer formed in a basic environment than in an acid one and tends to accumulate within it. Moreover, the accumulation of this element, facilitated by the presence of Ca in solution, tends to increase the passivation properties of this layer. Consequently, the diffusion coefficients obtained based on the tracer experiment are lower than the diffusion coefficients that were effective during glass alteration, which is consistent with the previous results. Recently it was observed that tracer experiments with ^{10}B provides more consistent results with Ca-free glasses (unpublished data from Gin et al.).

Finally, the gel may have evolved *a posteriori*, and the recondensation reaction of silanols continued despite the end of the experiment. A few days of delay occurred between the end of the experiment and the tracer experiment. Densification of the gel would then have the effect of decreasing the diffusion coefficients calculated based on the tracer experiment. Furthermore, the drop in the temperature may have impacted the saturation state of the poral solution with respect to amorphous silica, favoring the condensation reaction of silanols.

To conclude, none of the above-mentioned hypotheses provides an entirely satisfactory explanation for the discrepancies observed between the transport properties estimated from the tracer experiments and the ones estimated from the final thickness of the gel layer. However, it should be kept in mind that both types of estimations may not exactly capture the exact same processes.

IV.4.3.2. Incorporation of ^{10}B and S^- within the gel layer

Focusing on the tracer experiment, a diffusion coefficient was calculated based on two tracers: ^{10}B et S^- (proxy for methylene blue). Sample H4_1h shows a strong incorporation of S^- while the incorporation of ^{10}B is two orders of magnitude lower. Additionally, while sulfur penetrates into H4_1h, it does not diffuse as well into the same gel layer after 1 day and 10 days of tracing: the results for sulfur incorporation into the gel layer for H4_1h are inconsistent. Therefore, this experiment was excluded from the comparison of ^{10}B and S^-. With the remaining data, a strong correlation emerges ($R^2 = 1$) between the two tracers. On the one hand, this result could indicate an independent incorporation regardless of the atom/molecule size and that the transport of species is not limited by the size of pores and diffusion channels within the gel layer. On the other hand, the speciation of B changes with pH : Mesmer et al., 1972 [45] identified different species such as (from the smallest to the biggest) $B(OH)_3$, $B(OH)_4^-$, $B_4O_5(OH)_4^{2-}$ and $B_3O_3(OH)_5^{2-}$ which may form under alkaline conditions (pH 9 in their studies). Other studies [46,47], based on Raman spectroscopy, highlighted that $B(OH)_4^-$ was the most stable and most dominant boron complex at pH ranging from 9.3 to 14 at low temperature. The increase in temperature tends to stabilize $B(OH)_3$ relative to $B(OH)_4^-$ [47]. Furthermore, $B(OH)_3$ was still detected at pH 10.4 and, with $B(OH)_4^-$, they may condense into a dimer to form a bigger molecule [48]: the size difference between both tracers would be removed, explaining that similar results were obtained. Finally, the ^{10}B can also be adsorbed at the surface of ISG, creating both negatively charged tetrahedral B and neutral trigonal B. However, the adsorption of B_{IV} is favored in alkaline condition and in presence of calcium in solution [49,50]. As a consequence, the diffusion of ^{10}B within the gel is limited.

The value of b for ^{10}B and b' for S^- represent the average quantity of each element within the gel (Fig. IV-3d). It is observed that both elements diffuse up to the interface between the gel and the pristine material. The values of b and b' are rapidly similar regardless of the tracing time. They are therefore characteristic of the gel. The value of b seems to decrease with the increase in calcium in solution, except for H0 and H2, whose b value is null. This is consitent with the passivation effect of calcium: through recondensation and porosity closure, there is less diffusive chanels within the gel. However, the b' value is mostly constant with the exception of H3. Since the diffusion coefficient D_{TS}^{B} and D_{TS}^{S} are quite similar, identical b and b' would have been expected. The fact that b' remains constant would presume that the pore size and diffusive channels size are globally similar between each gel, indicating once again that it is not the gel porosity that limits the diffusion of species in the gel.

IV.5. CONCLUSION

In conclusion, this study provides new information in the understanding of the evolution of diffusivity within gel layer developed on ISG substrates at alkaline pH and elevated concentrations of dissolved Ca and Si. The isotopic signature has revealed both the presence of a first layer of secondary phases on the surface of the ISG glass and a gel layer formed by hydrolysis – recondensation. Following the formation of the gel layer, a strong correlation was found between the initial concentration of calcium in the solution and the total gel layer thickness. This correlation might be explained by i) the formation of a (Si, Ca)-rich layer that limits the transport of species within the gel, ii) the catalytic role of the calcium in the recondensation reactions of the gel layer, thus promoting its densification or iii) a combination of both previous hypotheses.

A difference of several orders of magnitude between the diffusion coefficients calculated based on the total gel layer thickness and the tracer experiment was observed. This difference was mainly explained by the temperature at which the two experiments were conducted: 90°C and 25°C. Despite the temperature correction, some differences remain, which several hypotheses can explain:

i) The diffusion coefficient calculated based on the gel layer thickness reflects the continuous evolution of transport properties of the gel during alteration, while the one derived from the tracer experiment only accounts for the final transport properties of the gel layer.

ii) A difference in diffusivity may exist within the gel depending on whether the element is incorporated from the solution (tracer experiment) or released to it (alteration experiment).

iii) The gel may have continued its densification reaction between the end of the alteration experiment and the beginning of the tracer one, resulting in an underestimation of the diffusion coefficient based on the later.

Finally, the comparison between the incorporation of ^{10}B and S^- during the tracer experiment reveals a strong correlation between the behaviors of the two elements that might be explained by i) the size of pores and diffusion channels that is not selective enough or ii) the speciation of B, which leads to the formation of dimers and, consequently, molecules with a larger size. If these species prevail, the size difference between the two tracers may be weak, explaining the similar diffusion coefficient results.

Overall, this study evidence the gel layer formation mechanism and provide insight on the calcium effect on its formation at short timescales. The precision of each method to determine a diffusion coefficient is discussed and the results support a diffusion coefficient that is slightly lower than the one in the literature.

DATA AVAILABILITY STATEMENT

The authors declare that the data supporting the findings of this study are available on demand (benjamin.cagnon@univ-grenoble-alpes.fr)

ACKNOWLEDGEMENTS

The authors thank Simona Denti (ISTerre), Delphine Tisserand (ISTerre), Sylvain Campillo (ISTerre) and Sabine Santenac (ISTerre) for helping and providing advice with the ICP-OES analysis. The authors are grateful to Loan Lai, Elodie Chauvet, Amandine David, Florian Cousy and Yves Depuydt from Tescan Analytics for performing ToF-SIMS analyses and operating FIB thin sections. Nicolas Michau and Christelle Martin from Andra, and Theo Montaigne from EDF are thanked for their inputs on an earlier version of this manuscript. This work was funded by Andra and EDF.

COMPETING INTERESTS

The authors declare no competing interests.

AUTHOR CONTRIBUTIONS

B.C. performed the experiments and analyzed data. M.C. performed and analyzed the TEM measurements as well as STEM-EDX characterization. D.D. and S.G. analyzed data and supervised the research. B.C., D.D., and S.G. wrote the manuscript, with contributions from all authors.

REFERENCES

1 Huntington, T. *et al.* Calcium depletion in a southeastern United States forest ecosystem. *Soil Science Society of America Journal* **64**, 1845-1858 (2000).

2 Daval, D. Carbon dioxide sequestration through silicate degradation and carbon mineralisation: promises and uncertainties. *npj Materials Degradation* **2**, 11, doi:10.1038/s41529-018-0035-4 (2018).

3 Grambow, B. Nuclear Waste Glasses - How Durable? *Elements* **2**, 357-364, doi:10.2113/gselements.2.6.357 (2006).

4 Frankel, G. S. *et al.* Recent Advances in Corrosion Science Applicable To Disposal of High-Level Nuclear Waste. *Chemical Reviews* **121**, 12327-12383, doi:10.1021/acs.chemrev.0c00990 (2021).

5 Gin, S., Delaye, J.-M., Angeli, F. & Schuller, S. Aqueous alteration of silicate glass: state of knowledge and perspectives. *npj Materials Degradation* **5**, 42, doi:10.1038/s41529-021-00190-5 (2021).

6 Zapol, P., He, H., Kwon, K. D. & Criscenti, L. J. First-Principles Study of Hydrolysis Reaction Barriers in a Sodium Borosilicate Glass. *International Journal of Applied Glass Science* **4**, 395-407, doi:https://doi.org/10.1111/ijag.12052 (2013).

7 K. Ferrand, A. A., B. Grambow,. Water diffusion in the simulated French nuclear waste glass SON 68 contacting silica rich solutions: Experimental and modeling,. *Journal of Nuclear Materials* **355**, 54-67, doi:https://doi.org/10.1016/j.jnucmat.2006.04.005 (2006).

8 Collin, M., Fournier, M., Charpentier, T., Moskura, M. & Gin, S. Impact of alkali on the passivation of silicate glass. *npj Materials Degradation* **2**, 16 (2018).

9 Petit, J. C., Dellamea, G., Dran, J. C., Schott, J. & Berner, R. A. MECHANISM OF DIOPSIDE DISSOLUTION FROM HYDROGEN DEPTH PROFILING. *Nature* **325**, 705-707 (1987).

10 Diane Rebiscoul, P. F., Stéphane Gin, André Ayral,. Protective properties and dissolution ability of the gel formed during nuclear glass alteration. *Journal of Nuclear Materials* **342**, 26-34, doi:https://doi.org/10.1016/j.jnucmat.2005.03.018 (2005).

11 Fournier, M. *et al.* Effect of pH on the stability of passivating gel layers formed on International Simple Glass. *Journal of Nuclear Materials* **524**, 21-38, doi:https://doi.org/10.1016/j.jnucmat.2019.06.029 (2019).

12 Gin, S. *et al.* A general mechanism for gel layer formation on borosilicate glass under aqueous corrosion. *The Journal of Physical Chemistry C* **124**, 5132-5144 (2020).

13 Vienna, J. D., Ryan, J. V., Gin, S. & Inagaki, Y. Current Understanding and Remaining Challenges in Modeling Long-Term Degradation of Borosilicate Nuclear Waste Glasses. *International Journal of Applied Glass Science* **4**, 283-294, doi:https://doi.org/10.1111/ijag.12050 (2013).

14 Rebiscoul, D. *et al.* Morphological evolution of alteration layers formed during nuclear glass alteration: new evidence of a gel as a diffusive barrier. *Journal of Nuclear Materials* **326**, 9-18, doi:http://dx.doi.org/10.1016/j.jnucmat.2003.10.015 (2004).

15 Nathalie Valle, A. V.-C., Jérôme Sterpenich, Guy Libourel, Etienne Deloule, Patrick Jollivet,. Elemental and isotopic (29Si and 18O) tracing of glass alteration mechanisms. *Geochim Cosmochim Ac* **74**, 3412-3431, doi:https://doi.org/10.1016/j.gca.2010.03.028 (2010).

16 Grambow, B. & Muller, R. First-order dissolution rate law and the role of surface layers in glass performance assessment. *Journal of Nuclear Materials* **298**, 112-124 (2001).

17 Bourcier, W. L., Peiffer, D. W., Knauss, K. G., McKeegan, K. D. & Smith, D. K. A Kinetic Model for Borosilicate Glass Dissolution Based on the Dissolution Affinity of a Surface Alteration Layer. *MRS Online Proceedings Library Archive* **176**, null-null, doi:doi:10.1557/PROC-176-209 (1989).

18 Jollivet, P. *et al.* Investigation of gel porosity clogging during glass leaching. *Journal of Non-Crystalline Solids* **354**, 4952-4958, doi:10.1016/j.jnoncrysol.2008.07.023 (2008).

19 Gin, S. *et al.* Dynamics of self-reorganization explains passivation of silicate glasses. *Nature communications* **9**, 2169 (2018).
20 Cailleteau, C. *et al.* Insight into silicate-glass corrosion mechanisms. *Nature Materials* **7**, 978-983, doi:10.1038/nmat2301 (2008).
21 Casey, W. H. GLASS AND MINERAL CORROSION Dynamics and durability. *Nature Materials* **7**, 930-932, doi:10.1038/nmat2326 (2008).
22 Maraghechi, H., Rajabipour, F., Pantano, C. G. & Burgos, W. D. Effect of calcium on dissolution and precipitation reactions of amorphous silica at high alkalinity. *Cement and Concrete Research* **87**, 1-13, doi:https://doi.org/10.1016/j.cemconres.2016.05.004 (2016).
23 Mercado-Depierre, S., Angeli, F., Frizon, F. & Gin, S. Antagonist effects of calcium on borosilicate glass alteration. *Journal of Nuclear Materials* **441**, 402-410, doi:https://doi.org/10.1016/j.jnucmat.2013.06.023 (2013).
24 Liu, S., Ferrand, K. & Lemmens, K. Transport- and surface reaction-controlled SON68 glass dissolution at 30°C and 70°C and pH=13.7. *Appl Geochem* **61**, 302-311, doi:https://doi.org/10.1016/j.apgeochem.2015.06.014 (2015).
25 Ferrand, K. *et al.* Dissolution Kinetics of International Simple Glass and Formation of Secondary Phases at Very High Surface Area to Solution Ratio in Young Cement Water. *Materials* **14** (2021).
26 Neeway, J. J. *et al.* Acceleration of glass alteration rates induced by zeolite seeds at controlled pH. *Appl Geochem* **113**, 104515, doi:https://doi.org/10.1016/j.apgeochem.2019.104515 (2020).
27 Ribet, S. & Gin, S. Role of neoformed phases on the mechanisms controlling the resumption of SON68 glass alteration in alkaline media. *Journal of Nuclear Materials* **324**, 152-164, doi:https://doi.org/10.1016/j.jnucmat.2003.09.010 (2004).
28 Ebert, W. L. & Bates, J. K. A Comparison of Glass Reaction at High and Low Glass Surface/Solution Volume. *Nuclear Technology* **104**, 372-384, doi:10.13182/nt93-a34898 (1993).
29 Van Iseghem, P. & Grambow, B. The Long-Term Corrosion and Modelling of Two Simulated Belgian Reference High-Level Waste Glasses. *MRS Proceedings* **112**, 631, doi:10.1557/proc-112-631 (1987).
30 Gin, S., Beaudoux, X., Angéli, F., Jégou, C. & Godon, N. Effect of composition on the short-term and long-term dissolution rates of ten borosilicate glasses of increasing complexity from 3 to 30 oxides. *Journal of Non-Crystalline Solids* **358**, 2559-2570, doi:https://doi.org/10.1016/j.jnoncrysol.2012.05.024 (2012).
31 Gin, S. *et al.* An international initiative on long-term behavior of high-level nuclear waste glass. *Materials Today* **16**, 243-248, doi:https://doi.org/10.1016/j.mattod.2013.06.008 (2013).
32 Dove, P. M. & Nix, C. J. The influence of the alkaline earth cations, magnesium, calcium, and barium on the dissolution kinetics of quartz. *Geochim Cosmochim Ac* **61**, 3329-3340, doi:Doi 10.1016/S0016-7037(97)00217-2 (1997).
33 Wallace, A. F., Gibbs, G. V. & Dove, P. M. Influence of Ion-Associated Water on the Hydrolysis of Si−O Bonded Interactions. *The Journal of Physical Chemistry A* **114**, 2534-2542, doi:10.1021/jp907851u (2010).
34 Aréna, H. *et al.* Impact of Fe, Mg and Ca elements on glass alteration: Interconnected processes. *Geochim Cosmochim Ac* **239**, 420-445, doi:https://doi.org/10.1016/j.gca.2018.08.007 (2018).
35 CHAVE, T., Frugier, P., Gin, S. & Ayral, A. Glass–water interphase reactivity with calcium rich solutions. *Geochim Cosmochim Ac* **75**, 4125 - 4139, doi:10.1016/j.gca.2011.05.005 (2011).
36 Damodaran, K., Delaye, J.-M., Kalinichev, A. G. & Gin, S. Deciphering the non-linear impact of Al on chemical durability of silicate glass. *Acta Materialia*, 117478, doi:https://doi.org/10.1016/j.actamat.2021.117478 (2021).

37 Ryan, J. V. *et al.* ISG-2: properties of the second International Simple Glass. *npj Materials Degradation* **7**, 47, doi:10.1038/s41529-023-00352-7 (2023).
38 Wild, B. *et al.* pH-dependent control of feldspar dissolution rate by altered surface layers. *Chem Geol* **442**, 148-159, doi:http://dx.doi.org/10.1016/j.chemgeo.2016.08.035 (2016).
39 Daval, D. *et al.* Mechanism of wollastonite carbonation deduced from micro- to nanometer length scale observations. *Am Mineral* **94**, 1707-1726, doi:10.2138/am.2009.3294 (2009).
40 Damodaran, K., Gin, S., De Montgolfier, J.-V., Jegou, C. & Delaye, J.-M. Behavior of B in passivating gels formed on International Simple Glass in acid and basic pH. *Journal of Non-Crystalline Solids* **598**, 121938, doi:https://doi.org/10.1016/j.jnoncrysol.2022.121938 (2022).
41 Gin, S. *et al.* Insights into the mechanisms controlling the residual corrosion rate of borosilicate glasses. *npj Materials Degradation* **4**, 1-9 (2020).
42 Gin, S. *et al.* The fate of silicon during glass corrosion under alkaline conditions: A mechanistic and kinetic study with the International Simple Glass. *Geochim Cosmochim Ac* **151**, 68-85, doi:https://doi.org/10.1016/j.gca.2014.12.009 (2015).
43 Gin, S. *et al.* Origin and consequences of silicate glass passivation by surface layers. *Nat Commun* **6**, doi:10.1038/ncomms7360 (2015).
44 Cagnon, B., Daval, D., Cabié, M., Lemarchand, D. & Gin, S. A comparative study of the dissolution mechanisms of amorphous and crystalline feldspars at acidic pH conditions. *npj Materials Degradation* **6**, 34, doi:10.1038/s41529-022-00240-6 (2022).
45 Mesmer, R. E., Baes, C. F., Jr. & Sweeton, F. H. Acidity measurements at elevated temperatures. VI. Boric acid equilibriums. *Inorganic Chemistry* **11**, 537-543, doi:10.1021/ic50109a023 (1972).
46 Janda, R. & Heller, G. Ramanspektroskopische Untersuchungen an festen und in Wasser gelösten Polyboraten / Investigations of Solid Polyborates and their Aqueous Solutions by Raman Spectroscopy. **34**, 585-590, doi:doi:10.1515/znb-1979-0411 (1979).
47 Schmidt, C., Thomas, R. & Heinrich, W. Boron speciation in aqueous fluids at 22 to 600°C and 0.1 MPa to 2 GPa. *Geochim Cosmochim Ac* **69**, 275-281, doi:https://doi.org/10.1016/j.gca.2004.06.018 (2005).
48 Ingri, N. *et al.* Equilibrium Studies of Polyanions. 8. On the First Equilibrium Steps in the Hydrolysis of Boric Acid, a Comparison between Equilibria in 0.1 M and 3.0 M NaClO4. *Acta Chemica Scandinavica* **16**, 439-448 (1962).
49 Kim, Y. & Kirkpatrick, R. J. 11B NMR investigation of boron interaction with mineral surfaces: Results for boehmite, silica gel and illite. *Geochim Cosmochim Ac* **70**, 3231-3238, doi:https://doi.org/10.1016/j.gca.2006.04.026 (2006).
50 Saldi, G. D., Louvat, P., Schott, J. & Gaillardet, J. The pH dependence of the isotopic composition of boron adsorbed on amorphous silica. *Geochim Cosmochim Ac* **308**, 1-20, doi:https://doi.org/10.1016/j.gca.2021.05.052 (2021).

Supplementary Information

Impact of calcium on ISG alteration in alkaline conditions at 90°C: Mechanism of formation and transport properties of the gel layer

Benjamin Cagnon[1], Stéphane Gin[2], Martiane Cabié[3], and Damien Daval[1]

[1] Univ. Grenoble Alpes, Univ. Savoie Mont Blanc, CNRS, IRD, IFSTTAR, ISTerre, Grenoble, France

[2] CEA, DES, DPME, SEME, University of Montpellier, Marcoule, France

[3] Aix Marseille Univ, CNRS, Centrale Marseille, FSCM, CP2M, Marseille, France

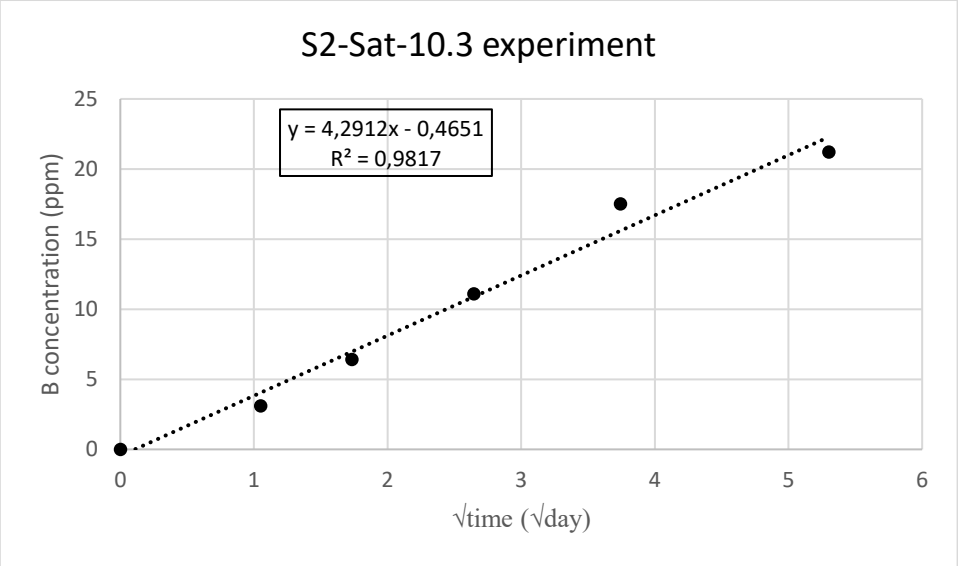

Supplementary Figure IV-1: Plots representing the concentration of B (ppm) in the solution as a function of the square root of time (day) for the experiment S2-Sat-10.3 from Fournier et al., 2019. A correlation is found with $R^2 = 0.98$.

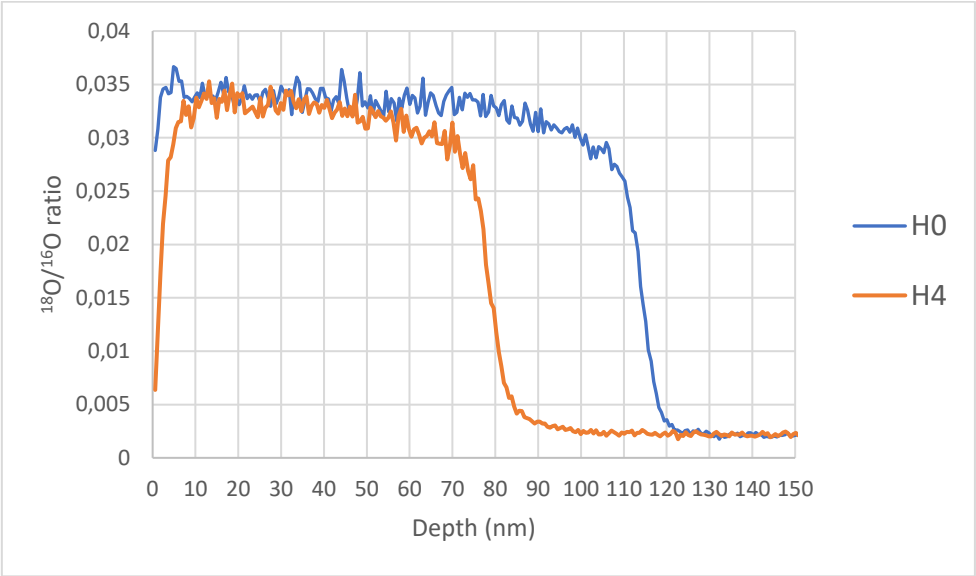

Supplementary Figure IV-2: Depth profiles of $^{18}O/^{16}O$ collected by a second ToF-SIMS analyses performed only on H0 and H4. The profiles were normalized to the natural abundance in the pristine glass.

Chapitre V. INTERNATIONAL SIMPLE GLASS (ISG) DISSOLUTION RATE IN A (Si, Ca)-RICH ENVIRONMENT AT 90°C AND ALKALINE CONDITIONS

Le chapitre précédent a révélé que le Ca avait un rôle modeste mais mesurable sur les propriétés de transport du gel formé sur ISG aux temps courts. Dans le présent chapitre, la dissolution du verre ISG a été étudiée à 90°C en condition basique avec différentes concentrations de Si et de Ca dissous pour comprendre les effets combinés de ces éléments sur la réactivité du verre. Les expériences ont été menées sur un temps court (environ 20 jours) et un temps long (environ 3 mois). À travers des caractérisations morphologiques, structurales et chimiques, nous montrons que la vitesse de dissolution du verre est fortement corrélée à l'activité de la silice en solution. La présence de calcium n'impacte pas significativement l'altération du verre. La précipitation des phases de silicates de calcium hydratés (CSH) pendant les expériences à temps long, a augmenté mais de manière assez faible la vitesse de dissolution du verre ISG. Les expériences de 3 mois ont souligné la forte corrélation entre le mécanisme de dissolution et l'évolution de la nature des phases secondaires en solution. Au cours des 20 premiers jours, les CSH ont précipité et se sont agrégés, sans impacter les propriétés de passivation du gel à la surface du verre : la dissolution du verre était principalement limitée par un mécanisme de diffusion. Entre le 19e jour et le 76e jour, une reprise d'altération s'est produite. Cette augmentation de la vitesse d'altération du verre a été attribuée à la croissance des CSH. Un possible changement mécanistique vers une vitesse d'altération contrôlée par l'hydrolyse a eu lieu. Enfin, dans certaines expériences, une baisse du pH due à la précipitation de carbonate a été observée, avec une diminution de la vitesse de dissolution du verre, revenant à un régime limité par la diffusion. Dans l'ensemble, cette étude montre qu'à $pH_{(90°C)}$ = 10 et avec des concentrations en Si > 50% de la saturation par rapport à la silice amorphe, indépendamment de la concentration en Ca, le verre ISG présente une très bonne durabilité chimique.

Le chapitre V fait l'objet d'un manuscrit en préparation pour la revue Journal of Nuclear Materials : "Cagnon, B., Gin, S., Cabié, M. & Daval, D. (in prep.). International Simple Glass (ISG) dissolution rate in a (Si, Ca)-rich environment at 90°C and alkaline conditions."

International Simple Glass (ISG) dissolution rate in a (Si, Ca)-rich environment at 90°C and alkaline conditions

Benjamin Cagnon[1], Stéphane Gin[2], Martiane Cabié[3] and Damien Daval[1]

[1] Univ. Grenoble Alpes, Univ. Savoie Mont Blanc, CNRS, IRD, IFSTTAR, ISTerre, Grenoble, France

[2] CEA, DES, DPME, SEME, University of Montpellier, Marcoule, France

[3] Aix Marseille Univ, CNRS, Centrale Marseille, FSCM, CP2M, Marseille, France

Correspondence : B. Cagnon (benjamin.cagnon@univ-grenoble-alpes.fr)

ABSTRACT

The dissolution of International Simple Glass (ISG) was investigated at 90°C and alkaline conditions with various concentrations of dissolved Si and Ca to unravel the combined effects of those elements on ISG reactivity. Experiments were conducted for 20 days up to 3 months. Through morphology, structural and chemical characterizations, the glass dissolution rate was proven to be strongly correlated with the activity of dissolved silica in the solution. While dissolved calcium did not significantly impact the dissolution rate, precipitation of calcium silicate hydrates (CSH) phases during the experiments enhanced ISG dissolution rate, though to a modest extent. The 3-months experiments highlighted the strong correlation between the dissolution mechanism and the evolution of the nature of secondary phases in saturated solution. During the first 20 days and at elevated Si and Ca concentrations, CSH precipitated and aggregated, without preventing the passivating impact of the gel layer at the surface of the glass: the dissolution was controlled by diffusion. Then, a resumption of dissolution occurred between 19 days and 76 days, corresponding to the CSH growth, and a possible mechanistic switch to a hydrolysis-controlled reaction rate. Finally, in some experiments, a drop in pH due to carbonate precipitation was observed along with a decrease in the dissolution rate, falling back in a diffusion-limited regime. Overall, this study shows that at pH(90°C) = 10 and concentrations of Si > 50% of saturation with respect to amorphous silica, irrespective of Ca concentration, ISG exhibits a very good chemical durability.

V.1.INTRODUCTION

For decades, several countries have produced borosilicate glass to confine high level radioactive waste arising from reprocessing of spent nuclear fuel[1]. After cooling and interim storage, glass canisters will be disposed in a deep geological repository. The safety demonstration of such a disposal relies on a multi-barrier system in which glass is the primary barrier. Studying the long-term behavior of these materials represents a challenge for the scientific community as glass dissolution results from multiple processes which in turn depends on several intrinsic and environmental parameters[2-6]. One of the main scenarios of glass degradation involves a solution enriched in Si and Ca, which alters the glass under alkaline conditions. To better understand basic mechanisms of glass dissolution, nuclear glass research community selected a six-oxide borosilicate glass called International Simple Glass (ISG) to provide a common benchmark material[7]. Many studies investigated the dissolution rate and dissolution mechanisms of this glass according to various parameters such as the pH, the temperature, silica concentration and calcium concentration as well as the Si-Ca interaction forming secondary phases[4,5,8-15]. Some of the main findings are briefly recalled below.

The dissolution rate of ISG has been investigated by several studies as a function of pH and temperature[8,16,17]. The relation between the initial dissolution rate and the pH was further evidenced by Inagaki et al., 2013[8] as a "V-shaped" curve with a minimum dissolution rate at pH 4 for temperatures ranging from 25°C to 90°C. With several other studies[4,14,18], the authors supported a surface-reaction mechanism controlling the initial dissolution rate in a vast range of pH (1 – 10.7).

Focusing on ISG and the stability of gel alteration layers in silica saturated solution and deionized water, Fournier et al., 2019[14] highlighted a negligible effect of the concentration of dissolved silica on the dissolution rate of ISG under acidic conditions, up to pH 7. The passivating gel layer formed at higher pH (around pH 9) undergoes an *in-situ* reorganization, resulting in the decrease of the rate of the underlying glass[15]. However, this passivating layer becomes unstable when the pH increases, leading to the alteration resumption[14,15]. The presence of secondary phases at pH(90°C) > 10.1, such as calcium silicate hydrates (CSH) or zeolites neoformations, is also detrimental for the passivating properties of the gel[15,19] and can promote the hydrolysis of the silica network which becomes the driving force of the alteration resumption[15].

Regarding calcium, antagonist effects on glass dissolution rate were highlighted by several studies depending on the pH, the glass surface-area-to-solution-volume ratio (SA/V) and then the concentration of Ca[20-23]. Four different behaviors were proposed by Mercado-Depierre et al., 2013[9]:

(i) at pH 7 – 8 and low SA/V ratio (25 – 50 m^{-1}), Ca formed metal complex on the surface of the material, increasing the initial dissolution rate of the glass.

(ii) at similar SA/V ratio but in basic pH conditions, Ca penetrated within the gel layer and due to Ca-Si reactivity, its transport properties decreased and thus, the initial dissolution rate was significantly reduced[20].

Those two cases (i) and (ii) correspond to scenarios where the low concentration of Si in solution prevented the precipitation of CSH and other Si-bearing secondary phases.

(iii) at a high SA/V ratio (1 000 – 20 000 m^{-1}) and near neutral pH conditions, a Si-Ca rich passivating layer was suspected to form at the surface [9]. Furthermore, calcium also played a catalytic role in the densification of the gel layer, leading to the closure of porosity and then, a decrease in the transport properties of the gel layer[10]. The presence of elements poorly soluble such as Al can enhance the passivating properties of the gel[24,25].

(iv) at high SA/V ratio and basic pH, the solution is rapidly supersaturated with respect to CSH. As long as CSH precipitate, it was suggested that the glass dissolve at a rate close to the initial dissolution rate[21,26]. Conversely, Maraghechi (2016)[23] proposed a protective layer formed by a dense, non-porous and strongly bounded CSH layer on the surface of the glass that could limit the glass dissolution rate.

It is widely known that the formation of secondary phases such as zeolites or CSH can significantly increase the dissolution rates of silicate glasses[9,27,28], especially in hyperalkaline pH[29]. However, some recent studies in which ISG was altered under alkaline conditions in young cement water reported the formation of secondary phases identified as zeolites and phyllosilicates, either without CSH[30], or with CSH having a low Ca/Si ratio[26] with no resumption of glass dissolution. This observation was related to the decrease in pH after some time of experiment[26]. The formation of CSH follows the general law of nucleation where the degree of supersaturation in solution controls the homogenous nucleation rate[31]. However, a most recent study demonstrated a two-steps CSH formation process. The first step consists in the formation of amorphous dispersed spheroids which are depleted in Ca compared to regular CSH (meaning a ratio of Ca/Si < 0.6) and sodium plays the role of a charge compensator. After some time, the amorphous spheroids aggregate and sodium is exchanged with calcium, leading to the crystallization of the aggregates into a tobermorite-type CSH[32-34](Ca/Si ratio close to 0.8). Other crystalline CSH phases have been under study over the years. Blanc et al., 2010[35,36] summarized the thermodynamic properties of nanocrystalline and crystalline CSH phases with various structures.

In presence of carbon dioxide, CSH phases are metastable and are susceptible to carbonation. This process has been extensively investigated[37-43]. The Ca/Si ratio strongly influences the carbonation

resistance of the CSH, but a consensus is yet to be reached on this issue. Some studies support that a lower Ca/Si ratio implied a higher carbonation resistance[44] and other studies support the opposite[38,43], i.e., CSH with a lower Ca/Si ratio tend to decompose faster in presence of carbonate. Due to their carbonation properties, some studies were carried out to investigate the sequestration of CO_2 using various calcium silicate hydrated phases[37,45,46]. The carbonation of CSH leads to mainly four carbonate by-products which are aragonite, vaterite, calcite and amorphous carbonate[40,47]. Following the CSH decomposition, a silica gel is formed. Liu et al., 2022[37] demonstrated that the by-products of carbonation, their proportions and the carbonation rate is strongly related with the initial Ca/Si ratio in the CSH. On another note, they divided the carbonation process into 3 steps: a dissolution period where a progressive decrease of both Ca/Si and pH is observed with the formation of calcium carbonate, a diffusion period where small portions of CSH crosslink, leading to an amorphous phase they called "calcium modified silica gel", and a reaction period where the CSH fully dissolve into calcium carbonates with the amorphous phases remaining as a calcium modified silica gel.

Of note, another impact of Ca had also been reported at various temperatures (from 30°C to 90°C), and at high pH (near pH 12.5), in presence of boron[12]. Initially, dissolved Ca precipitated with the boron leached from the borosilicate sample to form $Ca[B(OH)_4]_2(s)$. To some extent, this first precipitate can prevent the glass dissolution by limiting the hydrolysis of the silicate matrix. However, when the solubility limit of CSH was reached, $Ca[B(OH)_4]_2(s)$ became unstable and dissolved, releasing $B(OH)_4^-$ and Ca^{2+} into the solution. The calcium was then consumed to form increasing amounts of CSH, promoting the glass dissolution by trapping the silicon from the solution and from the borosilicate material [21,26]. In conclusion, the presence of B in the Ca-Si system resulted in an incubation period at the beginning of the glass dissolution process. This incubation period is shorter as the temperature increases (from 30°C to 70°C) and almost disappears at 90°C.

Overall, the dissolution rate of borosilicate glass has been previously studied as a function of various parameters such as pH and temperature. The effect of Si and Ca were also investigated separately from each other. The formation of CSH during the dissolution of silicate glass was observed but their effect on the dissolution rate remains debated. Furthermore, a proper understanding of the combined effect of Si and Ca on the dissolution rate during the full process of CSH formation and carbonation is still lacking.

This study attempts to address these concerns, focusing on the evolution of ISG dissolution in Si- and/or Ca-rich solutions at 90 °C and pH (90 °C) =10 (except when mentioned, all pHs below are given at 90 °C). The effect of CSH neoformation on the ISG dissolution rate and insights on the CSH formation kinetics during 20-day and 3-month experiments are reported.

V.2.MATERIALS AND METHODS

V.2.1. Overall presentation

Tableau V-1: Summary of the initial conditions for all series run in the present study. The first column refers to the name of the experiment. The second and third columns refer to the $SiO_2(aq)/SiO_2(aq)_{eq}$ ratio and the concentration of Ca (ppm) in the solution. The fourth and fifth columns refer to the logarithm of the activity of $SiO_2(aq)$ and that of the $Ca^2/H+^2$ activity ratio. The sixth column refers to the duration of the experiment at the time of collection. The seventh, eighth and ninth column refer to the difference in Gibbs energy related to the dissolution of CSH0.8, CSH1.2 and CSH1.6 respectively based on JChess calculations. Note that the concentration of Ca reported with (*) are the theoretical values based on weighing, as the ICP-OES analyses failed for the corresponding samples.

Name	Si/Si_{eq}	Ca(ppm)	$log(a(SiO_2))$	$Log[a(Ca^{2+})/a(H^+)^2]$	Time (days)	ΔG(CSH0.8) ($J.mol^{-1}$)	ΔG(CSH1.2) ($J.mol^{-1}$)	ΔG(CSH1.6) ($J.mol^{-1}$)
D1	44%	0.01	-2.820	13.173	15.1	-5682.7	-11212.3	-17436.4
E2	79%	1.00	-2.462	14.891	14.0	-448.9	-3902.6	-8050.8
F1	0%	280.30	-5.074	17.457	18.0	-2140.6	-2494.9	-3543.8
F2	0%	276.90	-5.044	17.459	18.0	-2044.5	-2395.6	-3441.3
F3	1%	264.20	-4.555	17.428	18.0	-640.5	-1029.3	-2112.6
G2	0%	9.10	-4.863	16.087	17.0	-4813.2	-6822.2	-9525.8
G3	0%	60*	-4.877	16.604	17.0	-3603.2	-4987.0	-7065.4
G4	0%	380*	-4.880	16.466	17.0	-3947.6	-5498.6	-7744.2
G5	0%	780*	-4.889	16.762	17.0	-3258.7	-4452.2	-6340.3
Gbis1	2%	5.30	-4.033	15.889	17.1	-2783.2	-5031.6	-7974.6
Gbis2	2%	44.90	-4.062	16.751	17.1	-787.2	-1993.7	-3894.9
H0	35%	2.50	-2.697	13.964	21.0	-3402.4	-7976.6	-13245.3
H1	54%	1.72	-2.528	15.133	21.0	-64.7	-3226.1	-7082.1
H2	55%	73.91	-2.512	16.756	21.0	3903.5	2703.0	807.9
H3	57%	117.26	-2.512	16.936	21.0	4338.1	3355.0	1677.2
H4	56%	280*	-2.521	16.450	21.0	3139.3	1569.2	-695.6
I4	49%	639.76	-2.615	17.846	23.8	6227.6	6344.1	5766.1
Hbis1	84%	7.00	-2.353	15.863	19.0	2227.9	-51.1	-3024.8
Hbis2	86%	55.56	-2.350	16.759	19.0	4400.9	3204.3	1313.0
Hbis3	86%	299.48	-2.362	17.468	101.0	6078.4	5737.5	4702.0
Hbis4	100%	761.89	-2.321	17.832	101.0	7079.7	7178.9	6583.5
J3	97%	449.10	-2.321	17.620	101.0	6567.9	6411.2	5560.0
J3bis	44%	149.73	-2.626	17.261	101.0	4781.5	4190.8	2905.6
J4	82%	764.95	-2.406	17.859	101.0	6890.3	7022.3	6459.7
J4bis	103%	894.25	-2.317	17.893	101.0	7242.2	7415.5	6894.1
K1	9%	1.64	-3.266	15.480	21.0	-1454.1	-4193.1	-7628.6
K3	18%	0.03	-2.975	13.720	21.0	-4827.0	-9691.9	-15253.3

Various series of experiments were conducted at 90°C to unfold the relation between the concentration of Si and Ca in solution and the alteration of ISG samples in alkaline conditions. Si and Ca are expected to interact and potentially form CSH. The composition domain that we investigated was delimited by the solubility of amorphous silica ($SiO_2(am)$) for the Si endmember, and portlandite ($Ca(OH)_2$) for Ca endmember. Using the thermodynamic code JChess[48] and the Thermochimie database

provided by Andra[35,36,49-52] (https://www.thermochimie-tdb.com/), the domain of stability of CSH was calculated with 3 different Ca/Si ratios that are provided in the database (CSH0.8, CSH1.2 and CSH1.6, where each number refers to the Ca/Si ratio in the structure of the CSH). Those solubility lines are displayed in Fig. V-4 to evidence their domain of stability in the activity diagram.

The saturation state of the solution with respect to amorphous silica corresponds to a theoretical concentration of dissolved Si of 8.75 $x10^{-2}$ $mol.L^{-1}$ at pH = 10. The activity of $H_4SiO_4(aq)$ in these conditions corresponds to 0.0052 molal, which determines the solubility limit of $SiO_{2(am)}$ in the activity diagram (see Fig. V-4), i.e., $\log(a(SiO_2)) = -2.286$. Regarding calcium, the saturation with respect to portlandite corresponds to 1.5 $x10^{-1}$ $mol.L^{-1}$ at pH 10. The equilibrium activity of Ca^{2+} (0.034447 molal) and the activity of H^+ (8.0058 $x10^{-11}$ molal) provide the solubility limit of portlandite under such conditions, i.e., $\log(a(Ca^{2+})/a(H^+)^2) = 18.73$.

The domain of precipitation of CSH is clearly defined and several experiments were conducted to investigate the reactivity of ISG in this field of thermodynamic conditions. The name and initial conditions of each series are described in Table V-1.

As the experiments were conducted in static conditions, a shift in pH and solution composition was expected, as the solution was not restricted precisely to a specific, well-defined condition. Flow-through experiments would have had the ability to circumvent this issue. However, the likely precipitation of secondary phases in tubings prevented us from conducting the experiments in flow-through set-ups. In case of experiments conducted near the saturation state with respect to amorphous silica, the high level of dissolved Si species contributed to buffer the solution since H_4SiO_4 is a weak acid.

V.2.2. Experiment preparation

The ISG used in this study is referred to as ISG-1 (wt% 56.2 SiO_2, 17.3 B_2O_3, 12.2 Na_2O, 6.1 Al_2O_3, 5.0 CaO, 3.3 ZrO_2) and its elaboration conditions is detailed in Ryan et al., 2022[53]. Glass coupons with dimensions of 2x2x0.1 cm^3 originated from CEA Marcoule, France, were polished by PrimeVerre, France, following their 6 faces with a 1/4 µm diamond grain paste at the last step. Once polished, ISG coupons were cut into smaller pieces using a diamond saw. From the series G, a small part (<1 mm^2, on average <5% of the polished surface) of the top and bottom surfaces of ISG samples was protected with room-temperature-vulcanizing (RTV) glue spots to create a non-reacted reference surface used for subsequent topography analyses run with vertical scanning interferometry (VSI, see below). From the series I, the entire ISG glass coupon was used for the experiment, and 4 small parts of the top and bottom surfaces were protected with RTV glue. Once the experiment was over, the coupon was cut

into smaller pieces using a diamond saw in dry conditions in order to prevent further degradation of the materials after the experiment due to the presence of a solvent.

The experiments were conducted in solutions with various concentrations of Ca and Si (see Table V-1). A first solution was saturated with respect to amorphous silica (SiO_2(am)) using nanopowder silica (specific surface area 175 – 225 $m^2.g^{-1}$, 99.8% trace metals basis). The pH was measured at high temperature (90°C) and adjusted to 10.1 ± 0.1 by addition of LiOH (Prolabo) on a daily basis. After the solution stabilized (approximately 10 days), the CO_2 in the solution was removed by degassing with N_2 (0.15 $L.min^{-1}$) at high temperature (near water ebullition, T > 90°C) during 30 min for 500 ml of solution. The presence of dissolved CO_2 in the solution favors the precipitation of calcium carbonate, preventing possible reaction between calcium and dissolved silica. PFA Savillex® vessels, containing a PTFE tripod for the first series (up to series F) or a Teflon basket (from series F onwards), were filled with approximately 50 mL of solution and placed in a N_2 atmosphere-controlled glove box. The appropriate amount of Ca was added to each reactor by sampling aliquots from a stock solution prepared with dissolved $CaCl_2$. Only 1 mL or 2 mL of solution containing Ca was added. The addition of calcium during the series D revealed an immediate precipitation of secondary phases. A lack of control on the chemical evolution of the solution was noticed based on this sample collection before the equilibrium of the solution. As a consequence, for all experiments (but D1), after the addition of calcium, each reactor was placed in an oven at 90°C for an incubation time of 24 h. The initial sample was collected right before the addition of the ISG glass. Each reactor was then placed in an oven at 90°C and the solutions were continuously stirred with magnetic bars. The collected sample was filtered using a 0.45 µm pore size filter before dilution. For the series I, Hbis and J, the collected sample was diluted with a factor x5, x150 and x1500 using ultrapure water (18.2 MOhm.cm) and the supernatant from the solution diluted 5x was collected before analysis with a micropipette.

After introducing the samples in the reactors containing the prepared solution, the dissolution of the glass started in the oven at 90°C (see Fig. V-1). After an intermediate timestep of 7 to 10 days, each reactor was placed in the glove box in order to collect a second sample. At the end of the experiment, every reactor was placed in the glove box to recover both the solution and the ISG coupon.

The ISG coupons were dipped three seconds in ultrapure water (18.2 MOhm.cm) before being immersed for three seconds in ethanol. They were dried and stored in the glove box at room temperature until surface analyses were conducted. After the last sampling collection of the solution, the remaining precipitates were collected with two centrifugation steps: the aim of the first one was to concentrate the solid to remove the solution and the aim of the second one, conducted in ethanol, was to remove the remaining water to ease the collection of precipitates. They were then stored in

the glove box prior to Infra-Red (IR) spectroscopy analyses and Scanning Electron Microscopy (SEM) observations coupled with Energy Dispersive X-Ray Analysis (EDX).

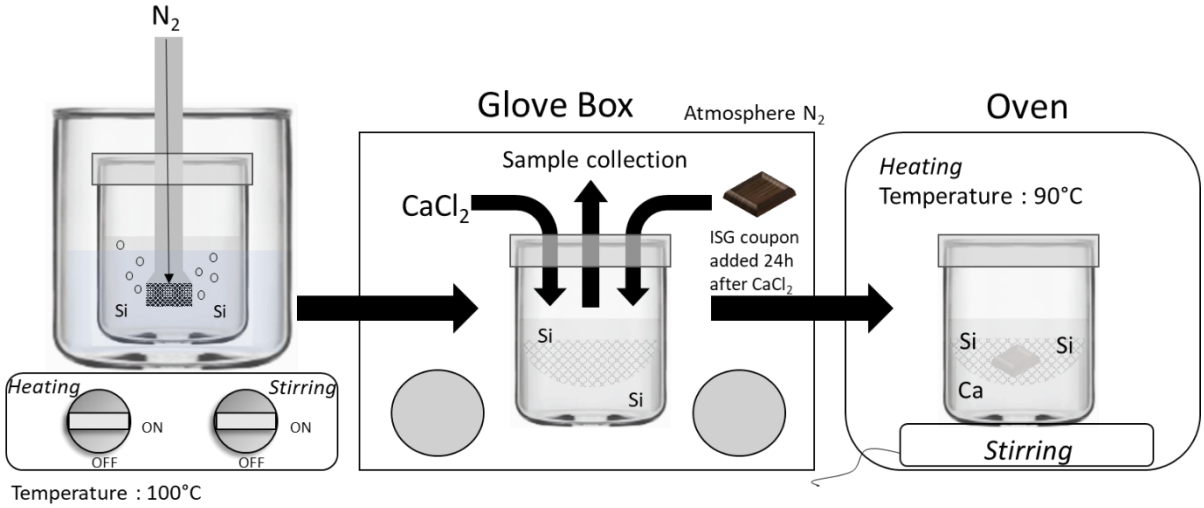

Figure V-1: Schematic representation of the various steps of experiments preparation. After degassing the 500 mL Si-rich solution with N_2 during 30min, the reactor was placed in the glove box where Ca was added in the form of $CaCl_2$ from a concentrated solution. The reactor was placed in an oven heated at 90°C for 24h and then put back in the glove box for sample collection and the addition of the ISG coupon. Finally, the reactor was placed back in the oven, which represented the onset of the dissolution experiments.

V.2.3. Fluid and solid analyses

V.2.3.1. ICP-OES analyses of aqueous solution

The dissolution process was monitored by collecting 2 mL of the solution at the beginning of the experiment, after 7 to 10 days of reaction and at the end of the experiment. The samples, filtered or not, were then diluted 5x, 150x and 1500x and analyzed with Inductively Coupled Plasma Optical Emission Spectrometer (ICP-OES) (Varian 720-ES) for Na, B, Al, Si and Ca. At each sampling duration, the concentration of Si and Ca was measured in the solution in order to account for the saturation state of the solution. The concentrations were implemented in JChess[48] to calculate the activity of those two elements and then position the chemical status of the solution in the activity diagram shown in Fig. V-4.

The measured concentrations of B and Na were used to calculate the location of the 'internal interface' (interface between the gel layer and the pristine (non-reacted) glass) and the glass dissolution rate (see Wild et al., 2016[13] for details). This dissolution rate may correspond to the growth rate of the gel layer if the external interface of the layer is stable (i.e., if it does not dissolve, as can be expected when the solution is saturated with respect to SiO_2(am)).

The equivalent thickness, $Eth(i)$ (mm), of altered glass was calculated based on ICP-OES measurements of the amount of B and Na released into the fluid, following:

$$Eth(i) = \frac{[i]_t \times F_t \times V_t}{SA \times \rho \times x(i)} \qquad (1)$$

where $[i]_t$ is the concentrations (ppm) of element *i* (B or Na) at time *t* measured by ICP-OES, F_t is the dilution factor of the aqueous sample collected at time *t*, V_t is the volume (L) of the solution in the reactor just before collection, SA is the sample surface area (mm²), ρ is the specific volume of ISG glass ($\rho = 2.498\ \mathrm{mg.mm^{-3}}$) and $x(i)$ is the mass proportion of the element *i* in ISG ($x(i) = 0.0905$ for Na in ISG and $x(i) = 0.0537$ for B in ISG). *Eth*(i) is equal to the gel layer thickness when the alteration is isovolumetric (see Fig. V-2).

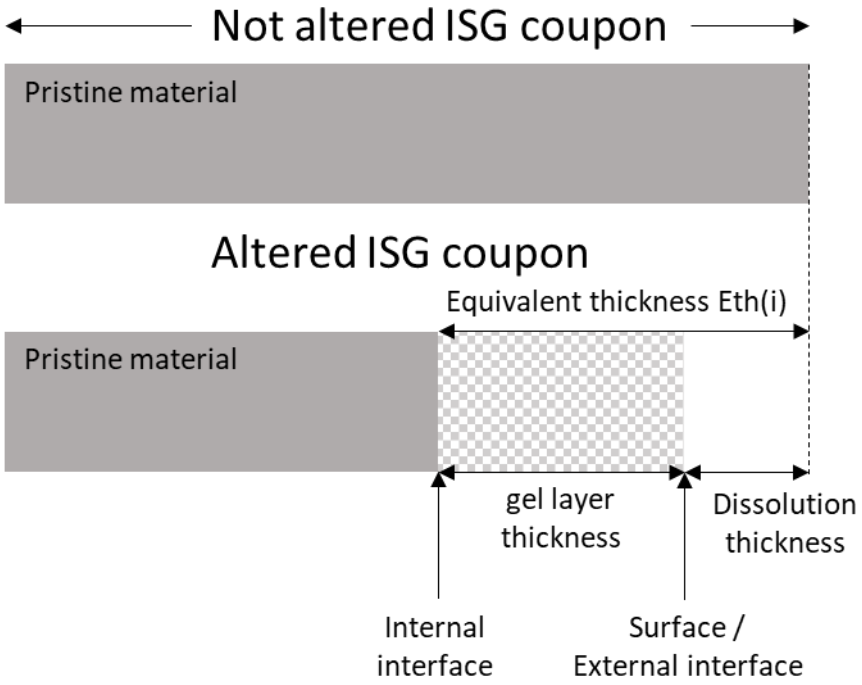

Figure V-2: Schematic representation of the interfaces and terminology used in this study.

Based on the equivalent thickness of B and Na calculated at two different stages, the corresponding dissolution rates were calculated following:

$$r\_disso(i) = \frac{\Delta Eth(i) \times \rho}{\Delta t} \qquad (2)$$

where $r\_disso(i)$ is the dissolution rate (g.m^{-2}.d^{-1}) calculated based on the release of the element *i*, $\Delta Eth(i)$ is the difference between two consecutive equivalent thickness of the element *i*, and Δt is the time interval between two consecutive samples.

Overall, the dissolution rate calculated based on the release of B in solution ($r\_disso(\mathrm{B})$) was in good agreement with the dissolution rate calculated based on the release of Na in solution ($r\_disso(\mathrm{Na})$). They were linearly correlated with a correlation coefficient R^2 = 0.92 (see Supplementary Fig. V-1). However, $r\_disso(\mathrm{Na})$ was systematically lower than $r\_disso(\mathrm{B})$, shifting

the linear regression to a slope with a value of 1.3. Furthermore, the Na and B analyzed concentrations are low (ppb to ppm) and Na is an element that is more sensitive to contamination than B. As shown below, $r\_disso(\mathrm{B})$ was found to be in better agreement with the dissolution rate calculated based on the solid characterization (see Fig. V-5), so that in the following, $r\_disso(\mathrm{B})$ was considered to better reflect ISG reactivity, and $r\_disso(\mathrm{Na})$ was not considered in the subsequent analyses.

V.2.3.2. VSI, IR and SEM-EDX analysis of the sample

The retreat of the glass resulting from dissolution was measured using RTV glue masks to create a non-reactive reference surface. Topography analyses were then conducted using VSI (newview9000, zygo) (Fig. V-6 and V-7). For all samples, the images were taken at 10x-magnification, corresponding to a lateral resolution of 1.7 µm, while the vertical resolution was on the order of 1 nm. Table V-2 provided information on the dissolution thickness on some substrates measured by VSI.

SEM observations were conducted with a Tescan Vega 3 operated at ISTerre (Grenoble, France). SEM analyses were performed on each sample which was gold-coated (1 nm) beforehand. Energy Dispersive X-ray (EDX) spectra were acquired with an SDD detector from Rayspec to probe the chemical composition of both the surface of each reacted coupon and the precipitates formed in the solution or on the surface. The used incident energy was 16 keV.

Finally, infrared (IR) analyses were performed using a Thermoscientific infrared analyses instrument in Attenuation Total Reflectance (ATR) mode to probe the surface of the altered sample. Before analysis, ISG samples were cleaned with ethanol and air-dried. A background analysis was conducted before each measurement. The thickness of the analyzed surface was up to 1 µm. In the present study, the direct use of IR often proved challenging to directly detect the presence of CSH because the vibration modes characteristic of CSH structures (980 cm^{-1} to 920 cm^{-1}, according to their Ca/Si ratio) overlap with those of amorphous silica (Fig. V-3). The IR analyses were then coupled with SEM-EDX and thermodynamic modeling to infer indirectly the presence of CSH, i.e., CSH precipitation was suspected when the characterizations observed the three following conditions: i) The solution is close to saturation or supersaturated with respect to CSH, ii) SEM-EDX analyses of the reacted ISG coupon reveal a Ca/Si ratio higher than on a pristine ISG coupon and the observed morphology typical of CSH and iii) IR analyses do not reveal peaks related to calcium carbonates, which are the main phases with which CSH compete for Ca consumption.

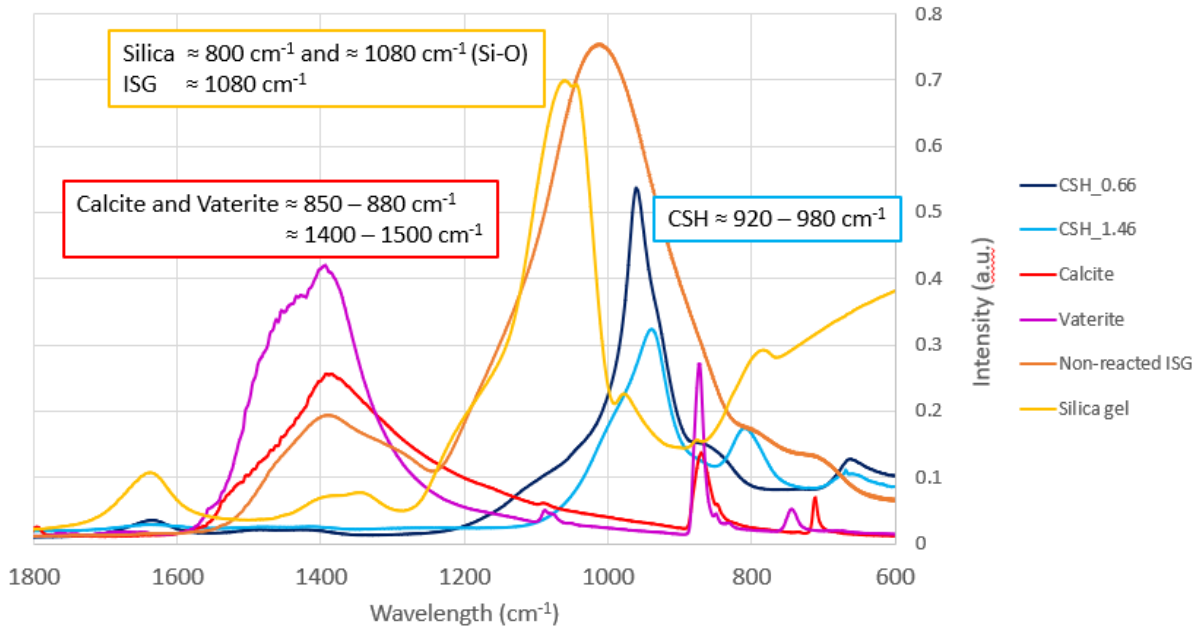

Figure V-3: Infrared characterization of various samples. The yellow and orange curves represent the IR spectra of the silica gel and ISG coupon respectively. The red and purple curves represent calcium carbonates (aragonite and vaterite, respectively). The dark and light blue curves represent CSH precipitates with a Ca/Si ratio of 0.66 and 1.46 respectively. The calcium carbonates and CSH synthesis and their analysis were performed in Zhakiyeva (2021)[54].

V.2.3.3. ToF-SIMS analyses of the sample

The altered solid samples were analyzed by an IONTOF GmbH® TOF 5 spectrometer from TESCAN Analytics (France). The external surface was abraded on an area of 200x200 µm² for an analyzed area of 50x50 µm². The ToF-SIMS operated as cycles of abrasion and analysis. After each cycle, the surface charge was neutralized by a low energy electron beam (< 20 eV) in order to prepare the area for the next cycle. The depth of the crater (h_{crater}) created by ion milling after a given number of abrasion cycles (N_{cycles}) was measured using 3D profilometer. The depth associated to one cycle of abrasion (z_{cycle}) is then assumed to be simply given by:

$$z_{cycle} = h_{crater} / N_{cycles} \quad (3)$$

Uncertainties are approximately 15 % of the result value. Depth profiles of positive ions, O^+, Na^+, Al^+, $^{28}Si^+$ and $^{29}Si^+$ were recorded thanks to Bi_1^+ 25 keV, 1.2 pA beam for the analyses and O_2^+ 2 keV, 600 nA beams for the ablation. Only information related to the thickness of the gel layer, analyzed by ToF-SIMS, are reported in this study as presented in Table V-2. The detailed profiles are provided in Chapter IV.

V.2.3.4. FIB-TEM analyses of the sample

The reacted samples were platinum-coated at TESCAN Analytics (France), and ultrathin electron transparent cross sections were subsequently prepared by focused ion beam (FIB) milling

following methods previously described by Daval et al., 2009[55] and summarized in Cagnon et al., 2022[24]. FIB foils were then analyzed using transmission electron microscopy (TEM) and scanning transmission electron microscopy (STEM) using a FEI Tecnaï G2 microscope with a LaB6 electron source operating at 200 kV, operated at CP2M (Marseille, France). EDX spectra were acquired in STEM mode to probe the chemical composition of the interface between the gel layer and the substrate, with an Energy Dispersive X-ray Detector (Oxford XMax 80). The analysis was conducted on some substrates as presented in Table V-2.

Tableau V-2: Summary of the substrates from which a gel layer thickness (µm) was measured by solid characterization. The first column refers to the name of the experiment. The second, third and fourth columns refer to the type of solid characterization, i.e. VSI, ToF-SIMS and FIB-TEM characterization respectively.

Name	VSI analysis (µm)	ToF-SIMS analysis (µm)	FIB-TEM analysis (µm)
D1	N/A		0.24
E2	N/A		0.05
G2	15.4		
G3	17.3		
G4	≈ 30		
G5	33.3		
Gbis1	13.6		
Gbis2	9.7		
H0	0	0.122	0.125
H1	0	0.116	
H2	0	0.103	
H3	0	0.091	
H4	0	0.082	0.089
I4	N/A		0.035
Hbis2	0		0.043
J3	0		1.1
J4bis	0		0.88

V.3.RESULTS

In this section, the results regarding the dissolution rates calculated using solution analyses are presented first, before being compared to the dissolution rates calculated from solid characterizations. As precipitates were observed in the solution, their effects on the dissolution rates are discussed. To reach this goal, the nature of those precipitates was studied before relation between those phases and

glass dissolution rate could be made. Finally, long-duration experiments (101 days) were investigated through the chemical composition of the solution and their precipitates.

V.3.1. Dissolution rates calculated using solution analyses

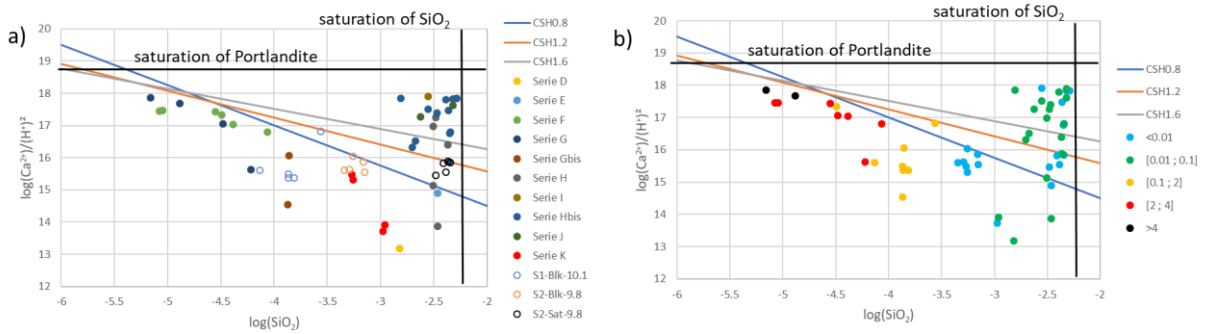

Figure V-4: Activity diagrams for the system CaO-SiO_2-H_2O representing the chemical composition of the solution of each reactor at the moment of the aqueous sample collection. The blue, orange and grey lines represent the saturation lines of CSH0.8, CSH1.2 and CSH1.6 respectively. The black horizontal line corresponds to the saturation line with respect to portlandite and the black vertical line corresponds to the saturation line with respect to amorphous silica. In the left plot a), the filled circles correspond to experiments carried out during this study while the open circles correspond to experiment carried out in Fournier et al., 2019[14]. In the right plot b), each color corresponds to a range of glass dissolution rates (in g.m^{-2}.d^{-1}) with the color code corresponding to decreasing rates from black to blue.

Fig. V-4a shows an activity diagram plotted using the fluid data coming from the different series conducted in the present study. Additional data on ISG alteration from Fournier et al. (2019)[14], which were collected in a solution with no initial addition of Ca in the solution, were also reported to the figure. The subset of data that we selected from their study observed the following conditions: i) no zeolite or other secondary phase precipitated in the solution; ii) The initial pH was not significantly lower than the pH at which the experiments of this study were conducted (i.e., 10 ± 0.2 after 20 days of alteration). This second condition ruled out all the experiments from Fournier et al. (2019)[14] conducted at pH ≤ 9.5. According to the above-mentioned criteria, only three sets of experiments were selected for comparison: S1-Blk-10.1, S2-Blk-9.8 and S2-Sat-9.8. ISG dissolution rates calculated from B release were then reported in Fig. V-4b.

From the activity diagram where the saturation curves with respect to 3 different CSH are displayed, two domains can be defined: the one where the solution is undersaturated with respect to all of the 3 CSH, and another one where the solution is saturated with respect to all of the 3 CSH. Most rate data from Fournier et al. (2019)[14] fall in the undersaturated domain (open circles in Fig. V-4a). Most rate data collected in the present study are situated in the stability field of the 3 CSH compositions mentioned previously. Of note, the evolution of the chemical composition of the solution from series G followed the saturation line of the CSH0.8 (Fig. V-4a). Therefore, the solutions were assumed to remain in equilibrium with the selected CSH0.8 throughout the experiment, which was confirmed by IR and SEM characterizations (see section b in Discussion), while no carbonate was found in this series.

The dissolution rates of ISG are reported in Fig. V-4b. The main observation is that the dissolution rate decreases with increasing SiO_2(aq) up to near saturation conditions with respect to amorphous silica. The highest dissolution rate is observed with the lowest concentration of silica in the solution, i.e. log(SiO_2) = -5.16 and -4.88. No significant differences were observed at this stage in the dissolution rate between experiments where CSH precipitated and where they did not. However, when experiments near saturation with respect to amorphous silica are compared with S2-Blk-9.8 from Fournier et al., 2019[14], a discrepancy is observed. The rates calculated from this latter specific experiment, with a log(SiO_2) between -3.5 and -3, appear as blue circles in Fig. V-4b, meaning that they are lower than those from other experiments from the series H, Hbis, I and J that have a higher silica concentration, and which were all conducted in the CSH saturation domain.

V.3.2. Dissolution rates calculated using solid and solution analyses

As mentioned above, glass dissolution rates were estimated using different methods, i.e., ICP-OES, which was used to monitor the release of B in the solution, and a combination of VSI to measure the surface retreat, and ToF-SIMS and FIB-TEM to determine the gel layer thickness. Dissolution rates based on solid characterizations (r_solid) are in reasonable agreement with those calculated from elemental release, though generally lower. Overall, the dissolution rate decreases with the increase in $[SiO_2(aq)]/[SiO_2(aq)]_{eq}$ ratio regardless of the method of calculation, which is consistent with the observations reported in Fig. V-4. In this figure, $[SiO_2(aq)]$ represents the total concentration of Si in solution and $[SiO_2(aq)]_{eq}$ represents the total concentration of Si in solution to reach the saturation with respect to amorphous silica. Consequently, $[SiO_2(aq)]/[SiO_2(aq)]_{eq}$ ratio is the distance to the saturation state of the solution with respect to amorphous silica.

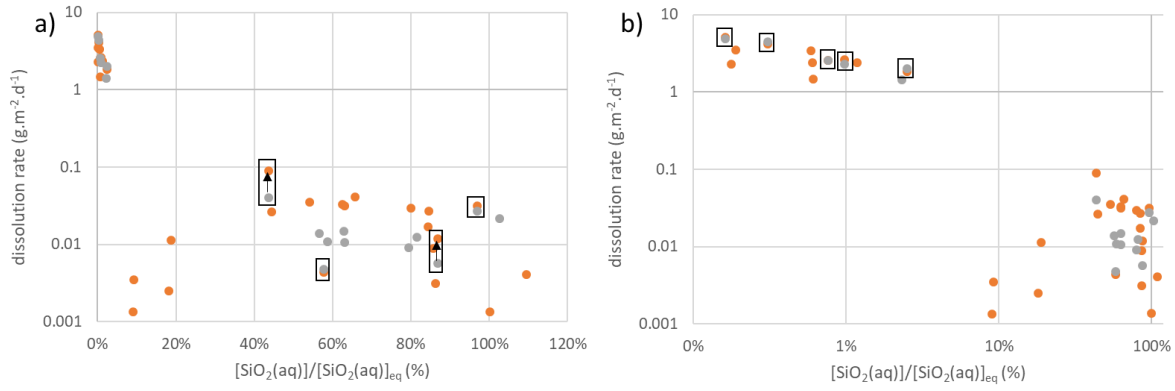

Figure V-5: Dissolution rate of ISG ($g.m^{-2}.d^{-1}$) as a function of the $[SiO_2(aq)]/[SiO_2(aq)]_{eq}$ ratio (%). The orange circles represent the dissolution rates calculated based on the release of B in the solution determined by ICP-OES, while the grey circles represent the dissolution rates calculated based on solid analyses (VSI + ToF-SIMS or FIB-TEM). The conditions for which the rate calculation was performed for a same experiment based both on the solution and the solid analyses are highlighted in rectangles. (a) Semi-log plot of the relation between aqueous Si concentration and rate data, highlighting experiments conducted in Si-rich solutions. (b) Log-log plot of the relation between aqueous Si concentration and rate data, highlighting experiments conducted in Si-low solutions.

From Fig. V-5, two groups of dissolution rates are observed. The first one corresponds to a high dissolution rate with a low $[SiO_2(aq)]/[SiO_2(aq)]_{eq}$ that ranges from 0% to 2%. The calculated dissolution rate is greater than 1 $g.m^{-2}.d^{-1}$ without exceeding 10 $g.m^{-2}.d^{-1}$ and both $r\_disso(B)$ and r_solid are equivalent, within experimental uncertainties. The second group corresponds to lower dissolution rates, for $[SiO_2(aq)]/[SiO_2(aq)]_{eq}$ greater than 9%. The dissolution rates range from 0.1 $g.m^{-2}.d^{-1}$ to 0.001 $g.m^{-2}.d^{-1}$ for $[SiO_2(aq)]/[SiO_2(aq)]_{eq}$ ranging between 9% and 100%.

V.3.3. Characterization of the precipitates

Typical characterizations of the run products collected at the end of experiments are reported in Fig. V-6 and Fig. V-7. The characterizations were reported according to the two domains previously mentioned, with either a low (Fig. V-6) or a high (Fig. V-7) $[SiO_2(aq)]/[SiO_2(aq)]_{eq}$ ratio. IR analyses were also reported and were used, coupled with SEM-EDX to determine the presence of CSH (see "Material and Methods" for more details).

V.3.3.1. Experiments run with a low $[SiO_2(aq)]/[SiO_2(aq)]_{eq}$ ratio

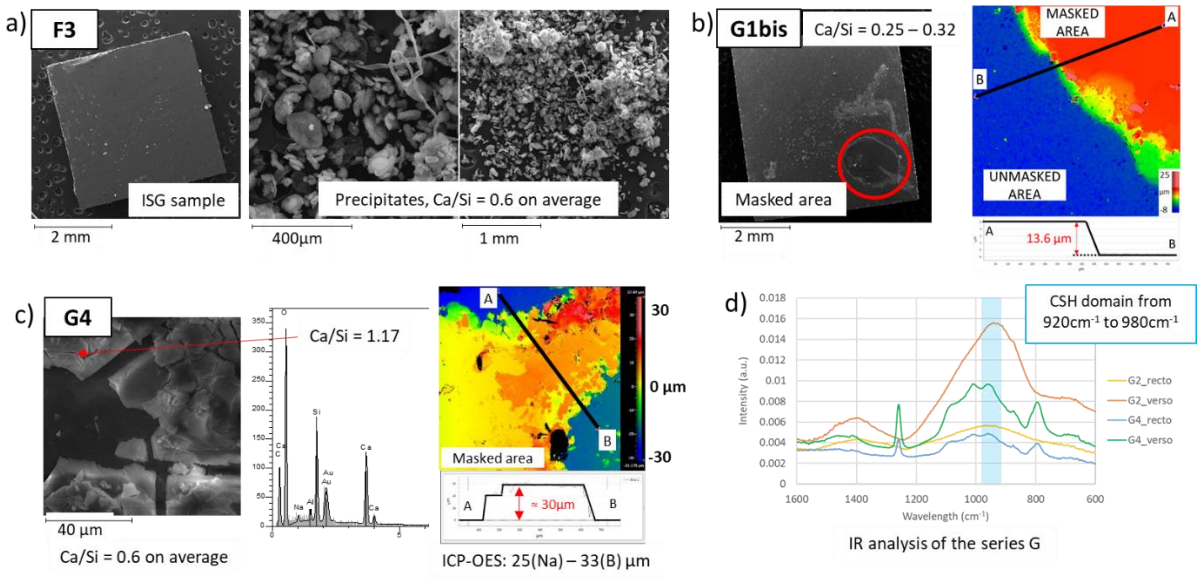

Figure V-6: Representative SEM, EDX and VSI characterizations of solids recovered from various experiments with a low $[SiO_2(aq)]/[SiO_2(aq)]_{eq}$ after 20 days at pH 10, 90°C. a) SEM pictures of F3 coupon and precipitates. b) SEM picture and VSI analysis of G1bis sample. c) SEM picture of G4 sample with an EDX analysis of the precipitates located in the upper left part of the image. A VSI analysis of the masked area is also shown. d) IR analysis on the series G. The yellow, orange, blue and green lines correspond to G2_recto, G2_verso, G4_recto and G4_verso faces, respectively. The blue area is the domain where the peak of CSH with a Ca/Si ratio from 0.66 to 1.46 is expected.

Regarding the experiments conducted with a low $[SiO_2(aq)]/[SiO_2(aq)]_{eq}$ ratio, the series F were run with a high initial concentration of Ca (> 260ppm). The initial concentration of Si increased from F1 to F3. While the initial amount of aqueous silica remains low (from 0 to 1% of saturation with respect to amorphous silica, see Table V-1), the amount of precipitates in the solution and their morphology were different. Almost no precipitate was observed in F1, a small amount of gel-like precipitate was

observed in F2, and more precipitates were observed in F3 (Fig. V-6a). The F3 coupon surface remained neat and the precipitates in the solution were thin and presented a layer-like morphology. As it can be seen in Fig. V-6a, they aggregated to form bigger precipitates with an average Ca/Si ratio around 0.6. IR analyses provided insight on the potential presence of CSH with a Ca/Si ratio of 0.7 for F3, which is consistent with the SEM-EDX analyses and with the fluid composition, which follows the saturation limit of CSH0.8 (Fig. V-4). Those observations strongly suggested the presence of CSH in the F3 experiments' precipitates.

The series G and Gbis were also carried out with no or little Si added (between 0% and 2% of SiO_2(am) saturation). The amount of calcium initially introduced increased from Gbis1 to Gbis2 and from G2 to G5. Precipitates were observed in both Gbis1 and Gbis2 and were also observed from G2 to G5. The average value of the Ca/Si ratios of the precipitates ranged between 0.25 and 0.32 for G1bis (Fig. V-6b) and was around 0.6 for G4 (Fig. V-6c). The VSI analyses highlighted a step at the edge of the RTV glue mask, which results from the dissolution of the glass (Fig. V-6b). The step height was 13.6 µm for G1bis and around 33 µm for G4, which compares favorably with the alteration thicknesses of 12.4 µm for G1bis and 34 µm for G4 calculated from ICP-OES data. Note that G4 and F3 possessed a similar solution composition. The IR analyses are presented in Fig. V-6d for the series G. Except for G5 and Gbis2, no calcium carbonate peak was found for Gbis1 and G2, G3 and G4. However, peaks related to CSH were found and presented a local maximum between 980 cm^{-1} and 920 cm^{-1}. Based on Zhakiyeva (2021)[54] work, these maxima correspond to a standard CSH with a Ca/Si ratio close to 0.66 for G4, and 1.26 for Gbis1, respectively, strongly suggesting the presence of CSH in the solution.

V.3.3.2. Experiments run with a high $[SiO_2(aq)]/[SiO_2(aq)]_{eq}$ ratio

Strikingly, the apparent solubility of the gel seemed to be reached for a $[SiO_2(aq)]/[SiO_2(aq)]_{eq}$ as low as 9% (series K): the surface retreat is below 20 nm, while the thickness of the gel is around 40 nm. Experiments D1 and E2 are representative of series where no calcium was added in the solution, but with high $[SiO_2(aq)]$ concentrations, (i.e. $[SiO_2(aq)]/[SiO_2(aq)]_{eq}$ = 44% for D1; and 79% for E2). Fig. V-7a is a typical SEM image representative of the corresponding coupons reacted in conditions close to the saturation with respect to amorphous silica and a low concentration of Ca (a few tens of ppm). The precipitates were essentially made up of a Si-rich gel-like surface coating. The TEM characterizations revealed that the gel layer thickness was 243 nm. E2 precipitates are shown in Fig. V-7b. The amount of aqueous silica was higher compared to D1, and the gel layer thickness was thinner, about 50nm, as inferred from TEM analyses.

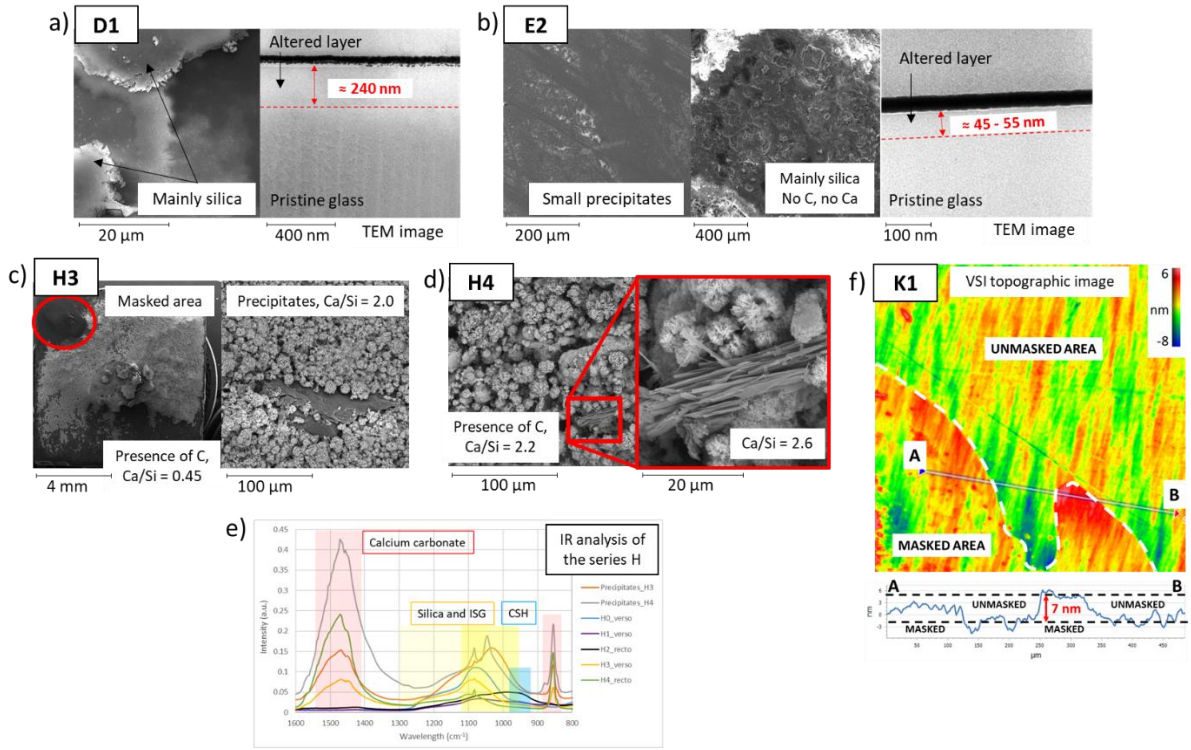

Figure V-7: Representative SEM, EDX and VSI characterizations of solids recovered from various experiments with a high $[SiO_2(aq)]/[SiO_2(aq)]_{eq}$ after 20 days at pH 10, 90°C. a) SEM and TEM pictures of D1 coupon. b) SEM and TEM pictures of E2 coupon. The precipitates on the surface were too small to be analyzed by EDX. Neither C nor Ca was detected. c) and d) SEM pictures of H3 and H4, respectively. Calcium was exceptionally introduced in those two reactors under the form of calcium carbonates. e) IR analysis on the series H. The orange, grey, blue, violet, yellow and green lines correspond to the precipitates of H3, H4, H0_verso, H1_verso, H3_verso, H4_verso respectively. The red, yellow and blue areas respectively indicate the domains where the peak of calcium carbonate, silica and ISG, and CSH with a ratio from 0.66 to 1.46 are expected. f) VSI picture of K1 surface coupon that is representative of experiments run in the high $[SiO_2(aq)]/[SiO_2(aq)]_{eq}$ ratio domain. No step was observed between the reacted area and the non-reacted area.

Finally, the series H was carried out with a solution close to saturation with respect to amorphous silica, and an increasing amount of calcium from H0 to H4. Note that for both H3 (Fig. V-7c) and H4 (Fig. V-7d), Ca was introduced in the solution in the form of $^{44}CaCO_3$, instead of CaCl2, to trace the incorporation of Ca in secondary phases (the corresponding results were discussed in the previous chapter). On the surface of ISG coupon, the average Ca/Si ratio ranged between 0.2 – 0.3 for H2, 0.45 for H3 and 0.60 for H4. The precipitates of both latest experiments are mainly calcium carbonates with a morphology of either cauliflowers or elongated crystals that may correspond to vaterite and aragonite, respectively. The first one was present in large amount whereas the second one was present as a minor phase. The EDX analyses confirmed an enrichment in Ca in those precipitates with a Ca/Si ratio between 2.0 and 2.6. Regarding H2, amorphous silica were the main precipitates with Ca/Si ratios that can reach up to 1.88. The IR analyses of the series H are presented in Fig. V-7e. Peaks related to calcium carbonates were only observed in the H3 and H4 precipitates, as well as on the surface of H3 and H4 coupons. No local maximum related to CSH precipitate could be isolated in the range of wavenumbers characteristic of these phases, except for H2, which peaks

correspond to a Ca/Si ratio of 1.6. Those observations suggested that out of the 5 series H experiments, CSH only precipitated in H2 experiment.

Of note, the VSI images shown in Fig. V-7f are representative of the VSI analyses made on every experiment with a $[SiO_2(aq)]/[SiO_2(aq)]_{eq}$ exceeding 9%, including the series H. Little to no retreat was observed between the masked and unmasked areas of those series.

V.3.4. Dissolution rate comparison according to the presence of CSH

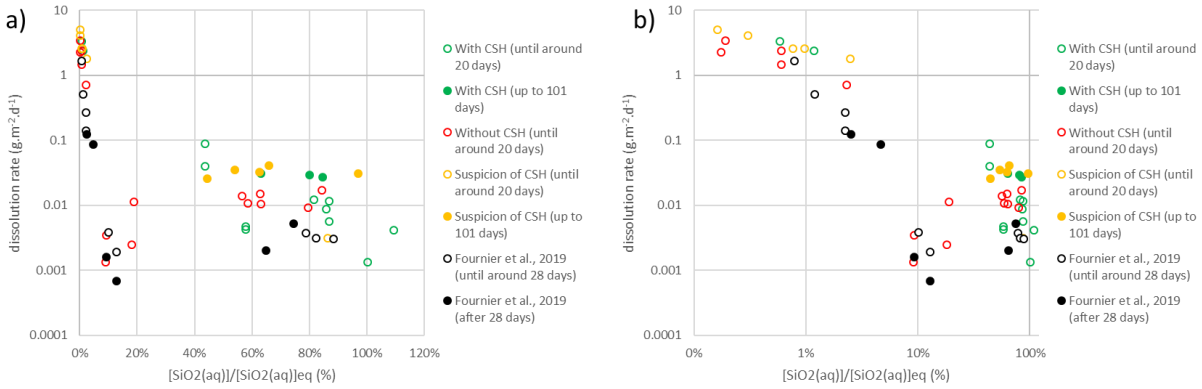

Figure V-8: Plots representing the dissolution rate of ISG in $g.m^{-2}.d^{-1}$ as a function of the $[SiO_2(aq)]/[SiO_2(aq)]_{eq}$ ratio (%) and of the presence of CSH in the precipitates. Green open and filled circles correspond to experiments where CSH were positively found in the precipitates at the end of the 20-days and 101-days experiments, respectively. Red circles correspond to experiments where CSH did not precipitate until the end of the 20-days experiments. Yellow open circles and yellow filled circles correspond to experiments where CSH precipitation was highly suspected at the end of the 20-days and 101-days experiments, respectively. Black open circles and black filled circles refer to short-term and long-term (respectively) dissolution rates calculated from the data of Fournier et al., 2019[14], corresponding to experiments where no secondary precipitate was observed. Both (a) and (b) refer to the same dataset, where (b) corresponds to a semi-log representation to better emphasize the results from experiments run at low Si concentrations.

Regarding the $[SiO_2(aq)]/[SiO_2(aq)]_{eq}$ ratio from 0% to 2% (Fig. V-8b), the experiment with CSH corresponds to F3 while the open yellow circles correspond to the series G. All experiments in this domain lasted around 20 days and regardless of the presence of CSH, the dissolution rate varies within the same order of magnitude. When the rate data obtained in the present study are combined with those collected by Fournier et al. (2019)[14], a continuous decreasing trend from $[SiO_2(aq)]/[SiO_2(aq)]_{eq}$ ≈2% to ≈15% is evidenced. Around this latter $[SiO_2(aq)]/[SiO_2(aq)]_{eq}$ ratio, the dissolution rate ranges from $7x10^{-4}$ to $4x10^{-3}$ $g.m^{-2}.d^{-1}$, which is of a same order of magnitude as the dissolution rate of experiments carried out at $[SiO_2(aq)]/[SiO_2(aq)]_{eq}$ > 9% in our study. Thus, a discontinuity between both domains is observed.

According to our results, at $[SiO_2(aq)]/[SiO_2(aq)]_{eq}$ > 44%, the dissolution rate varies from $1.4x10^{-3}$ to $8.8x10^{-2}$ $g.m^{-2}.d^{-1}$. The rate data from Fournier et al. (2019)[14] lies in the lower part of this range, between $2.0x10^{-3}$ and $5.2x10^{-3}$ $g.m^{-2}.d^{-1}$. Therefore, in this range, the dissolution rates are overall higher for experiments conducted in the saturation domain of CSH. Furthermore, the dissolution rates

from short-term experiments range within one order of magnitude, regardless of the presence of CSH or not in the solution, while the dissolution rates from long-terms experiment lie in the upper part of this range. As a consequence, two conditions seem to be required to observe enhanced ISG dissolution rates at high at $[SiO_2(aq)]/[SiO_2(aq)]_{eq}$ ratios: (i) Secondary precipitates are mainly or only made up of CSH and ii) the experiments have to last longer than 20 days.

V.3.5. Longer-term experiments, relation between secondary precipitates and ISG dissolution rate.

As described previously, the experiments were designed so as to minimize the impact of CO_2 on the chemical composition of fluid and hence, on ISG reactivity. The protocol adopted in this study proved successful for durations lasting up to ~3 weeks. Over longer durations, the penetration of CO_2 in the reactor was large enough to modify the sequence of precipitates. In this section, we present results of long-term experiments aimed at getting insights into the impact of the competition between CSH growth and carbonate precipitation on ISG dissolution rate.

The series Hbis and J were designed to alter the ISG coupon under similar conditions: the solution was saturated with respect to amorphous silica and a significant amount of Ca was added initially in the reactor to reach 340ppm of Ca for Hbis3, J3 and J3bis, and 620 ppm for Hbis4, J4 and J4bis. The main difference between both series was that the solution was sampled only at the beginning and at the end of the experiment of J series in order to minimize handling of the reactor and accordingly, decrease the risk of carbonation (which eventually proved unsuccessful). Conversely, the series Hbis was sampled regularly to monitor the evolution of the solution composition.

From the Fig. V-9, the initial and final chemical compositions of the solution are similar between both series. As J3bis and J4bis are duplicates of J3 and J4, their solution chemical composition was not reported. The series Hbis reveal that the activity of $SiO_2(aq)$ in the solution first decreased, followed by both an increase in $SiO_2(aq)$ activity and a decrease in the $(Ca^{2+})/(H^+)^2$ activity ratio. Initially, the solution is supersaturated with respect to CSH1.6, while at the end of the experiment, the solution is at equilibrium with respect to CSH0.8. Regarding the evolution of the pH of the solution, an acidification was observed for all experiments. Every solution was initially adjusted to pH 10.1 but after 101 days of alteration, the pH decreased to 9.9 and 9.5 for Hbis3 and Hbis4 respectively, with a measure of 9.8 for Hbis4 at 89 days. Regarding the series J, the pH decreased to 9.7 for both J3 and J3bis, and to 8.9 and 9.0 for J4 and J4bis respectively.

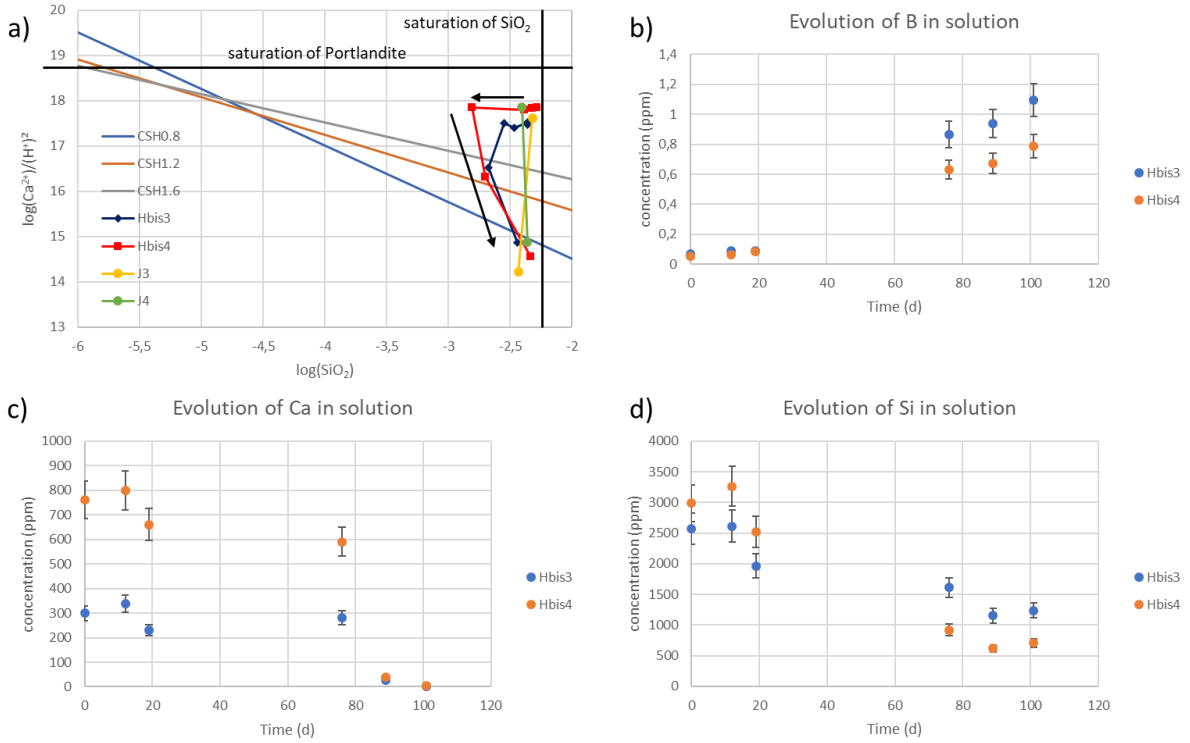

Figure V-9: Main results of fluid characterizations for series run over long (~3 months) durations (i.e., series Hbis, J). (a) Activity diagram for the system CaO-SiO_2-H_2O representing the chemical composition of the solution for experiments Hbis3, Hbis4, J3 and J4. The blue, orange and grey lines represent the saturation curves of CSH0.8, CSH1.2 and CSH1.6 respectively. The black horizontal line corresponds to the saturation line with respect to portlandite and the black vertical line corresponds to the saturation line with respect to amorphous silica. The plots reported in b), c) and d) represent the evolution of the concentration of dissolved B, Ca and Si respectively, as a function of time (days) for the experiment Hbis3 (blue circles) and Hbis4 (orange circles).

The evolution of the concentration of B, Ca and Si in the solution of Hbis3 and Hbis4 is reported in Fig. V-9b, c and d. During the first 12 days, the B concentration observed a minute increase, while the concentration of Ca and Si remained constant, within uncertainties. Between 12 and 19 days, the concentration of Ca and Si decreased simultaneously. The decrease in Ca concentration reached 107 ppm and 138 ppm for Hbis3 and Hbis4 respectively, while the decrease in Si concentration reached 649 ppm and 744 ppm for Hbis3 and Hbis4, respectively. Between 19 and 76 days, the concentration of B in the solution significantly increased by about one order of magnitude (from 0.09 ppm to 0.87 ppm for Hbis3 and from 0.09 ppm to 0.63 ppm for Hbis4) whereas the concentration of Ca remained constant for both experiments. The concentration of Si in Hbis4 decreased significantly by a 2.7-factor, from 2500 ppm to 900 ppm while it only slightly decreased for Hbis3. Between 76 and 89 days, the remaining amount of Ca in the solution precipitated, as suggested by the drop in Ca concentration. The concentration of B in the solution steadily increased, but with a much slower pace and the concentration of Si decreases slightly. Finally, between 89 and 101 days, the concentration of

Ca decreases to a few ppm for both series while the amount of Si remained constant. The concentration of B kept increasing at a slower rate.

The precipitates of those series were analyzed by EDX-SEM and representative images are reported in Fig. V-10. The picture and EDX characterization in Fig. V-10a are characteristic of the others ISG coupons from series Hbis and J collected at the end of the experiments. The common observation is a low Ca/Si ratio at 0.26 to 0.45 for Hbis4, around 0.7 for J4, and between 0.44 and 0.67 for J4bis. Such Ca/Si ratios were typically found on the surface of ISG coupons or precipitates after alteration in a (Ca, Si)-rich solution.

The precipitates shown in Fig. V-10b presented two morphologies with two distinct values of Ca/Si ratios. The first one, with a Ca/Si value of 0.7 on average, presented an amorphous gel-like morphology whereas the second one, with a higher Ca/Si value of 1.1 on average, exhibited layers of euhedral crystals. Finally, another type of precipitates was present in J4bis that resembled cauliflowers and grew out of the amorphous gel-like precipitates. Both the amorphous and cauliflowers precipitates were characterized by TEM (Fig. V-11b and V-11c). Electron diffraction was performed on both precipitates and revealed an amorphous structure for the early precipitates (Fig. V-11e) and a crystalline structure for the subsequent ones (Fig. V-11d). The d-spacing measured on this image was as follow: 7.41 Å, 4.48 Å, 3.85 Å, 3.48 Å, 2.90 Å, 2.79 Å, 2.44 Å, 2.06 Å and 1.74 Å. EDX spectra on both precipitates showed that they both contain carbon, a significant amount of silicon and some calcium. The amount of calcium in the crystalline precipitates was higher, with Ca/Si ratio reaching up to 0.36, whereas the amorphous precipitates had a Ca/Si ratio of 0.06.

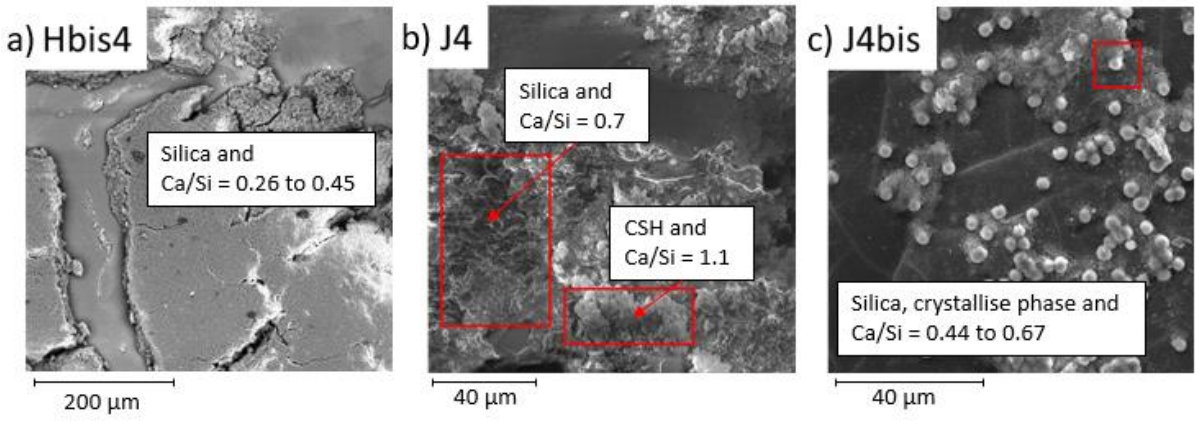

Figure V-10: SEM characterizations of the surface of ISG coupons after 101 days of alteration from the experiment a) Hbis4, b) J4 and c) J4bis at 90°C, and an initial pH of 10.1. EDX characterizations were performed in order to determine the morphology and chemical composition of the precipitates.

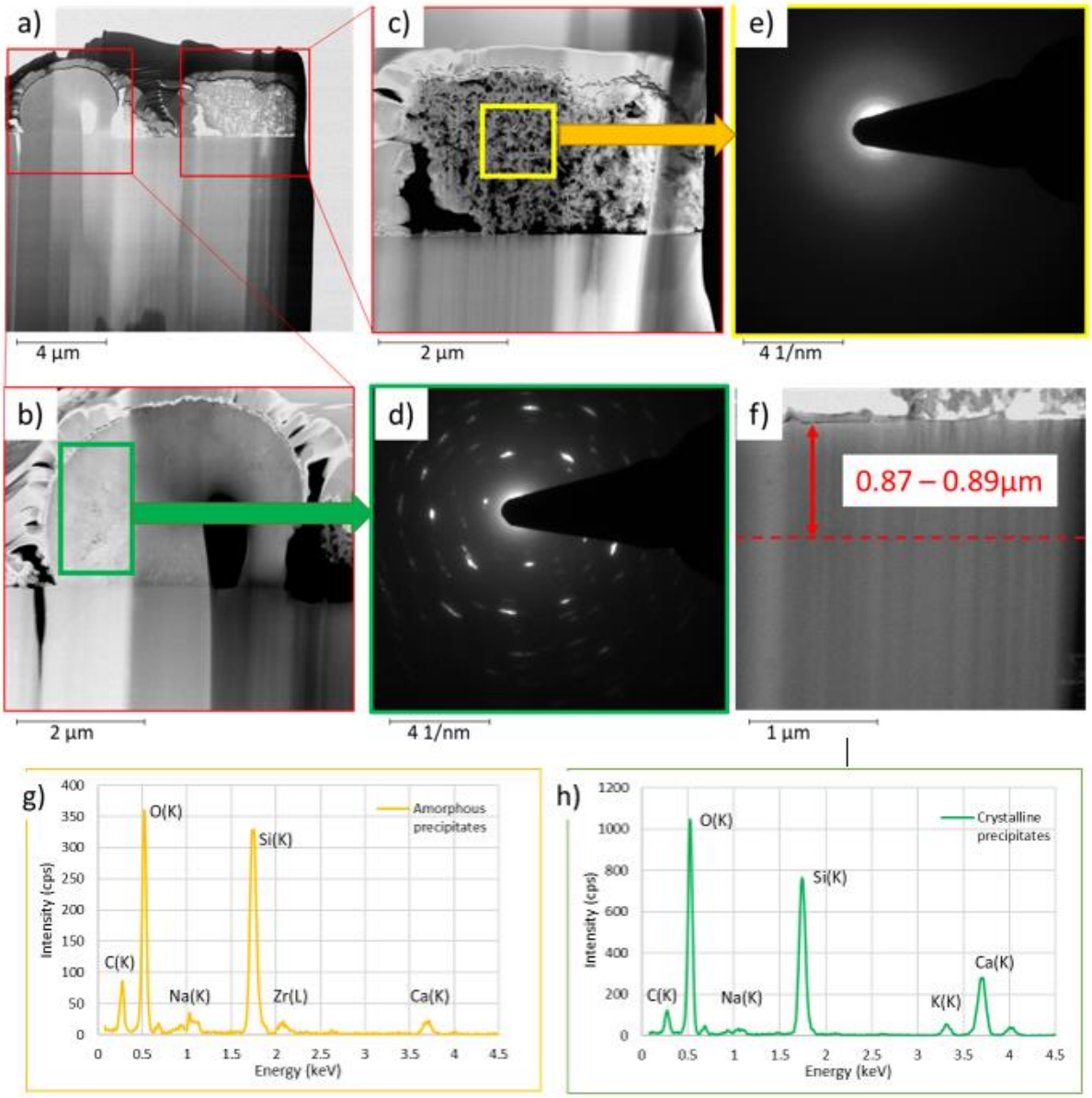

Figure V-11: FIB-TEM characterization of the surface ISG coupon and associated precipitates from J4bis experiments, collected after 101 days of alteration at pH 10.1. The composition of both crystalline and amorphous precipitates was obtained by STEM-EDX. a) TEM bright field image of the surface with both crystalline precipitates on the left and amorphous precipitates on the right. b) and c) TEM dark field close up views on the crystalline precipitates and the amorphous precipitates respectively. d) and e) Electron diffraction of the crystalline precipitates and the amorphous precipitates respectively. f) TEM image of the surface, showing that the thickness of the gel layer ranges between 0.87 and 0.89 µm. This observation was supported by STEM-EDX map of the area at the Ca K edge, K K edge, Na K edge, Si K edge and Al K edge (not reported). g) and h) EDX spectra collected on the crystalline precipitates and the amorphous precipitates respectively.

V.4.DISCUSSION

To unravel the reactivity of ISG at basic pH conditions in solutions enriched with dissolved Si and Ca, our dataset was compared to that of Fournier et al. (2019)[14], which was collected at the same temperature and similar pH conditions, but in Ca-low solutions. Over long-term durations (more than 3 weeks), we found that ISG dissolution rate is slightly higher (around 1.8x higher on average) when CSH formed.

Below, we first examined the extent to which ISG dissolution rate can be predicted using the well-known first order dissolution rate law proposed by Grambow (2001)[56], which links glass dissolution rate to SiO_2(aq) activity. Then the impact of the calcium concentration was studied, with a specific emphasis on the impact of CSH formation. The chemical evolution of Hbis3 and Hbis4 solutions allowed us to further understand the different stages of evolution of the glass dissolution rate, which can be related to the maturation of CSH precipitates in the solution. Finally, the alteration mechanism of ISG was addressed. In particular, the dissolution rate evolution exhibited a resumption of alteration after 20 days, which may be attributed to an intrinsic evolution of the transport properties of the gel layer and/or its consumption by CSH precipitates.

V.4.1. Relation between ISG dissolution rate and SiO_2(aq) concentrations

The rate and mechanisms of borosilicate glass dissolution has been studied for over 50 years[15,18,56-63]. In their study, Grambow et al., 1985[64] and Grambow et al., 2001[56] proposed a general dissolution rate law, based on the work of Aagaard et al., 1982[65], which is often referred to as 'first order dissolution rate law'. A simplified equation of this rate law is reported in equation 4:

$$r_{disso} = k(T) \times \left(1 - \frac{a_{Si}}{K_{SiO_2}(T)}\right) \qquad (4)$$

where $k(T)$ is a rate constant (g.m^{-2}.d^{-1}) that depends on the temperature T (K) and $K_{SiO_2}(T)$ is the solubility constant at the dissolving glass surface, which depends on the temperature.

This law ensures that when the solution is highly undersaturated with respect to amorphous silica, the dissolution rate of the borosilicate glass (r_{disso}), is equal to the forward dissolution rate, r_0. When the solution approaches the saturation of the gel (approximated to that of amorphous silica for instance), the dissolution rate is supposed to drop down to zero. Note that similar rate laws proved satisfactory to describe the reactivity of some silicate minerals[66-68] and basaltic glass[69]. The rate law can be refined using the actual solubility of the gel layer instead of that of SiO_2(am)[14,70-72]. However, above that threshold, a residual dissolution rate was observed as the (boro)silicate glass kept dissolving beyond saturation[73-75]. Mechanisms behind the residual rate is still debated within the community[63]. One of the hypotheses is that the reaction is controlled by the ingress of reactants and products through the gel layer[67,76].

In the present study, when the solution was saturated with respect to amorphous silica, which is the most soluble polymorph of SiO_2, the dissolution rate of ISG reached a minimum for two reasons: (i) the chemical affinity between the solution and the solid was the lowest[24,77] and (ii) there is a possibility of forming a passivating layer in alkaline pH[9]. These two mechanisms are additive. This latter

mechanism can be annihilated by the precipitation of silicate secondary phases, such as zeolites or CSH[15,78].

The dissolution rates calculated in this study, and that of Fournier et al. (2019)[14] were compared with the first order dissolution rate law in Fig. V-12b, where the rate plateau corresponding to the forward rate r_0 was set to 11.2 $g.m^{-2}.d^{-1}$ according to the study of Fournier et al. (2016)[79]. As can be seen in Fig. V-12b, the general trend depicted by the rate data do not follow the first order dissolution rate law.

A correction to the first order dissolution rate law was then applied, by adjusting the solubility limit of SiO_2, considering that the gel layer is less soluble that amorphous silica because of the presence of Al[80]. In order to apply this correction, two different domains of dissolution rate were drawn based on $[SiO_2(aq)]/[SiO_2(aq)]_{eq}$ ratio. The first one corresponds to a high dissolution rate, > 1 $g.m^{-2}.d^{-1}$, when $[SiO_2(aq)]/[SiO_2(aq)]_{eq}$ is below to 2% and a second one that corresponds to a low dissolution rate, < 0.1 $g.m^{-2}.d^{-1}$, where $[SiO_2(aq)]/[SiO_2(aq)]_{eq}$ is greater than 9%. These two domains were supported by solid characterization and VSI analyses (Fig. V-6 and V-7). The important surface retreat highlighted by VSI characterization (up to 33 µm) and the very thin (a few 100s of nm at most according to the solution analyses) gel layer testified that the solution was very far from the solubility of the gel layer. Conversely, the surface retreat was very low for $[SiO_2(aq)]/[SiO_2(aq)]_{eq}$ ratios ranging from 9% to 18% (< 20 nm) and below the VSI quantification limit (< 2 nm) for $[SiO_2(aq)]/[SiO_2(aq)]_{eq}$ ratios greater than 44%. For $[SiO_2(aq)]/[SiO_2(aq)]_{eq}$ ratios between 9% and 18%, the surface retreat was between 10 and 20nm. In this latter domain, the thickness of the gel layer, calculated based on ToF-SIMS, FIB-MET or even ICP-OES, were on the same order of magnitude after 20 days of alteration (a few tens of nanometers up to a hundred nanometers). These observations suggest that the solubility of the gel layer is lower than that of SiO_2(am) and may be around 12% of SiO_2(am) saturation (Fig. V-12), in reasonable agreement with the apparent solubility reported in Gin et al. (2012) at pH = 9 (~20% of SiO_2(am) saturation). Of note, the threshold where the alteration process switches from hydrolysis-controlled mechanism ($[SiO_2(aq)]/[SiO_2(aq)]_{eq}$ < 9%) to diffusion-controlled mechanism ($[SiO_2(aq)]/[SiO_2(aq)]_{eq}$ > 9%) lies in the range of the solubility of quartz, which is the most insoluble silica phase (17% of SiO_2(am) saturation).

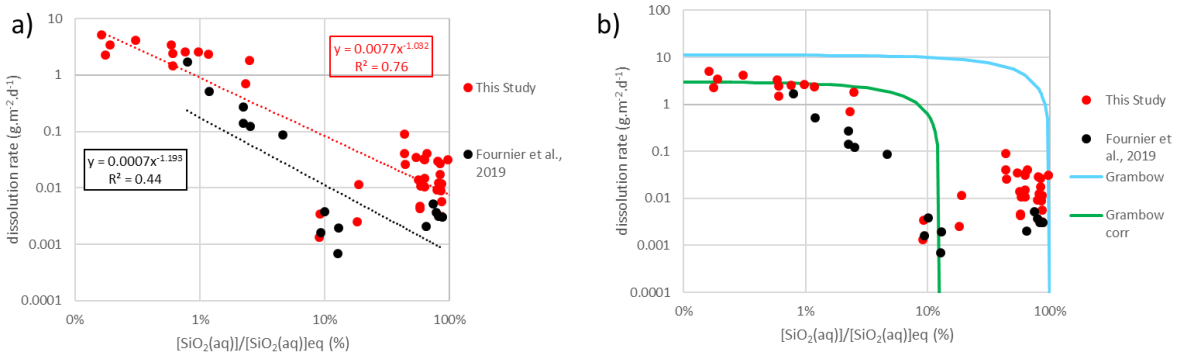

Figure V-12: Glass dissolution rate ($g.m^{-2}.d^{-1}$) as a function of $[SiO_2(aq)]/[SiO_2(aq)]eq$. The red circles correspond to the data from this study. The black circles correspond to the data from Fournier et al., 2019[14]. a) Dissolution rate and $[SiO_2(aq)]/[SiO_2(aq)]eq$ is represented with a linear regression on both data set. b) Both data set are compared with the first order alteration law from Grambow et al., 2001[56]. The blue line refers to the original first order alteration law and the green one to a first order law corrected by the solubility of the gel layer based on this study and the best forward dissolution rate based on this study.

Of note, the low dissolution rate (< 0.01 $g.m^{-2}.d^{-1}$) reported by Fournier et al. (2019)[14] for experiments carried out with a $[SiO_2(aq)]/[SiO_2(aq)]_{eq}$ between 9% and 13% is an additional independent argument supporting that the apparent solubility for the passivating gel layer formed on ISG ranges from 9% to 18% of the saturation state of the solution with respect to amorphous silica at pH 10 and 90 °C.

Finally, in addition to the concerns regarding the gel layer solubility, the first order dissolution rate law does not capture the far-from-equilibrium rates ($[SiO_2(aq)]/[SiO_2(aq)]_{eq}$ <2%) reported both in the present study or that of Fournier et al. (2019)[14]. Indeed, the dissolution rates in this domain can be up to one order of magnitude lower. Furthermore, the rate data from Fournier et al. (2019)[14] steadily decreases with increasing $SiO_2(aq)$ concentrations, without describing an initial rate plateau (Fig. V-12b). A reasonable agreement can be highlighted from the dissolution rates in this study with the corrected first-order dissolution rate law when considering a lower forward dissolution rate of around 3 $g.m^{-2}.d^{-1}$. However, this law cannot explain the dissolution rates that are measured for saturation states exceeding 12%.

ISG dissolution rate is unquestionably negatively correlated with the increase in $SiO_2(aq)$ activity in solution. While the data collected in the present study observe a rather linear correlation between dissolution rates and $[SiO_2(aq)]/[SiO_2(aq)]_{eq}$ in a log-log plot (Fig. V-12a) with a strong correlation coefficient ($R^2 \approx 0.76$), the rate data calculated from the experiments conducted by Fournier et al. (2019)[14] exhibit a weaker linear correlation ($R^2 = 0.44$). The observations collected in the present study support that ISG dissolution rate obeys a general empirical rate law related to the activity of silica in solution, although following a more complicated relation than the first order alteration rate law suggested by Grambow et al., (2001)[56].

V.4.2. Impact of aqueous Ca and Ca-bearing secondary phases on ISG dissolution rate during short-term experiments

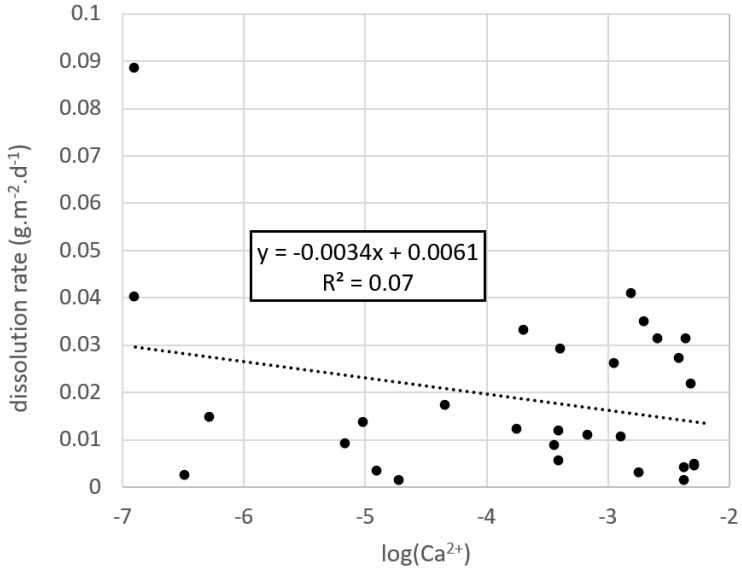

Figure V-13: ISG dissolution rate ($g.m^{-2}.d^{-1}$) measured in the present study as a function of the logarithm of Ca^{2+} activity in solution, for $[SiO_2(aq)]/[SiO_2(aq)]_{eq}$ > 9%. The dotted line corresponds to the linear regression.

After analyzing the effect of Si on the dissolution rate, the effect of calcium was investigated. As calcium may play a role in the transport properties of the gel layer formed on ISG[9,11], the rate data were plotted as a function of the concentration of calcium in solution, for all experiments conducted in the domain where the solution composition exceeds the solubility of the gel layer (i.e., $[SiO_2(aq)]/[SiO_2(aq)]_{eq}$ > 9%). For Ca concentrations covering a range of ~5 orders of magnitude, the dissolution rate did not appear to be correlated with the concentration of calcium in solution (Fig. V-13), contrasting with results obtained on short-term experiments only, where the heterogeneous precipitation of CSH at the surface of ISG was weak or absent (see previous Chapter).

The investigation thus focused on the impact of Ca-bearing secondary phases such as CSH and calcium carbonates. To unravel their effect on the dissolution rate, the experiments in this study where calcium was added initially to the solution were compared to the experiments of Fournier et al. (2019)[14], where no calcium was added.

The dissolution rates calculated by Fournier et al. (2019)[14] are lower than the ones calculated in this study (Fig. V-12a) by about an order of magnitude (intercept of the linear regression is -3.15 for the data from Fournier et al. (2019)[14] and -2.11 for this study). Focusing on the experiments with a $[SiO_2(aq)]/[SiO_2(aq)]_{eq}$ ratio > 9% for both studies, some discrepancies can be highlighted. Despite the correlation between the dissolution rate and the activity of silica in solution, S2-Blk-9.8 experiment conducted with a $[SiO_2(aq)]/[SiO_2(aq)]_{eq}$ ratio around 10%, exhibits a dissolution rate that is lower (<

0.01 $g.m^{-2}.d^{-1}$) than some experiments conducted in the present study with a $[SiO_2(aq)]/[SiO_2(aq)]_{eq}$ ratio between 44% to 100% (0.01 $g.m^{-2}.d^{-1}$< dissolution rate < 0.1 $g.m^{-2}.d^{-1}$).

Because no correlation was found between dissolved calcium concentrations and the dissolution rate, the hypothesis that CSH are the source of the discrepancies between the rate data collected by Fournier and coworkers and the results from the present study was therefore investigated next. As a reminder, no secondary precipitates were reported in the datasets selected from Fournier et al. (2019)[14], whereas most rate data collected in the present study at $[SiO_2(aq)]/[SiO_2(aq)]_{eq}$ > 44% were obtained in the saturation domain with respect to CSH0.8 and/or CSH1.2 and/or CSH1.6.

These precipitates were characterized using IR and SEM-EDX to determine their composition and nature. Considering the temperature of 90°C, the pH around 10 and the Si and Ca chemical composition of the solution, three different secondary phases were mainly expected: (i) amorphous silica, as it corresponds to the SiO_2 polymorph with the highest precipitation rate in this range of temperature; (ii) CSH, as the experiments were designed to favor the precipitation of these minerals[26], and (iii) calcium carbonates in case the solution got in contact with the atmosphere and CO_2 dissolved in the solution[37,39,40,47]. Some other phases such as zeolites might precipitate but as minor phases (see Ferrand et al., 2021[26] for more details), and were not evidenced from our experiments. Conversely, amorphous silica, CSH and calcium carbonates precipitates were actually evidenced in the present study (see Results and Fig. V-6 and V-7).

A clear increase in dissolution rate was observed only when CSH precipitated in experiments lasting more than 20 days (see Fig. V-8). As little to no difference was highlighted from the short-term experiments dissolution rate with or without CSH (Fig. V-8), an induction period, here lasting around 20 days, seem to be required for CSH precipitation to significantly impact ISG reactivity. According to Mercado-Depierre et al. (2013)[9], the precipitation of CSH lowers the activity of SiO_2(aq), and the glass dissolution rate is expected to be equal to the forward dissolution rate, at the maximum. As a conclusion, the presence of CSH has little to no effect on the dissolution rate for short-term experiment and increases the dissolution rate for longer-term experiment, up to one order of magnitude. However, the increase is only of second order compared to the effect of the activity of aqueous silica in the solution.

V.4.3. Alteration mechanism and dissolution resumption, insight from 101 days alteration experiments

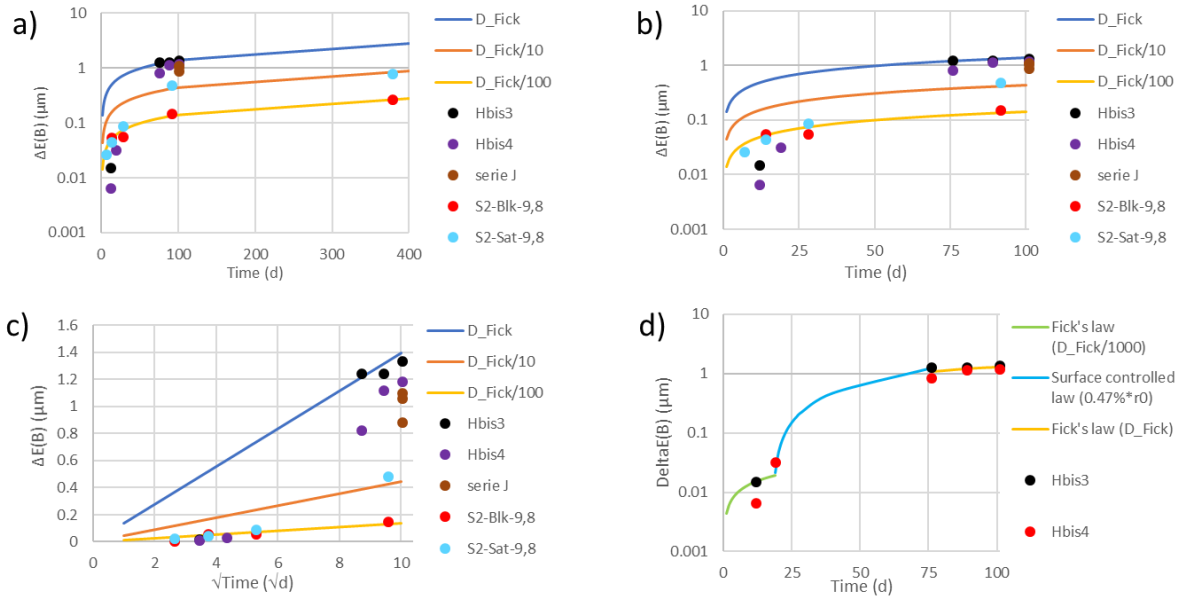

Figure V-14: Graphics representing the gel layer thickness (µm) based on the release of B in the solution as a function of time (day). a) and b) represents the dissolution rate of a few selected experiments. The experiment duration is up to a) 379 days for Fournier's data, but this study's data stopped after b) 101 days. The dissolution rate is compared to the diffusion-controlled dissolution rate established by Fick's law. The diffusion coefficient is D_Fick = 1.78 x10^{-19} m².s^{-1} from Gin et al., 2020[63]. The other curves refer to a lower diffusion coefficient. c) is another representation of b). d) models of the dissolution rate evolution by combining Fick's law and the forward dissolution rate of ISG sample that is of r_0 = 11.2 g.m^{-2}.d^{-1} from Fournier et al., 2016[79]. This forward dissolution rate is, however, adjusted to only 0.47% of r0.

After addressing the impact of dissolved Si and Ca, and Ca-precipitates on ISG dissolution rate over short-time experiments, we attempted to determine the rate-controlling processes and associated mechanisms of ISG dissolution based on long-term experiments. In that respect, experiments labelled Hbis3 and Hbis4 were carried out over 101 days and were submitted to time-resolved aqueous sampling (Fig. V-9). To verify that this sampling did not disturb the progress of the experiments, J3 and J3bis were prepared as replicates of Hbis3, and J4 and J4bis were prepared as replicates of Hbis4, although none of these replicates experienced time-resolved aqueous sampling (the corresponding reactors remained closed until the end of the experiments). The starting and final compositions of the fluid were found similar, suggesting a similar fluid evolution in all experiments (Fig. V-9a).

These experiments, and especially Hbis3 and Hbis4, were compared to S2-Sat-9.8 and S2-Blk-9.8 from Fournier et al. (2019)[14], for which the experiments lasted up to 379 days. For the record, all these experiments were run at high $[SiO_2(aq)]/[SiO_2(aq)]_{eq}$, corresponding to conditions where the passivating layer was not supposed to dissolve (see above). In these conditions, the dissolution of ISG

is typically thought to be diffusion-controlled[24,77]. To test this hypothesis, the equivalent thickness calculated from long-term experiments were fitted following:

$$\Delta Eth = \frac{2}{\sqrt{\pi}}\sqrt{D_{Fick} \times t} \qquad (5)$$

where t corresponds to the time in days and D_{Fick} refers to a diffusion coefficient extrapolated from Gin et al., 2020[63] and is equal to 1.8 x 10^{-19} $m^2.s^{-1}$ at pH 10.

On the one hand, the experiments carried out by Fournier et al. (2019)[14] are in reasonable agreement with a diffusion-limited regime throughout the duration of the experiment, although the diffusion coefficient (D_{Fick}) is one (S2-Sat-9.8) to two (S2-Blk-9.8) orders of magnitude lower than the one extrapolated from Gin et al., 2020[63] (Fig. V-14a, b).

On the other hand, the release of B from experiments Hbis3 and Hbis4 followed a more complex evolution:

- For durations shorter than 20 days, the release rate of B is close to (or even lower than) that observed from experiments S2-Sat-9.8 and S2-Blk-9.8 (Fig. V-14a-c).

- A sudden increase in the calculated equivalent thickness is then observed (Fig. V-14a, b) between 19 days and 76 days, as the experimental data points deviate from the Fickian trend described for time ranging from 0 to 19 days (Fig. V-14c).

- Finally, for durations longer than 76 days, the concentration of B keeps increasing, though to a much lower pace. In parallel, no retreat at the surface of the coupon was measured with VSI in areas devoid of secondary phases. In addition, the precipitates from J4 and J4bis presented both silica gel with a Ca/Si ratio of 0.7, CSH precipitates with a layer-like morphology and a Ca/Si ratio of 1.1 at the surface of ISG sample, and faceted CSH with a Ca/Si ratio between 0.44 and 0.67 (Fig. V-10b and V-10c). The FIB thin section realized on J4bis coupon positively supports the presence of both amorphous silica (Fig. V-11e and V-11g), calcium carbonate (as inferred from the presence of Ca and C in the precipitates, Fig. V-11g), and CSH, as the electron diffraction pattern shown in Fig. V-11d is in good agreement with the d-spacing of okenite ($Ca_3[Si_6O_{15}]\bullet 6H_2O$) (7.66 Å, 4.53 Å, 3.97 Å, 3.49 Å, 2.92 Å, 2.80 Å and 2.39 Å)[81]. Okenite is known to be a crystallized CSH that is highly keen to precipitate during ISG dissolution in hyperalkaline condition at 70°C[26,38,44].

Based on the abovementioned observations, we suggest the following scenario to describe the reactivity of ISG in a (Si, Ca)-rich environment at 90°C and alkaline conditions:

(1) First, the precipitation of CSH occurred at the very moment of Ca addition in the solution and was visually observed through the turbidity of the solution, which increased with the amount of

Ca added. This first precipitation step corresponds mainly to homogenous CSH nucleation in the solution, as inferred from the analyses of the solids filtered from the solution (see e.g., Fig. V-6a). This nucleation marked the first step of CSH formation, as described in the literature[32,34]. Small CSH clusters then aggregated slowly and started growing layer by layer before a potential crystallization. This aggregation and growth represented the second step of CSH nucleation[34], which occurred in this study between 12 days and 19 days, as suggested by the sudden decrease in aqueous Ca and Si concentrations in Hbis and J series (Fig. V-9). However, even if the loss of Ca and Si concentrations was similar in both experiments, the corresponding aqueous Ca/Si ratio suggested (0.12) that a significant amount of amorphous silica precipitated along with the CSH. The SEM pictures of F3 experiment confirmed the precipitation of both phases (e.g., Fig. V-6a). As CSH precipitates were formed mainly in the bulk solution while the $[SiO_2(aq)]/[SiO_2(aq)]_{eq}$ ratio did not reach the solubility threshold of the gel (suggested to be close to 9% in this study), the precipitation of CSH had only a very modest impact on ISG dissolution rate, which was similar to or slightly higher than the dissolution rates from Fournier et al. (2019)[14], measured in absence of precipitates (Fig. V-8 and Fig. V-12).

(2) For durations exceeding ~20 days, CSH also started to aggregate and grow at the surface of the ISG coupons (Fig. V-7, Fig. V-10, Fig. V-11). The resumption of glass alteration revealed in Fig. V-14 may be ascribed to the precipitation of CSH. Considering that if the alteration was only diffusion-controlled, no resumption of evolution would have been observed, a shift in the rate-controlling process from transport-limited to hydrolysis-limited may be proposed (Fig. V-14d). This shift was supposedly due to i) the dissolution or consumption of the gel layer locally by the CSH precipitates, allowing a faster alteration from the opening of the porosity within the gel layer and ii) the shift of the solution away from amorphous silica saturation. Supporting this assertion, the dissolution rate between 19 and 76 days increased up to around 15x compared with the dissolution rate between 0 and 19 days which is in reasonable agreement with previous findings. According to Fournier et al., 2017[82], the precipitation of secondary phases at pH 10 could raise ISG dissolution rate up to 10^{-2} $g.m^{-2}.d^{-1}$, which remains much lower than r_0 at the corresponding pH of 10. Although the phases that precipitated in Fournier's study were zeolites instead of CSH, it gives an indicative value of the glass dissolution rate controlled by secondary silicate phases precipitation. Thus, it seems reasonable to observe a resumption of alteration at a quite low dissolution rate relative to r_0.

In addition, our study suggests that the impact of CSH must have remained local (i.e., at the contact between CSH and the surface of the altered coupon), since the Si concentration in the bulk solution remained such that $[SiO_2(aq)]/[SiO_2(aq)]_{eq} > 9\%$, which is a reasonable estimate for the solubility of the passivating gel layer (in other words, the decrease in the bulk aqueous Si concentration could not account for a such a drastic resumption of ISG dissolution). This suggestion would be

supported by the observation that $r\_disso(B)$ from ICP-OES analyses were equal or greater in general than r_solid from solid characterization (Fig. V-5), while the VSI analyses did not evidence any surface retreat (i.e., the consumption of the gel layer did not occur in areas devoid of secondary phases, and must have occurred below the CSH, which was impossible to probe with VSI). Of note, the resumption of the alteration due to the growth of secondary phases at the expense of the silica gel was also studied by Gin et al. (2015)[15]. After perturbating the environment by increasing the pH from 9 to 11.5, they observed the precipitation of CSH and zeolites that maintained the dissolution rate close to the forward dissolution rate until complete dissolution of ISG. However, contrary to Gin et al. (2015)[15], the forward dissolution rate was not reached during our study, likely because the pH was lower than in this previous study[82].

(3) Between 76 days and 89 days, the concentration of calcium in the solution decreased to a few tens of ppm, which represent between 9% and 5% of the initial concentration of calcium in the solution for Hbis3 and Hbis4, respectively. Because the evolution of Si in the solution did not correlate with that of Ca, the crystallization of CSH can be dismissed. As a drop in pH was observed during that time, the consumption of Ca most likely resulted from the precipitation of calcium carbonates phases, probably due to a slow dissolution of CO_2 in the solution, as the reactor is not fully impermeable. The ingress of CO_2 in the reactors in long-term experiments shifted the composition of the solution outside of the stability field of CSH that were formed at early stages (Fig. V-9a), resulting in their transformation in favor of carbonate and amorphous silica, as confirmed by TEM observations (Fig. V-11a). Ultimately, if the resumption of ISG dissolution observed between 19 and 76 days was due to the destabilization of the gel layer because of the growth of CSH, then the carbonation of CSH is a likely mechanism that could explain why ISG dissolution shifts back to a diffusion-controlled process, as the driving force for the gel layer destabilization has vanished.

Tableau V-3: Comparison of the gel layer thickness (µm) for the series J and Hbis after 101 days of alteration based on ICP-OES analysis in the second column and on the solid characterization in the third column. In the white cases where nothing is written, information was not coherent or was not collected.

Name of the experiment	ICP-OES analysis (µm)	Solid characterization (µm)
J3	1.25	1.1
J3bis	1.1	
J4bis		0.88
Hbis3	1.19	
Hbis4	0.87	

As a conclusion, whereas ISG dissolution rate is negatively correlated to first order with the activity of dissolved silica in the solution, to second order, the precipitation of CSH in the solution has likely contributed to a transient increase in the dissolution rate, but not up to the forward dissolution rate. If the dissolution rate resumption were to be compared with the forward dissolution rate, it would amount to ~0.5% of r_0. A hypothesis was proposed for this increase in the dissolution rate: the gel layer is dissolved or consumed locally by the CSH precipitates.

V.5.CONCLUSION

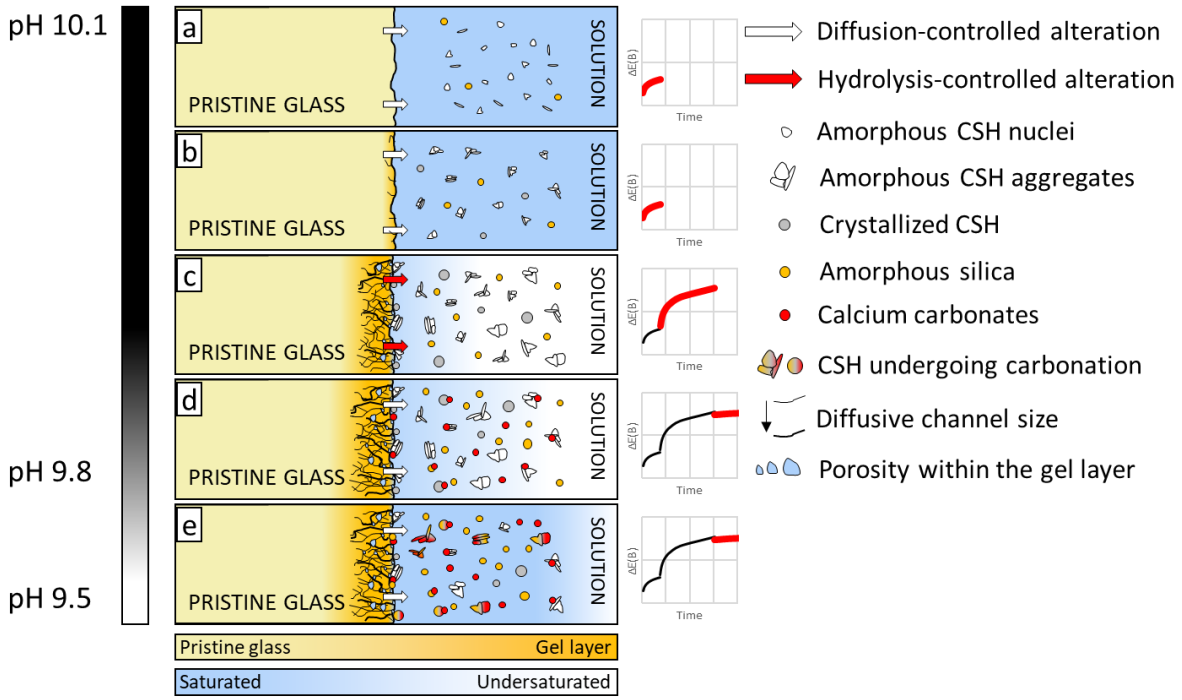

Figure V-15: Schematic summary of the proposed ISG alteration process in a (Ca, Si)-rich solution and pH 10, with possible influence of CO2. a) After the addition of Ca in the pH 10.1 saturated solution with respect to amorphous silica, homogeneous precipitation of CSH occurs. The alteration of ISG is diffusion-controlled. b) During the 20 first days, CSH aggregate, with possible modification of crystal-chemistry. They start growing and some undergo a crystallization process. c) The dissolution rate increases by a x15 factor. The alteration mechanism switches from diffusion-controlled to hydrolysis-controlled during the growth of the CSH. The calcium in the solution is consumed by the CSH growth and regenerated by the local dissolution of ISG due to the presence of CSH on the sample surface. In spite of glass dissolution, the concentration of silica in the solution decreases due to CSH consumption and amorphous silica precipitation. The solution becomes undersaturated with respect to amorphous silica. Until the end of the CSH growth, the pH remains mostly constant. d) After 76 days, the pH starts to decrease (ingress of CO2). Calcium carbonates precipitate at the expense of CSH and Ca in solution. The dissolution rate decreases, and the alteration mechanism shifts back to a diffusion-limited process. Since the pH has decreased, the solution slowly saturates with respect to amorphous silica. e) A competition between CSH and calcium carbonates arises. CSH starts to undergo a carbonation process with amorphous silica and calcium carbonates as by-products. The pH keeps decreasing, bringing back the solution close to the saturation state with respect to amorphous silica. The alteration remains diffusion-controlled.

While the mechanisms and kinetics of ISG dissolution have been extensively investigated over the past decade (Gin et al., 2018[62] and references therein), the reactivity of ISG at basic pH and in (Ca, Si)-rich environment remained essentially unexplored. By studying the reactivity of ISG in alkaline

condition at 90°C with various dissolved calcium and silicon concentrations, the following conclusions can be drawn:

(i) The dissolution rate of ISG is strongly correlated with the activity of dissolved silica in the solution. The solubility of the gel layer may range between 2% and 9% of that of amorphous silica. Above that threshold, the dissolution rate remains low (< 0.1 $g.m^{-2}.d^{-1}$) and is diffusion-controlled.

(ii) The secondary phases, and in particular CSH precipitates, have only a second order effect on the dissolution rate of ISG during the 19 first days of alteration. These conclusions contrast with those offered by Mercado-Depierre et al. (2013)[9], who observed that the dissolution rate increases up to the forward dissolution rate as soon as the solution is saturated with respect to CSH.

(iii) A resumption of the dissolution rate is observed between 19 and 76 days. It can be explained by a shift in the alteration mechanism from diffusion to hydrolysis. However, the forward dissolution rate remains unattained.

(iv) The competition between the formation of CSH and calcium carbonates likely limited the resumption of ISG dissolution in the experiments conducted in the present study. For experiments run over durations exceeding 76 days, the precipitation of calcium carbonates consumed CSH while resulting in the acidification of the solution, which in turn was responsible for a shift in the solution composition towards conditions closer to amorphous silica saturation. As a consequence, the dissolution process returned back to a diffusion-limited regime, though with a diffusion coefficient higher than in the previous step of the process.

This study proposes a general understanding of borosilicate glass behavior in (Si, Ca)-rich environment under alkaline condition which is of interest concerning the present concepts of deep geological repository in France. One of the main concerns of the borosilicate glass dissolution in interaction with a cementitious grout is the alteration resumption due to secondary phases. The results presented here tend to confirm this concern, however, the presence of carbonates in solution might prevent or limit the resumption of glass alteration from CSH precipitates. Therefore, we suggest that in addition to the impact of dissolved Ca and Si, future studies should be directed at assessing the impact of carbonates and investigating the state of the altered glass after the alkaline alteration.

DATA AVAILABILITY STATEMENT

The authors declare that the data supporting the findings of this study are available on demand (benjamin.cagnon@univ-grenoble-alpes.fr)

ACKNOWLEDGEMENTS

The authors thank Simona Denti (ISTerre), Delphine Tisserand (ISTerre), Sylvain Campillo (ISTerre) and Sabine Santenac (ISTerre) for helping and providing advice with the ICP-OES analysis. Luca Stigliano (ISTerre) for performing VSI measurement alongside D.D. Nathaniel Findling (ISTerre) and Rachel Martin (ISTerre) for teaching and providing assistance with the MEB-EDX characterizations. The authors are also grateful to Loan Lai, Elodie Chauvet, Amandine David, Florian Cousy and Yves Depuydt from Tescan Analytics for performing ToF-SIMS analyses and operating FIB thin sections. Nicolas Michau and Christelle Martin from Andra, and Theo Montaigne from EDF are thanked for their inputs on an earlier version of this manuscript. This work was funded by Andra and EDF.

COMPETING INTERESTS

The authors declare no competing interests.

AUTHOR CONTRIBUTIONS

B.C. performed the experiments and analyzed data. M.C. performed and analyzed the TEM measurements as well as STEM-EDX characterization. D.D. and S.G. analyzed data and supervised the research. B.C., D.D., and S.G. wrote the manuscript, with contributions from all authors.

REFERENCES

1 Ojovan, M. I. & Lee, W. E. Glassy Wasteforms for Nuclear Waste Immobilization. *Metallurgical and Materials Transactions A* **42**, 837-851, doi:10.1007/s11661-010-0525-7 (2011).

2 Cassingham, N. *et al.* The initial dissolution rates of simulated UK Magnox–ThORP blend nuclear waste glass as a function of pH, temperature and waste loading. *Mineral Mag* **79**, 1529-1542, doi:10.1180/minmag.2015.079.6.28 (2015).

3 Diane Rebiscoul, P. F., Stéphane Gin, André Ayral,. Protective properties and dissolution ability of the gel formed during nuclear glass alteration. *Journal of Nuclear Materials* **342**, 26-34, doi:https://doi.org/10.1016/j.jnucmat.2005.03.018 (2005).

4 K. Ferrand, A. A., B. Grambow,. Water diffusion in the simulated French nuclear waste glass SON 68 contacting silica rich solutions: Experimental and modeling,. *Journal of Nuclear Materials* **355**, 54-67, doi:https://doi.org/10.1016/j.jnucmat.2006.04.005 (2006).

5 Neeway, J., Abdelouas, A., Grambow, B. & Schumacher, S. Dissolution mechanism of the SON68 reference nuclear waste glass: New data in dynamic system in silica saturation conditions. *Journal of Nuclear Materials* **415**, 31-37, doi:https://doi.org/10.1016/j.jnucmat.2011.05.027 (2011).

6 Icenhower, J. P. & Steefel, C. I. Experimentally determined dissolution kinetics of SON68 glass at 90°C over a silica saturation interval: Evidence against a linear rate law. *Journal of Nuclear Materials* **439**, 137-147, doi:https://doi.org/10.1016/j.jnucmat.2013.04.008 (2013).

7 Gin, S. *et al.* An international initiative on long-term behavior of high-level nuclear waste glass. *Materials Today* **16**, 243-248, doi:https://doi.org/10.1016/j.mattod.2013.06.008 (2013).

8 Inagaki, Y., Kikunaga, T., Idemitsu, K. & Arima, T. Initial Dissolution Rate of the International Simple Glass as a Function of pH and Temperature Measured Using Microchannel Flow-Through Test Method. *International Journal of Applied Glass Science* **4**, 317-327 (2013).

9 Mercado-Depierre, S., Angeli, F., Frizon, F. & Gin, S. Antagonist effects of calcium on borosilicate glass alteration. *Journal of Nuclear Materials* **441**, 402-410, doi:https://doi.org/10.1016/j.jnucmat.2013.06.023 (2013).

10 CHAVE, T., Frugier, P., Gin, S. & Ayral, A. Glass–water interphase reactivity with calcium rich solutions. *Geochim Cosmochim Ac* **75**, 4125 - 4139, doi:10.1016/j.gca.2011.05.005 (2011).

11 Collin, M., Fournier, M., Charpentier, T., Moskura, M. & Gin, S. Impact of alkali on the passivation of silicate glass. *npj Materials Degradation* **2**, 16 (2018).

12 Utton, C. *et al.* Dissolution of Vitrified Wastes in a High-pH Calcium-Rich Solution. *Journal of Nuclear Materials* **435**, 112–122, doi:10.1016/j.jnucmat.2012.12.032 (2013).

13 Wild, B. *et al.* pH-dependent control of feldspar dissolution rate by altered surface layers. *Chem Geol* **442**, 148-159, doi:http://dx.doi.org/10.1016/j.chemgeo.2016.08.035 (2016).

14 Fournier, M. *et al.* Effect of pH on the stability of passivating gel layers formed on International Simple Glass. *Journal of Nuclear Materials* **524**, 21-38, doi:https://doi.org/10.1016/j.jnucmat.2019.06.029 (2019).

15 Gin, S. *et al.* The fate of silicon during glass corrosion under alkaline conditions: A mechanistic and kinetic study with the International Simple Glass. *Geochim Cosmochim Ac* **151**, 68-85, doi:https://doi.org/10.1016/j.gca.2014.12.009 (2015).

16 Vienna, J. D., Neeway, J. J., Ryan, J. V. & Kerisit, S. N. Impacts of glass composition, pH, and temperature on glass forward dissolution rate. *npj Materials Degradation* **2**, 22, doi:10.1038/s41529-018-0042-5 (2018).

17 Backhouse, D. J. *et al.* Corrosion of the International Simple Glass under acidic to hyperalkaline conditions. *npj Materials Degradation* **2**, 29, doi:10.1038/s41529-018-0050-5 (2018).

18 Gin, S. *et al.* A general mechanism for gel layer formation on borosilicate glass under aqueous corrosion. *The Journal of Physical Chemistry C* **124**, 5132-5144 (2020).

19 Fournier, M., Gin, S. & Frugier, P. Resumption of nuclear glass alteration: state of the art. *Journal of Nuclear Materials* **448**, 348-363 (2014).
20 Aréna, H. *et al.* Impact of Fe, Mg and Ca elements on glass alteration: Interconnected processes. *Geochim Cosmochim Ac* **239**, 420-445, doi:https://doi.org/10.1016/j.gca.2018.08.007 (2018).
21 Liu, S., Ferrand, K. & Lemmens, K. Transport- and surface reaction-controlled SON68 glass dissolution at 30°C and 70°C and pH=13.7. *Appl Geochem* **61**, 302-311, doi:https://doi.org/10.1016/j.apgeochem.2015.06.014 (2015).
22 Jollivet, P., Gin, S. & Schumacher, S. Forward dissolution rate of silicate glasses of nuclear interest in clay-equilibrated groundwater. *Chem Geol* **330–331**, 207-217, doi:http://dx.doi.org/10.1016/j.chemgeo.2012.09.012 (2012).
23 Maraghechi, H., Rajabipour, F., Pantano, C. G. & Burgos, W. D. Effect of calcium on dissolution and precipitation reactions of amorphous silica at high alkalinity. *Cement and Concrete Research* **87**, 1-13, doi:https://doi.org/10.1016/j.cemconres.2016.05.004 (2016).
24 Cagnon, B., Daval, D., Cabié, M., Lemarchand, D. & Gin, S. A comparative study of the dissolution mechanisms of amorphous and crystalline feldspars at acidic pH conditions. *npj Materials Degradation* **6**, 34, doi:10.1038/s41529-022-00240-6 (2022).
25 Damodaran, K., Delaye, J.-M., Kalinichev, A. G. & Gin, S. Deciphering the non-linear impact of Al on chemical durability of silicate glass. *Acta Materialia*, 117478, doi:https://doi.org/10.1016/j.actamat.2021.117478 (2021).
26 Ferrand, K. *et al.* Dissolution Kinetics of International Simple Glass and Formation of Secondary Phases at Very High Surface Area to Solution Ratio in Young Cement Water. *Materials* **14** (2021).
27 Aréna, H., Rébiscoul, D., Garcès, E. & Godon, N. Comparative effect of alkaline elements and calcium on alteration of International Simple Glass. *npj Materials Degradation* **3**, 10, doi:10.1038/s41529-019-0072-7 (2019).
28 Neeway, J. J. *et al.* Acceleration of glass alteration rates induced by zeolite seeds at controlled pH. *Appl Geochem* **113**, 104515, doi:https://doi.org/10.1016/j.apgeochem.2019.104515 (2020).
29 Mercado-Depierre, S., Fournier, M., Gin, S. & Angeli, F. Influence of zeolite precipitation on borosilicate glass alteration under hyperalkaline conditions. *Journal of Nuclear Materials* **491**, 67-82, doi:https://doi.org/10.1016/j.jnucmat.2017.04.043 (2017).
30 Mann, C. *et al.* Influence of young cement water on the corrosion of the International Simple Glass. *npj Materials Degradation* **3**, 5, doi:10.1038/s41529-018-0059-9 (2019).
31 Garrault-Gauffinet, S. & Nonat, A. Experimental investigation of calcium silicate hydrate (C-S-H) nucleation. *Journal of Crystal Growth* **200**, 565-574, doi:https://doi.org/10.1016/S0022-0248(99)00051-2 (1999).
32 Krautwurst, N. *et al.* Two-Step Nucleation Process of Calcium Silicate Hydrate, the Nanobrick of Cement. *Chem Mater* **30**, 2895-2904, doi:10.1021/acs.chemmater.7b04245 (2018).
33 Krautwurst, N. *Nucleation of calcium silicate hydrate in aqueous solution and the influence of biomolecules on cement hydration*, Dissertation, Mainz, Johannes Gutenberg-Universität, 2017, (2017).
34 Aretxabaleta, X., López-Zorrilla, J., Etxebarria, I. & Manzano, H. CSH nucleation pathway from atomistic simulations. (2023).
35 Blanc, P., Bourbon, X., Lassin, A. & Gaucher, E. C. Chemical model for cement-based materials: Temperature dependence of thermodynamic functions for nanocrystalline and crystalline C–S–H phases. *Cement and Concrete Research* **40**, 851-866, doi:https://doi.org/10.1016/j.cemconres.2009.12.004 (2010).
36 Blanc, P., Bourbon, X., Lassin, A. & Gaucher, E. C. Chemical model for cement-based materials: Thermodynamic data assessment for phases other than C–S–H. *Cement and Concrete Research* **40**, 1360-1374, doi:https://doi.org/10.1016/j.cemconres.2010.04.003 (2010).

37 Liu, X. *et al.* Carbonation behavior of calcium silicate hydrate (C-S-H): Its potential for CO2 capture. *Chemical Engineering Journal* **431**, 134243, doi:https://doi.org/10.1016/j.cej.2021.134243 (2022).
38 Wu, B. & Ye, G. Study of carbonation rate of synthetic CSH by XRD, NMR and FTIR. *Heron* **64**, 21-38 (2019).
39 Morandeau, A. E. & White, C. E. In situ X-ray pair distribution function analysis of accelerated carbonation of a synthetic calcium–silicate–hydrate gel. *Journal of Materials Chemistry A* **3**, 8597-8605, doi:10.1039/c5ta00348b (2015).
40 Chang, J. & Fang, Y. Quantitative analysis of accelerated carbonation products of the synthetic calcium silicate hydrate(C–S–H) by QXRD and TG/MS. *J Therm Anal Calorim* **119**, 57-62, doi:10.1007/s10973-014-4093-8 (2015).
41 Garbev, K. *et al.* Structural Features of C–S–H(I) and Its Carbonation in Air—A Raman Spectroscopic Study. Part I: Fresh Phases. *Journal of the American Ceramic Society* **90**, 900-907, doi:https://doi.org/10.1111/j.1551-2916.2006.01428.x (2007).
42 Black, L. *et al.* Structural Features of C–S–H(I) and Its Carbonation in Air—A Raman Spectroscopic Study. Part II: Carbonated Phases. *Journal of the American Ceramic Society* **90**, 908-917, doi:https://doi.org/10.1111/j.1551-2916.2006.01429.x (2007).
43 Sevelsted, T. F. & Skibsted, J. Carbonation of C–S–H and C–A–S–H samples studied by 13C, 27Al and 29Si MAS NMR spectroscopy. *Cement and Concrete Research* **71**, 56-65, doi:https://doi.org/10.1016/j.cemconres.2015.01.019 (2015).
44 Li, J., Yu, Q., Huang, H. & Yin, S. Effects of Ca/Si Ratio, Aluminum and Magnesium on the Carbonation Behavior of Calcium Silicate Hydrate. *Materials* **12** (2019).
45 Young, J. F., Berger, R. L. & Breese, J. Accelerated Curing of Compacted Calcium Silicate Mortars on Exposure to CO2. *Journal of the American Ceramic Society* **57**, 394-397, doi:https://doi.org/10.1111/j.1151-2916.1974.tb11420.x (1974).
46 Fernández Bertos, M., Simons, S. J. R., Hills, C. D. & Carey, P. J. A review of accelerated carbonation technology in the treatment of cement-based materials and sequestration of CO2. *Journal of Hazardous Materials* **112**, 193-205, doi:https://doi.org/10.1016/j.jhazmat.2004.04.019 (2004).
47 Goto, S., Suenaga, K., Kado, T. & Fukuhara, M. Calcium Silicate Carbonation Products. *Journal of the American Ceramic Society* **78**, 2867-2872, doi:https://doi.org/10.1111/j.1151-2916.1995.tb09057.x (1995).
48 van der Lee, J. & De Windt, L. *CHESS Tutorial and Cookbook. Updated for version 3.0.*, Vol. Manual Nr. LHM/RD/02/13 (2002).
49 Blanc, P. *et al.* ThermoChimie database developments in the framework of cement/clay interactions. *Appl Geochem* **55**, 95-107, doi:https://doi.org/10.1016/j.apgeochem.2014.12.006 (2015).
50 Marty, N. C. M. *et al.* A database of dissolution and precipitation rates for clay-rocks minerals. *Appl Geochem* **55**, 108-118, doi:https://doi.org/10.1016/j.apgeochem.2014.10.012 (2015).
51 Grivé, M., Duro, L., Colàs, E. & Giffaut, E. Thermodynamic data selection applied to radionuclides and chemotoxic elements: An overview of the ThermoChimie-TDB. *Appl Geochem* **55**, 85-94, doi:https://doi.org/10.1016/j.apgeochem.2014.12.017 (2015).
52 Giffaut, E. *et al.* Andra thermodynamic database for performance assessment: ThermoChimie. *Appl Geochem* **49**, 225-236, doi:https://doi.org/10.1016/j.apgeochem.2014.05.007 (2014).
53 Ryan, J. V. *et al.* ISG-2: properties of the second International Simple Glass. *npj Materials Degradation* **7**, 47, doi:10.1038/s41529-023-00352-7 (2023).
54 Zhakiyeva, Z. *Structure et dynamique de l'eau dans le ciment Portland et dans des ciments bas carbone*, (2021).
55 Daval, D. *et al.* Mechanism of wollastonite carbonation deduced from micro- to nanometer length scale observations. *Am Mineral* **94**, 1707-1726, doi:10.2138/am.2009.3294 (2009).

56 Grambow, B. & Muller, R. First-order dissolution rate law and the role of surface layers in glass performance assessment. *Journal of Nuclear Materials* **298**, 112-124 (2001).
57 Doremus, R. H. Diffusion-controlled reaction of water with glass. *Journal of Non-Crystalline Solids* **55**, 143-147, doi:https://doi.org/10.1016/0022-3093(83)90014-5 (1983).
58 Bourcier, W. L., Peiffer, D. W., Knauss, K. G., McKeegan, K. D. & Smith, D. K. A Kinetic Model for Borosilicate Glass Dissolution Based on the Dissolution Affinity of a Surface Alteration Layer. *MRS Online Proceedings Library Archive* **176**, null-null, doi:doi:10.1557/PROC-176-209 (1989).
59 Hellmann, R. The albite-water system .4. Diffusion modeling of leached and hydrogen-enriched layers. *Geochim Cosmochim Ac* **61**, 1595-1611 (1997).
60 Hellmann, R. & Tisserand, D. Dissolution kinetics as a function of the Gibbs free energy of reaction: An experimental study based on albite feldspar. *Geochim Cosmochim Ac* **70**, 364-383 (2006).
61 Hellmann, R. *et al.* Unifying natural and laboratory chemical weathering with interfacial dissolution–reprecipitation: A study based on the nanometer-scale chemistry of fluid–silicate interfaces. *Chem Geol* **294–295**, 203-216 (2012).
62 Gin, S. *et al.* Dynamics of self-reorganization explains passivation of silicate glasses. *Nature communications* **9**, 2169 (2018).
63 Gin, S. *et al.* Insights into the mechanisms controlling the residual corrosion rate of borosilicate glasses. *npj Materials Degradation* **4**, 1-9 (2020).
64 Grambow, B. A general rate equation for nuclear waste glass corrosion. *Mater. Res. Soc. Symp. Proc.* **44**, 15-27 (1985).
65 Aagaard, P. & Helgeson, H. C. THERMODYNAMIC AND KINETIC CONSTRAINTS ON REACTION-RATES AMONG MINERALS AND AQUEOUS-SOLUTIONS .1. THEORETICAL CONSIDERATIONS. *Am J Sci* **282**, 237-285 (1982).
66 Berger, G., Beaufort, D. & Lacharpagne, J. C. Experimental dissolution of sanidine under hydrothermal conditions: Mechanism and rate. *Am J Sci* **302**, 663-685 (2002).
67 Daval, D. *et al.* Influence of amorphous silica layer formation on the dissolution rate of olivine at 90 degrees C and elevated pCO(2). *Chem Geol* **284**, 193-209, doi:10.1016/j.chemgeo.2011.02.021 (2011).
68 Daval, D., Hellmann, R., Saldi, G. D., Wirth, R. & Knauss, K. G. Linking nm-scale measurements of the anisotropy of silicate surface reactivity to macroscopic dissolution rate laws: New insights based on diopside. *Geochim Cosmochim Ac* **107**, 121-134, doi:http://dx.doi.org/10.1016/j.gca.2012.12.045 (2013).
69 Daux, V., Guy, C., Advocat, T., Crovisier, J. L. & Stille, P. Kinetic aspects of basaltic glass dissolution at 90 degrees C: role of aqueous silicon and aluminium. *Chem Geol* **142**, 109-126 (1997).
70 Frugier, P. *et al.* SON68 nuclear glass dissolution kinetics: Current state of knowledge and basis of the new GRAAL model. *Journal of Nuclear Materials* **380**, 8-21, doi:10.1016/j.jnucmat.2008.06.044 (2008).
71 Frugier, P., Chave, T., Gin, S. & Lartigue, J. E. Application of the GRAAL model to leaching experiments with SON68 nuclear glass in initially pure water. *Journal of Nuclear Materials* **392**, 552-567, doi:https://doi.org/10.1016/j.jnucmat.2009.04.024 (2009).
72 Frugier, P., Minet, Y., Rajmohan, N., Godon, N. & Gin, S. Modeling glass corrosion with GRAAL. *npj Materials Degradation* **2**, 35, doi:10.1038/s41529-018-0056-z (2018).
73 Vienna, J. D., Ryan, J. V., Gin, S. & Inagaki, Y. Current Understanding and Remaining Challenges in Modeling Long-Term Degradation of Borosilicate Nuclear Waste Glasses. *International Journal of Applied Glass Science* **4**, 283-294, doi:https://doi.org/10.1111/ijag.12050 (2013).
74 Gin, S. Protective Effect of the Alteration Gel: A Key Mechanism in the Long-Term Behavior of Nuclear Waste Glass. *MRS Online Proceedings Library (OPL)* **663**, 207, doi:10.1557/proc-663-207 (2000).

75 Gin, S. & Frugier, P. SON68 Glass Dissolution Kinetics at High Reaction Progress: Experimental Evidence of the Residual Rate. *MRS Online Proceedings Library (OPL)* **757**, II5.9, doi:10.1557/proc-757-ii5.9 (2002).
76 Gin, S., Jegou, C., Frugier, P. & Minet, Y. Theoretical consideration on the application of the Aagaard-Helgeson rate law to the dissolution of silicate minerals and glasses. *Chem Geol* **255**, 14-24, doi:10.1016/j.chemgeo.2008.05.004 (2008).
77 Pollet-Villard, M. *et al.* Does crystallographic anisotropy prevent the conventional treatment of aqueous mineral reactivity? A case study based on K-feldspar dissolution kinetics. *Geochim Cosmochim Ac* **190**, 294-308, doi:http://dx.doi.org/10.1016/j.gca.2016.07.007 (2016).
78 Ribet, S. & Gin, S. Role of neoformed phases on the mechanisms controlling the resumption of SON68 glass alteration in alkaline media. *Journal of Nuclear Materials* **324**, 152-164, doi:https://doi.org/10.1016/j.jnucmat.2003.09.010 (2004).
79 Fournier, M. *et al.* Glass dissolution rate measurement and calculation revisited. *Journal of Nuclear Materials* **476**, 140-154 (2016).
80 Damodaran, K., Gin, S., Narayanasamy, S. & Delaye, J.-M. On the effect of Al on alumino-borosilicate glass chemical durability. *npj Materials Degradation* **7**, 46, doi:10.1038/s41529-023-00364-3 (2023).
81 Merlino, S. Okenite, Ca 10 Si 18 O 46 . 18H 2 O; the first example of a chain and sheet silicate. *Am Mineral* **68**, 614-622 (1983).
82 Fournier, M., Gin, S., Frugier, P. & Mercado-Depierre, S. Contribution of zeolite-seeded experiments to the understanding of resumption of glass alteration. *npj Materials Degradation* **1**, 17, doi:10.1038/s41529-017-0018-x (2017).

Supplementary Information

International Simple Glass (ISG) dissolution rate in a (Si, Ca)-rich environment at 90°C and alkaline conditions

Benjamin Cagnon[1], Stéphane Gin[2], Martiane Cabié[3] and Damien Daval[1]

[1] Univ. Grenoble Alpes, Univ. Savoie Mont Blanc, CNRS, IRD, IFSTTAR, ISTerre, Grenoble, France

[2] CEA, DES, DPME, SEME, University of Montpellier, Marcoule, France

[3] Aix Marseille Univ, CNRS, Centrale Marseille, FSCM, CP2M, Marseille, France

Supplementary Note 1 : Fluid data

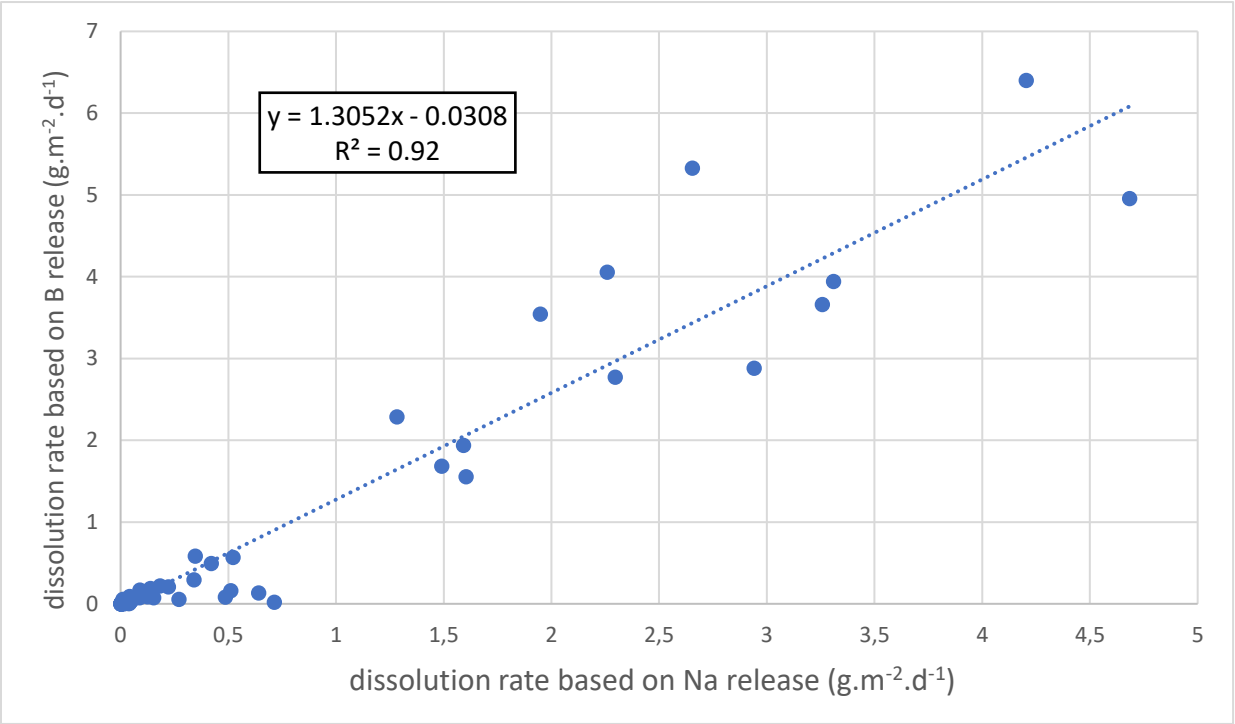

Figure V-16: Graphic representing the dissolution rate calculated based on the release of B in solution as a function of the dissolution rate calculated based on the release of Na in solution.

The dissolution rate calculated from both Na and B release are in good agreement ($R^2 > 0.9$) even though $r\_disso(B)$ is 1.3x higher than $r\_disso(Na)$ on average. Fig. V-5 shows a good agreement between $r\_disso(B)$ and r_solid with similar dissolution rate. As a consequence, the B element was considered as a better tracer of the alteration than Na element during the fluid composition analysis.

In the following tables, the fluid data (Ca, B, Na and Si element in ppm) are reported for each experiment alongside the time of collection (days), the volume of solution in the reactor (ml), the coupon's surface (mm^2) and the pH, if measured. NA means "Not analyzed" or "Not measured" and LoQ means "Limit of Quantification".

Series D

	Ca (ppm)	B (ppm)	Na (ppm)	Si (ppm)	Time (days)	Vol. (ml)	S (mm^2)	pH
D1_ini	0.01	0.12	0.31	944.0	0	45.0	82.0	10
D1_fin	-	0.26	0.42	1012.3	15.1	44.4	82.0	10

Series E

	Ca (ppm)	B (ppm)	Na (ppm)	Si (ppm)	Time (days)	Vol. (ml)	S (mm^2)	pH
E2_ini	1.01	0.046	0.47	1718.0	0	47.0	47.4	10
E2_fin	0.78	0.081	0.22	1658.6	14.0	45.6	47.4	10

Series F

	Ca (ppm)	B (ppm)	Na (ppm)	Si (ppm)	Time (days)	Vol. (ml)	S (mm²)	pH
F1_ini	280.3	0.081	0.49	3.8	0	49	59.4	10
F1_mid	254.0	1.85	2.19	13.1	11	45.8	59.4	NA
F1_fin	252.4	2.09	2.47	14.7	18	42.8	59.4	9.95
F2_ini	276.9	0.073	0.035	4.1	0	40	38.9	10
F2_mid	209.3	2.16	1.99	13.1	11	38.5	38.9	NA
F2_fin	227.8	2.53	2.46	15.1	18	37	38.9	9.95
F3_ini	264.2	0.013	0.00	12.7	0	40	57.8	10
F3_mid	139.4	3.01	2.78	25.4	11	38.5	57.8	NA
F3_fin	107.6	3.58	3.45	25.7	18	37	57.8	9.95

Series G

	Ca (ppm)	B (ppm)	Na (ppm)	Si (ppm)	Time (days)	Vol. (ml)	S (mm²)	pH
G2_ini	9.1	<LoQ	0.029	5.70	0	42.1	47.0	10
G2_mid	4.4	2.74	3.91	21.02	11	39.9	47.0	NA
G2_fin	3.8	3.18	4.81	23.00	17	35.2	47.0	9.9
G3_ini	60*	<LoQ	0.07	5.60	0	49.7	46.5	10
G3_mid	68.4	2.03	3.11	16.50	11	49.6	46.5	NA
G3_fin	61.6	2.48	3.48	18.14	17	44	46.5	9.9
G4_ini	380*	<LoQ	0.08	5.80	0	51.2	42.9	10
G4_mid	393.4	1.49	2.65	6.60	11	48.9	42.9	NA
G4_fin	359.5	3.42	4.81	6.22	17	47.2	42.9	9.9
G5_ini	780*	<LoQ	0.02	5.80	0	53.4	45.9	10
G5_mid	793.9	2.62	4.20	3.50	11	51.2	45.9	NA
G5_fin	817.7	4.40	5.80	5.73	17	48.4	45.9	9.9

Value with (*) correspond to potential error of analysis and theoretical value is reported instead.

Series H

	Ca (ppm)	B (ppm)	Na (ppm)	Si (ppm)	Time (days)	Vol. (ml)	S (mm²)	pH
H0_ini	2.5	0.99	<LoQ	NA*	0	32.5	960	10.3
H0_mid	<LoQ	1.40	0.41	3150.0	13	30	960	NA
H0_fin	<LoQ	0.96	0.65	3055.4	21	27.5	960	10.3
H1_ini	1.7	0.96	<LoQ	2677.1	0	32.5	960	10.3
H1_mid	1.8	1.19	<LoQ	2831.3	13	30	960	NA
H1_fin	4.8	1.01	0.35	2832.1	21	27.5	960	10.3
H2_ini	73.9	1.04	<LoQ	2761.4	0	32.5	960	10.3
H2_mid	38.0	1.27	0.13	NA*	13	30	960	NA
H2_fin	39.6	1.04	0.25	2588.3	21	27.5	960	10.3
H3_ini	117.3	0.80	<LoQ	2862.6	0	32.5	960	10.3
H3_mid	128.7	1.11	0.08	2932.8	13	30	960	NA
H3_fin	161.0	1.11	0.63	2993.7	21	27.5	960	10.3
H4_ini	NA*	0.84	<LoQ	2819.7	0	32.5	960	10.3
H4_mid	260.9	1.33	0.33	3158.5	13	30	960	NA
H4_fin	227.7	1.18	0.31	3003.9	21	27.5	960	10.3

Value with (*) correspond to potential error of analysis and theoretical value is reported as followed: H0_ini(Si) = 2600 – 2800 ppm, H2_mid(Si) = 2580 – 2760 ppm and H4_ini(Ca) = 280 ppm.

Series I

	Ca (ppm)	B (ppm)	Na (ppm)	Si (ppm)	Time (days)	Vol. (ml)	S (mm²)	pH
I4_ini	639.8	0.060	0.72	1455.6	0	57.1	81.4	10.1
I4_mid	784.1	0.055	0.73	1724.8	10	48.1	81.4	NA
I4_fin	1189.9	0.064	0.86	2283.9	23.8	45.1	81.4	10.1

Series Hbis

	Ca (ppm)	B (ppm)	Na (ppm)	Si (ppm)	Time (days)	Vol. (ml)	S (mm²)	pH
Hbis1.ini	7.0	0.086	0.28	2516.7	0	56.2	229.2	10.1
Hbis1.mid	5.3	0.148	0.25	2691.1	12	49.6	229.2	NA
Hbis1.fin	4.2	0.151	0.26	2381.6	19	46.8	229.2	10.1
Hbis2.ini	55.6	0.072	0.12	2555.5	0	53.6	217.2	10.1
Hbis2.mid	62.2	0.100	0.27	2590.9	12	51	217.2	NA
Hbis2.fin	62.0	0.134	0.26	2232.0	19	48.1	217.2	10.1
Hbis3.ini	299.5	0.071	0.11	2574.8	0	53.8	223.2	10.1
Hbis3.mid	338.3	0.087	0.32	2610.0	12	48.8	223.2	NA
Hbis3.fin	230.8	0.088	0.49	1961.4	19	45.8	223.2	NA
Hbis3.fin2	282.2	0.866	0.89	1612.1	76	42.3	223.2	NA
Hbis3.fin3	25.5	0.939	0.86	1151.2	89	39.1	223.2	10.1
Hbis3.fin4	1.3	1.096	0.99	1238.1	101	36	223.2	9.9
Hbis4.ini	761.9	0.056	0.30	2986.7	0	55.4	223.2	10.1
Hbis4.mid	798.8	0.066	0.23	3262.3	12	50	223.2	NA
Hbis4.fin	660.9	0.086	0.25	2518.7	19	47.1	223.2	NA
Hbis4.fin2	590.3	0.632	0.68	919.4	76	43.7	223.2	NA
Hbis4.fin3	41.2	0.671	0.80	616.0	89	40.4	223.2	9.8
Hbis4.fin4	3.2	0.787	0.70	709.2	101	37	223.2	9.5

Series J

	Ca (ppm)	B (ppm)	Na (ppm)	Si (ppm)	Time (days)	Vol. (ml)	S (mm²)	pH
J3.ini	449.1	0.078	0.20	2891.5	0	46.9	223.2	10.1
J3.fin	0.7	0.962	0.68	749.6	101	43	223.2	9.7
J3bis.ini	149.7	0.098	0.08	1325.5	0	50.2	223.2	10.1
J3bis.fin	159.7	0.811	0.92	NA	101	46.2	223.2	9.7
J4.ini	764.9	0.079	0.25	2437.3	0	49.9	223.2	10.1
J4.fin	89.9	NA	NA	256.5	101	46.2	223.2	9.0
J4bis.ini	894.3	0.101	0.50	3059.3	0	51	223.2	10.1
J4bis.fin	574.5	NA	NA	NA	101	46.9	223.2	9.0

Series K

	Ca (ppm)	B (ppm)	Na (ppm)	Si (ppm)	Time (days)	Vol. (ml)	S (mm²)	pH
K1.ini	1.641	0.014	0.03	270.1	0	50.6	960	10.1
K1.mid	1.109	0.074	0.14	275.4	10	50.6	960	NA
K1.fin	0.765	0.096	0.21	274.2	21	47.6	960	10.1
K3.ini	0.032	0.026	<LoQ	540.9	0	49.4	960	10.1
K3.mid	0.049	0.252	0.35	561.5	10	48.9	960	NA
K3.fin	0.060	0.362	0.52	566.6	21	45.9	960	10.1

Chapitre VI. CONCLUSION GENERALE ET PERSPECTIVES

En France, les produits de fission et actinides mineurs, issus des combustibles nucléaires, sont vitrifiés puis entreposés sur leur site de production (La Hague, Marcoule), en attendant l'ouverture du site de stockage géologique profond dans la Meuse/Haute-Marne, Cigéo (**chapitre I**). La sûreté du site repose sur un concept multi-barrières. La première barrière est le verre nucléaire, spécifiquement formulé pour confiner les radionucléides. Chaque colis, constitué d'une enveloppe en acier inoxydable et de 400 kg de verre, sera ensuite placé dans un conteneur de stockage en acier faiblement allié avant d'être placé dans des alvéoles de stockage, forage horizontal soutenu par un tube guide, lui aussi en acier faiblement allié. La dernière barrière est la roche hôte, une couche d'argilite du Callovo-Oxfordien d'environ 120 m d'épaisseur. Cette couche possède une faible perméabilité aqueuse, une faible porosité et diffusivité ainsi qu'une très bonne stabilité géologique. L'espace entre le tube guide et la formation argileuse est rempli d'un matériau cimentaire destiné à neutraliser les effets de l'oxydation des argilites et à constituer un environnement favorable à la corrosion lente des aciers. Malgré les divers dispositifs de sûreté mis en place pour retarder et limiter l'action de l'eau, il est estimé qu'après quelques centaines à quelques milliers d'années après la fermeture du site, de l'eau entrera en contact avec le verre sous forme de vapeur puis après plusieurs centaines de milliers d'années, sous forme liquide.

Le verre nucléaire est un matériau silicaté présentant un ordre à courte distance (comme les cristaux) mais dénué d'ordre à plus longue distance (> 1nm). Pour des raisons thermodynamiques, le verre s'altère en milieu aqueux, et par ce processus libère dans la phase liquide les radioéléments solubles qu'il contenait. Dès lors, **la compréhension des mécanismes d'altération des verres est essentielle à l'établissement des modèles de relâchement des radionucléides dans l'environnement**. Ces modèles sont une des composantes de l'analyse de sûreté du stockage géologique.

L'altération des verres dans l'eau liquide a été étudiée par de nombreuses équipes de recherche depuis le milieu des années 1980 (**chapitre II**). Une première phase d'hydratation permet aux molécules d'eau de pénétrer au sein de la structure vitreuse. Les premiers échanges commencent alors entre la solution et les éléments modificateurs du réseau vitreux : c'est la phase dite d'interdiffusion. Les molécules d'eau hydrolysent aussi les liaisons pontantes. Ces premiers stades de l'altération constituent le régime initial, caractérisé par une vitesse maximale de dissolution. Par la suite un gel protecteur se forme à la surface du verre. Durant la formation de ce gel, la vitesse d'altération diminue à cause i) du phénomène de diffusion qui prend place au sein du gel et limite le transport des espèces aqueuses et ii) de la diminution de l'affinité entre le verre sain et la solution dont la composition chimique se sature peu à peu par rapport à celle du verre. Cependant, le gel est

une entité dynamique qui évolue avec le temps : par des réactions de condensation des groupements silanols, le gel se densifie et augmente ainsi ses propriétés de passivation. La vitesse d'altération atteint alors un minimum, c'est la vitesse résiduelle. Dans certaines conditions, la précipitation de phases secondaires incluant les éléments relâchés par le verre, peut entraîner une reprise d'altération.

Ce processus d'altération, basé sur la réaction réversible d'hydrolyse de certains formateurs de réseau, est considéré comme commun à tous les silicates. De plus, un second mécanisme basé sur la rupture totale des liaisons reliant les constituants du verre et la reprécipitation au niveau d'un film fluide interfacial d'une couche enrichie en silice, a ensuite été proposé, d'abord pour les silicates cristallins, puis pour les silicates amorphes. Ce mécanisme considère la présence d'une pellicule de fluide nanométrique à l'interface entre le gel et le matériau sain, dans laquelle le matériau sain peut se dissoudre. Cette pellicule étant sursaturée par rapport à la composition du matériau sain, les éléments dissouts reprécipitent quasiment instantanément pour former le gel.

Une des différences fondamentales entre les deux mécanismes réside dans le fait que toutes les liaisons connectant un silicium à ses plus proches voisins sont coupées dans le cadre du mécanisme de dissolution – reprécipitation. Cet atome peut donc migrer avant que de nouvelles liaisons chimiques ne se reforment. Il en résulte que le gel qui se forme dans ces conditions n'est pas une relique du matériau sain mais une entité nouvelle de type précipité. De plus, les cinétiques de mise en solution des éléments solubles du verre diffèrent entre les deux mécanismes. **Ce mécanisme fondamental additionnel nécessite-t-il de revoir les modèles cinétiques de dissolution du verre établis jusque-là ?** Afin d'approfondir cette question, nous avons altéré un silicate amorphe, un verre albitique, et son équivalent cristallin, un feldspath de composition proche du pôle albitique, en milieu acide (pH 1,5 et 3) à 90°C pendant 12 jours et 33 jours (**chapitre III**). Les analyses FIB-MET ont révélé des processus de dissolution fondamentalement différents : la structure ordonnée de l'albite a mené à une dissolution préférentielle de certaines lamelles enrichies en Ca, en comparaison aux lamelles enrichies en Na , créant un motif particulier de rugosité en surface. A pH 3, l'albite cristallisée développe une surface complètement passivante après quelques jours d'altération. Initialement, la solution a été marquée au ^{29}Si afin de pouvoir suivre son incorporation au sein du gel et ainsi, questionner le mécanisme de formation de ce dernier. Les résultats ont démontré que, concernant l'albite cristallisée à pH 1.5, la contribution de la solution à la formation du gel est seulement de 35% à 45%. Ce résultat est surprenant puisqu'une contribution à hauteur de 100% serait attendue pour un mécanisme de dissolution – reprécipitation. Un mécanisme hybride a été suggéré où les propriétés de transport du gel ont progressivement évolué vers soit une dépolymérisation incomplète du réseau silicaté ou une repolymérisation du réseau en incorporant le SiO_2(aq) présent dans l'eau porale.

A l'opposé, les résultats de l'analyse du verre albitique ont démontré une contribution mineure du mécanisme de dissolution – reprécipitation (< 20%). Le principal mécanisme de dissolution est basé sur la diffusion des protons au sein de la structure amorphe et l'hydrolyse du réseau silicaté. Outre le mécanisme d'hydrolyse du Si, des effets antagonistes de l'Al sur la dissolution ont été mis en évidence. Ces effets s'expliquent de la façon suivante : les liaisons Al-O présentent une énergie d'activation pour leur hydrolyse plus faible que celles des liaisons Si-O. Elles sont donc plus facilement hydrolysables. En revanche la présence d'Al renforce les liaisons Si-O voisines. Dans la composition de l'albite (Si/Al = 3), l'aluminium a pour effet de renforcer la matrice silicatée dans les structures ordonnées mais de fragiliser celle-ci dans les structures désordonnées, en créant, notamment des canaux de diffusion pour les espèces aqueuses. Des travaux de modélisation et des calculs thermodynamiques ont été effectués afin de confirmer ces résultats et d'étendre les connaissances sur l'effet de cet élément sur l'altération des verres. **Cette étude montre ainsi l'importance de l'effet de la structure et de la composition des matériaux altérés sur leur mécanisme et leur vitesse de dissolution. Cependant, vis-à-vis des modèles cinétiques existants, leur révision sur la base du mécanisme de dissolution – reprécipitation ne semble pas nécessaire pour les verres malgré l'absence de prise en compte de l'Al comme pôle passivant dans le modèle.**

En plus de propriétés extrinsèques du matériau, les mécanismes de dissolution des silicates vitreux comme cristallins dépendent également des propriétés de la solution altérante. Concernant l'altération du verre en condition de stockage, il est attendu que l'eau soit enrichie en silice et calcium, notamment au contact du matériau de remplissage. Le calcium est un élément qui, d'après la littérature, produit des effets antagonistes sur l'altération des verres (**chapitre II**). En fonction du pH (7 – 11.7) et du rapport entre surface du verre et volume de solution altérante, plusieurs effets ont été mis en évidence. Dans un premier temps, le calcium de la solution peut pénétrer dans le gel et interagir avec la silice du verre pour augmenter la rétention des éléments et limiter le relargage des constituants du verre. De plus, il peut précipiter avec la silice pour former une couche protectrice riche en Ca et Si à la surface du gel. Par ailleurs, le calcium peut aussi participer à la recondensation du gel en jouant un rôle de catalyseur. **Quels effets le calcium induit-il sur les propriétés de transport des espèces aqueuses dans le gel ? Peut-on quantifier ces effets ?** Dans cette thèse, l'effet contributeur du Ca à la passivation du verre a été étudié en altérant un verre simplifié, dans une solution proche de 51% de la saturation par rapport à la silice amorphe et avec une concentration de calcium croissant de 0 ppm à 240 ppm pendant 21 jours (**chapitre IV**). Le verre étudié possède les 6 oxides majoritaires du verre nucléaire, c'est le verre ISG (International Simple Glass) – wt% 56.2 SiO_2, 17.3 B_2O_3, 12.2 Na_2O, 6.1 Al_2O_3, 5.0 CaO, 3.3 ZrO_2. La solution a été enrichie initialement en ^{29}Si et ^{18}O afin d'étudier leur incorporation au sein du gel. Les signatures isotopiques dans les produits d'altération ont révélé la

présence de phases secondaires à la surface du gel, l'absence de pénétration du ^{29}Si au sein du gel mais une forte présence de l'^{18}O qui parvient jusqu'au verre sain sans présenter de gradient marqué. Le mécanisme de dissolution – reprécipitation n'est pas dominant dans ces conditions : la réaction d'hydrolyse a permis l'échange entre les oxygènes de la solution et du gel tandis que la réaction de recondensation a empêché le relargage des atomes de Si en solution, et par conséquent leur échange avec ceux apportés par le fluide.

Concernant l'effet du calcium, une forte corrélation négative a été trouvée entre la quantité de calcium initialement en solution et l'épaisseur du gel après 21 jours d'altération, à pH 10.3. Cette corrélation peut s'expliquer par la formation d'une couche riche en silice et en calcium, comme mentionné précédemment. Cependant, les analyses de FIB-MET ont démontré l'existence d'une zone électroniquement plus dense à la surface du gel, suggérant une densification de cette zone. Il est alors possible que le calcium ait (aussi) participé à la réaction de recondensation des silanols en jouant un rôle de catalyseur. Quoiqu'il en soit, durant les 21 premiers jours d'altération, le calcium a participé à l'augmentation de l'effet de passivation du gel, bien que cette augmentation reste modeste (la diffusivité des couches diminue d'un facteur 2.2 lorsque la concentration initiale en Ca augmente de 0 à 240 ppm). A des fins de quantification, nous avons étudié les propriétés diffusives de 5 gels à travers différentes méthodes de calculs. Dans un premier temps, nous avons considéré les coefficients de diffusion sur la base de l'épaisseur totale du gel mesuré en ToF-SIMS et en ICP-OES, basé sur le relargage du B en solution. Une comparaison a ensuite été faite avec des coefficients de diffusion calculés sur la base d'une expérience de traçage permettant l'incorporation de ^{10}B et du bleu de méthylène (contenant du soufre) dans le gel. Si la principale différence peut s'expliquer par une différence de température entre l'expérience d'altération, qui a lieu à 90 °C, et celle de traçage, qui a lieu à 25 °C, plusieurs hypothèses ont été émises afin de questionner la précision des méthodes utilisées. Premièrement, les coefficients de diffusion estimés sur la base de l'épaisseur totale du gel englobent les variations des propriétés de passivation du gel qui ont eu lieu au cours de l'expérience alors que ceux issus de l'expérience de traçage ne rendent compte que de la diffusivité du gel à la fin de l'expérience. De plus, il existe potentiellement une différence de diffusivité entre un élément qui est incorporé dans le gel et un élément qui en est relargué. Enfin, il est aussi possible que le gel ait évolué après la fin de l'expérience en continuant sa densification ou en fermant sa porosité. Afin d'étudier plus en détails la porosité du gel et son effet sur la diffusivité, nous avons comparé l'incorporation du ^{10}B avec une molécule présentant *a priori* un plus fort encombrement stérique, le bleu de méthylène. Les résultats identiques entre ces deux éléments suggèrent soit i) que la taille des pores et des canaux est trop grande pour être discriminante et par conséquent, ne contrôle pas la diffusivité au sein du gel, ii) que la spéciation du B a permis la formation d'oligomères, de sorte que la

différence de taille entre les deux molécules est moindre que celle à laquelle on aurait pu s'attendre, expliquant les résultats similaires obtenus, iii) que le B est adsorbé dans la porosité d'ISG, créant des tétraèdres de B chargés négativement, limitant sa diffusivité au sein du gel.

Globalement, cette étude a permis de confirmer un rôle positif quoique minime du calcium sur la passivation des verres au cours de l'altération en milieu fortement basique (ici $pH^{90°C}$ 10.3) à temps courts. Sa présence au cours de l'altération agit sur la diffusivité des espèces dissoutes dans le gel et retarde l'altération du verre. Des coefficients de diffusion ont été calculés par différentes méthodes afin de quantifier les effets du calcium sur le gel. Par ailleurs, au cours de cette étude, plusieurs types de précipités ont été mis en évidence : de la silice (expériences à concentration nulle ou négligeable en Ca), des silicates de calcium hydratés (CSH) (expérience à [Ca] intermédiaire) et des carbonates de calcium (expériences les plus enrichies en [Ca]). Au terme des 21 jours d'altération, ces différentes phases secondaires ne semblent pas avoir eu d'effet sur la vitesse d'altération du verre. Il est cependant admis que la précipitation des CSH peut être à l'origine de reprise d'altération (**chapitre II**). Les CSH sont les principaux liants qui se retrouvent dans les ciments de Portland. Ils se caractérisent par leur ratio Ca/Si et leur structure cristalline est proche de celle de la tobermorite : une structure lamellaire en feuillets qui englobe une couche d'oxyde de calcium par deux chaines silicatées (*dreierketten*). On distingue généralement trois domaines de compositions de CSH : 0.6 < Ca/Si < 1.0, puis 1.0 < Ca/Si < 1.5 et enfin 1.5 < Ca/Si < 2.0 qui seront repris par la suite pour les calculs thermodynamiques comme les CSH0.8, CSH1.2 et CSH1.6. Cependant, les CSH sont des précipités qui se carbonatent très facilement en présence de CO_2 dissous. Afin de pouvoir étudier leur effet sur l'altération du verre, il est donc nécessaire de travailler dans une atmosphère exempte de CO_2.

Étant donné que le matériau cimentaire de remplissage contient du calcium et de la silice, il est attendu que la solution altérante venant de la formation argileuse se soit enrichie en calcium à son contact. Par conséquent, une précipitation de CSH dans le milieu réactionnel est envisagée. **A quel point la précipitation de CSH dans le milieu réactionnel peut être critique concernant les mécanismes et les cinétiques de dissolution du verre ?** Afin de répondre à cette question, mais aussi d'étendre l'étude aux effets de la silice et du calcium sur des temps d'altération plus longs, le verre ISG a été altéré à pH 10, 90°C dans des solutions plus ou moins concentrées en silice dissoute et en calcium pendant 20 jours environ pour les temps courts et 3 mois pour les temps longs. Il est à noter que la réactivité du verre ISG dans de telles conditions demeurait jusqu'à présent essentiellement inexplorée. A la suite de cette étude, une forte corrélation négative a été mise en évidence entre la concentration en silice dissoute et la vitesse d'altération du verre. La solubilité apparente du gel se situe entre 2% et 9% de celle de la silice amorphe. Au-delà, la dissolution demeure globalement faible et contrôlée par la diffusion au sein du gel passivant. **Ce résultat confirme qu'indépendamment de la présence de**

calcium dans le milieu, la présence de silice en solution suffit à réduire de plusieurs ordres de grandeurs la vitesse de dissolution du verre ISG. De manière similaire à l'étude précédente, les phases secondaires n'ont pas présenté d'effet sur la vitesse d'altération durant les 19 premiers jours d'altération. L'effet du calcium a, quant à lui, été masqué par celui du silicium. **Seule la néoformation des CSH présente un effet de second ordre, en comparaison avec la silice, sur la vitesse d'altération du verre.** En comparant ces résultats à ceux de l'étude précédente, on peut suggérer que le calcium, dont la contribution était masquée par celle du silicium, joue un rôle passivant dans les 20 premiers jours d'altération, notamment à travers la formation d'une couche riche en (Si, Ca). Cependant, après cette première période qui correspond à l'initiation de la formation des CSH en solution, ces derniers croissent suffisamment vite pour déstabiliser le gel passivant. C'est à partir de ce moment-là qu'une reprise d'altération est observée, après une durée comprise entre 19 jours et 76 jours d'altération dans nos conditions expérimentales. **En parallèle de la croissance des CSH, des carbonates de calcium précipitent en solution et limitent la reprise de dissolution du verre ISG. La formation de ces carbonates entraine une diminution du pH qui limite la solubilité de la silice, et par conséquent, sa disponibilité pour former des CSH. Suite à cette compétition entre formation de CSH et de carbonates de calcium, la vitesse de dissolution du verre diminue et le mécanisme limitant qui avait évolué durant la période de reprise d'altération, revient à un régime diffusif.**

Ces résultats soulignent globalement un impact modéré quant à l'effet des précipités sur une potentielle reprise d'altération du verre. En effet, le paramètre principal affectant la vitesse de dissolution du verre est l'état de saturation de la solution par rapport à la silice amorphe. Même si les CSH engendrent une reprise d'altération en consommant de la silice en solution, elle devrait être rapidement limitée par la présence de CO_2 dans le milieu qui permettra la formation de carbonate de calcium.

En replaçant l'ensemble des résultats obtenus au cours de ces travaux dans un contexte plus large, cette thèse revisite le débat sur la nature du mécanisme à l'origine de la formation des couches d'altération sur les silicates vitreux et cristallisés. Elle apporte ainsi des éléments de discussion aux modèles afin de les améliorer. Il est à noter cependant que cette comparaison a eu lieu en milieu acide et que les expériences menées en milieu basique ont porté sur l'altération d'ISG qui n'a pas d'équivalent cristallins. Afin d'améliorer notre compréhension de la dissolution des systèmes silicates, il serait potentiellement intéressant de reproduire ces expériences et cette comparaison entre silicate amorphe et cristallin à un pH basique. Cela permettra d'étudier l'effet du pH sur le mécanisme d'altération mais aussi de quantifier le poids de chacun des mécanismes dans un tel milieu.

Outre les conclusions qui peuvent être reliées directement aux conditions de stockage géologique profond des déchets radioactifs vitrifiés et à l'altération du verre nucléaire en milieu basique, cette thèse apporte des données qui peuvent être utilisées afin de tester les modèles prédictifs existants et leurs hypothèses constitutives. Initialement, un premier essai aurait dû être effectué dans le cadre de cette thèse sur le modèle GRAAL1 développé par le CEA. Cependant, il s'est révélé que ce modèle ne pouvait pas en l'état s'appliquer aux conditions de notre étude. En effet, le seul pôle passivant pour GRAAL1 est le pôle SiAl dont l'aluminium n'a jamais été détecté en ICP-OES. De plus, dans les conditions d'altérations de nos expériences, c'est le pôle SiCa qui est passivant alors que ce rôle ne lui est pas attribué dans GRAAL1. Un second modèle, GRAAL2, est en cours d'étude mais son développement n'était pas encore suffisamment avancé pour être utilisé au cours de cette thèse. Une piste serait de comparer dans le futur les résultats obtenus dans les chapitres IV et V avec ceux simulés par un tel modèle et, à terme, d'améliorer ce modèle sur la base de ces comparaisons.

Enfin, par soucis de clarté et de compréhension, nous avons simplifié le système étudié à un verre à 6 oxides dans un environnement chimique où les deux seuls éléments apportés par la solution sont le calcium et le silicium. Dans le cadre du stockage géologique, d'autres éléments comme le Mg, le Fe, ainsi que des anions seront présents. Le Mg peut former des argilites et des MSH (Mg-Si hydroxides) à plus faible pH (pH < 10) que les CSH, entrainant une consommation de silice en solution et par suite, ils deviennent un moteur de l'altération du verre. L'aluminium est aussi un candidat pour une complexification paramétrique étant un élément peu soluble qui favorise la précipitation de zéolites en milieu basique. Enfin, le Fe, comme le Mg, est un élément pouvant entraîner la formation d'argiles. Cependant, sa disponibilité en solution diminue avec l'augmentation de pH car l'acier tend à se passiver en milieu basique. Cette concentration seuil de fer en solution qui influence l'altération du verre n'a pas encore été déterminée. D'une façon plus générale, il convient d'étudier les effets des différentes phases néoformées sur l'altération du verre dans un système plus complexe. Ces phases néoformées peuvent impacter de manière plus ou moins importante la formation du gel et, par conséquent, le passage à la vitesse résiduelle d'altération sur le long terme.

Il conviendrait alors de complexifier cette étude par étapes successives afin de se rapprocher des conditions d'une solution saturée par rapport à la roche Callovo-Oxfordien et du verre nucléaire SON68, qui est le verre R7T7 désactivé. Concernant la complexification de la solution, des études sur le comportement du verre en présence d'eau proche de la composition de la roche Callovo-Oxfordien ont déjà vu le jour et d'autres études sont encore en cours. Néanmoins, la solution altérante le verre R7T7 ne sera pas seulement chargée en élément du Callovo-Oxfordien mais sera un mélange de cette roche et du matériau cimentaire. L'étude du comportement du verre en contact avec cette nouvelle solution peut représenter une nouvelle piste d'étude. Concernant la complexification de la

composition du verre, nous pouvons noter que ISG est un verre contenant seulement les 6 oxides majeurs présents dans le verre nucléaire SON68, lui-même contenant une trentaine d'oxides.

Cette thèse présente ainsi une méthodologie qui permet d'identifier les principaux paramètres clés, parmi ceux étudiés, de la durabilité des verres, et d'en étudier la sensibilité vis-à-vis de la cinétique d'altération. Même si le système étudié a été simplifié, il permet une approche étape par étape qui permet de distinguer, analyser et comprendre les différents mécanismes et procédés qui sont indispensables à la prédiction du comportement des verres sur des échelles de temps géologique.

RESUME VULGARISE

La sureté du stockage géologique des déchets nucléaires de haute activité est un sujet au cœur des grands challenges scientifique et technologique de notre siècle. Ces déchets, issus des combustibles nucléaires, sont vitrifiés et entreposés sur les sites de production (La Hague, Marcoule) en attendant l'ouverture d'un site de stockage. Leur durabilité chimique fait l'objet de nombreux travaux pour évaluer le temps caractéristique associé à l'éventuel relargage des radionucléides dans l'environnement. Cette thèse s'inscrit dans cette thématique et repose sur deux axes d'études : le premier concerne l'effet du désordre structural sur la dissolution. Ce premier axe a démontré que les silicates vitreux et cristallins s'altéraient suivant des mécanismes proches, une hydrolyse incomplète du réseau silicaté étant observée principalement pour les verres. Le deuxième axe concerne la dissolution d'un verre modèle dans un environnement riche en Ca et Si. Alors que le Si en solution ralentit l'altération du verre, les phases secondaires (principalement des silicates de calcium hydratés) entretiennent l'altération du verre, alors que la précipitation des carbonates de calcium inhibe cet effet. Enfin, nous avons confirmé que le Ca dissous a intrinsèquement un effet protecteur vis-à-vis de l'altération des verres.

POPULARIZED ABSTRACT

The safety of high activity nuclear waste geological storage is at the heart of great scientifical and technological challenges of this century. These waste materials, inherited from nuclear combustible, are vitrified, and stored on production site (La Hague, Marcoule), waiting for the opening of a storage site. The chemical durability of these materials is the object of extensive studies to evaluate the characteristic time associated with the possible release of radionuclides in the environment. To address this question, this thesis relies on two axes: the first concerns the effect of the structural disorder on dissolution. This first axis has demonstrated that vitreous and crystalline silicates undergo similar alteration mechanisms, with incomplete hydrolysis of the silicate network observed mainly for glasses. The second axis focuses on the dissolution of a model glass in an environment rich in dissolved Ca and Si. While Si in solution slows down the glass alteration, secondary phases (mainly calcium silicate hydrates) sustain glass alteration, whereas the precipitation of calcium carbonates inhibits this effect. Finally, we have confirmed that dissolved Ca inherently provides protection against glass alteration.